Max-Planck-Institut für Polymerforschung

Max Planck Institute for Polymer Research

Mesoporous Organosilica for Heterogeneous Visible Light Photocatalysis

Dissertation

Zur Erlangung des Grades

Doktor rerum naturalium (Dr. rer. nat.)

im Promotionsfach Chemie

dem Fachbereich Chemie, Pharmazie, Geographie und Geowissenschaften

der Johannes Gutenberg-Universität Mainz

Wenxin Wei

Geboren in Shaanxi (China)

Mainz 2021

JOHANNES GUTENBERG UNIVERSITÄT MAINZ

The thesis was carried out from September 2017 until September 2021 within the department of Physical Chemistry of Polymers under the supervision of Prof. Dr. Katharina Landfester and in the group of Prof. Dr. Kai Zhang at the Max Planck Institute for Polymer Research, Mainz.

Dekan: Prof. Dr. Tanja Schirmeister

Prodekan: Prof. Dr. Till Opatz

Prof. Dr. Tobias Reich

Gutachter 1: Prof. Dr. Katharina Landfester

Gutachter 2: Prof. Dr. Pol Besenius

Date of oral examination: 06/12/2021

Affidavit

I hereby declare that I wrote the dissertation submitted without any unauthorized external assistance and used only sources acknowledged in this work. All textual passages which are appropriate verbatim or paraphrased from published and unpublished texts, as well as all information obtained from oral sources, are duly indicated and listed in accordance with bibliographical rules. In carrying out this research, I complied with the rules of standard scientific practice as formulated in the statutes of Johannes Gutenberg-University Mainz to insure standard scientific practice.

……

(Wenxin Wei)

Acknowledgements

This PhD thesis is the output of the effort and support of several people to whom I am extremely grateful. First and foremost, I would like to thank my esteemed supervisor – ***Professor Dr. Katharina Landfester*** *for her invaluable supervision, support and tutelage during the course of my PhD degree. Despite her busy agenda, she supported me continuously and gave me constant encouragement and guidance in all stages of my doctoral journey. It has been a privilege and pleasure to conduct such interesting research for four years at the Max Planck Institute for Polymer Research with you.*

I also would like to express my deepest appreciation to my co-supervisor ***Professor Dr. Kai Zhang*** *for his scientific guidance, encouragement, patient explanation, and immense knowledge. He provided me the opportunity to join his research team, invested a lot of his time and efforts in me, guided me to explore the photocatalysis world. Especially when I met problems during experiments, he was patient and helped me solve those problems. Without his numerous encouragement and critical suggestions, it would have been difficult for me to achieve the current research. I am sincerely grateful for his presence, attention and guidance during the last 4 years.*

I would like to offer my thanks to my group leader ***Dr. Calum Ferguson*** *for his treasured support which was really influential in shaping my experiment methods and critiquing my results. I thank* ***Christoph Sieber*** *and* ***Katrin Kirchhoff*** *for TEM measurement and helpful discussions. I thank* ***Gunnar Glaßer*** *for SEM measurement and his interesting talk. I also thank* ***Christine Rosenauer*** *for DLS measurement. I also thank my former colleagues,* ***Dr. Wei Huang***, ***Dr. Run. Li***, ***Dr. Jeehye Byun*** *and* ***Dr. Niklas Huber*** *for their practical help, support, and assistance. I wish to express my deep gratitude to my fellow lab-mates,* ***Thomas***, ***Julian***

*and **Rong**, for the wonderful time we had in the lab as well as the fruitful discussions we had during our group meetings. And also to my friends from the institute: **Dr. Shuai Jiang**, **Dr. Yinzhou Guo**, **Dr. Zhaoliang Zheng**, **Shuai Chen**, **Junren Wang** for their support and giving me the courage to pass through the tough moments in both my study and life.*

I would like to give special thanks to my dissertation committee for agreeing to evaluate my work. I truly appreciate all of their time, and constructive comments.

I greatly appreciate the financial support from the China Scholarship Council (CSC) and the joint Max Planck graduate center (MPGC). I am really grateful for all opportunities they provided me to take part in workshops, seminars, international conferences and social events.

*Last but not the least, I would like to warmly thank my parents, my wife **Jiaxin Yang** and my friends for their unconditional support, encouragement and patience throughout my PhD.*

Abstract

The main target of this thesis is to develop a new class of mesoporous organosilica as metal-free, heterogeneous and visible light-active photocatalysts for organic synthesis and biocatalysis. The design and synthesis of organosilane monomers have been developed, and the relation of the structure and morphology of the obtained organosilica materials to their photocatalytic applications investigated.

First, a series of mesoporous organosilica photocatalysts are designed for visible light-promoted aryl azoline formation. Different ratios of 1,4-bromophenyltriethoxysilane (BPTS) (50%, 75% and 100%) were chosen as the monomers for the synthesis of the backbone precursor with tetraethyl orthosilicate (TEOS) by hydrolysis condensation. The photoactive diphenyl benzothiadiazole ($BTPh_2$) units were then formed via successive coupling methods, obtaining the final organosilica. Photocatalytic formation of aromatic aldehydes with various amines, 2-phenyl-2-imidazoline, 2-phenyl-2-oxazoline, 2-phenyl-2-thiazoline and their derivatives could be formed with high conversion (89%) and selectivity (97%). Additionally, the organosilica photocatalyst showed high stability and reusability.

Secondly, to solve the issue of cooperation between native enzymes and photocatalysis system in aerobic conditions, core-shell structured porous nanophotoreactors are designed for highly stable and recyclable photobiocatalysis under aerobic conditions. The enzymatic cofactor NAD^+ can be efficiently regenerated from NADH by the photoactive organosilica core, while photogenerated active oxygen species are trapped and deactivated through the non-photoactive shell, protecting the enzymatic material. The versatility of these photocatalytic core-shell nanoreactors was demonstrated in tandem with two different enzymatic systems, glycerol dehydrogenase and glucose 1-dehydrogenase, where long term enzyme stability was

observed for the core-shell photocatalytic system.

Finally, in order to improve the light absorption and energy transfer in organosilica photocatalysts, increasing photocatalytic efficiency, the photocatalytic center was embedded in an aromatic ring structure which was designed to enhance light collection. The aromatic ring effectively absorbs different wavelengths of light, and the excited energy is funneled into the photocatalytic center through energy transfer. Compared with the direct excitation of $BTPh_2$ as single photocatalytic units to regenerate NADH, the efficiency of the multi-component organosilica is increased by 50 %, and no additional hydrogen source was required. These results demonstrate the design principle of mesoporous organosilica photocatalysts containing multiple photoactive components that mimic the light-trapping antenna mechanism in natural photosynthesis.

Zusammenfassung

Das Hauptziel dieser Arbeit ist die Entwicklung einer neuen Klasse mesoporöser Organosilikamaterialien als metallfreie, heterogene und durch sichtbares Licht aktivierbare Photokatalysatoren für die organische Synthese und Biokatalyse. Das Design von Organosilanmonomeren und deren Synthese wurde entwickelt. Die Beziehung zwischen der Struktur und Morphologie der erhaltenen Organosilikamaterialien und ihren photokatalytischen Anwendungen wurde daraufhin untersucht.

Zunächst wurde eine Reihe von mesoporösen Organosilika-Photokatalysatoren für die durch sichtbares Licht geförderte Bildung von Arylazolin entwickelt. Verschiedene Mengen von 1,4-Bromphenyltriethoxysilan (BPTS) (50%, 75% und 100%) wurden als Monomere für die Synthese der Grundgerüstvorstufe mit Tetraethylorthosilikat (TEOS) durch Hydrolysekondensation genutzt. Die photoaktiven Diphenylbenzothiadiazol ($BTPh_2$)-Einheiten wurden anschließend durch aufeinanderfolgende Kopplungsmethoden gebildet, um das endgültige Organosiliciumdioxid zu erhalten. Die photokatalytische Bildung von aromatischen Aldehyden mit verschiedenen Aminen, 2-Phenyl-2-imidazolin, 2-Phenyl-2-oxazolin, 2-Phenyl-2-thiazolin und ihren Derivaten konnte mit einem hohen Umsatz von 89% und einer Selektivität von 97% erfolgen. Außerdem zeigte der Organosilica-Photokatalysator eine hohe Stabilität und Wiederverwendbarkeit.

Ebenfalls, um das Problem der Zusammenarbeit zwischen nativen Enzymen und dem Photokatalysesystem unter aeroben Bedingungen zu lösen, wurden poröse Nanophotoreaktoren mit Kern-Schale-Struktur für eine hochstabile und recycelbare Photobiokatalyse unter aeroben Bedingungen entwickelt. Der enzymatische Cofaktor NAD^+ kann durch den photoaktiven Organosiliciumdioxid-Kern effizient aus NADH regeneriert

werden, während die photogenerierten aktiven Sauerstoffspezies durch die nicht-photoaktive Schale eingefangen und deaktiviert werden, wodurch das enzymatische Material geschützt wird. Die Vielseitigkeit dieser photokatalytischen Kern-Schale-Nanoreaktoren wurde im Tandem mit zwei verschiedenen Enzymsystemen, der Glycerin-Dehydrogenase und der Glucose-1-Dehydrogenase, demonstriert, wobei eine langfristige Enzymstabilität für das photokatalytische Kern-Schale-System beobachtet wurde.

Um die Lichtabsorption und den Energietransfer in Organosilica-Photokatalysatoren zu verbessern und damit die photokatalytische Effizienz zu erhöhen, wurde das photokatalytische Zentrum in eine aromatische Ringstruktur eingebettet, die die Lichtsammlung verbessern soll. Der aromatische Ring absorbiert effektiv verschiedene Wellenlängen des Lichts, und die angeregte Energie wird durch Energietransfer in das photokatalytische Zentrum gelenkt. Verglichen mit der direkten Anregung von $BTPh_2$ als einzelne photokatalytische Einheiten zur Regeneration von NADH ist die Effizienz des mehrkomponentigen Organosilicas um 50 % erhöht, und es war keine zusätzliche Wasserstoffquelle erforderlich. Diese Ergebnisse demonstrieren das Konstruktionsprinzip mesoporöser Organosiliciumdioxid-Photokatalysatoren, die mehrere photoaktive Komponenten enthalten und den Licht einfangenden Antennenmechanismus in der natürlichen Photosynthese imitieren.

Contents

List of figures

List of tables

List of schemes

1. Introduction

Light is one of the foundations for the origin of life. The study of light derives from many major scientific fields, ranging from As for the studies of light in chemistry, photochemistry is an important branch of chemistry that studies the chemical effects of light during chemical reactions, which began in the early twentieth century.[1] Furthermore, photocatalysis, as part of photochemical research, has been the focus of research in the past 20 years. Compared with traditional catalysis, which mostly is carried out under thermal conditions, photocatalysis uses solar energy to complete various catalytic reactions under much milder conditions. To name a few, photocatalytic decomposition of water into hydrogen and oxygen, photocatalytic organic synthesis and photocatalytic wastewater treatment belong to the most attractive applications of photocatalysis. In order to effectively convert the energy of visible light – the most energetic part of the total solar spectrum – into chemical energy, chemists and materials scientists have made great efforts in the development of visible light-active photocatalytic systems in recent years. In the developed catalytic systems, transition metal complexes[2-6] and organic dyes[7-9] have been identified as highly efficient molecular photocatalysts. However, the high price, toxicity, scarcity of precious metals, especially low recyclability of these molecular catalysts significantly inhibit their application in the chemical and biological fields. To address these issues, metal-free alternatives as graphene oxide, carbon nitride, conjugated porous polymers, organic frameworks and conjugated triazine frameworks have attracted particular interest as a new generation of photocatalysts.

Furthermore, from the reaction kinetic standpoint, the rate of material transfer largely influences the catalytic efficiency of the catalyst. Therefore, highly porous materials are indeed highly advantageous for catalytic processes. In particular, mesoporous materials can significantly improve the mass transfer in the catalytic process, and the high specific surface

area caused by the mesoporous structure makes the catalytic sites more widely distributed, thereby improving the catalytic efficiency. However, there are relatively few studies on the application of photocatalysis. Therefore, it is very desirable to develop a heterogeneous non-metallic photocatalyst based on mesoporous organosilica.

2. Aim of work

In this thesis, the development of mesoporous organosilica as metal-free, heterogeneous and visible-light-active photocatalysts for challenging organic synthesis and biocatalysis is described. This thesis consists of the following main parts (**Scheme 1**):

1. Development of organosilane monomers containing photocatalytic units, which are able to construct mesoporous materials with Si-O-Si as the skeleton. The instability of siloxy groups in coupling reactions and acidic or basic environments affects the design of synthetic routes and the choice of purification methods. The replacement of sensitive groups and the design of synthetic routes are effective strategies to achieve monomer synthesis.

2. The structural design of mesoporous organosilicas, with particular attention to different structures and composition, are used to produce high value-added chemicals and expand the possibility of photocatalysis in the field of biocatalysis. First the sol-gel synthesis of mesoporous organosilica was achieved, where this photocatalytic material produced can be used for organic catalysis. Secondly, core-shell organosilica nanophotoreactors were synthesized which prevent active oxygen, generated by photocatalysis, from approaching and degrading biological structures. Finally, in order to improve the light absorption and energy transfer in organosilica photocatalysts with increasing photocatalytic efficiency, the photocatalytic center was embedded in an aromatic ring structure which was designed to enhance light collection.

3. Green reaction conditions were adopted, such as using molecular oxygen as oxidant, water as a green solvent and exploring new organic conversion and application systems suitable for the designed catalyst. Mesoporous organosilicon photocatalysts catalyze aryl azoline formation reaction which can be used to synthesize high-value products. Furthermore, core-

shell photocatalytic organosilica can protect enzymes from reactive oxygen species (ROS) generated by the photocatalytic process, and produce products through enzyme cascade reactions. In addition, the mesoporous organosilica containing photocatalytic center and aromatic ring framework improved energy transfer for NADH regeneration.

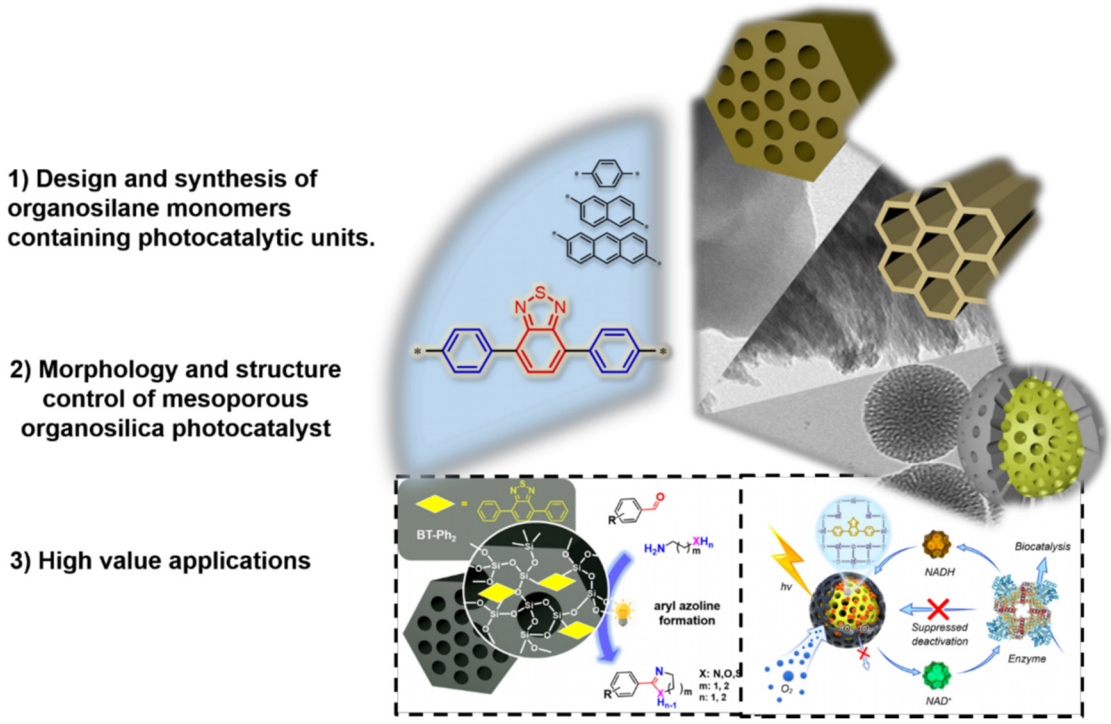

Scheme 1. Synthesis of mesoporous organosilica and application of heterogeneous visible light photocatalysis.

In order to facilitate a comprehensive study, this work is divided into five chapters: The first two chapters, chapter 1 and 2, cover the theory and aim of work, then the 3rd chapter gives an overview of the current state of art and presents the fundamental aspects of photocatalysis, visible light photocatalysis, organic porous photocatalysts, mesoporous organosilica and photobiocatalysis concept. Chapter 4 describes briefly the main characterization methods employed in this work. Chapter 5 reports and interprets thoroughly the results acquired in this work with a summary and perspective at the end. The experimental details are provided in chapter 6.

3. State of the art

3.1 Photocatalysis

In the past few decades, due to the consumption of fossil fuels, increasing challenges of energy demand and environmental issues have stimulated growing awareness in the society. With the rapid growth of industrialization and population, it is estimated that by 2050, the world will need twice the current energy supply.[10, 11] At present, the world's energy demand is mainly dependent on fossil fuels such as oil, coal, and natural gas, which are rapidly depleting. The consumption of fossil fuels inevitably produces harmful emissions to the environment. Therefore, discoveries and frontiers in the fields of energy-related materials science and engineering have been pursued to overcome barriers to effective energy conversion and environmental protection.[12] In various renewable energy projects, photochemistry or -catalysis, in which inexhaustible, clean solar energy can be collected as a viable technology,[13-27] has gained considerable interdisciplinary attention due to its different potentials in environmental applications. So far, the direct conversion of solar energy into chemical energy.and solar fuels have been regarded as one of the most green and sustainable ways to solve future energy and environmental crises.

In 1972, Fujishima and Honda[28] discovered that the photolysis of water on the TiO_2 electrode was considered a milestone in stimulating the photocatalytic method to study photon energy conversion, although the history of photocatalysis can be traced back to the 1960s.[29-32] Since then, people have conducted a lot of research on TiO_2 photocatalysis, focusing on understanding the basic principles,[33, 34] to improve the efficiency of photocatalysis and to expand the scope of application.[35] In 1976, Carey reported the photocatalytic degradation of organic pollutants when TiO_2 was present in the aqueous suspension.[36] Three years later, Inoue

and colleagues studied the photocatalytic reduction of CO_2 to various organic compounds using semiconductor powders (such as TiO_2, ZnO, SiC, GaP, and CdS) in aqueous solutions.[37] Since then, as reported in many reviews, significant progress has been made in the manufacture of high-efficiency semiconductor-based photocatalysts.[38-44]

The triggering process during photocatalysis is to initiate or accelerate specific reduction and oxidation (redox) reactions in the presence of irradiated semiconductors. When the energy of the incident photon matches or exceeds the energy bandgap of the semiconductor, subsequent separation of the electron-hole pairs occurs, which can then trigger reduction or oxidation reactions.[35, 45, 46] Initially, the energy of the incident photon is stored in the semiconductor by light excitation. It is converted into a chemical form through a series of electronic processes and surface/interface reactions.

Contrary to the thermodynamics of traditional catalysis, photocatalysis can promote not only spontaneous reactions ($\Delta G < 0$) but also promote non-spontaneous reactions ($\Delta G > 0$). In the former case, the input energy is used to overcome the activation barrier to promote photocatalysis at an increased rate or under milder conditions (**Figure 1a**). In the latter case, part of the input energy is converted into chemical energy and accumulated in the reaction product (**Figure 1b**).

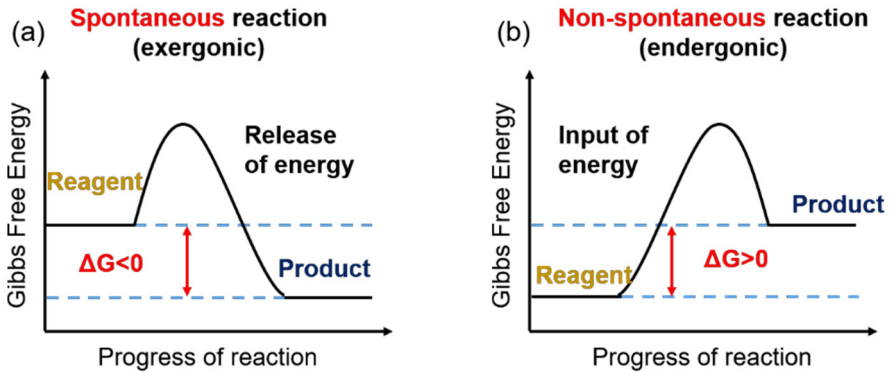

Figure 1. Changes in Gibbs free energy in case of (a) exergonic and (b) endergonic reactions.

Generally, the semiconductor photocatalytic cycle includes three steps: first, light induces electrons to transition from valence band (VB) to conduction band (CB), leaving the same number of vacancies (holes); second, the excited electrons and holes migrate to the surface; Third, they react with the absorbed electron donor (D) and electron acceptor (A) respectively. In the second step, most electron-hole pairs recombine, dissipating the input energy in the form of heat or emitted light. In order to prevent the recombination of electron-hole pairs, the commonly used method is to support co-catalysts such as Pt, Pd, NiO, and RuO_2 on the surface of the semiconductor. The heterojunction formed between the host semiconductor and the promoter provides an internal electric field, promotes the separation of electron-hole pairs, and induces faster carrier migration. In addition, these promoters exhibit better conductivity, lower overpotential, and higher catalytic activity than the host semiconductor, so they are usually ideal active sites for photocatalytic reactions.

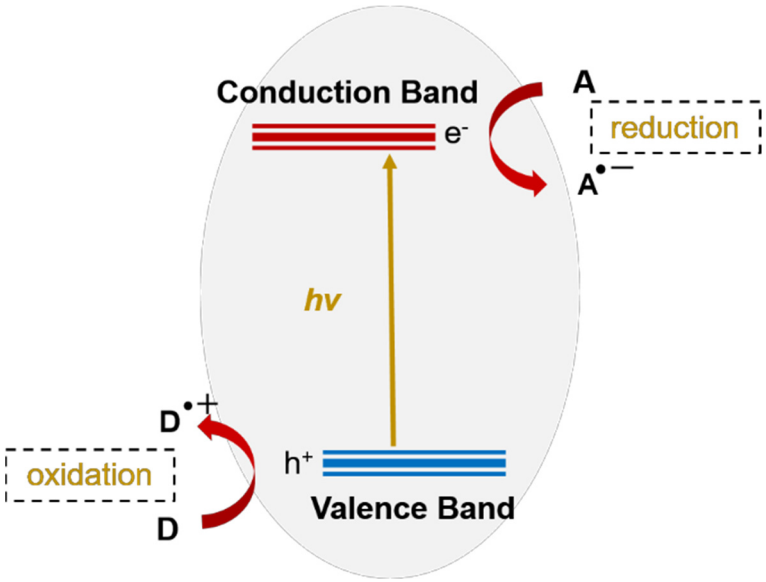

Figure 2. Schematic illustration of the formation of photogenerated electron-hole pairs upon absorption of light. A: electron acceptor, D: electron donor.

3.2 Visible light photocatalysis

Many inorganic semiconductors, such as TiO_2 and ZnO, have been widely used in water decomposition, dye degradation, and organic synthesis.[47, 48] However, due to its wide bandgap, only high-energy photons from the ultraviolet (UV) range can be used to initiate photocatalytic reactions. Since ultraviolet light only accounts for about 3% of the total solar energy, the use of ultraviolet light-active photocatalysts certainly leads to limited feasibility, and high-energy ultraviolet light likely causes undesirable site reactions. In order to overcome these limitations, considering that the visible light range of the solar spectrum covers approximately more than ten times of that of UV light, the design and development of visible light-active photocatalytic systems have recently attracted widespread attention. Visible light accounts for the largest part (44%) of the solar spectrum and artificial lighting sources. In the past ten years, a considerable number of visible light-responsive photocatalysts with efficient solar energy utilization have been developed. A wide range of photoredox reactions have been tested, such as transition metal complexes,[49-51] organic dyes,[52-57] Metal sulfides,[58] metal oxides,[59-61] graphite carbon

nitride,[62, 63] and metal/organic composite materials.[64-67]

3.2.1 Homogeneous visible light photocatalysts

Homogeneous photocatalysis means that the photocatalyst and the substrate are in the same solvent phase. Taking the widely studied transition metal complex $Ru(bpy)_3^{2+}$ as an example，which is the most comprehensively studied transition metal complex in organic synthesis via photocatalysis. The complex exhibits a strong and broad absorbance in the visible light range, resulting into a long-living excited state.[49, 68] This light-excited complex is both a more potent oxidant and a stronger reducing agent than its corresponding ground state; it is worth noting that both electrochemical potentials are within the range of practical chemical work. Therefore, photoactivation of $Ru(bpy)_3^{2+}$ is most commonly used to drive processes initiated by single electron transfer. This feature contributes to developing many strategies for converting solar energy into electrical energy and electrochemically produced chemical fuels.[69-71] In organic synthesis, $Ru^*(bpy)_3^{2+}$ can initiate the one-electron reduction of a variety of electron-deficient substrates and affect the one-electron oxidation of electron-rich substrates. In other words, the photoinduced electron transport properties of $Ru(bpy)_3^{2+}$ can be easily connected to the electrochemically induced transformation of organic molecules (**Figure 3**).

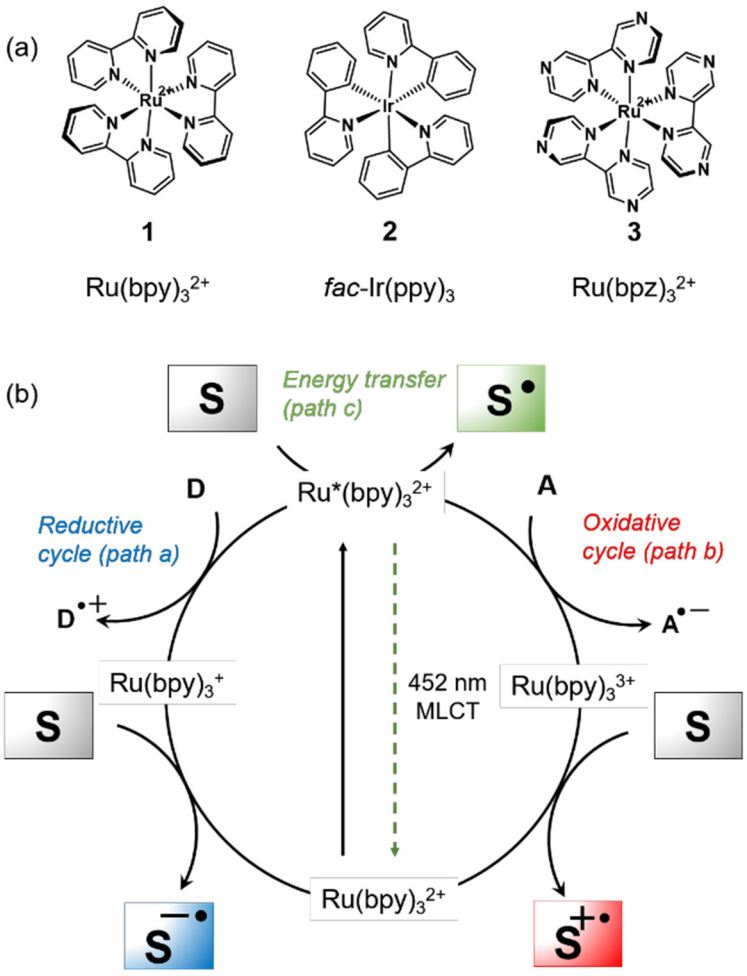

Figure 3. (a) Ruthenium and iridium complexes, (b) Photoexcited $Ru^*(bpy)_3^{2+}$.

Alternatively, $Ru^*(bpy)_3^{2+}$ can directly transfer energy to a suitable organic substrate (**Figure 3b**, path c).[68] The resulting electrons stimulate the reaction of the organic compound to be completely different from the ground state. These high-energy intermediates can usually be used to construct strained or other structurally abnormal molecular scaffolds, which are difficult to assemble by non-photochemical methods.[72, 73]

The photoactivation of organic molecules through the electron transfer process is called photo-induced electron transfer (PET) sensitization, or more recently, photoredox catalysis. Similarly, the indirect generation of electronically excited states of organic substrates is called photosensitization or energy transfer photocatalysis.[74]

Although metal complexes are at the forefront of homogeneous photocatalysis, metal systems still have drawbacks. For example, the high cost, rare availability and toxicity of precious metals have led to the further development of metal-free alternatives.[75] Recently, other metal bases based on chromium (III), iron (II), nickel (0), zirconium (IV), cerium (III), molybdenum (0), cobalt (III), and uranium (VI) Coordination compounds and copper (I) (**Figure 4a**) have attracted much attention as cost-effective alternatives to the Ru and Ir counterparts.[76-78] Among them, copper complexes have attracted attention due to their unique coordination chemistry and various redox chemical behaviors, leading to broad applications in different catalysis fields, namely, water splitting,[79] and CO_2 reduction.[80, 81] Nevertheless, these materials still face challenges related to the impact of metals on the environment. As photoredox catalysts for organic conversion, organic dyes (**Figure 4b**) have recently attracted special attention due to their low cost, metal-free properties, and high reproducibility.

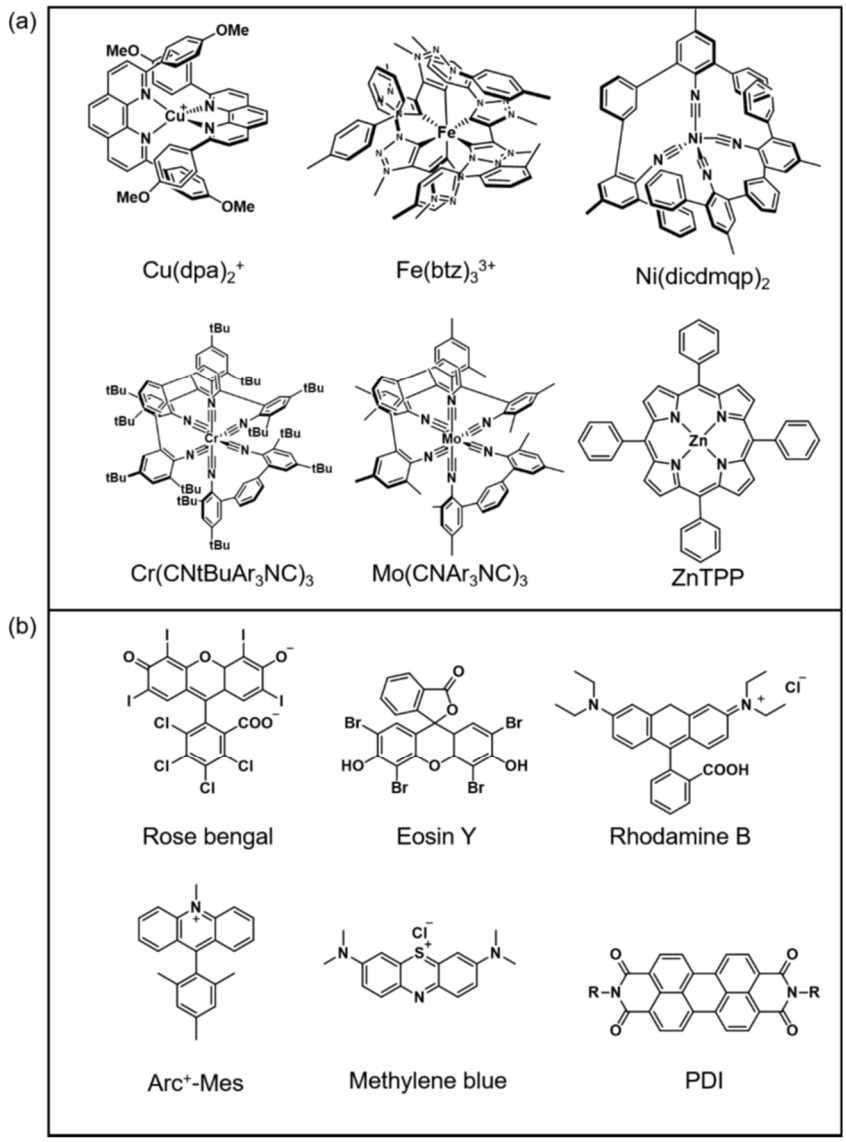

Figure 4. Chemical structures of (a) some metal complexes and (b) some organic dyes for photocatalysis.

Generally speaking, although homogeneous photocatalysts have high photocatalytic efficiency and considerable development, these molecular metal or organic systems still have inherent defects. In addition to the high cost and rarity of transition metals, common instability and homogeneity result in low recyclability and reusability of the catalyst. Therefore, people are paying more and more attention to the development of multiphase photocatalytic systems.

3.2.2 Heterogeneous visible light photocatalysts

Heterogeneous photocatalysis means that the photocatalyst and the substrate are in

different phases. This process mainly involves electron and energy transfer, similar to homogeneous photocatalysis (**Figure 5**): During the lighting, electrons are excited from the valence band (VB) of the photocatalyst to its conduction band (CB), and at the same time, oxidation and reduction entities are generated. On a single particle. Then, the photo-generated hole/electron pair can oxidize and reduce the electron donor/acceptor substrate through single electron transfer.[82-84] Intensive research work is devoted to the development of efficient heterogeneous photocatalysts for synthesis and environmental applications, including metal-based (for example, inorganic semiconductors: metal oxides, metal sulfides, modified metal oxides (Doping, surface modification, dye sensitization) and non-metallic bases; (for example organic semiconductors: carbon nitride, such as graphene, reduced graphene oxide, g-C3N4 and polyoxometalate (POM).[58-61, 63-66]

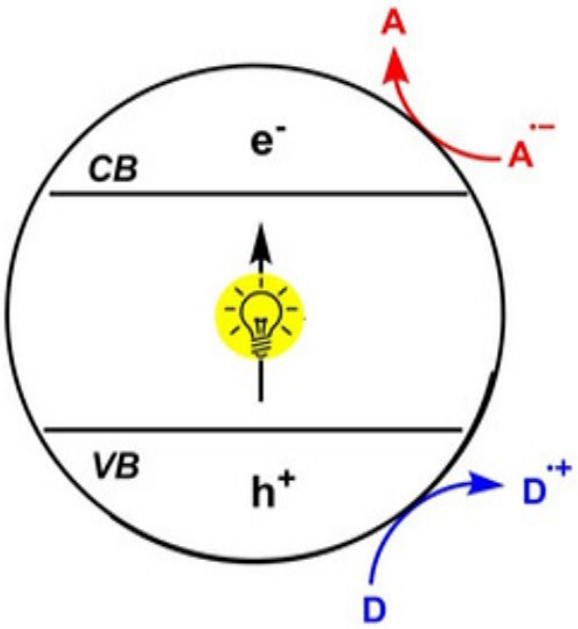

Figure 5. Heterogeneous photoredox catalysis. A: Acceptor; D: Donor, (e^-, h^+): photogenerated electrons and holes.[82] Copyright 2020 Wiley-VCH Verlag GmbH & Co. KGaA.

In order to extend their absorption range to the visible light range, different methods have

been developed, including foreign element doping,[85-91] dye sensitization,[92-94] hydrogenation[95, 96] and so on. Rueping and colleagues reported the use of TiO_2 P25 as an effective photocatalyst for visible-light-driven Meerwein arylation of heteroaromatic compounds in the presence of aryl diazonium salts.[97] The authors revealed that the surface complex between TiO_2 and the reagent is the cause of visible light absorption: The aryl diazonium salt contacts with the titanium dioxide P25 to form a titanium dioxide-diazonium ether complex, which establishes a new electron donor energy level above the VB of the metal oxide, thereby narrowing the bandgap. Other researchers focused on the so-called "dye sensitization technology" as a more effective strategy to increase the absorption of TiO_2 to a broader range of visible light.[98] In addition to TiO_2-based photocatalysts, several metal oxide semiconductors have been developed as effective heterogeneous photocatalysts that promote important organic transformations,[99] including zinc oxide (ZnO),[100-102] niobium pentoxide (Nb_2O_5),[103, 104] tungsten trioxide (WO_3),[105-107] bismuth oxide (iii) (Bi_2O_3),[108-111] and bismuth vanadate ($BiVO_4$).[112] For example, Furukawa and colleagues demonstrated the ability of Nb_2O_5 to oxidize primary, secondary, and cyclic amines under visible light irradiation.[104] Cadmium-based photocatalysts such as cadmium sulfide (CdS) and cadmium selenide (CdSe) have also been used in various visible light organic conversions.[113-116] One of the main advantages of these materials is the ability to adjust their optical properties by modifying the size of the nanoparticles.[117] For example, CdS nanosheets demonstrated their efficiency in the photocatalytic oxidative coupling of benzylamine and imine under visible light.[114] Interestingly, lead halide perovskite ($APbX_n$) has become a promising material with tunable optical properties used in organic synthesis.[118] The formation of symmetric and asymmetric disulfides by thiol photocatalysis has been achieved, for example, the use of $CsPbBr_3$ in the air and under blue light irradiation.[119]

Although various semiconductor photocatalysts have been developed as effective catalysts for organic conversion under visible light, the utilization of precious metals has severely hindered their practical application due to the high cost and limited variability of precious metals. In order to solve these problems, there is a great need to develop photocatalysts with earth-rich elements of heterogeneous photocatalysts without metals. In 2009, Antonietti and colleagues reported a metal-free photocatalyst based on graphite carbon nitride (g-C_3N_4) for hydrogen evolution.[120] The graphite plane is composed of tri-s-triazine units connected by plane amino groups (**Figure 6**). In recent years, many researchers have tried to improve the photocatalytic efficiency[121] and morphological engineering[122-124] of g-C_3N_4 by changing monomer precursors,[125] copolymerization,[126] hetero-element doping post-modification methods.[127-130] Since then, g-C_3N_4 has been widely used as an efficient metal-free visible light photocatalyst for various photocatalytic reactions, such as hydrogen evolution,[131, 132] CO_2 reduction, [133, 134] selective oxidation of alcohols,[135] oxidative coupling of benzylamine derivatives,[136] selective oxidation of sulfides,[137] hydrogenation of benzene[138] and photopolymerization.[139]

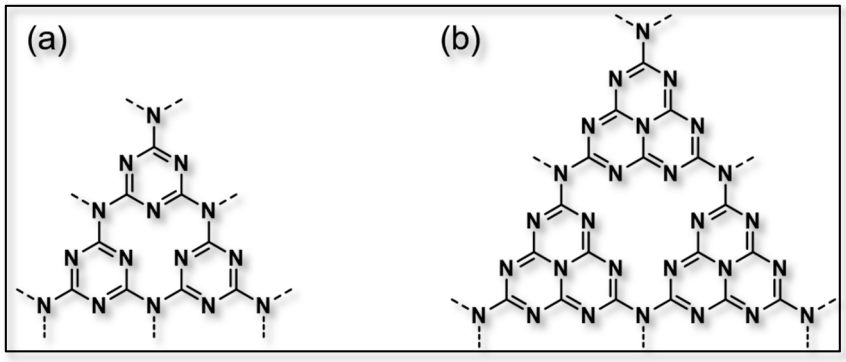

Figure 6. Structure of carbon nitrides consisting of (a) triazine (b) and heptazine.

There are also semiconductor materials that use different methods to make pores, which also belong to the category of porous photocatalysts. Zhao and coworkers used mesoporous

silica as a hard template to synthesize mesoporous metal oxides and chalcogenides, including Fe_2O_3, WO_3, CdS.[140] Kim et al. pre-hydrolyzed titanium alkoxides and used concentrated HCl solution to re-dissolve the obtained precipitate.[141] It is found that the aqueous solution of titanium oxychloride complex can easily penetrate into the mesopores of SBA-15, MSU-H and KIT-16 templates. After calcination at 450 °C to remove silica, a mesoporous TiO_2 material with clear and regular mesopores, a specific surface area as high as 258 $m^2 \cdot g^{-1}$, and a crystalline framework of anatase phase are obtained.[141] Using HNO_3 aqueous solution as the solvent, Yue et al synthesized a highly ordered mesoporous TiO_2 material.[142] Chandra et al. reported using an amphiphilic chelating surfactant as a soft template to synthesize a microporous TiO_2 material with a wormhole-like pore structure.[143] Chalcogenides, including CdS, CdSe, and ZnS, have been synthesized by direct templating of lyotropic organic liquid crystals derived from $(EO)_{10}$-oleyl.[144] Using Brij56 as a template, hierarchical large mesoporous photocatalysts have been successfully synthesized, such as titanium phosphate and binary metal oxides.[145-147] The group of Zhao developed a method of "acid-base pair" synthesis for mesoporous metal oxides.[148] With this method, the synchronous assembly of TiO_2 and SiO_2 oligomers in presence of P123 was achieved (**Figure 7**).[149]

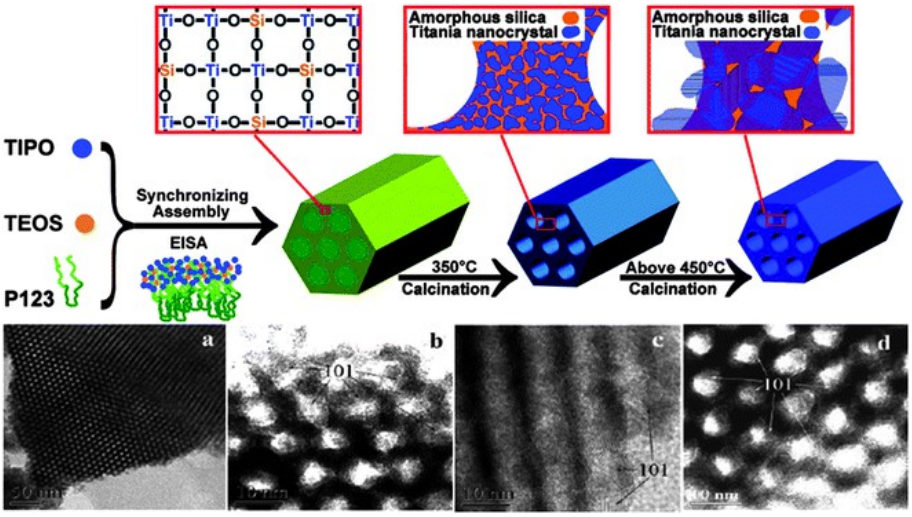

Figure 7. Schematic diagram (upper) illustrating the synchronous assembly of titanate oligomers due to the

hydrolysis of titanium isopropoxide (TIPO) and silicate species because of the hydrolysis of tetraethyl orthosilicate (TEOS) in the presence of P123 template to form a highly ordered mesoporous TiO_2–SiO_2 composite.[149] Copyright 2007 American Chemical Society.

Sanchez and coworkers used spray drying technology to prepare mesoporous hollow TiO_2 spheres by adding polystyrene (PS) spheres to the feed solution.[150] The team of Wiesner developed a combined assemble of soft and hard methods to prepare highly crystalline mesoporous TiO_2/PS spheres with sp2-hybrid carbon were used as soft templates to form macroporous metal oxides.[151] Subsequent calcination in an inert environment causes the PS spheres to be converted to carbon. Carbon serves as the structural support of the highly crystalline metal oxide without structural collapse. Hydrothermal treatment of a dilute hydrochloric acid solution containing TiF_4 can produce hollow TiO_2 spheres.[152, 153] In the presence of NH_4F, the large-scale synthesis of TiO_2 hollow spheres in an acidic mother liquor containing $Ti(SO_4)_2$[153] or $TiOSO_4$[154] has been described. Multi-component hollow spheres of TiO_2 coupled with SnO_2[154] or doped with N have been synthesized.

3.3 Organic porous polymer-based photocatalysts

Due to the direct correlation between the photocatalytic performance and the microstructure of the photocatalyst, finding new photocatalysts with suitable crystal structure and high surface area has always been a hot spot in heterogeneous photocatalysis research. Nano-sized particles with quantum size effect have obtained the most widespread success due to their large surface area and good dispersion ability and have excellent photocatalytic properties.[33, 45, 155, 156] Unfortunately, As one of the most popular photocatalysts, TiO_2 nanoparticles tend to aggregate in suspension, leading to a rapid loss of active sites and photocatalytic efficiency.[157] In addition, the separation, recovery and reuse of nanoparticles is another critical obstacle to practical applications. In addition, the management of nanoparticles also faces challenges because their particle size decreases, and their biocompatibility and

toxicity become more and more serious.[158-161]

These problems can be solved by creating a porous structured photocatalyst or dispersable nano-sized photocatalyst particles on a highly porous solid. The advantages of using porous photocatalysts are mainly in three aspects: (1) A high density of active centers on a large reactive surface during a photocatalytic reaction; (2) An enhanced light capture due to light reflection and scattering by the hollow spaces;[162] (3) Easily recycle and reuse of the photocatalyst after each photocatalytic process cycle.

3.3.1 Conjugated porous polymers

Conjugated porous polymers (CPPs) are a new class of metal-free pure organic heterogeneous photocatalysts composed of a completely π-conjugated system with delocalized electrons along the polymer backbone (**Figure 8**). The flexible combination of different electron donor and acceptor units endows CPPs with various physical and chemical properties, and the photocatalytic efficiency of specific reactions can be improved through structural adjustment. The cross-linked structure imparts permanent inherent (nano) porosity to CPPs, in addition, to complete π-conjugation, which makes them more unique among porous materials.[163, 164] These features are essential for photocatalysis. Therefore, CPPs are considered promising isomers and have developed rapidly in recent years.[165-167]

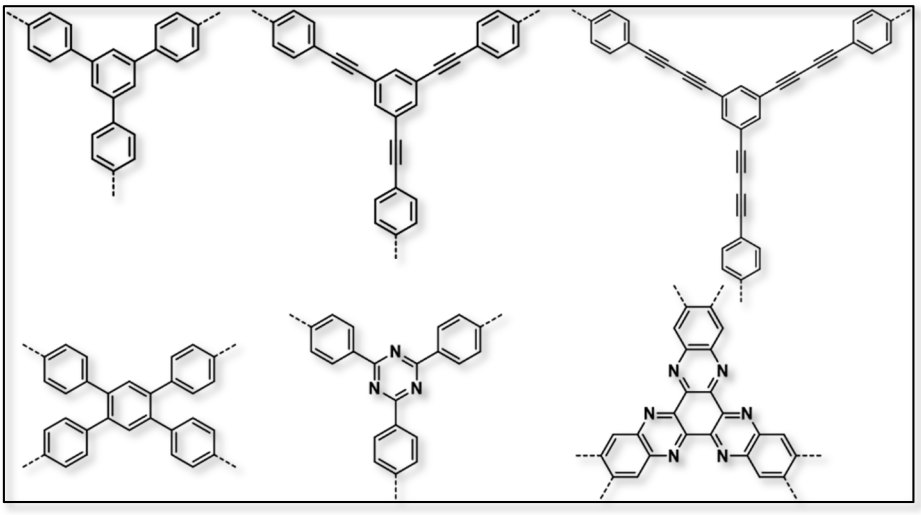

Figure 8. Some examples of conjugated porous polymers for photocatalysis.

In 2013, CPP was first demonstrated to be used for visible-light-induced chemical transformation. A series of polybenzothiadiazoles can catalyze the production of singlet oxygen ($^1O_2$) under blue light irradiation and α-terpinene into ascaridole.[168] Since then, many photoredox reactions have been carried out using CPP as a heterogeneous photocatalyst. Recent examples include radical polymerization,[169] selective oxidation of sulfides,[170] oxidative coupling of amines,[171] dehalogenation of halogenated ketones,[124] hydrogen[172-176] and oxygen evolution,[177, 178] reduction of 4-nitrophenol,[179] [2+2] cycloaddition,[180] metal-free Stille-type C-C coupling,[181] enantioselective α-alkylation[182] and so on.

A variety of synthetic schemes have been established to prepare CPP,[166] typical chemical routes are as follows (**Figure 9**): (i) metal-assisted cross-coupling reactions (such as Suzuki-,[169] Sonogashira-,[168, 183] Heck-,[184] Yamamoto-,[185] Glaser-,[186] Negishi-,[187] Kumada coupling reaction,[188] and oxidative polymerization,[189, 190] (ii) acid-[179, 191-193] and base-catalyzed polymerization,[172, 194] and (iii) thermally driven polymerization.[120, 195, 196] In addition, various template effects can be used to control the morphology. Post-synthetic modifications can also be considered to adjust the structure or function. Due to the strong covalent bonds within the

network, CPPs have excellent chemical stability, even in organic solvents, hydrofluoric acid and high-intensity radiation.[168, 197] Moreover, the critical feature of CPPs is their wide variety. The composition of different functionalized monomers can be incorporated into their main chain. This diversity of chemical reactions with various structural units has produced many CPPs in visible light-promoted photocatalytic applications.

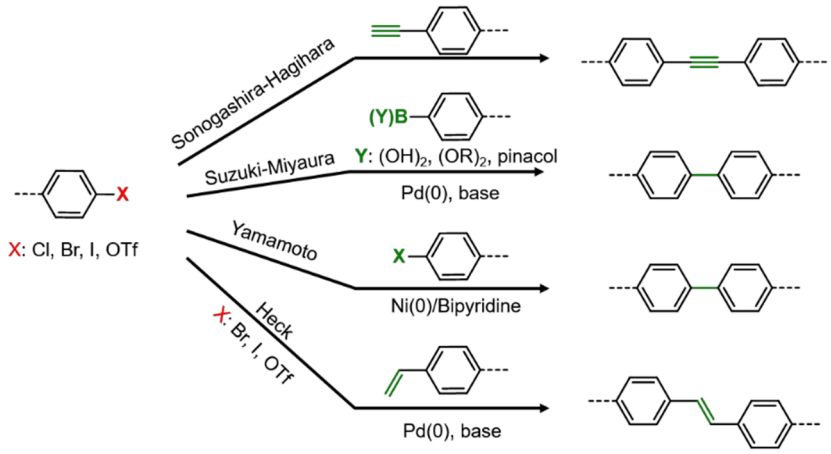

Figure 9. Most common synthetic routes of CMPs.

3.3.2 Covalent triazine frameworks

Covalent triazine framework (CTF) is regarded as a subclass of conjugated organic frameworks possessing the properties of fully conjugated polymers. They have a throughout fully π-conjugated backbone composed of triazine units with strong aromatic C=N bonds with permanent porosity (**Figure 10**). The first synthesis of CTF was carried out by trimerization of nitrile in molten $ZnCl_2$ at 400 °C for 40 h under ionic heating conditions.[198]

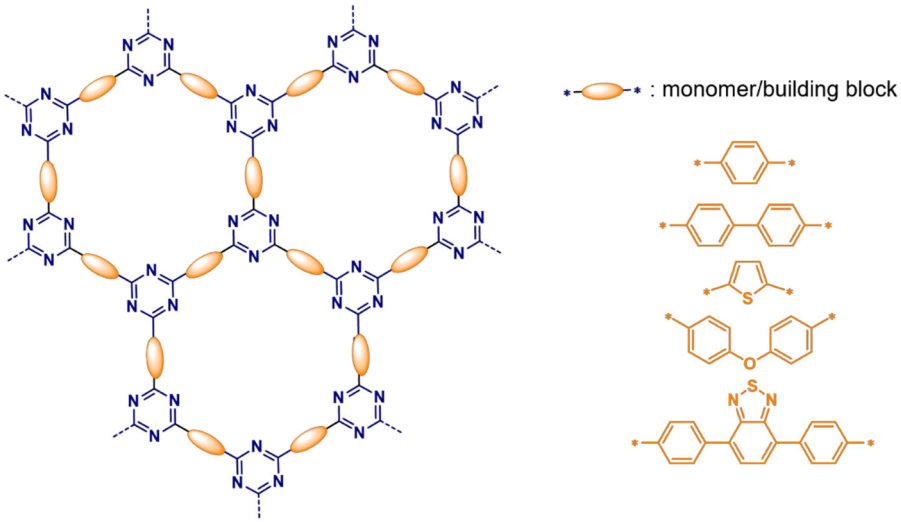

Figure 10. Schematic representation of covalent triazine frameworks.

In the past years, CTFs have demostrated applications in energy storage, gas absorption and catalysis relying on their excellent chemical stability and high porosity.[199-206] Importantly, their relatively low potential cost and avoidance of precious metal-catalyzed coupling chemistry make them attractive candidates for upgrades. For example, Thomas and colleagues reported a series of CTFs as effective metal-free base catalysts to convert CO_2 to organic carbonates.[207] A large number of basic nitrogen sites in the synthetic framework effectively catalyzes the formation of cyclic carbonates through the cycloaddition of CO_2 with different starting epoxides. A series of single-layer and multi-layer CTFs are edge-aligned through theoretical calculations.[208] They found that three strategies can effectively reduce the CTF bandgap, namely, interlayer coupling, adjustment of pore size, and nitrogen content to increase visible light absorption. Theoretical calculations clearly predict their semiconductor properties, their potential as metal-free visible light photocatalysts, and the advantages of low cost, excellent chemical and thermal stability .[208, 209]

However, traditional ionic thermal conditions quickly lead to undesirable partial carbonization of CTFs, making their energy levels thermodynamically unfavorable for the use of CTFs for photocatalytic conversion.[198, 210] To solve these problems, Lotsch and colleagues

synthesized polytriazine oligomers (PTO) under reduced temperature (300-350 °C) ionization heat conditions.[211] These oligomers show a good photocatalytic hydrogen evolution rate (HER) under simulated sunlight.

In order to avoid carbonization and use $ZnCl_2$ as a metal catalyst, a new method has been developed to prepare CTF-based membranes by low-temperature reaction (100 °C) in the presence of TfOH, using TfOH as a solvent and catalyst.[212] More recently, our research group has taken inspiration from these synthetic protocols together with their associated drawbacks and have developed a novel, facile, solvent-free synthesis route of CTFs under relatively mild conditions (**Figure 11**).[179, 213] In addition, Ren et al. used microwave-assisted synthesis to manufacture CTF.[214]

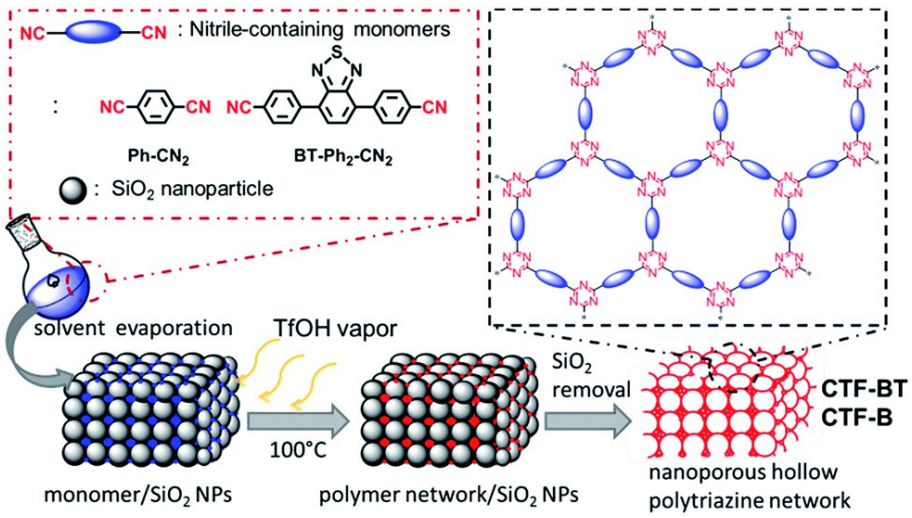

Figure 11. Schematic of solid state synthesis of CTFs.[179] Copyright 2016 Royal Society of Chemistry.

3.3.3 Covalent organic frameworks

Covalent organic frameworks (COFs) are a class of organic porous materials with a highly ordered and periodic network structure.[215, 216] By applying the principles of topological design to the synthesis of porous organic polymers through reversible chemical bonds, Yaghi and colleagues reported the first COF example in 2005.[216] Since then, the development of COF

with unique structural features and properties has aroused strong research interest in the scientific community (**Figure 12**). In order to obtain the COF with the required crystal structure and target function, various covalent bond strategies are used to guide the spatial orientation and determine the related topological structure. Covalent bond formation strategies can be divided into the following categories: boroxine linkage, borate linkage, triazine linkage, imine linkage, hydrazone linkage, β-ketoenamine linkage, azine linkage, imide linkage, carbon-carbon connection, *etc*.[217-220] COF synthesis methods, such as the most commonly used solvothermal method, usually require relatively harsh experimental conditions. In recent years, it has been reported that alternative methods including interface synthesis, mechanochemical synthesis, sonochemical synthesis, and post-synthesis modification help to prepare COF in a shorter time under less severe conditions and improve crystallization degree.[221, 222] Because COFs are connected by light elements (such as H, B, C, N, and O) through strong covalent bonds, they have many unique properties. Properties such as low density, high crystallinity, adjustable pore structure, good chemical stability, high surface area and easy surface modification make them particularly suitable for a variety of useful applications, including gas adsorption, storage and separation, catalysis, photoelectric conversion, and clean energy.[218, 219]

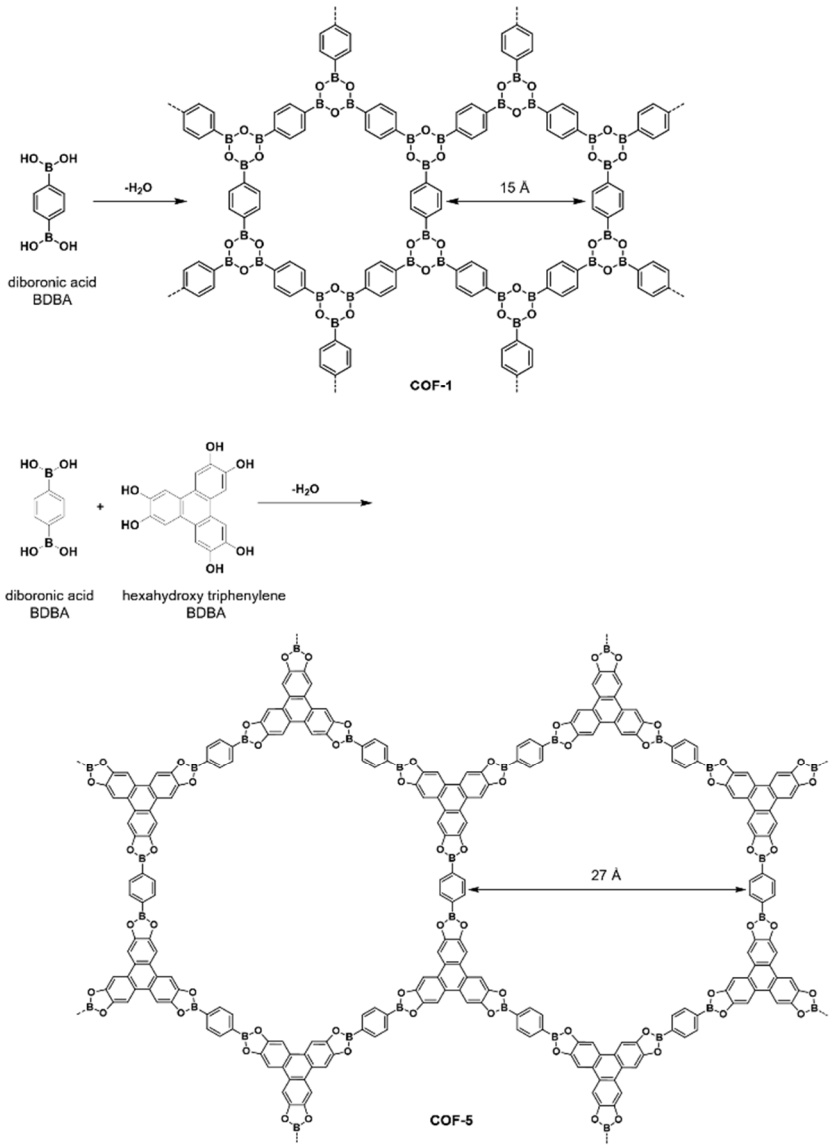

Figure 12. Condensation reactions of boronic acids used to produce discrete molecules and extended COFs.[223] Reprinted with permission from AAAS.

Compared with traditional semiconductors, COFs not only have some common characteristics but also have many notable advantages in photocatalysis: The structural design of COFs enables it to achieve the design of target structures and special properties related to photocatalytic reactions, such as excellent visible light-light absorption and rapid electron-hole separation and transfer; The large surface area of COFs enriches accessible catalytic sites. The highly crystalline and porous structure enables COFs to accelerate the transfer of charges to the surface and reduce the possibility of charge trapping caused by defects, thereby helping to

inhibit electron-hole recombination; COF with strong covalent bonds shows high chemical and thermal stability. The photosensitive unit fixed in a strong frame can avoid photo-corrosion and increase the lifetime of the excited state; The extended π conjugate structure in the plane and the stacking direction can achieve high charge carrier mobility.

3.3.4 Metal-organic frameworks

Metal-organic frameworks (MOFs) are a class of porous crystalline materials composed of metal nodes (metal ions or clusters) and organic linkers.[224] Due to their ultra-high specific surface area (over 6000 $m^2 \cdot g^{-1}$),[225] rich topological and easy-to-adjust porous structures,[226] MOFs have recently attracted more and more attention in the field of photocatalysis.[227-231] Distinct from classical inorganic semiconductors with delocalized conduction band (CB) and valence band (VB), MOF can be recognized as molecules arranged in a crystal lattice. In addition, some MOFs, such as MOF-5 ($Zn_4O(BDC)_3$, BDC: 1,4-benzodicarboxylate), UiO-66 ($Zr_6O_4(OH)_4(BDC)_6$) and MIL-125 ($Ti_8O_8(OH)_4(BDC)_6$) shows semiconductor-like behavior. Here, metal oxygen clusters and organic linkers can be regarded as isolated semiconductor quantum dots and light-absorbing antennas, respectively (**Figure 13**).[232-234] In the past few years, with the development of water/acid resistant MOF materials,[235] more and more light-responsive MOFs have been reported for photocatalytic removal of pollutants,[229, 236] bacteria disinfection,[237] H_2 production,[238, 239] CO_2 fixation,[240] selective transformation of organics[241-243] *etc.*

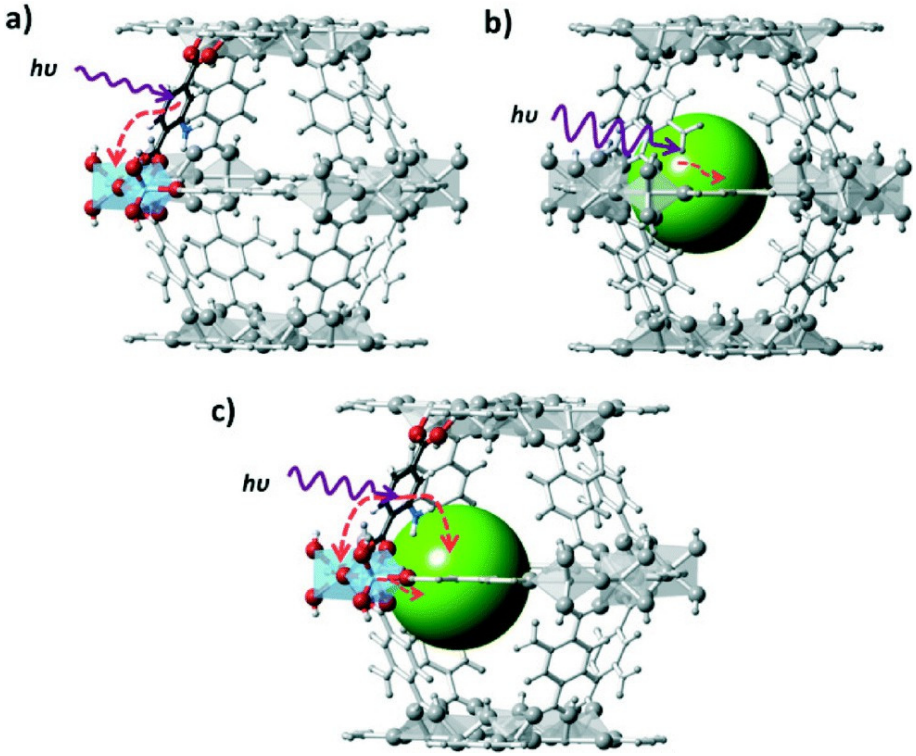

Figure 13. Different approaches to induce photocatalytic activity in a MOF scaffold: a) the organic linker is used as an antenna for light sensitizing and charge transfer to the inorganic cluster occurs; b) the MOF is used as a container for the encapsulation of a photocatalyst that directly absorbs light and c) charge transfer occurs between the MOF scaffold and the encapsulated catalyst.[233] Copyright 2014 Royal Society of Chemistry.

Due to many selections between metal ions/clusters and organic linkers, MOF has been given an extremely tunable photocatalyst to use sunlight effectively. For example, Wang summarized the photocatalytic degradation of organic pollutants in wastewater in 2014.[244] At that time, most photoactive MOFs were used to degrade dyes under ultraviolet or ultraviolet-visible light irradiation. A few MOFs that use visible light are listed, and H_2O_2 is usually needed as an oxidant. Later, Wang et al. further conducted a mini-review on the photocatalytic reduction of Cr(VI) by MOFs.[229] In the same year, Ye's group also summarized the progress of MOF photocatalysis. They mainly focus on several representative MOFs, including MOF-5, UiO-66(Zr), MIL-125(Ti) and MIL-101(Fe). Compared with traditional semiconductors, the reported MOF or MOF-based composite materials show good photocatalytic performance, especially in CO_2 reduction.[40] Qiu et al. also commented on modified MOF as a

photocatalyst.[245] They focused on the development of various modification strategies for typical light-responsive MOFs. Enhanced photocatalytic performance (pollutant removal, CO_2 reduction, H_2 production or organic conversion) has been reported using UV, UV-vis or visible light. Meanwhile, Bedia et al. conducted a review on the synthesis and characterization of MOFs for photocatalytic water purification.[228] Besides, a brief review of iron-based MOFs for visible light-induced photocatalysis was reported.[246] Jiang's research group summarized their recent contributions in MOF-based photocatalysis and photothermal catalysis, mainly focusing on H_2 production and selective organic conversion.[247] In addition, the highly migratable Cr(VI) and radiative U(VI) can be photoreduced to their corresponding trivalent states,, which are easily precipitated and separated from aqueous solutions. Gaseous pollutants such as NO and toluene can be photo-oxidized into harmless products and reported bacterial inactivation.[248, 249]

However, MOF-based photocatalysis is currently in its infancy and still faces some challenges and obstacles: Most photoactive MOFs are still in the lab-scale stage, and some preparation methods are complex and difficult to control; The stability of MOFs under harsh conditions (strongly acidic and alkaline pH) still needs to be improved; most of the metal nanoparticles supported by the photoactive MOF are precious metals (Pd, Pt, Au and Ag).

3.4 Mesoporous organosilica

Developed in 1999, periodic mesoporous organosilica (PMOs) are essentially ordered mesoporous organosilica prepared from a surfactant combination as a template and a sesquisiloxane an organosilica precursor. They are one of the first examples of so-called "hybrid" organic/inorganic materials (**Figure 14**). In the following years, various functional groups, forms and applications were developed. The most notable feature of PMO is the presence of organic parts in its framework, which can be modified and functionalized through

the use of various organic reactions. In addition, the presence of organic fragments and their adjacent silanol groups provides the possibility to synthesize well-defined bifunctional structures. Synergistic effects can enhance the potential applications of these materials, especially in applications such as adsorption and catalysis. PMO overcomes some of the problems associated with classical mesoporous silica, especially the low hydrothermal stability of the latter. In this sense, PMO materials have obvious advantages in many applications where water is unavoidable, such as adsorption, catalysis, and electrons.

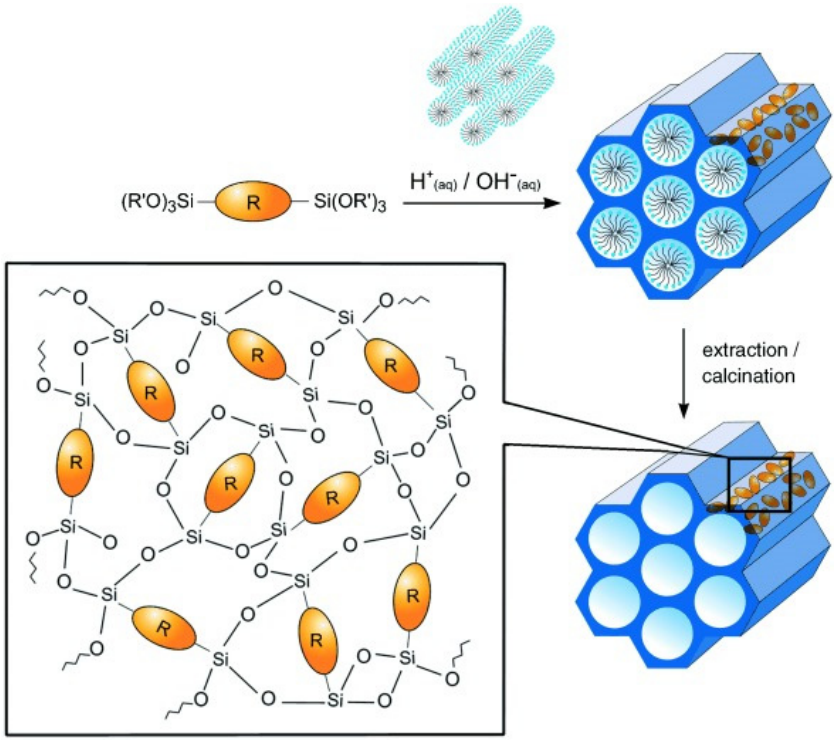

Figure 14. Schematic overview of the synthesis of a PMO.[250] Copyright 2006 WILEY‐VCH Verlag GmbH & Co. KGaA.

PMOs with simple organic functions are the most studied PMOs. Ethane-PMOs are prepared by cationic surfactants ("MCM-41/48 mimics"). In one of the very first reports on PMOs, Inagaki synthesized ethylene-bridged mesoporous silicas using OTAC as a template. They realized a one-dimensional arrangement, showing 2D hexagon (*P6mm*) or 3D hexagon ($P6_3/mmc$) symmetry, which depends on the molar composition of the starting synthetic

mixture and has a high degree of mesoscopic order. [251] Also, in 1999, Stein and coworkers reported another synthesis procedure similar to MCM-41 material using classic CTAB surfactant.[252] A few years later, the group of Mokaya realized the first ordered hexagonal (*P6mm*) ethylene bridged PMO with crystal-like pore walls.[253, 254] There is apparent interest in the synthesis of PMOs with ethylene bridges because they have great potential, mainly in functionalizing their frameworks through subsequent double bond modification. The group of Ozin reported that the first time benzene-PMO synthesis using CPCl as a template. [255] Later, other cationic surfactants, CTAB, CCP1, or C_{16}TEABr, were used to prepare 3D cage \materials. According to the characteristics of the material obtained, the most suitable template is CPCl, because it has a sizeable hydrophilic head group, which can form a 3D cage-like microstructure through spherical micelles. The triblock copolymer F88 (EO_{100}-PO_{39}-EO_{100}) provides materials with the exact symmetry and larger pores but with relatively large micropores in the pore wall.[256] Inagaki et al. made meaningful progress in PMO by synthesizing 2D hexagonal phenylene-bridged PMO with crystal-like pore walls under alkaline conditions.[257] This material exhibits a surface structure composed of alternating hydrophilic and hydrophobic layers, composed of silica and benzene, respectively, with a periodicity of 7.6 Å along the channel direction. This periodicity of the molecular scale in the wall is believed to be caused by the self-organization of precursor molecules through hydrophobic-hydrophilic or π-π interactions. In addition to the typical single-bridge silane, Ozin's team also developed a new type of PMO composed of multi-bridge organic groups. The main advantage of these high organic content PMOs is that more organic functional groups are directly incorporated into the silica network. The first PMO with high organic content contained interconnected $[Si(CH_2)]_3$ rings reported in 2003. The synthesis of these "cyclic PMOs" is similar to the synthesis of single-bridge PMO, but in this case, 1,1,3,3,5,5-hexaethoxy-1,3,5-trisilacyclohexyl Alkane is used as the silane precursor.[258]

The ethane-, ethylene-, and benzene-containing PMOs (**Figure 15**) discussed in the previous section have relatively inert surfaces. Although this is useful for some applications (such as chromatography), more active surface functions are required in other cases. It can be done by directly introducing higher functional groups. One of the first attempts to construct advanced PMOs was to combine a benzene ring with a simple organic bridge into the same precursor. In 2001, Ozin and his group reported the synthesis of three new aromatic PMOs, in which aryl organic bridging groups were incorporated in the framework.[259] The group used toluene, xylene and dimethoxybenzene bis(triethoxysilyl) derivatives as precursors, through the corresponding brominated compounds and chlorotriethoxy silane is prepared by Grignard reaction and exists in the acidic medium of SDA as CPCl. The groups of Hunks and Ozin prepared a precursor composed of two structural organic bridging units-1,4-bis(triethoxysilylmethyl)-benzene, in order to obtain a "short flexible" sub methyl and "rigid" phenylene are integrated into the PMO of the pore wall.[260] However, it has a similar precursor of "long and flexible" ethylene units-1,4-bis(trimethoxysilylethyl)benzene – they only produce amorphous materials.[261] Only by adding excess TMOS to the reaction mixture can an ordered mesoporous material be provided.[262] The group of Fröba uses the same precursor to obtain a similar PMO. The group emphasized that the combination of vinyl and aromatic groups provides new possibilities for further functionalization.[263] The authors also synthesized a highly conjugated organosilica precursor – 4,4'-bis((E)-2-(triethoxysilyl)vinyl) stilbene, obtained using the 18 π electron system colored material with adsorption effect in the ultraviolet-visible region.[264] By changing the length of the π system in the organic bridge, Inagaki et al. added oligo(phenylvinyl) groups to the framework of the intermediate structure film.[264] Other advanced precursors are of great interest in only π-aromatic systems. In 2002, Inagaki et al. an synthesize a new PMO with the crystal-like arrangement of biphenylene units in the pore wall with a period of 11.6 Å.[265] 4,4'-Bis(triethoxysilyl)-1,1'-biphenyl is also used

together with other silsesquioxanes containing aromatic hydrocarbon systems to produce films through evaporation induced self-assembly.[266] There is growing interest in adding chromonic units to mesoporous films used in the field of optical materials, which has prompted these researchers to study the optical properties of PMOs containing anthracene or naphthalene bridges.[267, 268]

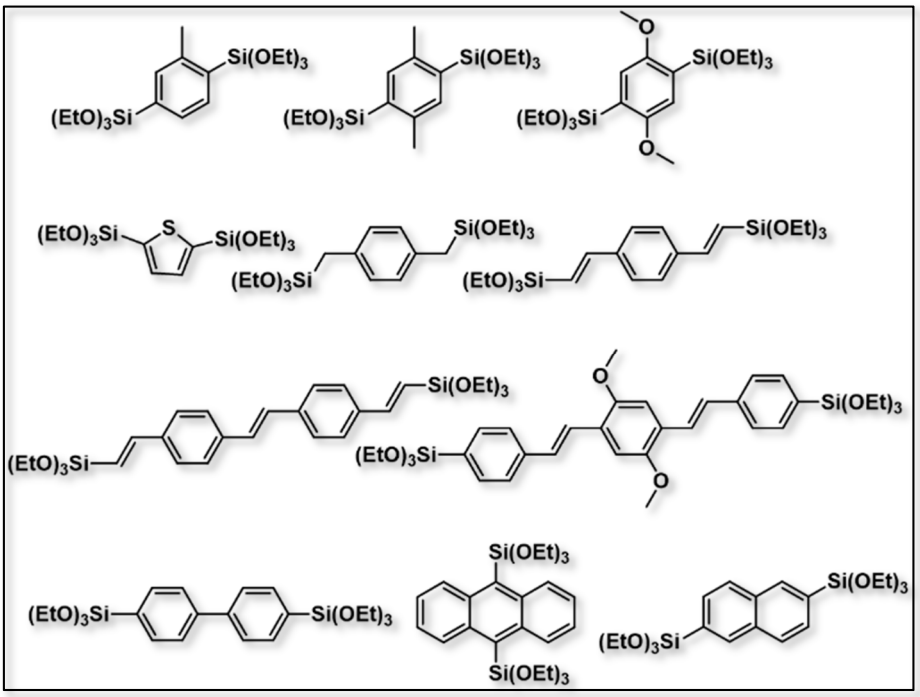

Figure 15. bis-silylated precursors containing aromatic bridging groups.

Another class of advanced PMO materials is that with nitrogen or sulphur containing bridges. It is complicated to incorporate "long" and flexible functionalities into PMOs. In these cases, TEOS or TMOS are added to assist in forming more rigid and ordered mesophases. Alvaro et al. added the azobenzene unit to the silica framework by co-condensing the corresponding azo derivative with TEOS.[269] Both materials show the photochemical cis/trans isomerization of the azo group, leading to different behaviors in the adsorption of Au particles. An extension of the π-system was carried out by Fröba, who synthesized to obtain colored mesoporous silicas of great use for chemical sensors, although no hexagonal structure was

realized.[270] However, other PMOs containing diimine Schiff basic units have strong photoluminescence properties and show highly ordered structures.[271] Lu successfully prepared the first PMO material containing diacetylene units embedded in the pore walls.[272] The assembly of bridged diacetylene silsesquioxanes around template micelles causes a certain spatial arrangement of diacetylene units. In 2002, Corriu reported the synthesis of a PMO material with large cyclam molecules, 1,4,8,11-tetraazacyclotetradecanecyclam added to the pore wall.[273] At about the same time, other methods focused on the introduction of tris[3-(trimethoxysilyl)propyl]isocyanurate heterocycles into the pore walls.[274] Like the cyclomycin unit, the isocyanurate ring is known for its ability to bind to transition metals. The groups of Fischer,[275] Jaroniec,[276] and Kim[277] reported an attempt to prepare bifunctional PMO materials containing isocyanurate and mercaptopropyl. There are two different functional groups with chelating metal properties in the same material, which has significant advantages for selective adsorption. Recently, Inagaki's team designed a new precursor containing carbazole, acridone or pyridine units, and was able to synthesize a crystalline PMO with photochemical[278, 279] or good chelating properties.[280, 281]

The $[(R'O)_3Si\text{-}R^+\text{-}Si(OR')_3X^-]$ type precursor is incorporated into the framework of PMO (**Figure 16a**), leading to advanced materials for heterogeneous catalysis, adsorption and photochemical process. In 2001, Alvaro et al. reported for the first time the synthesis of a new PMO with an electron acceptor viologen unit (4,4'-bipyridine) embedded in the pore wall.[282] Researchers extended their photochemical studies to include PMO containing trans-1,2-bis(4-pyridyl)ethylene units into the silica framework. By exposure to UV light, these materials show photoresponsiveness, showing a significant change in their double bond from trans to cis isomerization, accompanied by a significant change in porosity[283](**Figure 16b**). It must be pointed out that the organic loading in these PMOs is relatively low because a significant excess

of TEOS is required to ensure that the material has sufficient stiffness. A similar problem was encountered when synthesizing PMO with a large diazapyrene ion portion. When the loading of diazapyrene in the mixture is higher than 3%, the ordering disappears.[284] Mizoshita et al. successfully constructed a mesoporous membrane (with a thickness of about 4 μm) with a cationic methylacridine substructure derived from a solution containing pure organic silica precursor and Brij-76.[285] So far, the most suitable PMOs in this series are those derivatives with imidazolium or dihydroimidazolium units in the wall. Lee et al.[286] synthesized the bridging precursor, which was subsequently used to synthesize PMO anion exchange resin and Karimi et al.[287] immobilized Pd in PMO based on imidazolium ionic liquid. Adding new imidazolium substructures to PMO and forming a supported N-heterocyclic carbene complex may produce fascinating heterogeneous catalysts.[288, 289]

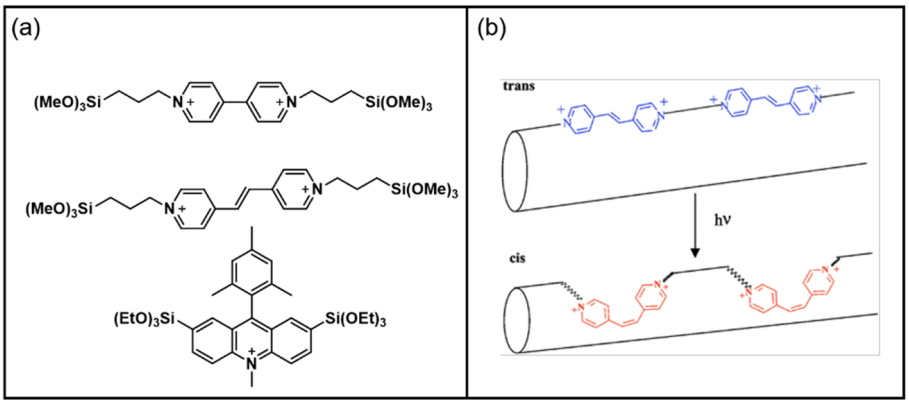

Figure 16. (a) Some ionic bridged precursors used in the synthesis of PMOs and (b) pictorial interpretation of the variation of the textural parameters in photoactive PMO upon irradiation.[283] Copyright 2002 Royal Society of Chemistry.

The use as a catalyst is undoubtedly one of the main applications of PMO. Melero and his group illustrated the effect of the local hydrophilicity/hydrophobicity on the catalytic activity of PMOs in the etherification of vanillyl alcohol with 1-hexanol.[290] Compared with their silica counterparts, they provided higher activity. The authors showed by HETCOR experiments that

the acid sites of the PMOs were not poisoned by water molecules released during the reaction. Kapoor et al. described the synthesis of dendritic silica hybrids and phenylene-PMO grafted with 3-aminopropyltrimethoxysilane.[291] These materials are used as catalysts for the Knoevenagel condensation between benzaldehyde and malononitrile PMOs are more active than mesoporous silica. The same reaction was tested on a crystalline phenylene-PMO undergoing a two-step amination process.[292] Hankari et al. reported on the synthesis of tris(3-(trimethoxysilyl)propyl)amine and its used as a precursor for the synthesis of mesoporous organosilica.[293] The tertiary amine present in the pore wall has high activity as a catalyst for the Knoevenagel condensation between benzaldehyde and malononitrile and the Henry reaction of benzaldehyde and nitroethane.

Among different metals, Ti, Sn, V and Nb have been successfully incorporated into the framework of PMOs as isolated tetrahedral sites. It was found that Ti-PMO has a moderate activity for the selective epoxidation of α-pinene[294] and 1-octene[295] with 30% H_2O_2 and TBHP, respectively. In addition, Sn[296] and V[297] substituted ethane-PMO and Nb substituted ethane- and octane-PMO[298] are used as catalysts for the epoxidation of different olefins with H_2O_2 as oxidants. Cr-PMOs have also been prepared by using BTEE or BTEE/TEOS mixtures and cationic surfactants under alkaline conditions.[299]

Teal's team obtained benzene-PMO with crystal-like pore walls, in which sulfonic acid (1.10 mmol·g^{-1}) and amino group (1.79 mmol·g^{-1}) were connected to the hydrophobic phenylene layer and the hydrophilic silica layer.[300] It's worth noting that this material allows benzaldehyde dimethyl acetal and nitromethane to be converted into trans-β-nitrostyrene (yield = 97.5%) in one pot, which involves deacetalization. The nitroaldol condensation is then carried out through acid and base groups, respectively. Inagaki et al. completed a similar method, but using ethylene-PMO.[301] Through co-condensation and post-functionalization, they

synthesized two materials with sulfonic acid groups and amino groups, which were exchanged between the hydrophobic layer and the hydrophilic layer. Regardless of the material, the amounts of -SO_3H and -NH_2 groups are approximately 1.1 and 1.3 mmol·g^{-1}, respectively. The group of Polarz also used a similar method to studies the distribution of amino and carboxylic acid groups attached to the phenylene bridge.[302]

The preparation of efficient heterogeneous catalysts for the enantioselective synthesis of chiral compounds is essential, especially for the pharmaceutical industry. Yang and coworkers synthesized various bis-silylated R-(+)-BINOL derivatives. These derivatives were later co-condensed with TMOS or BTME, which resulted in higher catalyst activity and stability.[303, 304] By co-condensation with TEOS, the same bridge is incorporated into PMO nanospheres with different pore structures. Both ee and activity increase with the order of the structure, that is, from worm-like to *P6mm* mesostructure. The nanospheres with a highly ordered two-dimensional hexagonal structure of radiation channels show excellent catalytic performance for adding diethyl zinc to various aromatic aldehydes. The ee value of benzaldehyde is 94% (99% conversion), indicating that PMO is even more enantioselective than homogeneous catalysts. These results highlight the critical role of frame stiffness in the correct placement of BINOL occlusal angles. The BINAP bridge incorporated in the mesoporous silica wall produces an excellent PMO catalyst after complexing with ruthenium, showing very high enantioselectivity, close to its counterpart (99.9% ee).

In addition to being a catalyst, PMO can also be used as adsorbents,[305-309] stationary chromatographic phases,[310-312] biological structures (such as enzymes and amino acids) and drug carriers.[313-319]

3.5 Photobiocatalysis

In the past 20 years, because of the generally mild and environmentally friendly reaction conditions, and the extremne high product selectivity, biocatalysis has become a recognized green tool in synthetic organic chemistry.[319-324] Very recently, essential developments have transformed biocatalysis into alternatives to metals or organic catalysis.[325] Especially the progress in directed evolution can directly modify enzymes and adapt them to different reaction conditions.[326] Enzymes can be designed to accept non-natural substrates, produce new products, and withstand extreme temperatures or pH values. At ambient temperature and pH value, and in the presence of water or organic solvents, the possibility of specific, stereoselective and complex reactions with enzymes has led to an increasing impact of biocatalysis in the pharmaceutical and chemical industries.[327-331]

At the same time, photocatalysis has also developed into a widely respected research field. Photocatalysis using (transition) metals or organic catalysts has become a topic of concern.[332-339] For many reactions, photocatalytic reactions were found that show an extended substrate scope and proceed under milder conditions compared to the light-independent alternatives. Therefore, it is not surprising that attempts are being made to combine the advantages of photocatalysis with biocatalysis. It brings together two of the most intensively researched areas in catalysis in the last decade. As a result, much progress has been made in combining photochemical principles and catalysis with biocatalysis, ranging from the field of light-driven enzymes to the use of light-activated cofactor recycling and light-dependent organisms.

Many enzymes have been found to show completely different or extended response spectra under light irradiation in recent years.[340, 341] In addition, published methods focus on the light-driven activation of oxidoreductases. In particular, the required electron donors,

photosensitizers, and mediators suitable for the direct or indirect transfer of photoelectrons to enzymes have been studied. In this case, the photochemical regeneration of cofactors also plays a vital role because it is a very effective and simple method that combines photocatalysis and biocatalytic conversion. Therefore, many biocatalytic redox reactions are combined with a photocatalytic step catalyzed by a photosensitizer.[340] For example, porphyrins,[342] transition metal complexes of iridium and ruthenium,[340] eosin Y,[343] or xanthene[344] are used as photosensitizers, which can transfer electrons directly to the oxidation reduction of enzymes. Pro-prosthetic groups can indirectly transfer electrons to enzymes through media, or indirectly photochemically regenerate natural cofactors.[340, 345] The most-reported photobiocatalytic system probably consists of a photochemically catalyzed reaction that provides redox equivalents for the biocatalytic conversion catalyzed by an oxidoreductase (**Figure 17**).[340, 346, 347]

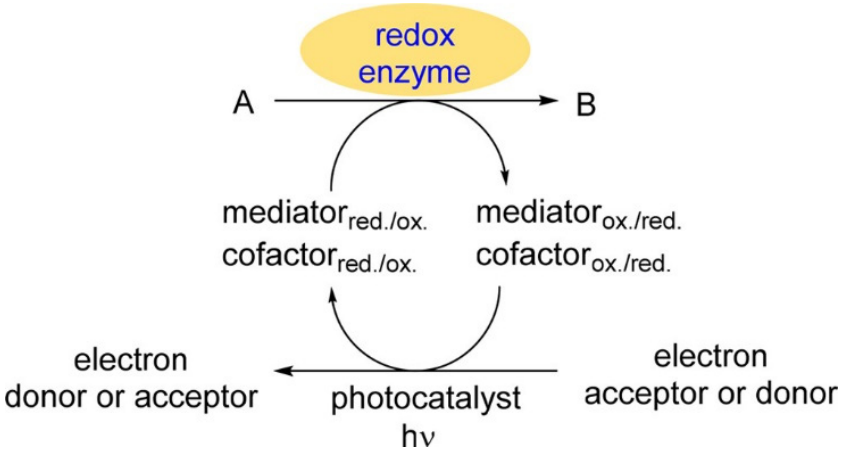

Figure 17. Photocatalytic generation of redox equivalents for a redox-enzyme in a parallel cascade.

Generally, the photosensitizer (or photomediator)[340] is coupled with a sacrificial electron donor (such as EDTA or water) to provide a reduced cofactor [such as NAD(P)H or $FMNH_2$] or an oxidizing agent (such as H_2O_2) drives the photobiocatalytic redox reaction. In detail, when the photosensitizer is excited by light, its electrons become the lowest unoccupied

molecular orbital (LUMO) of the photosensitizer. This excited state enables the photosensitizer to obtain electrons or hydrides from the electron donor. Then the electron (hydride) is transferred directly to the cofactor or indirectly through the mediator, and then the cofactor is generated.[333, 340] A wide range of photosensitizers, including semiconductor quantum dots, chlorophyll, metal nanoparticles and organic dyes, are used to activate oxidoreductases through the direct or indirect transfer of photogenerated electrons.[348-350] In these systems, sacrificial electron donors such as ethylenediaminetetraacetic acid (EDTA), triethanolamine (TEA), ascorbic acid (AA) and even water are used to recover media or cofactors to achieve the A catalytic cycle.[351, 352]

Several photochemical systems have been developed for this. For example, NADPH uses photosensitizers to recover light energy and media to transfer electrons to cofactors. This system is composed of a graphene-based light-trapping photocatalyst and a metal-based medium $[Cp^*Rh(bpy)H]^+$ for light-driven activation of NAD(P)H-dependent alcohol dehydrogenases (ADHs) to achieve the environmentally friendly synthesis of chiral alcohol (**Figure 18**).[353]

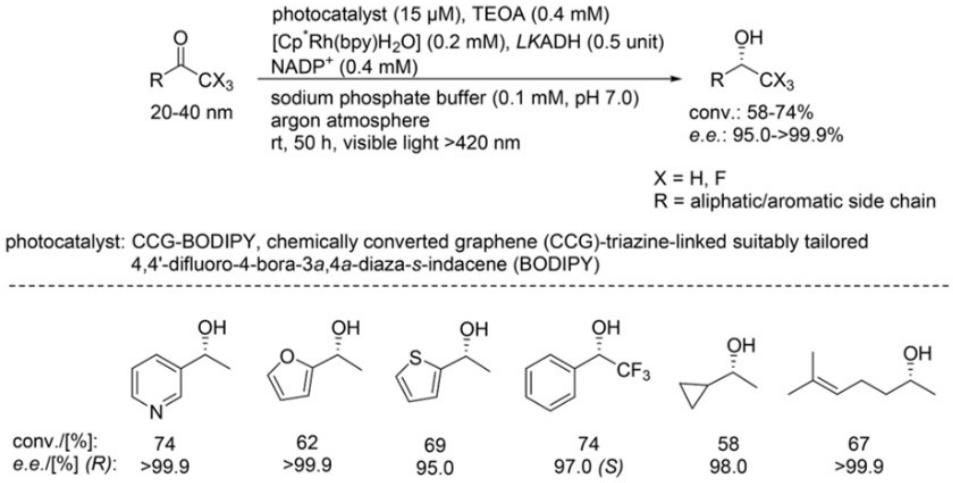

Figure 18. General photocatalytic method to regenerate NADPH for enabling an ecofriendly synthesis of chiral alcohols.[353] Copyright 2014 Royal Society of Chemistry

Further research reported that a biological hybrid complex composed of CdSe quantum dots and ferredoxin $NADP^+$ eductase was used for the photochemical regeneration of NAD(P)H.[354] Another example is the use of nitrogen-doped carbon nanodots as photocatalysts for photocatalytic reduction of C=C bonds, which are used to reduce artificial nicotinamide analogs, combined with rhodium-based composites as a medium.[355] In another case, the photosensitizer TCPP [5,10,15,20-tetra(4-carboxyphenyl)porphyrin] was fixed on the thiol-containing polydopamine/polyethyleneimine coated On silica microspheres, it is used for visible light NADH regeneration.[348] After optimizing the reaction conditions, the NADH yield can reach 82% after 60 min of light.

On the other hand, photocatalytic reactions involve the production of oxidants or the supply of electrons required by enzymes. In the first example, an inorganic Au-TiO_2 photocatalyst was used to generate H_2O_2 for non-specific peroxidase.[356] Since the application of peroxidase is generally less robust in the presence of hydrogen peroxide, this method allows the in-situ generation of H_2O_2 through the reduction and activation of ambient oxygen under light, which can reduce peroxidase. The amount of oxide is adjusted to ensure that the enzyme remains highly active and stable.

In another method, H_2O_2 is produced using enzymatic formic acid oxidation. In NADH formation from NAD^+, the formate dehydrogenase from *Candida boidinii* oxidizes formic acid to CO_2 (**Figure 19**). In the second catalytic step, in the presence of a photocatalyst (such as FMN, phenol safranine or methylene blue) and visible light, molecular oxygen is converted into H_2O_2 at the expense of NADH. The generated H_2O_2 can then be used for the activation of UPO.[357] The cascade combining photochemical catalysis and biocatalytic conversion is another system that has been reported more frequently. The photocatalyst/light first converts the substrate here before the enzymatic reaction, and vice versa.

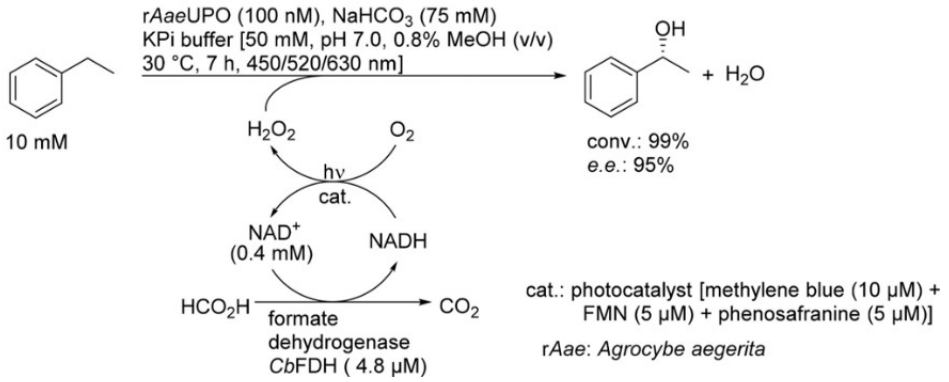

Figure 19. H_2O_2 generation by coupling a photocatalyst with a NAD^+/formate/formate-dehydrogenase system.[357] Copyright 2018 American Chemical Society.

Many chemical enzymatic cascades have been published, in which biocatalysis and chemical catalytic conversion are carried out simultaneously or sequentially in one pot.[358-361] However, due to the different reaction conditions, it is still challenging to carry out the reaction catalyzed by enzymes and chemical catalysts simultaneously in a one-pot method.[362] In particular, the combination of different solvent requirements for enzymes and transition metal catalysts represents an obstacle. The combination of the photochemical synthesis step and the biocatalytic conversion additionally leads to the problem that the biocatalyst may be inhibited due to the formation of highly active oxygen or free radical species in the presence of light.[363] This may be why there are very few examples of the combination of biocatalytic conversion and photochemical catalysis. The first one-pot sequential cascade combines photocatalytic thiol-Michael addition and biocatalytic ketone reduction (**Figure 20a**).[364] In this way, 1,3-mercaptoalkanols with high (S)- and (R)- stereoselectivity were synthesized from α,β-unsaturated ketones and mercaptans. The first step of the cascade is to use $[Ru(bpy)_3]Cl_2$ as a photocatalyst through visible light catalysis. After this conversion, the ketone group is enantioselectively reduced by the alcohol dehydrogenase variant to form 1,3-mercaptoalkanol with a moderate to good yield and an ee value as high as 99%. The enantioselective reduction of the carbonyl group is carried out using commercial enzymes with complementary

stereoselectivity, so two stereoisomers can be used. The photocatalytic step achieves a high conversion rate within 5 min, of which 24 h are required for the subsequent reduction of the ketone group.

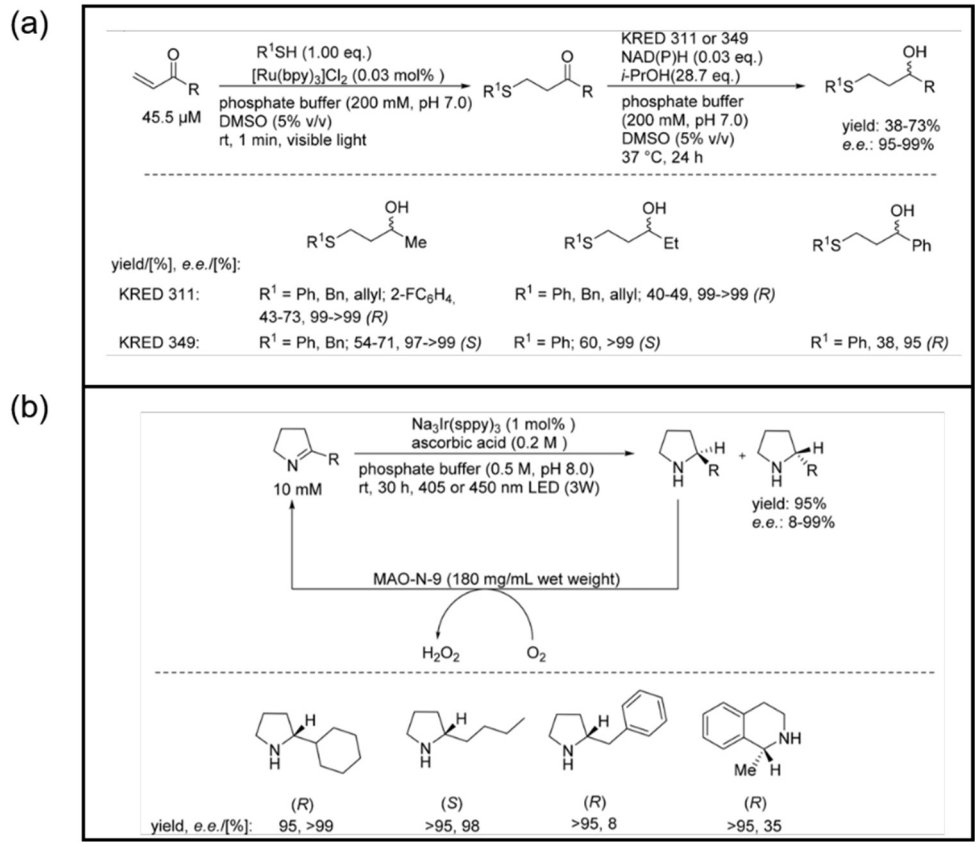

Figure 20. Cascades combining photo-chemocatalytic and biocatalytic transformations.[364, 365] Copyright 2018 WILEY‐VCH Verlag GmbH & Co. KGaA.

The second photoredox-biocatalytic cascade was developed for the enantioselective synthesis of amines (**Figure 20b**).[365] Using $Na_3[Ir(ppy)_3]$ as a photocatalyst, the cyclic imine is converted into a racemic amine through visible light-driven reduction in the first step of the cascade reaction. In the second step, one enantiomer of the amine is enantioselectively oxidized to imine by monoamine oxidase (MAO-N-9, used as a whole-cell catalyst for overexpression in *E. coli*) at the expense of molecular oxygen. The continuous cycle of non-selective reduction and enantioselective oxidation leads to overall deracemization. The cascade is only feasible in

the presence of ascorbic acid, which transfers hydrogen atoms to unstable α-amino-alkyl radicals, which are formed by light-induced electron transfer. Unfortunately, the cascade is limited to a few 1-pyrrolines with a phenyl, alkyl, or benzyl substituent in positions 2. The yields of all tested imines were very high, up to 95%. In addition, yields of up to 99% were achieved for cyclic imines with alkyl substituents.

Whole-cell biotransformation has many advantages, primarily reducing the availability of the nicotinamide cofactor [NAD(P)H] in metabolism and the stability of the enzyme, regeneration due to continuous expression and avoiding enzyme purification steps. Although NAD(P)H can usually be recovered by the metabolism of glucose or other additives, oxygen-containing photosynthetic-photoautotrophic organisms such as cyanobacteria (prokaryotes), purple bacteria (prokaryotes), algae (eukaryotes and prokaryotes) Biology) and plants (eukaryotes) provide a desirable option to regenerate NAD(P)H through water splitting, at the cost of luminescent protons and molecular oxygen as the only by-products (**Figure 21**).The solar energy captured by photosynthetic pigments such as chlorophyll a is converted into electrochemical energy, and NADPH is regenerated from $NADP^+$ through a photosynthetic electron transfer reaction. The link between photosynthetic electron flow and oxidoreductase will involve ferredoxin or NADPH through ferredoxin-NADPH reductase.[366-369]

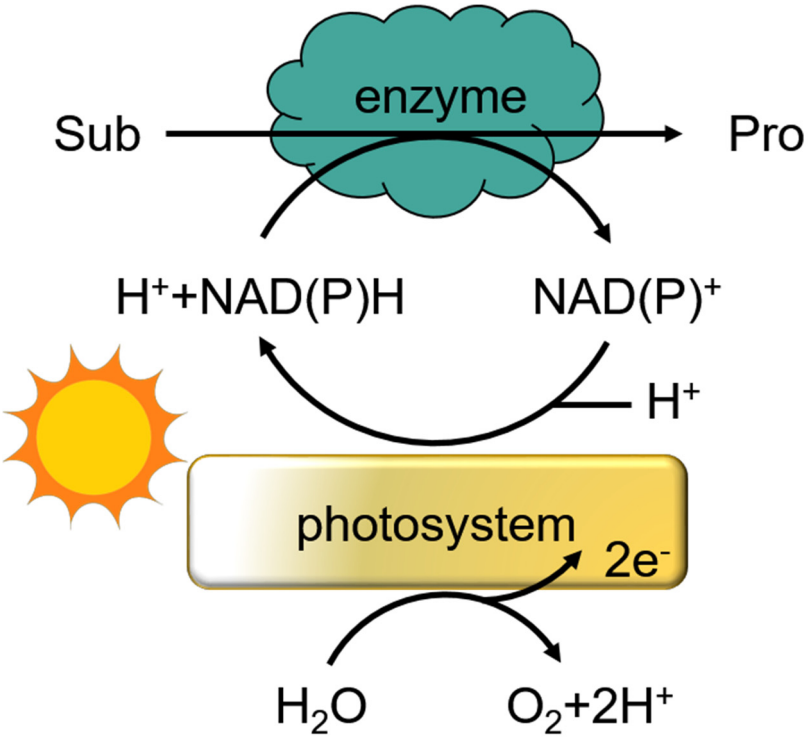

Figure 21. Regeneration of NADPH with photo-autotrophic organisms and coupling with NADPH-dependent biotransformations.

It may be because the currently known catalytically active enzymes require a relatively small amount of light in actual reactions (photosystems, photolyases, decarboxylase, PCB reductase), using the concept of combining photochemical catalytic reactions with biocatalysis. There are more examples than photobiocatalytic steps. In most cases, photochemical catalytic processes provide cofactors or redox co-substrates in the appropriate redox state, or are coupled with biocatalytic steps in a linear sequence. From the research described so far, it is clear that there are new opportunities, but there are also various challenges, such as primarily low TTN and TOF. Another challenge comes from the possible generation of strong oxidants and reactive free radicals (for example, from oxygen) in the presence of light, which may cause undesirable side reactions or enzyme damage. Another critical point is to demonstrate the reaction on a larger scale. Since most of the reactions discussed are shown on an analytical scale, the next logical step is to demonstrate their synthetic suitability for larger volumes and

higher concentrations. However, contrary to classical biotransformation, which usually allows direct volume amplification, parameters such as light intensity and the depth of light penetration associated with this are critical for photocatalysis.[370-376] Therefore, in order to push photobiocatalysis to a new level, the development of new photocatalysts, biological enzymes and reactors are all crucial. In any case, light can be considered a unique environmentally compatible option that can trigger reactions that would otherwise be impossible. The basic concept has been formed but needs to be expanded, and new reactions and concepts are expected.

4. Characterization techniques

4.1 Cyclic voltammetry (CV)

Cyclic voltammetry is an electrochemical technique that measures the current produced in an electrochemical cell when the voltage exceeds the value predicted by the Nernst equation. CV is performed by cycling the potential of the working electrode and measuring the current generated. The typical CV system (**Figure 22a**) consists of an electrolytic cell, a potentiostat, a current-to-voltage converter and a data acquisition system. The electrolyzer is composed of a working electrode, counter electrode, reference electrode and electrolyte. The working electrode's potential changes linearly with time, while the reference electrode maintains a constant potential. The counter electrode conducts current from the signal source to the working electrode. The purpose of the electrolyte is to provide ions to the electrode during oxidation and reduction. A potentiostat is an electronic device that uses a DC power supply to generate a potential that can be maintained and accurately determined while allowing a small current to be drawn into the system without changing the voltage. The current-to-voltage converter measures the generated current, and the data acquisition system generates the generated voltammogram.[377, 378]

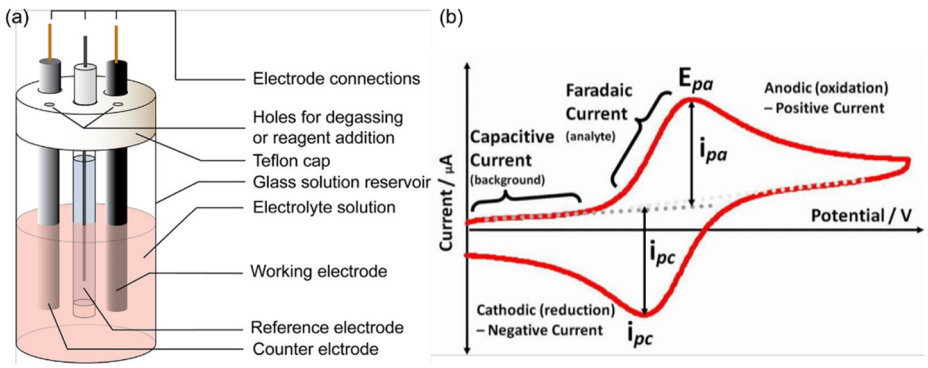

Figure 22. Schematic illustration of (a) an electrochemical cell and (b) a typical result from CV measurements.[378] Copyright 2018 American Chemical Society

In this work, CV measurements were used for experimental determination of the highest occupied molecular orbital (HOMO) and the lowest unoccupied molecular orbital (LUMO) levels of the organosilica nanomaterials as well as the redox potentials of some substrates.[379]

4.2 Electron microscopy

An electron microscope is a microscope that uses an accelerated electron beam as an illumination source. Since the wavelength of electrons is shorter than that of the visible light source, electron microscopes produce higher resolution images than standard light microscopes, with more reliable surface features and topological structures (**Figure 23**). In addition, they have higher resolution, so even too small structures can be detected.

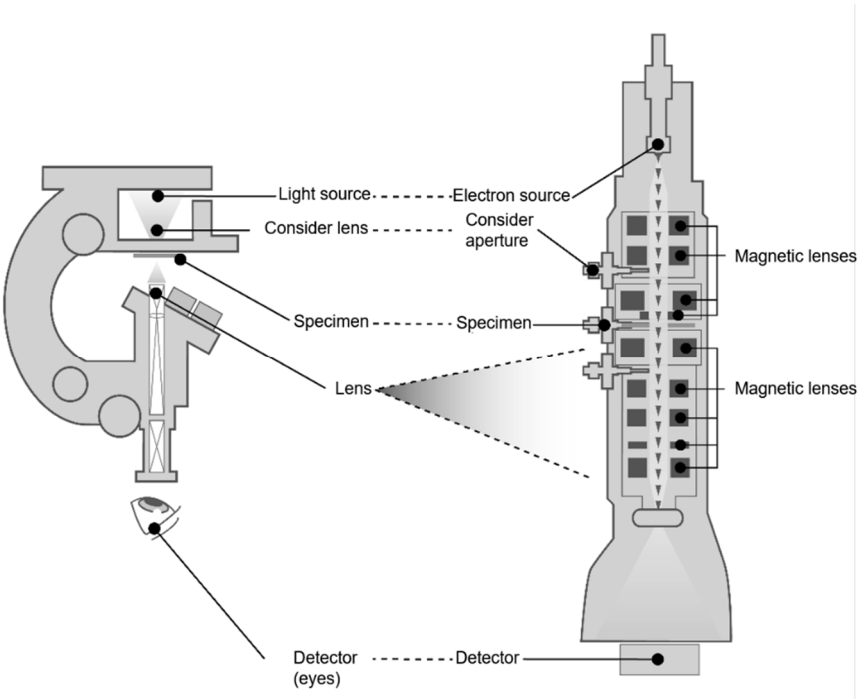

Figure 23. Side-by-side comparison of a transmission electron microscopy and an optical microscope, with analogous parts connected.

4.2.1 Scanning electron microscopy

Scanning electron microscopy (SEM) provides topographic, morphological and

compositional information of a sample. It can scan the surface from a few nanometers to micrometer scale. SEM has two main parts: electronic column and electronic console. The electron column contains an electron gun, which generates and accelerates electrons with an energy of 0.1-30 KeV. Therefore, a beam of high-energy electrons is formed, the energy of which is dissipated when it comes into contact with the sample surface, and various signals are generated, mainly secondary electrons, backscattered electrons, diffracted backscattered electrons, *etc*. These signals are then collected and detected by a positively charged detector to form the final image. The secondary and backscattered electrons reveal the topographical and elemental contrasts between regions of different chemical compositions within the sample. A scanning electron microscope (SEM) is used to evaluate the morphological properties of organosilica in this work.

4.2.2 Transmission electron microscopy

Transmission electron microscopy (TEM) is a microscopy technique that can observe the internal structure of a given sample. The difference with SEM is that the electron beam is transmitted through an ultra-thin specimen, instead of hitting the surface. The specimen can be an ultrathin part with a thickness of fewer than 100 nm or suspended on a grid. Since the much lower electron wavelength, TEM can generate images with a resolution close to a few Ångström. These images result from the interaction of the electron beam with the specimen as it passes through it. Some of the incident electrons are scattered and disappear from the electron beam. In contrast, the unscattered electrons produce "shadow images" of different darkness according to the composition density of the sample. In this work, TEM was used to capture the very fine details of the internal structure of the organosilica.

4.2.3 Energy dispersive x-ray analysis

Energy dispersive x-ay analysis (EDX), referred to as EDS or EDAX, is an x-ray technique used to identify the elemental composition of materials. EDX systems are attachments to electron microscopy instruments (Scanning Electron Microscopy (SEM) or transmission electron microscopy (TEM)) instruments where the imaging capability of the microscope identifies the specimen of interest. The data generated by EDX analysis consist of spectra showing peaks corresponding to the elements making up the true composition of the sample being analyzed. Elemental mapping of a sample and image analysis are also possible. The technique can be qualitative, semi-quantitative, and quantitative and provide the spatial distribution of elements through mapping. The EDX technique is non-destructive, and specimens of interest can be examined in situ with little or no sample preparation. In this work, EDX was used to view the distribution of different elements in organosilica.

4.3 Electron paramagnetic resonance (EPR)

Electron paramagnetic resonance is similar to Nuclear magnetic resonance (NMR), both of which describe the situation in which atomic particles resonate due to the absorption of high-frequency electromagnetic radiation in the presence of an external magnetic field. The main difference is that NMR spectroscopy is related to the nucleus, while EPR spectroscopy is related to unpaired electrons.

As a charged rotating particle, the electron possesses a magnetic field, making the electron look like a tiny magnet.[380] Under normal circumstances, for unpaired electrons (single electrons), the spin energy levels are degenerate, and the electrons spin randomly. The detectable ESR systems include: free radicals, point defects in solids or localized crystal imperfections, systems with conducting electrons (semiconductors and metals), transition

metal ions (Mn^{2+}, Fe^{3+}, Cu^{2+}, VO^{2+}, Mo^{5+}, Cr^{3+}, *etc*.) and some rare-earth ions.

After an external magnetic field is applied, the spin energy levels are split, and the electrons align with the direction of the magnetic field or spin oppositely. The splitting of spin energy levels leads to the appearance of some energy difference (ΔE); therefore, there are more electrons arranged in parallel with the external magnetic field and occupying lower energy levels than electrons arranged antiparallel to the external magnetic field and occupying higher energy levels. When the incident photon energy (high voltage) matches the energy difference between the two energy levels, some electrons are excited at the upper energy level and reverse their spin direction. After the relaxation time (t_1), the excited electron returns to its original state, and the emission energy is equal to ΔE.

Such process is expressed by the following formula:

$$h\nu = \Delta E = g_e \mu_B B$$

where h is Planck's constant, ν is the microwaves frequency, and g_e is the spectroscopic splitting factor: g_e = 2.002319304386(20).[381, 382] μ_B is Bohr magneton. B is magnetic field. **Figure 24** represents the process of electron spin resonance.

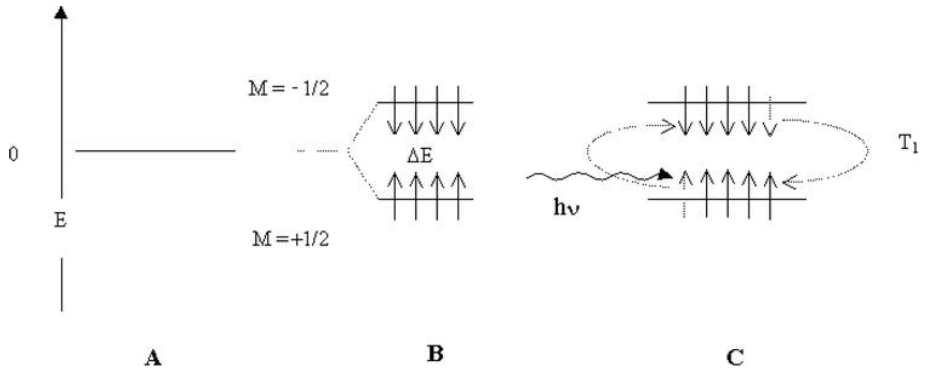

Figure 24. (A) No applied magnetic field and no spin levels splitting. (B) Energy separation of an unpaired electron spin under a magnetic field (Zeeman effect). (C) Flipping of spins by microwave absorption and flopping of spins within the spin-lattice relaxation time(T_1).

In the application of heterogeneous photocatalysis, before and after ultraviolet irradiation, different types of paramagnetic substances can be produced in the main body of the photocatalyst or on the surface. The versatility of this technology enables multiple interfacial phases involved in the photocatalytic process to be characterized in situ under different experimental conditions. The extraction of spin Hamiltonian parameters identifies certain paramagnetic substances on the catalyst surface or in the reaction solution.[383] In this work, the EPR spectroscopy was used for the detection and characterization of radicals and some reactive intermediates during the photocatalytic processes.

4.4 Gas sorption and porosity analysis according to the Brunauer–Emmett–Teller (BET) theory

The Brunauer, Emmett, and Teller (BET) theory,[384] proposed in 1938, is the basis for measuring the specific surface area of materials. It is based on the multilayer physical adsorption of an inert gas (adsorbent) on a solid surface (adsorbate). The most commonly used inert gas is nitrogen because of its availability, high purity, and ability to interact with most solids. The amount of gas adsorbed depends on the exposed surface, the interaction between the solid and the gas, the gas pressure and the temperature. This approach also allows the evaluation of pore size from micropores (size < 2 nm), mesopores (2 nm-50 nm) to macropores (size > 50 nm). Thus, different types of isotherms can be derived depending on the physicochemical conditions and the solid porous structure.[385] According to the IUPAC definition, six types can be distinguished, as shown in **Figure 25**.

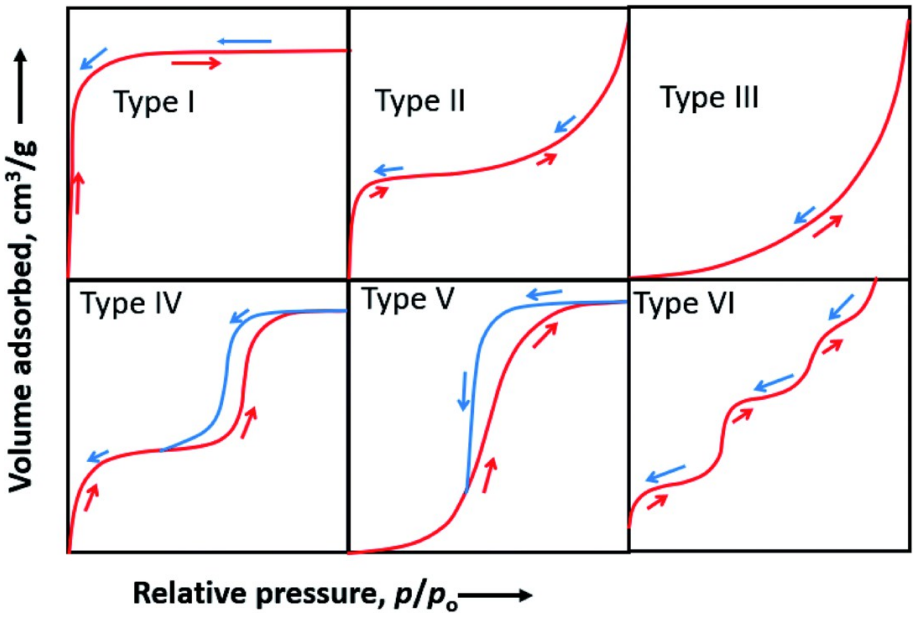

Figure 25. Different types of adsorption isotherms as classified by IUPAC.[386] Copyright 2015 IUPAC.

Type I isotherms are characteristic for microporous materials, and the gas molecules adsorb just as a monolayer at very low relative pressures. Type II corresponds to non-porous or macroporous materials. In this case, the available sites could be filled as monolayer at low relative pressure until complete coverage. More layers are adsorbed on the previously formed multilayer at high relative pressure, leading to a continuous increase in the adsorbate thickness. Type III fits the low adsorption capacity of solids, revealed by an increase of the isotherm at higher relative pressures. Type IV isotherms are obtained for mesoporous materials with characteristic hysteresis loop and a saturation plateau at p/p_0 = 0.6-0.95. Type V isotherms correspond to porous materials with pore size range similar to that of type IV isotherms. However, its initial part indicates a low adsorption capacity between the adsorbent and adsorbate. Type VI isotherms show a stepwise multilayer formation on a highly uniform non-porous surface. The sharpness of the steps is related to the system and the temperature and the step heights depend on the capacity of the monolayer to adsorb the next layer. In this work, the BET gas adsorption was used to assess the organosilica's surface area and pore size distribution.

4.5 Gas chromatography-mass spectrometry (GC-MS)

Gas chromatography-mass spectrometry (GC-MS) is an analytical tool, which combines gas chromatography (GC) and mass spectrometry (MS) (**Figure 26**). It permits the separation of different compounds of a mixture and their identification according to their molecular weights. The separation is based on the volatility of the pure compounds, which are carried through a fixed stationary phased in the column by the flow of an insert gaseous mobile phase, including helium, nitrogen, carbon dioxide, and hydrogen. Once separated by the GC, they are transported directly into the mass detector, in which they are ionized and fragmented under a stream of the electron beam. The mass-to-charge ratio (*m*/z) of each positive ionic fragment is then recorded and identified by comparison with a sample library or standards. In this work, GC-MS was used to monitor photocatalytic reactions and kinetics, to identify eventual intermediates, and to confirm final products' structure.

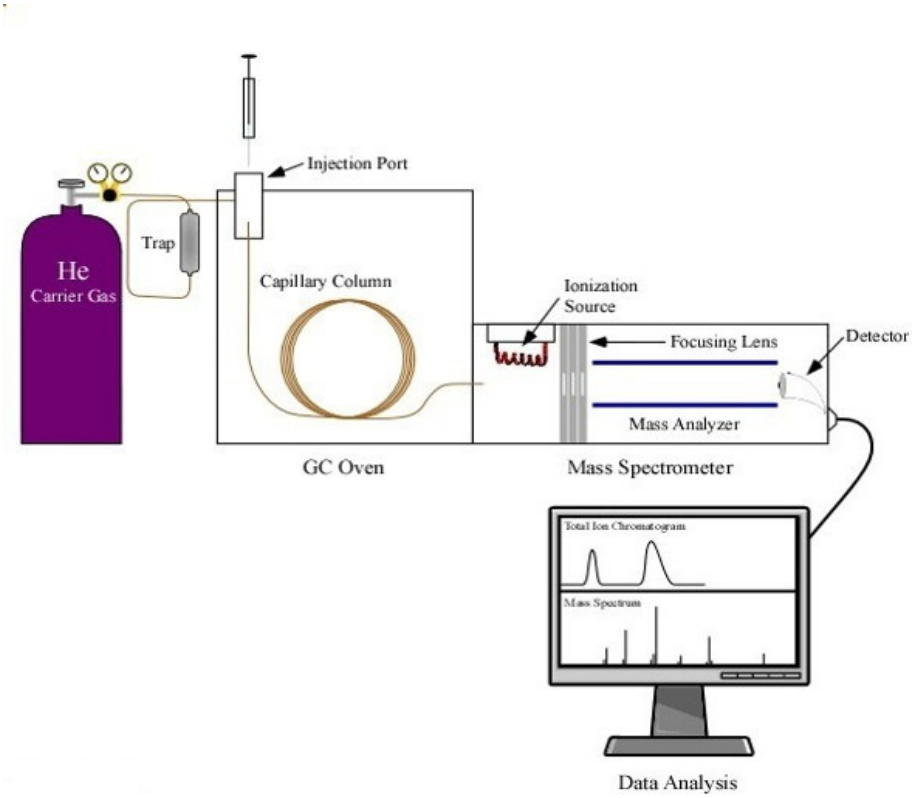

Figure 26. Block diagram for GC-MS.

4.6 Fourier transform infrared spectroscopy (FT-IR)

A Fourier transform infrared (FT-IR) spectrometer is an instrument that acquires broadband near infrared (NIR) to far infrared (FIR) spectra. It gives an insight into the chemical composition and the bonding arrangement of constituents within a material. When IR radiation is passed through a sample, some radiation is absorbed by the sample and passes through (transmitted). The resulting signal at the detector is a spectrum representing a molecular 'fingerprint' of the sample. FT-IR was used as an important technique to identify the specific functional groups in the organosilica in this work.

4.7 Nuclear magnetic resonance (NMR) spectroscopy

Nuclear magnetic resonance spectroscopy is a spectroscopic technique to observe local magnetic fields around atomic nuclei. The sample is placed in a magnetic field. The NMR

signal is produced by excitation of the nuclei sample with radio waves into nuclear magnetic resonance, which is detected with sensitive radio receivers. The intramolecular magnetic field around an atom in a molecule changes the resonance frequency, thus giving access to details of the electronic structure of a molecule and its individual functional groups. NMR spectroscopy is usually used to determine the chemical structure of organic compounds. The nuclei of many elemental isotopes have a characteristic spin (I). The most used isotopes are ^{1}H and ^{13}C with a specific nuclear spin $I = 1/2$. In the presence of an external magnetic field (B_0), two possible spin states exist, including low energy +1/2 and high energy -1/2 spin state. Their energy difference (ΔE) is described in the following equation:

$$\Delta E = \frac{\mu B}{I}$$

where μ is the magnetic moment, B is the magnetic field strength, which is determined by the external magnetic field strength. The precise resonant frequency of the energy transition is dependent on the effective magnetic field at the nucleus. This field is affected by electron shielding which is in turn dependent on the chemical environment. As a result, information about the nucleus' chemical environment can be derived from its resonant frequency. In general, the more electronegative the nucleus is, the higher the resonant frequency. In this work, liquid NMR spectroscopy was used for structural elucidation of the monomers and photocatalytic products.

4.7.1 Solid-state nuclear magnetic resonance spectroscopy (solid-NMR spectroscopy)

Solid-state NMR spectroscopy is a special nuclear magnetic resonance spectroscopy technique used for molecular structure determination in solid states. Unlike the NMR spectra taken in solutions, the experimental sample for solid-state NMR spectroscopy is contained in

media with little or no mobility, such as a crystalline or powder state, characterized by anisotropic interactions. However, due to the lack of extensive dynamics in the solid-state, NMR spectra of solid materials are enormously broadened by the anisotropic interactions. Therefore, magic-angle spinning (MAS) is usually applied to reduce such a broadening effect, which simulates the rapid isotropic tumbling motion of a molecule in solution by rotating the sample at a frequency around an axis inclined at β_R to the B_0-field (**Figure 27**).[387] The average of orientation dependence interactions can be described as following:

$$\int_0^{\pi} (3cos^2\theta - 1) \sin\theta \, d\theta = \frac{1}{2}(3cos^2\beta_R - 1)(3cos^2\beta - 1)$$

when $\beta_R = 54.7°$, the term in β is zero and MAS will scale the anisotropic part of the interaction to zero. In this thesis, solid-state NMR spectroscopy was used to determine the chemical structure of solid organosilica networks.

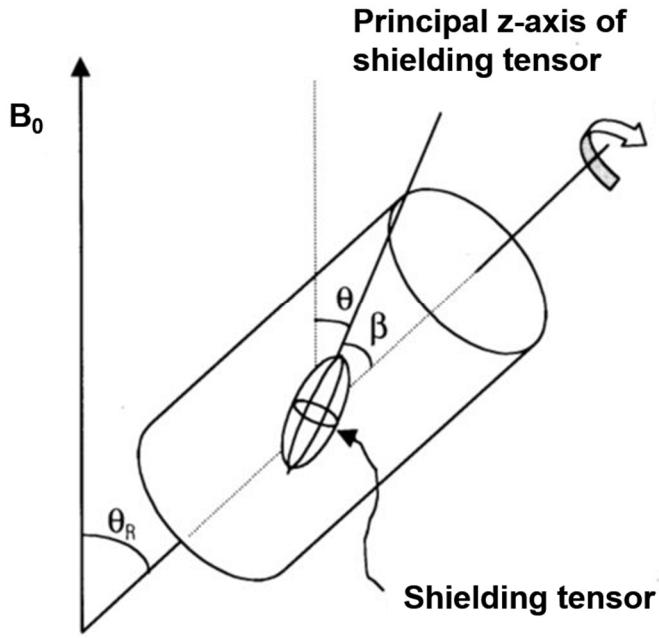

Figure 27. Principle of magic angle spinning (MAS) sample alignment for solid-state NMR spectroscopy.

4.8 Time-resolved photoluminescence (TRPL)

The fluorescence lifetime is an intrinsic characteristic of a luminescent species that can provide insight into the species excited state dynamics. Time-Resolved Photoluminescence (TRPL) is the tool of choice for studying fast electronic deactivation processes that result in the emission of photons, a process called fluorescence. The lifetime of a molecule in its lowest excited singlet state usually ranges from a few picoseconds up to nanoseconds. The molecular environment can influence this fluorescence lifetime (e.g., solvent, presence of quenchers, or temperature) and interactions with other molecules. Processes like Förster Resonance Energy Transfer (FRET), quenching, solvation dynamics, or molecular rotation also affect the decay kinetics. Lifetime changes can therefore provide information about the local chemical environment or insights into reaction mechanisms. In this work, TRPL was used in the study of photocatalytic mechanism.

4.9 Ultraviolet–visible (UV-vis) spectroscopy

UV-vis spectroscopy is an analytical technique that measures the amount of discrete wavelengths of UV or visible light absorbed by or transmitted through a sample compared to a reference or blank sample. When the sample absorbs light with suitable energy photons, the constituent atoms and molecules undergo electronic transitions from a ground state (valence band) to an excited state (conduction band), resulting in a distinct spectrum. The absorption intensity (A) follows the Lambert-Beer law and is proportional to the intensity of the incident monochromatic radiation before and after passing the measurement cell (I_0 and I):

$$A = \log\left(\frac{I_0}{I}\right) = \varepsilon * c * d$$

where ε, c and d are extinction coefficient, concentration of the solution and thickness of the

measurement cell, respectively. In this work UV-vis spectroscopy have been used to monitor the reaction kinetics by colorimetric methods.

4.9.1 UV-vis diffuse reflectance (DR) spectroscopy

UV-vis diffuse reflectance spectroscopy is an important technique to study the absorption property of insoluble materials. In UV-vis spectroscopy, one measures the relative change of transmittance of light as it passes through a solution or a film. In contrast, UV-vis DR spectroscopy measures the relative change in the amount of reflected and scattered light off of a surface. Reflection includes specular and diffuse reflection. Specular reflection follows the path of the incident beam but in the reverse direction. However, diffuse reflection is isotropic and distributed in a different direction.

In addition, the optical band gap (Eg) could be deduced from the onset absorption in UV-vis spectra following this equation:

$$E_{photon} = E_g$$

$$E_g = h * \nu = \frac{h * c}{\lambda} = \frac{1238}{\lambda}$$

where h, ν, c and λ are Planck's constant, frequency of light, speed of light, wavelength of light, respectively. UV-vis DR spectroscopy was conducted to characterize the optical properties of the organosilica.

5. Results and discussion

This chapter focuses on the design, synthesis and characterization of organosilica for challenging photocatalytic applications as organic synthesis and biocatalysis under visible light irradiation. The main emphasis is paid to creating desirable properties of silica structure, such as mesoporous structure as morphology, hydrophilicity, combined with photocatalytic units, which meet the redox potential for the targeted photocatalytic reactions.

The chapter is divided into three main projects. First, a series of mesoporous organosilica photocatalysts are designed for visible light-promoted aryl azoline formation. Different ratio of 1,4-bromophenyltriethoxysilane (BPTS) (50%, 75% and 100%) was chosen as the monomers for the synthesis of the backbone precursor with tetraethyl orthosilicate (TEOS) by hydrolysis condensation. The photoactive diphenyl benzothiadiazole ($BTPh_2$) units were then formed via successive coupling methods, obtaining the final organosilica. Via formation of aromatic aldehydes with various amines, 2-phenyl-2-imidazoline, 2-phenyl-2-oxazoline, 2-phenyl-2-thiazoline and their derivatives could be formed with high conversion 89% and selectivity 97%. (**Section 5.1**)

Next, new synthetic routes for the monomers with photocatalytic activity were developed. Furthermore, to solve the problem of deactivation of biological structures by the photogenerated oxygen species during photocatalysis, core shell-structured mesoporous organosilica photocatalysts were synthesized. Combined with two different enzymes, stable and continuous photobiocatalytic reactions were conducted (**Section 5.2**).

At last, in addition to the participation of enzymatic reactions by photo-oxidation, special attention was paid to the photoreduction of enzymatic cofactors. By combining the photocatalytic unit with an organosilicon backbone containing extra light-absorbing aromatic

groups, the organosilica effectively absorbs different wavelengths of light, and the excited energy is funneled into the photocatalytic center through energy transfer to enhance photocatalytic ability. As result, NADH can be regenerated without transition metal complexes in a non-oxidizing atmosphere, and the light-harvesting effect of the aromatic groups in the backbone was investigated (**Section 5.3**).

5.1 Visible light-promoted aryl azoline formation over mesoporous organosilica as heterogeneous photocatalyst

This subchapter is based on the published article "Visible light-promoted aryl azoline formation over mesoporous organosilica as heterogeneous photocatalyst *ChemCatChem*. **2021**, *13*, 3410-3413" (Copyright 2021 Wiley-VCH Verlag GmbH & Co. KGaA). Wenxin Wei designed and performed the main part of the experiments, analyzed the data and wrote the first draft of the manuscript. Dr. Run Li did a pre-study on the catalytic reaction. Dr. Niklas Huber performed the ^{13}C solid-state NMR measurements. Dr. Gönül Kizilsavas performed the EPR measurements. Wenxin Wei, Dr. Calum Ferguson, Prof. Dr. Kai Zhang and Prof. Dr. Katharina Landfester contributed to the final version of the manuscript. Prof. Dr. Kai Zhang and Prof. Dr. Katharina Landfester supervised the project.

Herein, a photocatalytic route for aryl azoline formation by mesoporous organosilica is present as visible light-active and heterogeneous photocatalyst. Via formation of aromatic aldehydes with various amines, 2-phenyl-2-imidazoline, 2-phenyl-2-oxazoline, 2-phenyl-2-thiazoline and their derivatives could be formed with high conversion and selectivity. Additionally, the organosilica photocatalyst showed high stability and reusability.

5.1.1 Motivation

N-heterocyclic compounds are widely used as important basic structure for

pharmaceuticals, agrochemicals or ligands in organometallic chemistry.[388, 389] Among the vast number of *N*-heterocycles, 2-imidazolines, 2-oxazolines, and 2-thiazolines have received most attention as ubiquitous building blocks in biologically active natural products, drugs and enzyme inhibitors, *etc*.[390, 391] Until now, different preparative strategies have been developed to synthesize azoline derivatives.[392, 393] Conventionally, the synthesis for *N*-heterocycles is conducted under thermal conditions, in which precisely designed catalysts such as Lewis acids[394-396] or transition metals are used.[397, 398] Recently, more environmentally benign and milder reaction conditions involving photocatalysts has been reported.[399] Most of the used photocatalysts are of homogeneous nature. Heterogeneous systems, which combine the advantages of photocatalysis and reusable heterogeneous catalyst, have barely been applied for the synthesis of *N*-heterocycles so far. Further studies in this field are highly desired.

Recently, visible light-active, porous organic and metal-free materials have been employed as photocatalysts in a variety of photoredox applications. Among them, covalent organic frameworks (COFs),[400-402] carbon nitride[403, 404] and conjugated microporous polymers (CMPs)[405] have been developed for visible light-driven redox reactions such as water splitting, CO_2 reduction,[406] biosensing[407] and wastewater treatment[408], *etc*. These emerging photocatalysts have demonstrated advantages as low toxicity, low cost, stability and reusability. Taking advantage of the well-designed porous structure, the photocatalysts can be further endowed with high specific surface area with accessible active sites and further facilitating photocatalytic reactiohns with enhanced efficiency.[409] The diffusion of substrate molecules during the catalytic process into the micropores and therefore efficient contact to the active sites are limited.[410] To overcome this challenge, synthesis of heterogeneous photocatalysts with larger pores, in particular, mesoporous has been a focus for the chemists.

Mesoporous organosilica, with their throughout porous structure in the meso range,

designable organic content and robust nature, could offer a promising platform for photocatalytic applications.[250, 411] A well-designed morphology allows reagent molecules to easily diffuse into the mesopores and therefore the active catalytic centers within the photocatalysts.[179, 412, 413] Recent studies involving mesoporous silica-based materials have showed rather grafting methods for catalyst design.[414, 415] Achieving high catalyst loading onto mesoporous silica is indeed challenging.[416] Light-driven organic redox reactions have been barely reported. It is indeed highly desired to develop mesoporous organosilica as efficient heterogeneous photocatalysts with high effective catalyst content and accessible pore structure for organic photoredox reactions.

In this chapter, we report the design and synthesis of mesoporous organosilica with integrated 4,7-diphenylbenzothiadiazole ($BTPh_2$) units as efficient photocatalyst for the photocatalytic formation of N-heterocycles (Scheme 1). The content of the effective photocatalytic moieties within the organosilica network was controllable and their structure is easily designable. The organosilica showed a pore size of about 5.7 nm. Via formation of aromatic aldehydes with various diamines, 2-phenyl-2-imidazoline, 2-phenyl-2-oxazolines, 2-phenyl-2-thiazolines and their derivatives could be formed over the mesoporous organosilica as heterogeneous photocatalyst with high conversion and selectivity.

5.1.2 Synthesis and characterization of mesoporous organosilica photocatalyst

1,4-bromophenyltriethoxysilane (BPTS) was chosen as the monomers for the synthesis of the backbone precursor MOS−Br. The photoactive diphenyl benzothiadiazole ($BTPh_2$) units were then formed via successive coupling methods, obtaining the final organosilica MOS−BT.

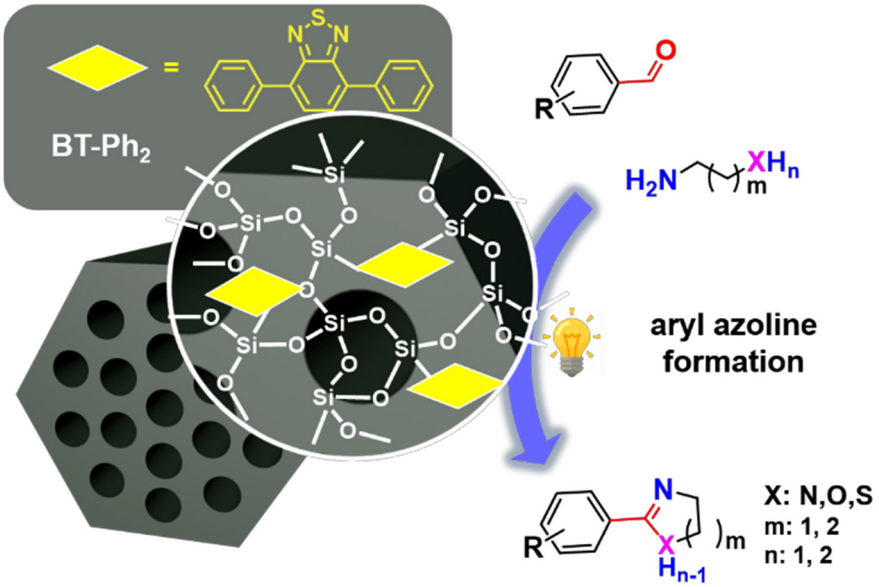

Scheme 2. Illustration of the design concept of the photocatalytic mesoporous organosilica and their application in aryl azoline formation via addition of aryl aldehydes and amine derivatives.

Scanning electron microscopy (SEM) and transmission electron microscopy (TEM) images showed a fused particle-like morphology of the organosilica (**Figure 28**).

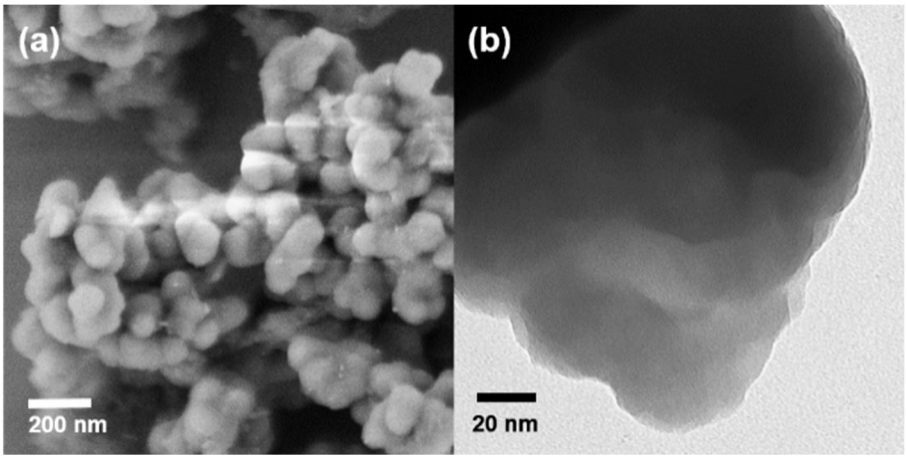

Figure 28. (a) SEM and (b) TEM images of MOS-BT.

TEM energy dispersive X-ray spectroscopy (TEM-EDX) of MOS−Br and MOS−BT revealed the successful conversion of the bromide groups on MOS−Br, proving the chemical composition of MOS−BT (**Figure 29**).

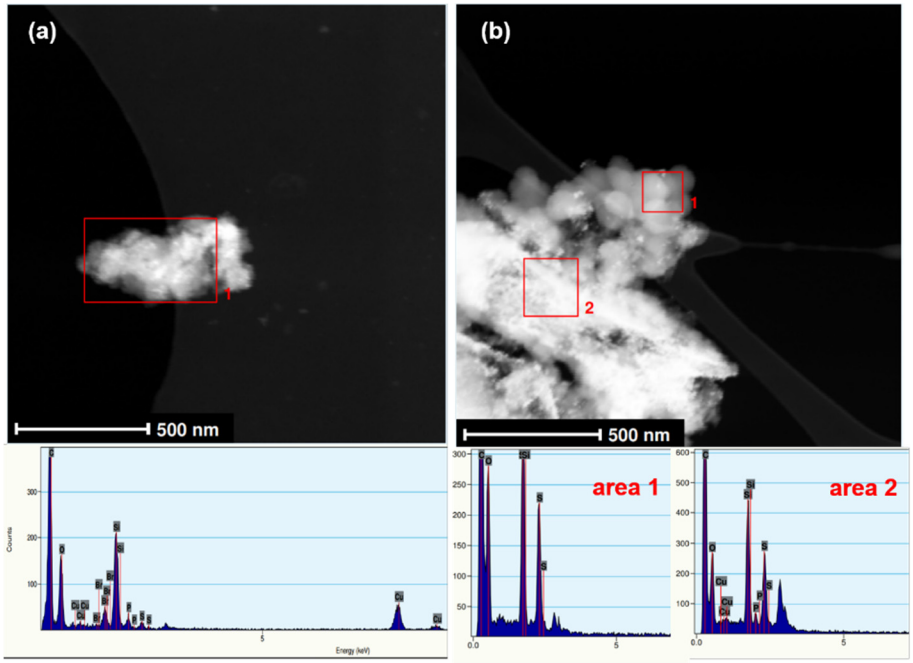

Figure 29. TEM-EDX of (a) MOS-Br, and (b) MOS-BT.

Fourier transform infrared (FTIR) spectroscopy (**Figure 30**) revealed recognizable signals at 1348, 1377, 1567 and 1577 cm^{-1}, which are the typical characteristics for C=N and N−S stretching modes in benzothiadiazole units. The strong and wide absorption signals at 1095 cm^{-1} can be assigned to Si−O−Si antisymmetric stretching vibration.

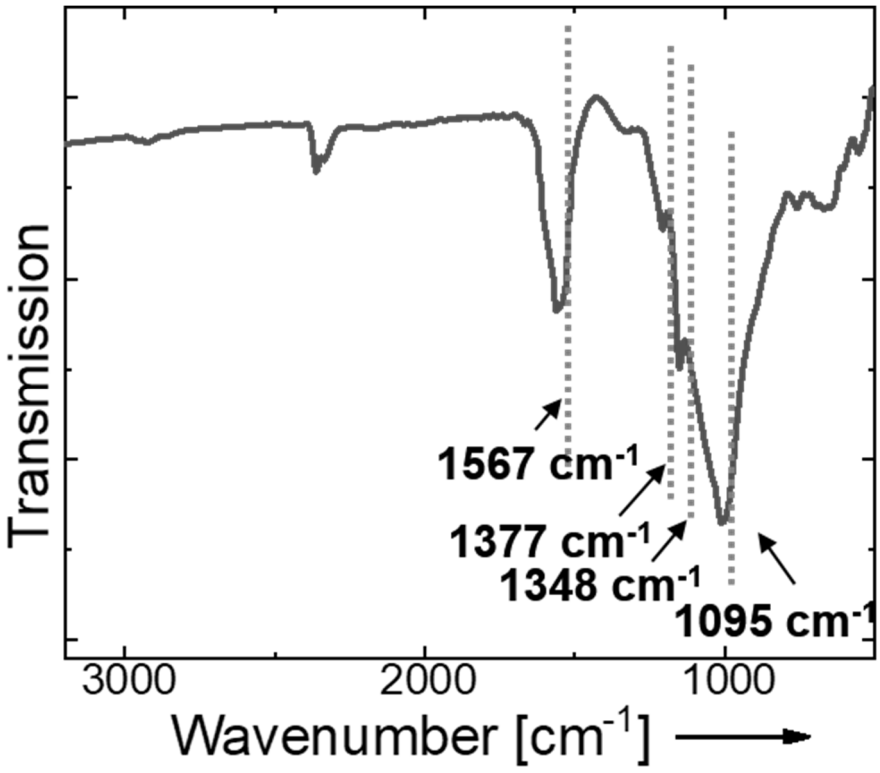

Figure 30. FTIR spectrum of MOS-BT.

The Brunauer-Emmett-Teller (BET) surface area of MOS−BT was determined to be 339 m^2/g, with pore size of ca. 5.7 nm (**Figure 31**).

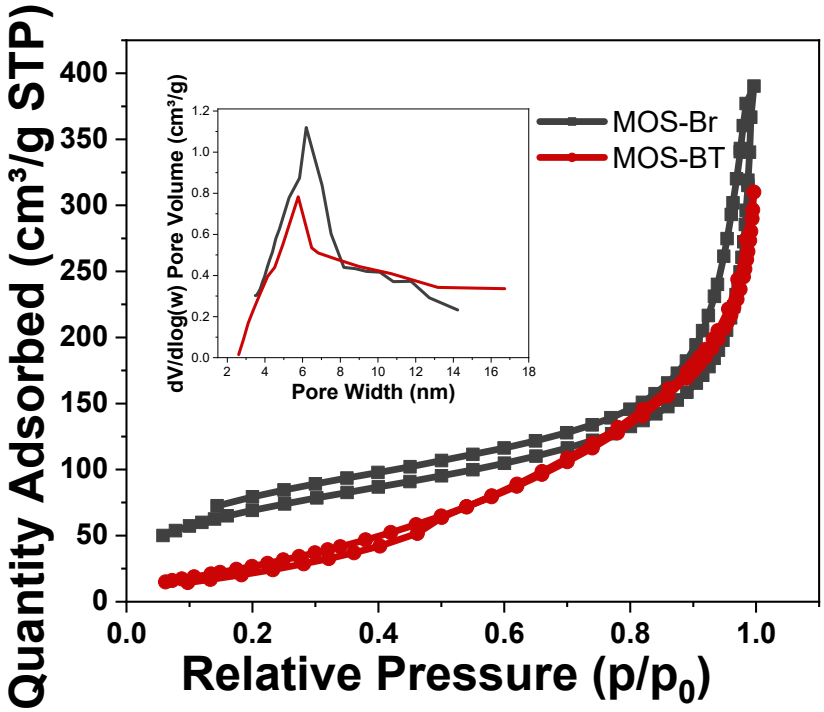

Figure 31. Nitrogen sorption and desorption isotherms, and pore size distributions of MOS-Br and MOS-BT.

UV-vis diffuse reflectance spectrum (DRS) of MOS−BT (**Figure 32**) revealed a broad absorption range until 800 nm. The absorption maximum at 395 nm can be assigned to that of the $BTPh_2$ unit. Photoluminescence spectrum showed a range between 425 nm and 700 nm with a maximum at 521 nm, which is similar to that of the $BTPh_2$ unit (**Figure 32**).[417, 418] The slightly red shift of MOS−BT compared to the single $BTPh_2$ could be attributed to the hyper conjugation effect of the photoactive unit in MOS−BT. The optical properties of MOS−BT of emission and absorption behaviors are similar to those of *fac*-$[Ir(ppy)_3]$, a well-established molecular transition metal photocatalyst.[419]

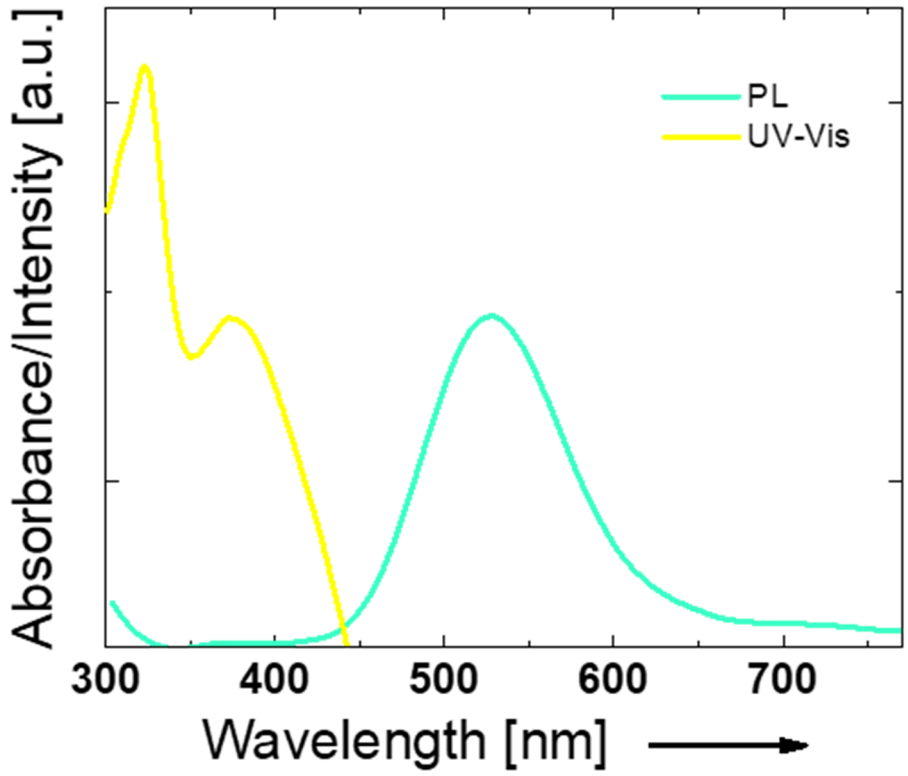

Figure 32. UV-vis DR and photoluminescence (PL) spectra of MOS-BT.

The optical band gap of 2.84 eV for MOS−BT could be derived from the Kubelka-Munk-function (**Figure 33a**). Cyclic voltammetry measurements indicated that the lowest unoccupied molecular orbital (LUMO) position of MOS−BT was at −1.30 V vs SCE (**Figure 33b**). And the highest occupied molecular orbital (HOMO) position at 1.60 V vs SCE (**Figure 33c**). The HOMO and LUMO levels of MOS−BT matched the energy positions of $BTPh_2$. Theoretical calculations for the repeating unit (O−Si−Ph−BT−Ph) using density functional theory (DFT) on rB3PW91/6-311+g(d,p) level (**Figure 33d**) revealed that the electron densities on HOMO and LUMO are mainly located on the $BTPh_2$ unit, indicating that the electronic structure is determined by the donor-acceptor (D−A)-type unit $BTPh_2$. Under nitrogen atmosphere, MOS−BT could remain intact up to 400 °C as revealed by thermogravimetric analysis (TGA). Inductively coupled plasma spectrometry (ICP) revealed the content of Pd residue below 0.5 ppm.

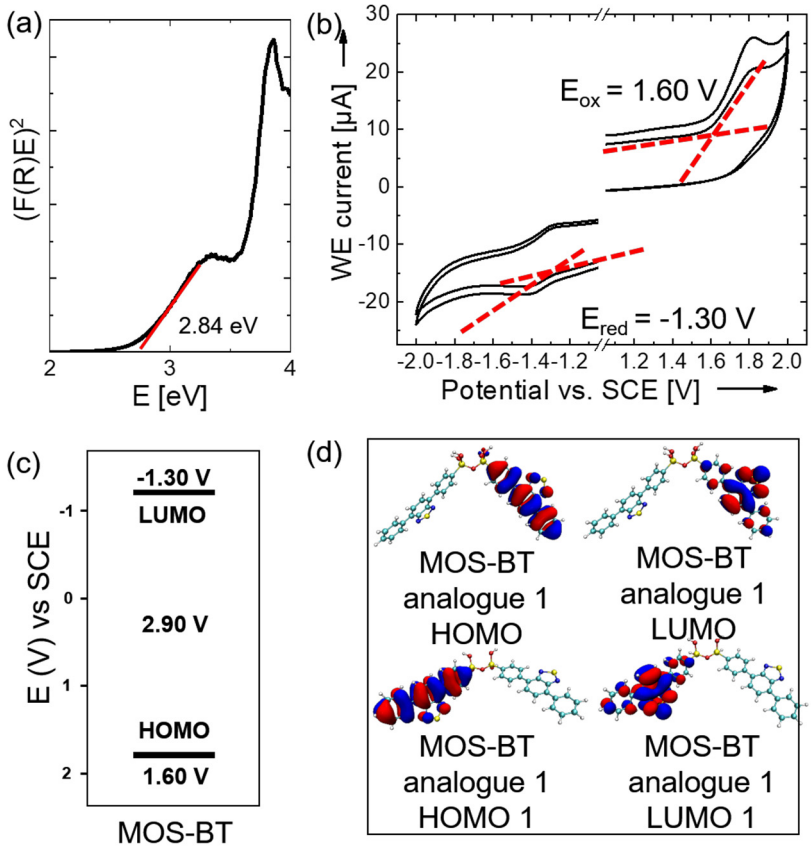

Figure 33. (a) Kubelka-Munk plot, (b) cycle voltammetry, (c) HOMO and LUMO band positions and (d) DFT and TDDFT-calculated molecular orbital of MOS-BT.

5.1.3 Visible light-promoted aryl azoline formation

To investigate the photocatalytic activity of MOS−BT, the aryl azoline formation was chosen as model reaction for the photocatalytic formation of 2-phenyl-2-imidazoline. As listed in Table 1, the use of organosilica led to successful formation of phenyl azoline with selectivity higher than 97 %, with MOS−BT being the most effective catalyst for a reaction conversion of 89 % (entry 1). The molecular unit $BTPh_2$ used as homogeneous photocatalyst (applied with a similar loading) showed a full conversion of the 2-phenyl-2-imidazoline formation. MOS−BT showed a similar efficiency to its small molecular analogue. This indicates the good accessibility of the photocatalytically active moieties and diffusion of reactants throughout the pores in MOS−BT. Control experiments conducted in dark (entry 3), or without using

MOS−BT as photocatalyst led only to trace conversion, demonstrating the essential roles of light and photocatalyst. The same phenomenon was cognized by excluding thiophenol and oxygen from the reaction atmosphere (entries 4, 5 in **Table 1**). Furthermore, various solvents (entries 6, 7 and 8 in **Table 1**) were investigated. After comparing, the reaction containing dimethyl sulfoxide as solvent (entry 1 in **Table 1**) was found with highest conversion.

Table 1. Screening and control experiment of the formation of phenyl aldehyde with diamine as model reaction[a].

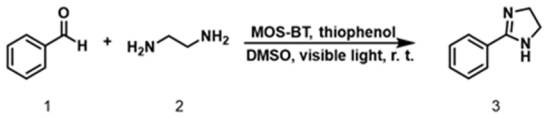

1 2 3

Entry	catalyst	reaction condition variations	conv. (%)[b]	selec. (%)[b]
1[a)]	MOS-BT	-	89	97
2	-	no catalyst	trace	0
3	MOS-BT	in dark	trace	0
4	MOS-BT	no thiophenol	trace	0
5	MOS-BT	no O_2, under N_2	12	14
6	MOS-BT	in acetonitrile	20	17
7	MOS-BT	in DMF	60	41
8	MOS-BT	in toluene	63	57
9[c)]	MOS-BT	electron scavenger	trace	0

10[d]	MOS-BT	hole scavenger	40	39
11[e]	$BTPh_2$	homogeneous system	>99	95

[a] Standard reaction conditions: [benzaldehyde] = 0.1 M, [1,2-diaminoethane] = 0.3 M, [thiophenol] = 0.1 M, [MOS-BT] = 1 mg/mL, 3 mL DMSO, blue LED lamp (460 nm, 0.26 W/cm^2), room temperature, oxygen, 12 h. [b] Conversion and selectivity determined by GC-MS. [c] Benzoquinone as electron scavenger. [d] KI as hole scavenger. [e] [$BTPh_2$] = 2.8 mM, 12 h.

Electron and hole scavengers were then included to exposure the mechanistic insight and the specific roles of the photogenerated electron/hole pair during the addition process. By adding benzoquinone as an electron scavenger, a reduced conversion was observed (entry 9). With the addition of KI as a hole scavenger, only trace conversion was observed (entry 10), indicating the essential role of holes for the formation of product. The result indicates that the electron-activated superoxide radical ($O_2^{\bullet-}$) could accelerate the addition process as active species. Notably, the catalytic efficiency and selectivity of MOS−BT was comparable with the homogeneous system using $BTPh_2$ (entry 11).

Electron paramagnetic resonance (EPR) experiments were then conducted to precisely study the role of superoxide radical during the reaction. As displayed in Figure 2a, an additional controlling experiment, which implemented the 5,5-dimethyl-1-pyrroline N-oxide (DMPO) as a superoxide radical trapping agent, had appealed typical EPR patterns for DMPO−$O_2^{\bullet-}$ adducts.

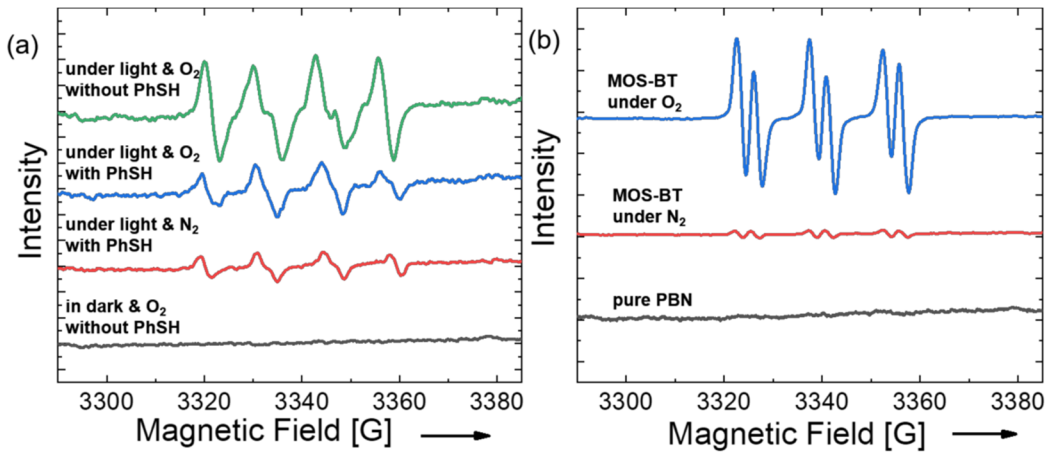

Figure 34. (a) EPR spectra of DMPO-$O_2^{\bullet-}$ adducts with MOS-BT in DMSO as photocatalyst in darkness, under blue light irradiation (λ = 460 nm, 1.2 W/cm^2) with thiophenol (PhSH) or without thiophenol. (b) EPR spectra using PBN as a radical trapping agent for the radical intermediate of thiophenol under light irradiation. Pure PBN (black), PBN and MOS-BT under N_2 atmosphere (red), under O_2 (blue).

Based on the observations, a possible mechanism for obtaining 2-phenyl-2-imidazoline by visible light assisted catalysis is described in **Figure 35**. First, 1,2-diaminoethane and benzaldehyde are dehydrated and condensed to form imine intermediate **a**. Under visible-light irradiation, intermediate **a** was oxidized by the photogenerated hole of MOS−BT and intramolecular cyclization to form its cationic radical intermediate **b**. Meanwhile, the activated superoxide obtained a hydrogen atom from thiophenol. The intermediate **b** donates one hydrogen atom to thiophenol radical and result in formation of intermediate **c**. Finally, the desired product 2-phenyl-2-imidazoline is produced by deprotonation of **c** by hydrogen abstraction with hydrogen peroxide. A practical proof of the formation of the radical intermediates could be observed using N-tert-butyl-α-phenylnitrone (PBN) and DMPO as a radical trapping agent (**Figure 34**). Thiophenol is oxidized by $O_2^{\bullet-}$ during the reaction, the signal of DMPO−$O_2^{\bullet-}$ in the sample added with thiophenol is weaker than that of the sample without thiophenol (**Figure 34a**). While by adding PBN, the formation of the thiophenol radical could be further observed and a typical pattern of PBN trapped radical was logged. Under oxygen atmosphere, the enhanced signal intensity indicated an essential role that oxygen played

within the photocatalytic cycle. (**Figure 34b**)..

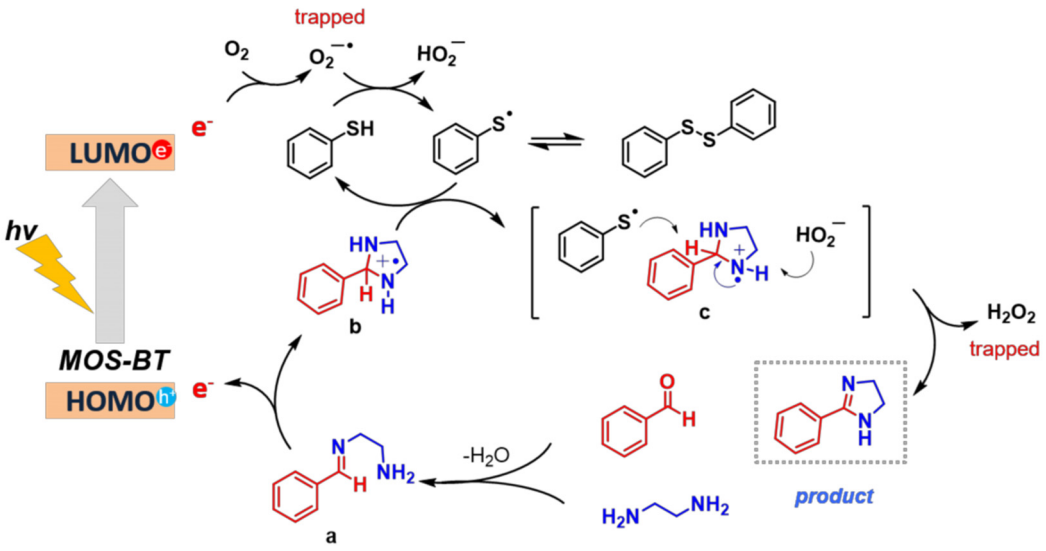

Figure 35. Proposed reaction mechanism for the photocatalytic formation of 2-phenyl-2-imidazoline.

To further explore the universal feasibility of MOS−BT as photocatalyst, various benzaldehydes and amine derivatives were tested for the azoline formation reaction. As displayed in **Figure 36**, high conversion and selectivity were achieved in most examples. Both electron-donating substitution groups on the aryl rings of the substrates (for example methoxy) and electron-withdrawing substitution groups (for example nitro or halides) did not affect the conversion and selectivity.

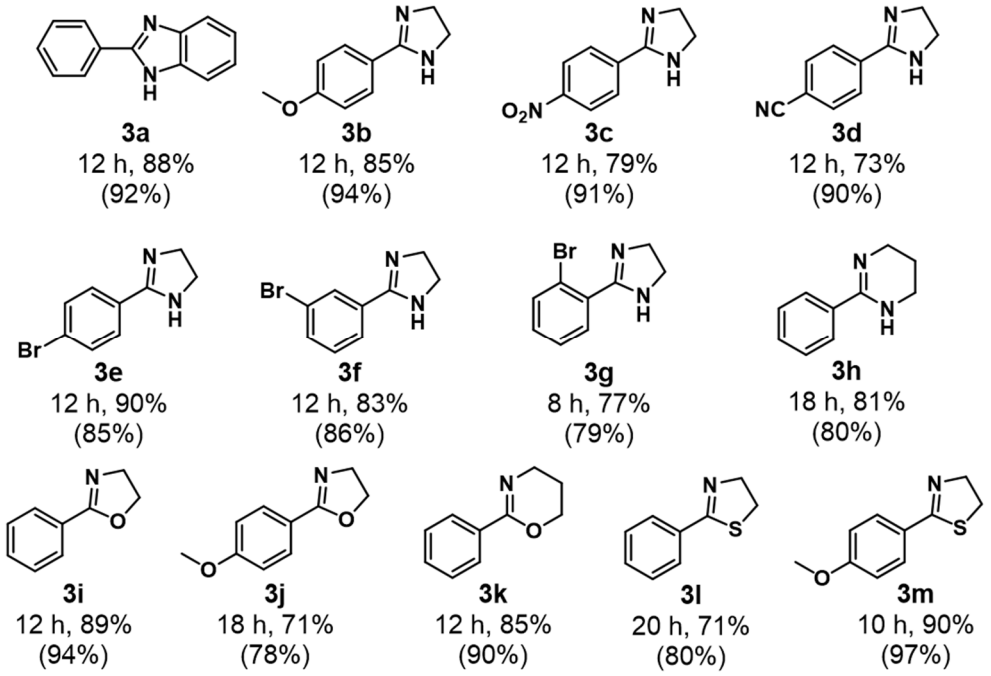

Figure 36. Scope of the reactions using MOS-BT as photocatalyst; the value shown in parentheses indicates the selectivity of product.

Moreover, the repeating experiments showed that MOS−BT could be reused for the azoline formation reaction for several cycles maintaining a stable level of conversion and selectivity (**Figure 37a**). The optical properties of MOS−BT barely changed after the recycling experiments, demonstrating its robust nature and reusability as heterogeneous photocatalyst (**Figure 37b**).

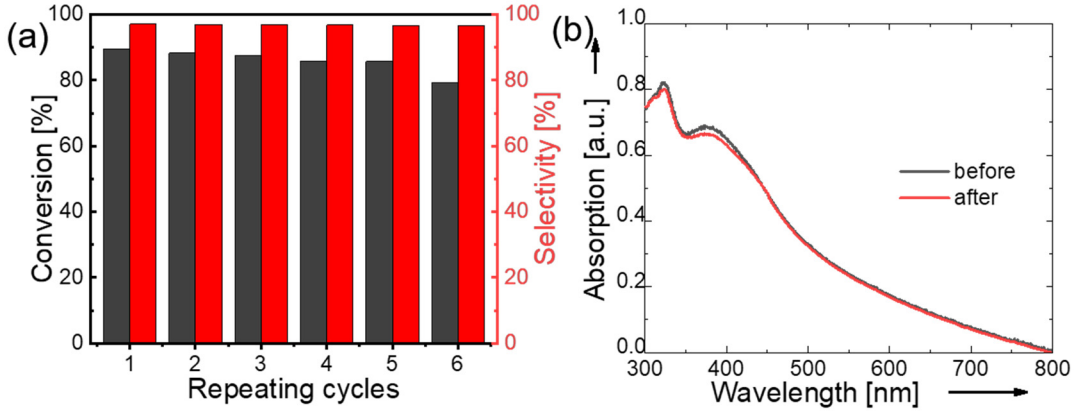

Figure 37. (a) Repeating experiment for 6 cycles and (b) UV-vis spectra of MOS-BT before and after the aryl azoline formation.

5.1.4 Conclusion

In summary, we designed organosilica containing 4,7-diphenylbenzothiadiazole as efficient heterogeneous and reusable photocatalyst for the formation of *N*-heterocyclic compounds. The mesoporous organosilica possessed a pore size of ca. 5.7 nm. Addition of aromatic aldehydes with various amines can be efficiently catalyzed, forming 2-phenyl-2-imidazoline, 2-phenyl-2-oxazolines, 2-phenyl-2-thiazolines and their derivatives with high conversion and selectivity. This study showed that mesoporous organosilica can be used as efficient photocatalyst with potential for a broader range of photocatalytic reactions.

5.2 Aerobic photobiocatalysis enabled by combining core-shell nanophotoreactors and native enzymes

This subchapter is based on the preparing article “Aerobic photobiocatalysis enabled by combining core-shell nanophotoreactors and native enzymes”. Wenxin Wei designed and performed the main part of the experiments, analyzed the data and drafted the manuscript. Francesca Mazzotta performed the TEM-EDX measurements. Wenxin Wei, Dr. Calum Ferguson, Prof. Dr. Kai Zhang and Prof. Dr. Katharina Landfester contributed to the final version of the manuscript. Dr. Calum Ferguson, Prof. Dr. Kai Zhang and Prof. Dr. Katharina Landfester supervised the project.

Herein, we have designed of core-shell structured nanophotoreactors, where the photocatalytic unit is concentrated in the particle core, and surrounded by a mesoporous silica outer shell. This configuration allows the enzymatic cofactors to be easily diffuse through the porous shell to the active centre, where they can be rapidly transformed to their active state. Conversely, the shell can be produced so that, by size exclusion, enzymes can be separated from the active photocatalytic core. Furthermore, the mesoporous shell of the photocatalyst can be designed so that the diffusion time of the active oxygen, out of the photocatalytic material, is long enough that the active oxygen species return to the ground state. This novel photocatalyst design, in combination with an enzyme species, enables the continuous production of a desired products under visible light irradiation. The photobiocatalytic activity was tested in tandem with two different enzymatic systems glucose dehydrogenase and glycerol dehydrogenase, where long term enzyme stability was observed for the core-shell nanophotoreactor.

5.2.1 Motivation

Biocatalysts have recently emerged as a new competitive tool in synthetic organic chemistry.[324, 420-422] Enzymatic systems have been implemented to produce highly selective compounds, under milder conditions, where enzymatic systems often require fewer synthetic steps, lower reaction temperatures and use greener solvents, compared to traditional synthetic methods.[423, 424] Moreover, in nature, enzymes have developed to mediate a myriad of different reactions, resulting in a vast array of potential high-value products. To date, a broad range of enzyme classes have been employed including halogenases,[425-427] oxidoreductases,[347, 428-435] and hydrolytic enzymes.[436-438] Some enzymes, such as dehydrogenases, are cofactor-dependent enzymes, limiting their broad industrial application.[439] Cofactors such as nicotinamide cofactors NADH (b-nicotinamide adenine dinucleotide) or NADPH (b-nicotinamide adenine dinucleotide phosphate) in their reduced forms are typically used by oxidoreductases in order to reduce a specific substrate. In nature a complicated electron transport chains exist in order to regenerate the required reduced cofactor species.[440] However, the synthetic replication of these natural systems has demonstrated to be extremely challenging, and rather difficult to maintain, therefore, alternative cofactor regeneration pathways have been investigated.

Visible-light mediated photocatalysis has been developed as a way to catalyse reactions under mild conditions. Typically, either photocatalysts based on transition metals or organic catalysts have been investigated.[340, 431] Recently, the implementation of photocatalytic systems for cofactor regeneration has been investigated. To date, many photocatalysts, such as TiO_2,[430, 441] organic dyes,[442] carbon quantum dots,[443] graphitic carbon nitride (g-C_3N_4),[435, 444-448] covalent organic frameworks,[443, 449] conjugated microporous polymers[450] and classical photocatalytic polymers[451] have shown great potential to regenerate enzymatic cofactors such as NADH/NAD^+.[341, 452] Unfortunately, these photocatalytic systems also produce active

oxygen species (ROS), which currently limits the combination of these materials with enzymes, due to rapid degradation of the biomaterial. There is therefore an urgent need to develop new photocatalytic materials with the ability to prevent the deactivation and degradation of biomaterials.

To mitigate the rapid degradation of enzymes, tandem photocatalyst-enzyme systems have been introduced, where reactions are often undertaken in anaerobic conditions, removing oxygen from the system.[453] Indeed, this does not prevent enzyme degradation by photocatalytic by-products, but it can significantly reduce the efficiency of the enzymatic and photocatalytic materials. Alternatively, the immobilization of the enzymatic material within silica nanoreactors has been investigated to eliminate contact of ROS from the biomaterial.[454] Furthermore, superoxide dismutase can be co-encapsulated, to further protect the active enzymatic material.[455] However, these methods require the immobilisation of the enzymatic material within a solid construct, which can significantly decrease its efficiency compared to the native enzyme.

Ideally, the synergistic cooperation between photocatalysts and enzymes, in their native state, would be achieved. Here, photocatalytic materials should be readily dispersible in aqueous environments and be able to regenerate enzymatic cofactors, whilst not effecting the efficiency of the enzymatic system. To achieve this, photocatalytic materials should be designed so that they enable easy portioning of the cofactors into an active centre, where they can be rapidly converted. Contrastingly, the photocatalytic material should not allow generated active oxygen species to come in contact with to the required biomaterials. To achieve this the relative short lifetime of ROS can be exploited. The photocatalytic material can be engineered so the diffusion of ROS from within the photocatalytic material exceeds the lifetime of ROS.

5.2.2 Synthesis and characterization of core-shell nanophotoreactor

The tandem system of an enzyme and the core-shell nanophotoreactor is depicted in **scheme 2**. The photocatalytic core material is formed from a diphenylbenzothiadiazole ($BTPh_2$) unit modified with two organosilane groups and tetraethoxysilane (TEOS), producing a porous photocatalytic nanoparticle (NP-C). This active core is encased in a secondary mesoporous silica layer to form a core-shell structure (NP-CS).

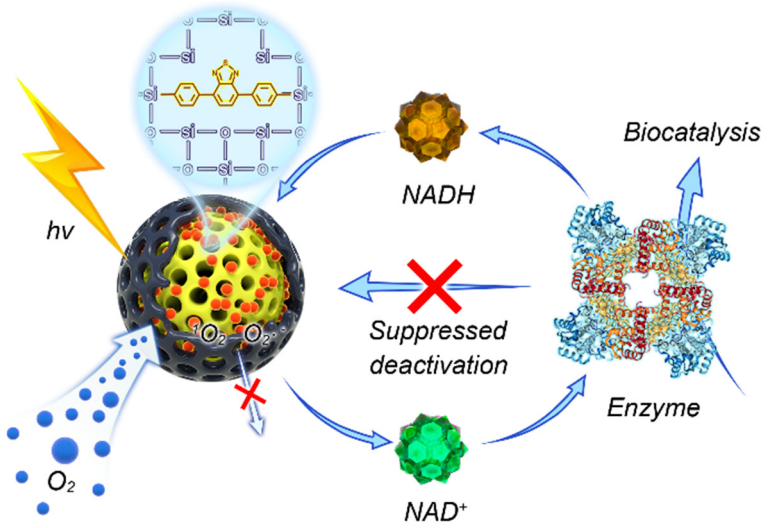

Scheme 3. Enzyme and photocatalyst cooperation system. The mesoporous photocatalyst completes the NADH/NAD^+ cycle together with the enzyme, and promotes the enzyme to catalyze the product.

To investigate the formation of the nanoparticles, transmission electron microscopy (TEM), and scanning electron microscopy (SEM) were conducted. As shown in **Figure 38**, the SEM and TEM images show that the synthesized nanoparticles have a porous structure. The core of the photocatalytic material has size range of 80-100 nm, while the core-shell nanoparticles have a size around 130 nm. The hydrodynamic radius of the photocatalytic core and the shell was investigated and a similar increase in size was observed from 200 to 250 nm (**Figure 39**).

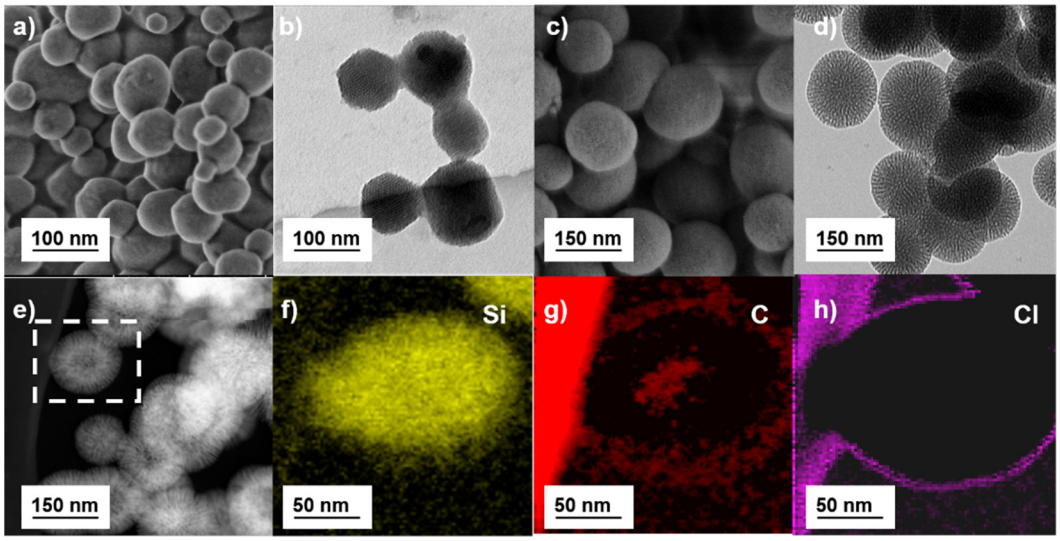

Figure 38. SEM and TEM image of a) and b) photocatalytic core (NP-C) and c) and d) core-shell (NP-CS). e) Annular dark-field (ADF) image shows the selected nanoparticle for f) - h) elemental mapping, which shows enriched contents of silicon in the shell and carbon in the core.

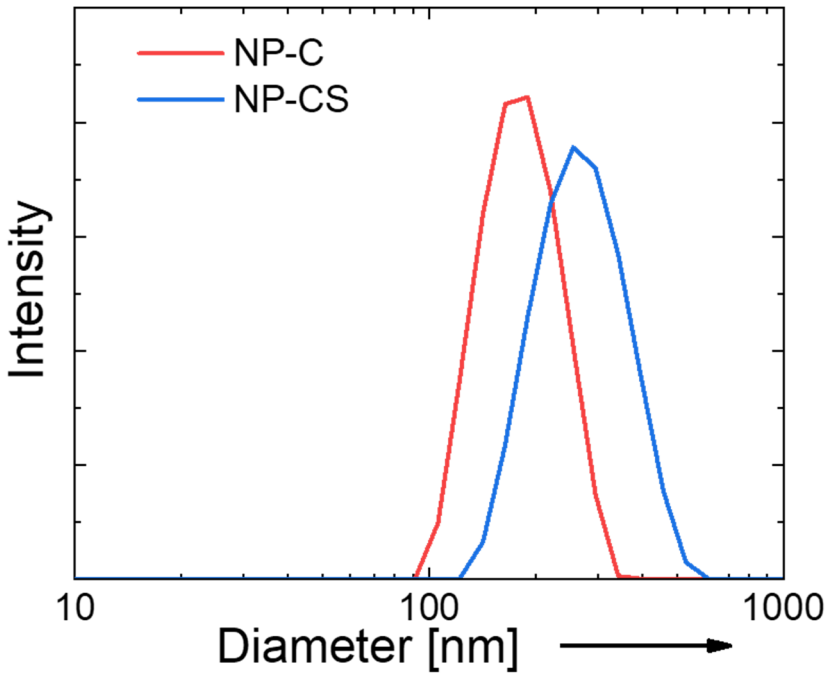

Figure 39. Dynamic light scattering (DLS) spectra of NP-C and NP-CS.

Energy dispersive X-ray (EDX) spectroscopy mapping was used to determine the composition of the photocatalytic particles. Elemental mapping was undertaken to determine the morphology of the core-shell particles. From the annular dark-field image we can see the

nanoparticle selected (**Figure 37e**). Here, a difference in contrast between the core and the shell of the particle is observed, suggesting a difference in the materials composition in these two regions. Electron energy loss spectroscopy (EELS) was used to determine the elemental composition of the nanoparticles. Silicon was detected throughout the particle, as expected due to the use of TEOS in both the core and the shell (**Figure 38f**). A strong signal for chlorine was detected on the shell of the nanoparticles (**Figure 38g**), this originates from the surfactant cetyltrimethylammonium chloride (CTAC) that was used in the formation of the nanoparticles as stabilizer. Carbon was detected on the surface of the nanoparticle (again due to the surfactant) and within the core. The carbon rich core is due to the presence of the photocatalytic aromatic $BTPh_2$ moiety, showing that it was successfully incorporated into the core particle (**Figure 38h**). From the carbon elemental cross-section (**Figure 40**), we can see a clear carbon free area corresponding to the shell of around 30 nm either side of the core. This would suggest that this region is free of the photocatalyst and is pure silica, supporting the core-shell morphology of the nanoparticles.

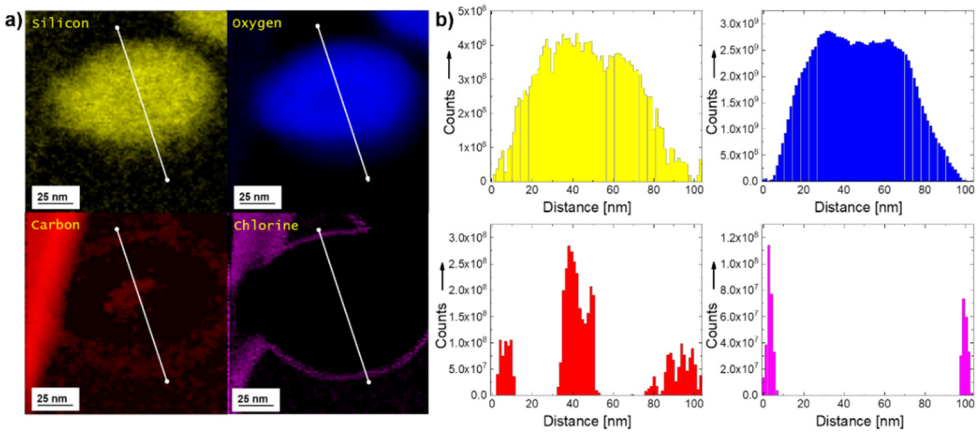

Figure 40. a) Elemental mapping and b) cross section elemental distribution of NP-CS.

To characterize the porosity of the core and core-shell nanoparticles, nitrogen gas sorption at 77 K was used (**Figure 40a**). The pore size of the materials was measured by BJH (Barrett-Joyner-Halenda) pore size analysis, the major peak of the pore size distribution for the

photocatalytic core material was centred on 2.5 nm (**Figure 41b**). Two peaks were observed for the core-shell material one centred at 2.5 nm (corresponding to the core) and one centred at 3.9 nm (corresponding to the shell). The shell pore diameter was designed so that it is smaller than the typical enzyme diameter, separating them from the active core. The BET (Brunauer–Emmett–Teller) surface area of the photocatalytic core and core-shell were determined over a relative pressure range of 0.01–0.3 P/P_0 **(Figure 41c**). The surface area of the photocatalytic core and core-shell material were found to be around 102 $m^2 \cdot g^{-1}$ and 664 $m^2 \cdot g^{-1}$.

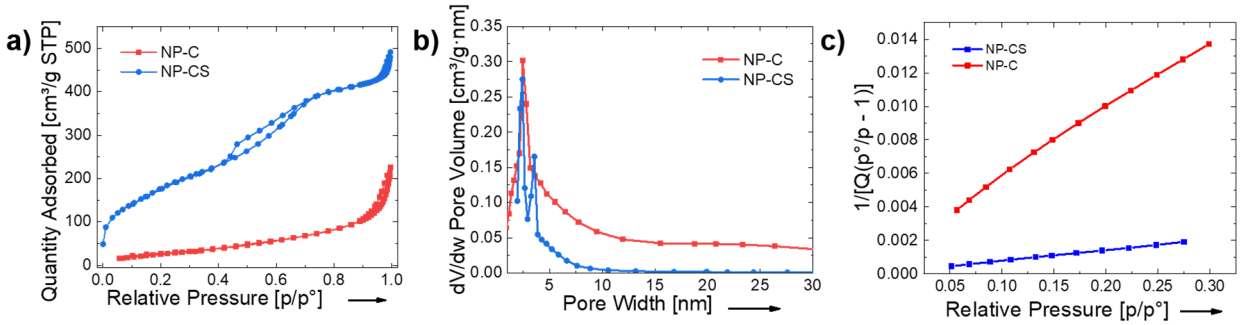

Figure 41. a) Gas sorption isotherms, b) BJH pore size distributions and c) BET surface area plot of NP-C and NP-CS.

Fourier transform infrared spectrum (FTIR) was obtained to show the incorporation of benzothiadiazole within the photocatalytic core. Peaks corresponding to 1347, 1390 and 1567 cm^{-1}, which are characteristic for C=N and N–S stretching modes in the benzothiadiazole moiety were observed.[456] The strong and wide absorption signals at 1095 cm^{-1} can be assigned to Si−O−Si antisymmetric stretching vibration[457] (**Figure 42**).

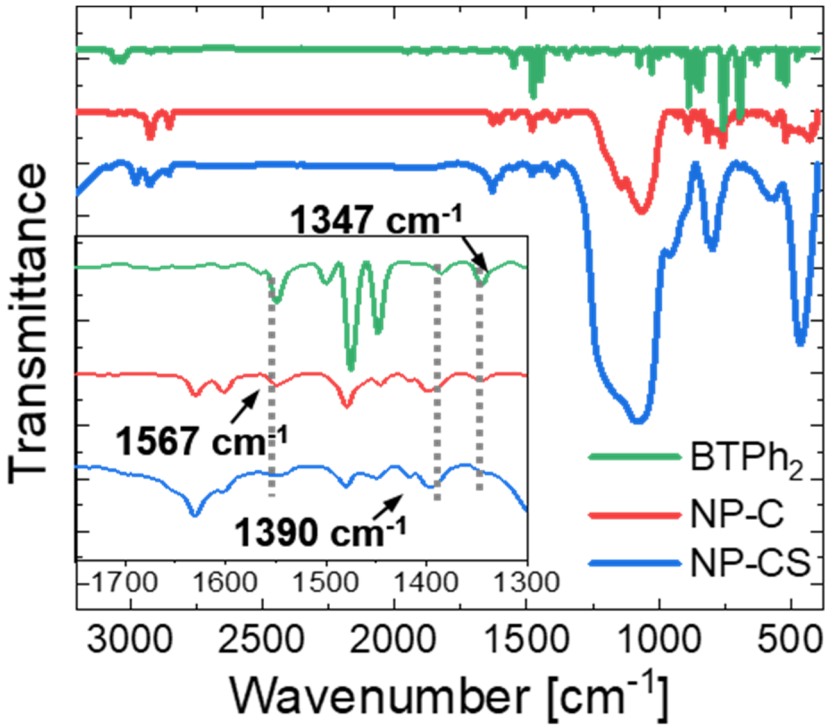

Figure 42. Fourier transform infrared (FTIR) spectra of small molecular $BTPh_2$ and NP-C and NP-CS.

Similar conclusions could be drawn from the corresponding solid-state ^{13}C cross-polarization magic-angle-spinning (CP-MAS) NMR spectrum (**Figure 43**). The pronounced signals at ca. 153, 134 and 129 ppm verified the presence of $BTPh_2$ unit within the nanophotoreactor and the signal at 6 ppm was considered to be the residual surfactant.[257]

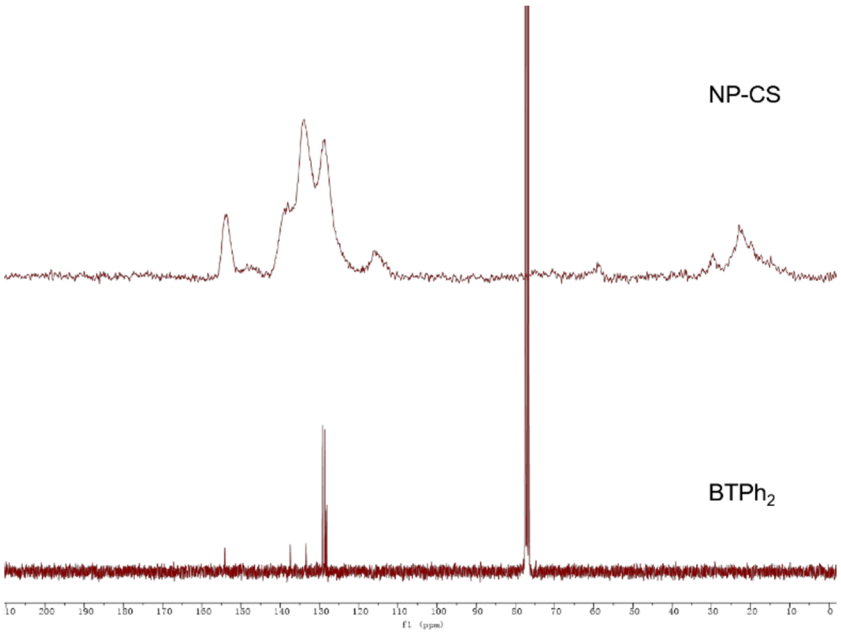

Figure 43. ^{13}C CP-MAS NMR spectrum of NP-CS and ^{13}C NMR ($CDCl_3$, 75 MHz) spectrum of diphenylbenzothiadiazole ($BTPh_2$).

UV-vis diffuse reflectance (DR) measurement was then used to characterize the optical properties of NP-C and NP-CS nanoparticles. As shown in the **Figure 44**, the maximum absorption for both the core and core-shell particles was at 410 nm. The absorption range of the nanoparticles extends to around 550 nm for the core particles, whereas the core-shell particles extend to around 500 nm. Currently, the cause of this difference is unknown, but both extend into the visible light spectrum. The emission range of the core particle of the photoluminescence spectrum is between 450 nm and 650 nm, and the maximum is 512 nm; the range of the core-shell particle is between 425 nm and 650 nm, and the maximum is 509 nm., which is similar to that of the $BTPh_2$ unit (**Figure 44b**).[417, 458]

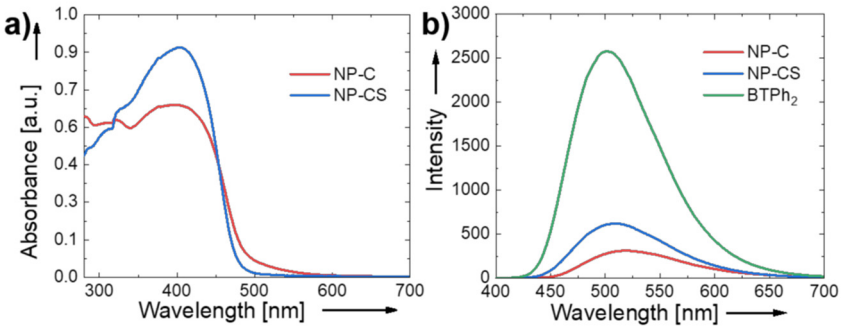

Figure 44. a) diffuse reflectance UV-vis spectra and b) comparison of the photoluminescence of $BTPh_2$, NP-C and NP-CS.

From the Kubelka-Munk function, it can be concluded that the optical band gaps of NP-C and NP-CS are 2.84 eV and 2.81 eV respectively (**Figure 45**).

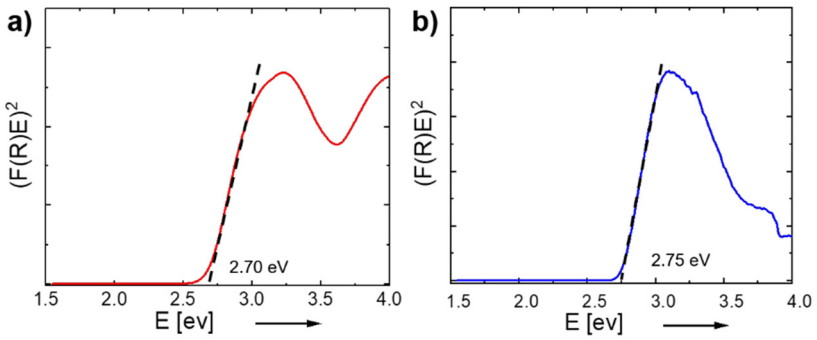

Figure 45. Kubelka-Munk transformed UV/Vis reflectance spectra of a) NP-C and b) NP-CS.

In order to evaluate the positions of the lowest unoccupied molecular orbital (LUMO) and the highest occupied molecular orbital (HOMO) of the material in this study, cyclic voltammetry (CV) measurements were performed (**Figure 46**). The HOMO/LUMO of NP-C and NP-CS were determined to be 1.65 V/-1.33 V and 1.63 V/-1.34 V (vs. saturated calomel electrode, SCE). This corresponds to the similar levels obtained for $BTPh_2$, with a HOMO/LUMO level of 1.65/-1.36 V (vs. SCE). This demonstrates that the incorporation of the photocatalytic moiety into the silica nanoparticle does not significantly affect the electronic structure of the material.

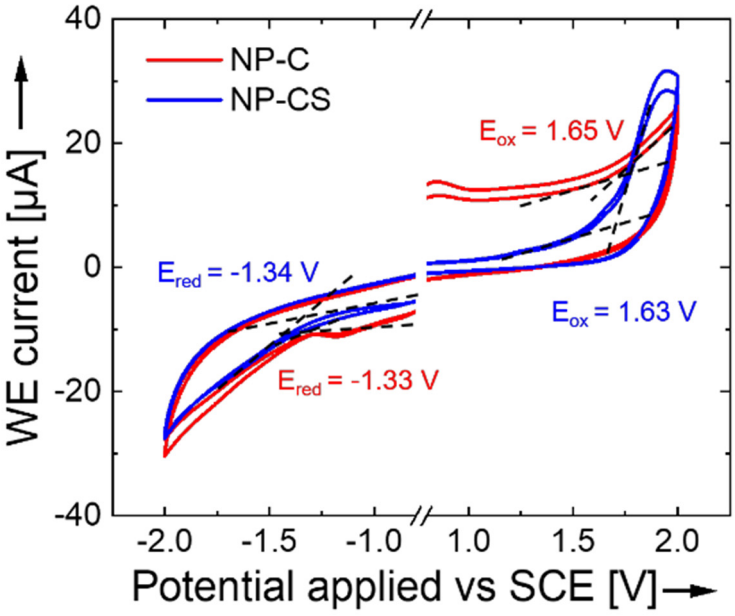

Figure 46. Cyclic voltammetry of nanophotoreactors.

5.2.3 Light driven regeneration of the enzymatic cofactor NAD^+ and subsequent utilization by enzymatic material

The ability of the photocatalytic particles to oxidize NADH was investigated, comparing both the core and the core-shell particles (**Figure 47**). The concentration of core (e.g. the photoactive portion) was kept constant at 1 mg·mL, the rate of the reaction was found to be quicker for the core particles compared to the core-shell, with 100% conversion in 30 and 50 min respectively. This difference was attributed to the diffusion time of NADH through the shell to the catalytic core.

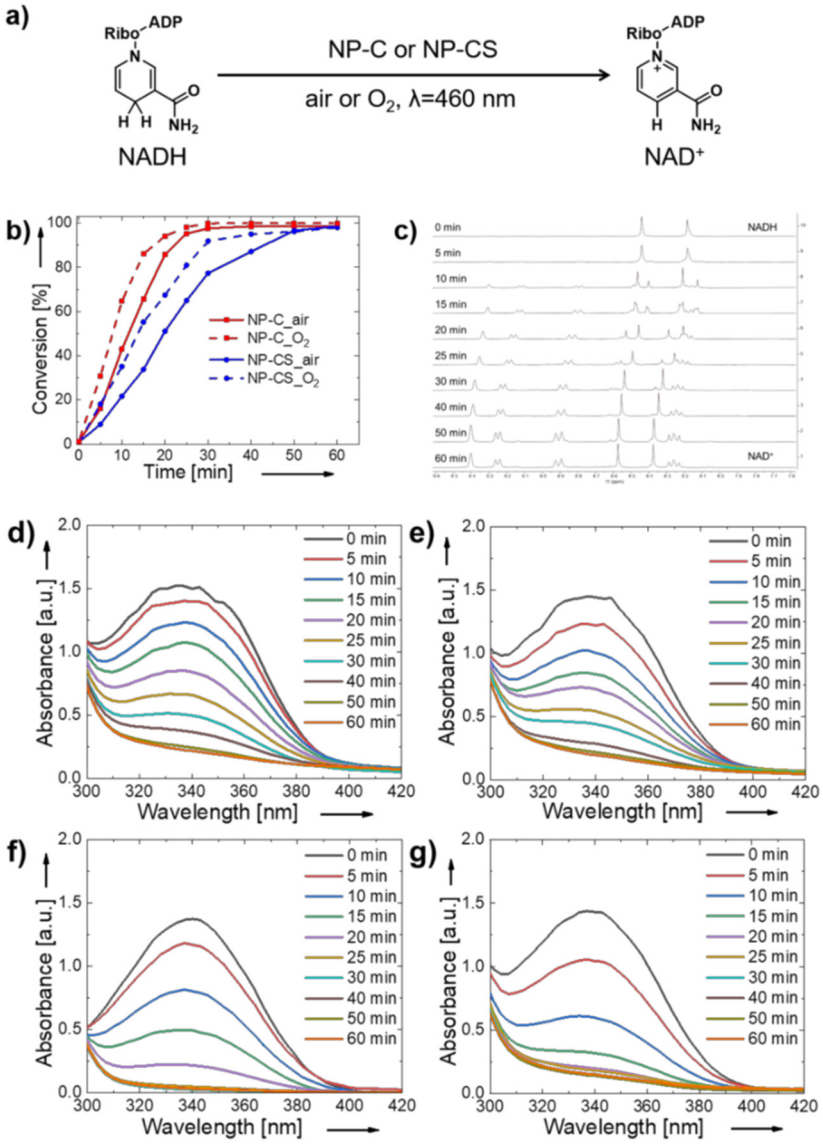

Figure 47. NADH oxidation with NP-C and NP-CS: a) equation; b) kinetic curve of NP-C and NP-CS in air and O_2 atmosphere respectively; c) ^{1}H NMR spectra of NADH to NAD$^+$ over time containing NP-CS in air and absorbance spectra of 1 h NADH oxidation containg d) NP-CS with air, e) NP-CS with O_2, f) NP-C with air and g) NP-C with O_2.

The presence of ROS species was determined using electron paramagnetic resonance (EPR) spectroscopy and the trapping agents 2,2,6,6-tetramethylpiperidine (TEMP) and 5,5-dimethyl-1-pyrroline-*N*-oxide (DMPO) to detect singlet oxygen and superoxide respectively (**Figure 48**). Here, the trapping agents are sufficiently small that they can diffuse into the core of the photocatalytic nanoparticle, and detect the production of ROS. For both the core and the core-

shell particles both singlet oxygen and superoxide were detected. However, due to the much larger nature of enzymes it is unlikely that they will come in contact with the active photocatalytic core. In fact, significant amounts of mainly hydroxyl (HO•) radicals could be detected in illuminated samples[428]. These hydroxyl radicals most likely may originate from water oxidation, from the reaction of superoxide ($O_2^{\bullet-}$, from O_2 reduction).

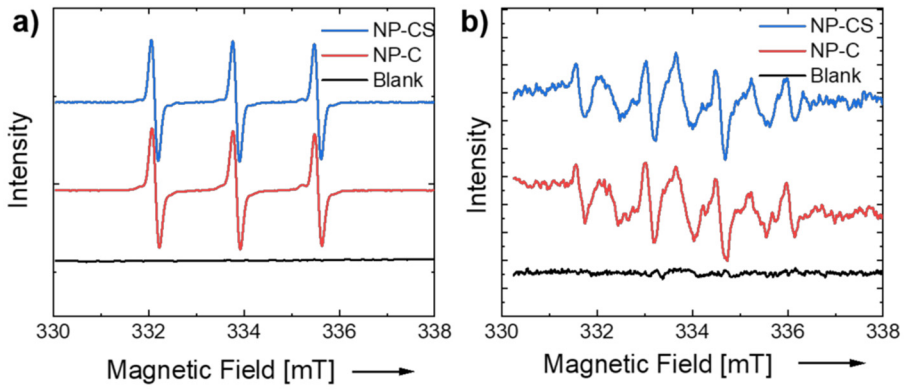

Figure 48. Electron paramagnetic resonance (EPR) spectra of NP-C and NP-CS with a) TEMP and b) DMPO in H_2O.

The light driven regeneration of the enzymatic cofactor NAD^+ and subsequent utilization by enzymatic material was tested using two model enzyme systems, glycerol dehydrogenase and glucose 1-dehydrogenase. Both of the enzymes chosen are oxidoreductases, a class of enzymes that has shown great promise for use in industrial processes[434]. Here, both enzymes are dependent on NAD^+ to oxidize a selective substrate, which can be regenerated by the photocatalytic material (**Figure 49**).

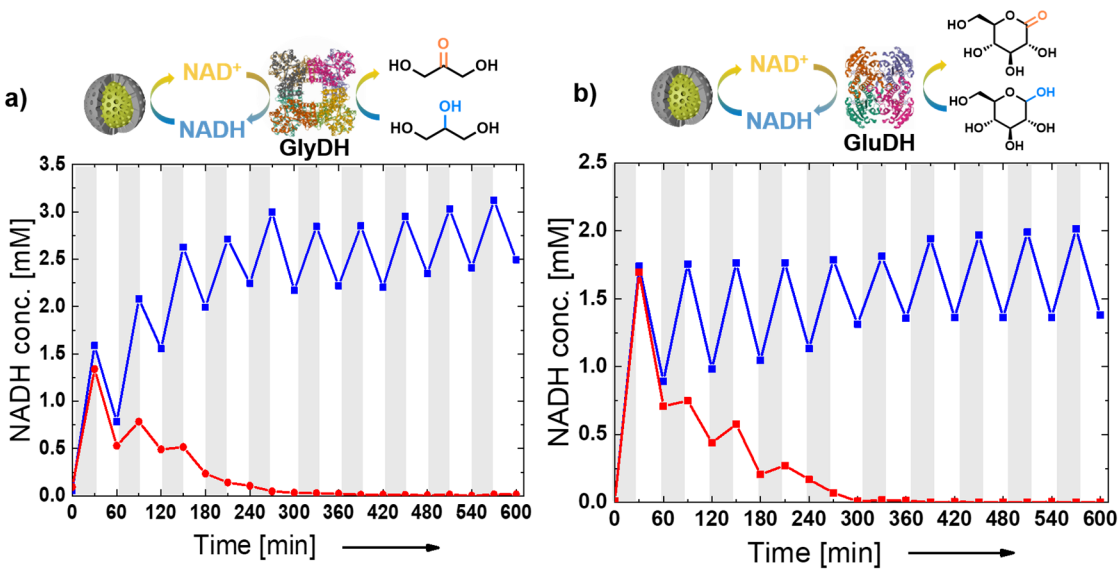

Figure 49. The core (red line) and core-shell (blue line) nanophotoreactor cooperate with the enzyme a) glycerol dehydrogenase and b) glucose dehydrogenase to recover NAD^+ and NADH by alternately adding reagents (glycerol and glucose) and light in the dark.

This photobiocatalytic system was initially tested using glucose 1-dehydrogenase, which converts glucose and NAD^+ into gluconic acid and NADH. Here, NAD^+ and glucose were added into the system, under dark conditions, enabling the enzyme to use the oxidized cofactor to convert glucose (**Figure 49b**). After 30 min, the sample was irradiated with blue LED for a further 30 min. During this period a decrease in the NADH concentration was observed, due to photocatalytic conversion back to NAD^+. From this, we can see that the photocatalytic rate of conversion of NADH to NAD^+ is much faster than the corresponding enzymatic reaction. After the photocatalytic regeneration of NAD^+ again the lights where turned off, and for the system containing core-shell particles the NADH conversion rose again. This shows that the enzyme is still in its active form and has not been denatured. In, contrast only a small increase in NADH concentration was observed for the system in the dark containing the unprotected core photocatalyst. The core-shell system could be successfully cycled over multiple iterations, without significant reduction in enzymatic activity. Conversely, complete loss in enzyme activity was observed after three cycles in the unprotected system.

To demonstrate the versatility of this photocatalytic system for use in photobiocatalysis a second enzymatic system was investigated. Glycerol dehydrogenase was used to convert glycerol and NAD^+ to dihydroxyacetone and NADH. Similarly, to the system with glucose 1-dehydrogenase multiple light dark cycles were used to demonstrate the synergistic combination of the photobiocatalytic system, with no loss in activity after 10 cycles observed. Once again the unprotected photocatalytic system resulted in rapid degradation of the biomaterial, showing the need for the protecting mesoporous silica shell.

5.2.4 Conclusion

In summary, core-shell structured nanophotoreactors have been synthesized that enable stable and recyclable aerobic photobiocatalysis to be undertaken. The obtained core-shell nanoparticles are composed of a photocatalytically active core and a silica shell, which have a mesoporous structure that facilitates easy diffusion through the material. This core-shell structure protects biomaterials from the active oxygen species such as superoxide radicals and singlet oxygen produced by the photocatalyst. Aerobic photobiocatalytic cascade reactions could be undertaken, where the photoactive material regenerates the cofactor NAD^+, this oxidised cofactor could then subsequently be used by two different oxidoreductases reducing the cofactor back to NADH. This circular process could be repeated over ten consecutive cycles demonstrating the stability of this system. Critically, this system keeps the enzymatic material in its native, and most active state, ensuring a highly efficient conversion. So far the use of this system has been limited to model enzyme systems but in principle any NAD^+ dependent enzyme could be used in this system. This paves the way for industrially relevant photobiocatalytic systems to be investigated in the future.

5.3 Enhanced photocatalytic NADH regeneration by improved light-harvesting mesoporous organosilica

The enhancement of photocatalytic NADH regeneration by photocatalytic centers embedded in a light harvesting framework was investigated. Enhanced light collection of a mesoporous organosilica photocatalysis containing additional aromatic units (benzene, naphthalene, and anthracene) is reported. Aromatic ring bridged organosilanes were co-condensed with a 4,7-diphenylbenzothiadiazole ($BTPh_2$) organosilane monomer in the presence of a template surfactant. The aromatic ring effectively absorbs lower wavelengths than absorption wavelength of $BTPh_2$, and this excited energy is funneled into the photocatalytic center through energy transfer. Compared with the direct excitation of $BTPh_2$ to regenerate NADH, the efficiency is increased. These results demonstrate the potential of mesoporous organosilica photocatalysts for harvesting more of the solar spectrum.

5.3.1 Motivation

A feature of natural photosynthetic systems is that they can operate under the low photon flux of sunlight, where the absorption of light and the transmission of photochemical potential to the catalytic center is low. One of the critical components of natural photosynthesis is the light-harvesting antenna, this wheel-shaped array of chlorophyll is observed in both the light-harvesting complex 1 (LH1) and light-harvesting complex 2 (LH2) of purple photosynthetic bacteria. This array effectively absorbs sunlight and transports the captured energy to the reaction center through resonance energy transfer (RET) with almost uniform quantum efficiency.[459, 460] The efficiency of RET strongly depends on the distance between the energy donor and acceptor molecules and their orientation. Thus three-dimensional organization of molecular parts, namely light absorbers and multi-electron catalysts, are of particular

importance in proper positions for the construction of an artificial photosynthesis system. [461, 462]

A series of supramolecular antenna systems, such as dendrimers, porphyrin arrays,[462] organogels,[463] dye-loaded zeolites,[464] and photopolymers[461] with controllable three-dimensional structure, have been reported that exhibits strong light absorption and can effectively funnels the captured energy into a small number of acceptors through RET. However, the application of traditional supramolecular antenna materials in RET-type photocatalytic systems is limited, mainly due to the difficulty in chromophore organization. In addition, the combination of reaction sites at appropriate positions in the antenna, and the limited internal void space, which hinders the catalytic reaction and mass transfer.[412]

Mesoporous organosilica are functional materials which have mesoporous structure and organic-inorganic hybrid framework.[250, 255, 415, 465] They have revealed unique fluorescence,[264, 266, 466] enable hole transport,[467] and electron-donating properties.[468] It was also found that the organosilicon skeleton exhibits unique light-harvesting antenna characteristics.[469, 470] The well-defined mesopores of periodic mesoporous organosilicas (PMOs) are advantageous for the construction of heterogeneous photocatalysis systems. Sufficient internal void spaces enable efficient mass transfer, even after the incorporation of a photocatalysts, because of larger pore sizes[471] compared with those of layered compounds,[472] and zeolites.[473] In addition, the high surface area of the mesoporous structure can accommodate reactive sites, thereby improving photocatalytic activity. Therefore, PMOs are considered to have the potential to enhance photocatalysis as solid-state supramolecular light-harvesting antennas.

Here, a new design for enhancing the photocatalytic activity of diphenylbenzothiadiazole ($BTPh_2$) in the framework through a light-harvesting antenna has been described. $BTPh_2$ was selected as the reaction center because of its excellent photocatalytic ability.[44, 176, 457, 474]

Aromatic rings (benzene, naphthalene, anthracene) contained in the skeleton are used as light-harvesting antennas because they have well-studied optical properties to achieve efficient RET.[265, 469, 475] The photocatalytic center and the light-harvesting unit are fixed in the frame for effective RET. The obtained system successfully collected the white light energy absorbed incident on the frame and energy transfer to $BTPh_2$ was observed. This energy transfer resulted in the enhanced photocatalytic regeneration of NADH.

5.3.2 Synthesis and characterization of aromatic/diphenylbenzothiadiazole mesoporous organosilica

Aromatic/diphenylbenzothiadiazole mesoporous organosilica (MOS-Ar/BT) was prepared by sol-gel process. MOS-Ar/BT anchoring $BTPh_2$ on the walls of the mesochannels with Si-O-Si covalent bonds was obtained by co-condensation of two-organosilane precursors in the presence of a octadecyltrimethylammonium chloride ($C_{18}TMACl$) surfactant template under a basic condition. MOS-Ar/BT containing 5 mol% $BTPh_2$ unit was synthesized.

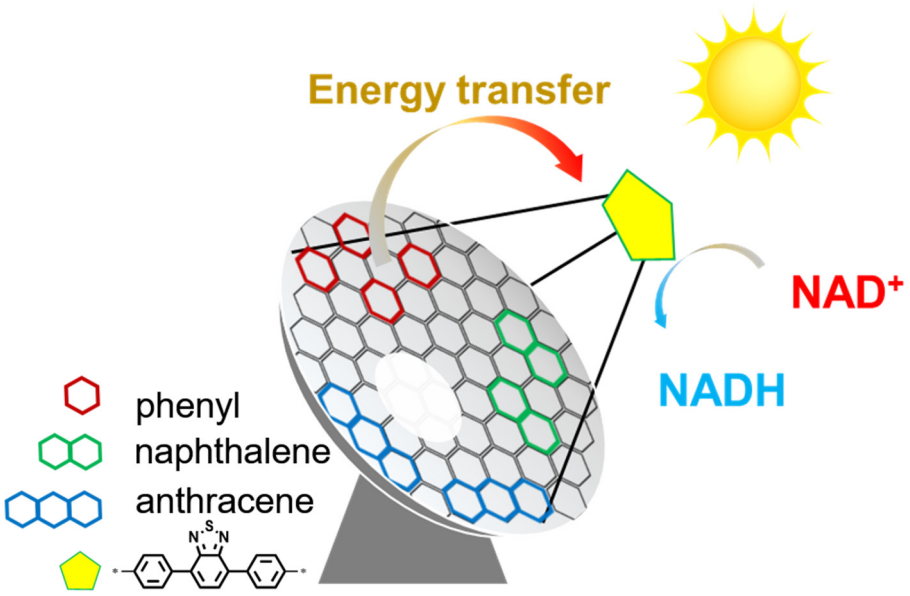

Scheme 4. Schematic representation of enhancement of photocatalytic NADH regeneration of the $BTPh_2$ center embedded in the framework by the light collection of mesoporous organosilica framework having a phenyl ring

structure.

The transmission electron microscopy (TEM) of MOS-Ph/BT (**Figure 50b**) confirmed the successful formation of a mesoporous structure consisting of one-dimensional uniform channels and periodic arrangement in the pore walls. The TEM images of MOS-Np/BT and MOS-Ant/BT did not show a prominent ordered structure, because naphthalene and anthracene are more hydrophobic than benzene, which affected the co-condensation process.

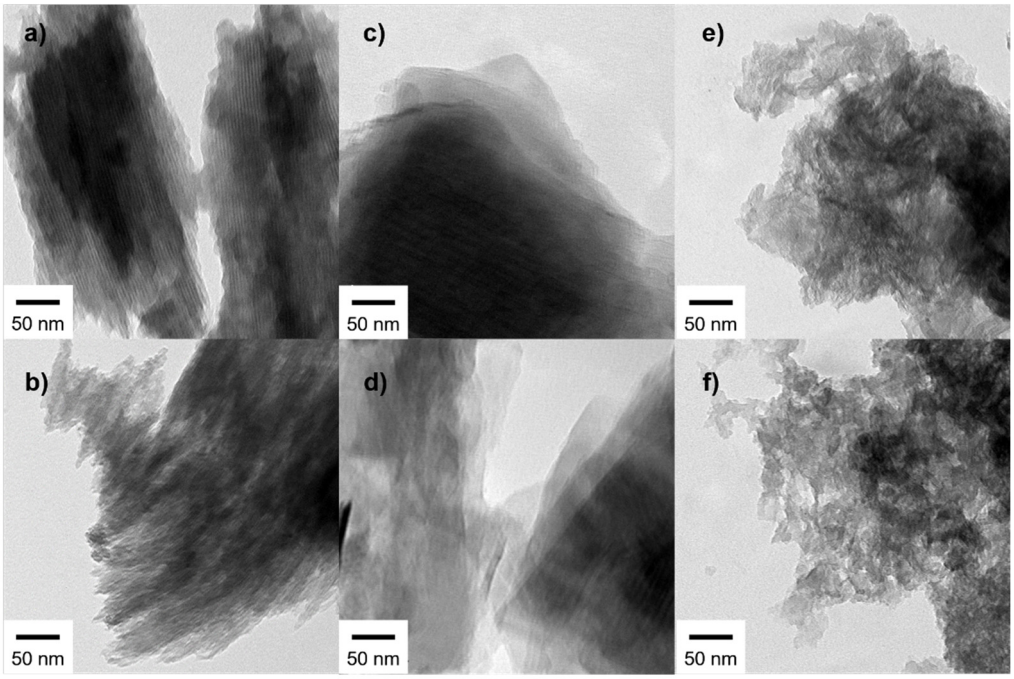

Figure 50. TEM images of a) MOS-Ph, b) MOS-Ph/BT, c) MOS-Np, d) MOS-Np/BT, e) MOS-Ant and f) MOS-Ant/BT.

The nitrogen adsorption/desorption isotherms (**Figure 51**) revealed that MOS-Ph/BT had large pore-volume (0.59 $cm^3 \cdot g^{-1}$), BET surface area (600 $m^2 \cdot g^{-1}$) and pore size (4.0 nm). BET surface area and pore volume of MOS-Ph/BT was smaller than MOS-Ph (789 $m^2 \cdot g^{-1}$, 0.84 $cm^3 \cdot g^{-1}$), but the diameter was larger than MOS-Ph (3.4 nm), which indicates that the addition of $BTPh_2$ precursor affected the expansion of micelles diameter during the hydrolysis process. The BET surface area and pore size of MOS-Nph were 647 $m^2 \cdot g^{-1}$, 3.6 nm, respectively, whereas for MOS-Nph/BT, these values were 549 $m^2 \cdot g^{-1}$, 3.8 nm, respectively. MOS-Ant's

BET surface area and pore size were 450 $m^2 \cdot g^{-1}$ and 4.3 nm, whereas for MOS-Ant/BT, these values were 356 $m^2 \cdot g^{-1}$ and 4.7 nm, respectively.

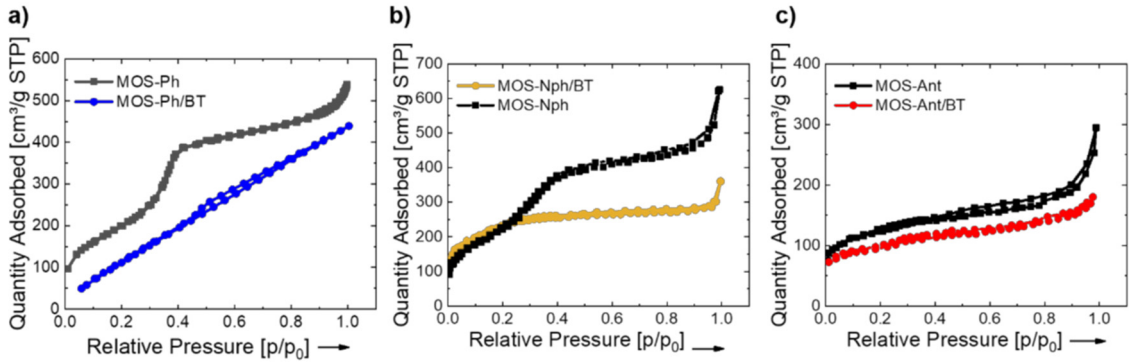

Figure 51. Nitrogen adsorption/desorption isotherms at 77 K of a) MOS-Ph and MOS-Ph/BT, b) MOS-Nph and MOS-Nph/BT and c) MOS-Ant and MOS-Ant/BT.

The UV-vis diffuse reflectance spectra (**Figure 52**) revealed a broad absorption range from 250 until 450 nm. The absorption maximum at 395 nm can be assigned to that of the $BTPh_2$ unit. And the absorption peak at 272 nm corresponded to phenyl ring. Similarly, MOS-Nph/BT also shown two absorption peaks. The absorption peak at 280 nm corresponded to naphthalene group and the maximum at 397 nm assigned to $BTPh_2$ unit. The absorption range of MOS-Ant was 318 nm to 423 nm, which overlapped with $BTPh_2$ partially.

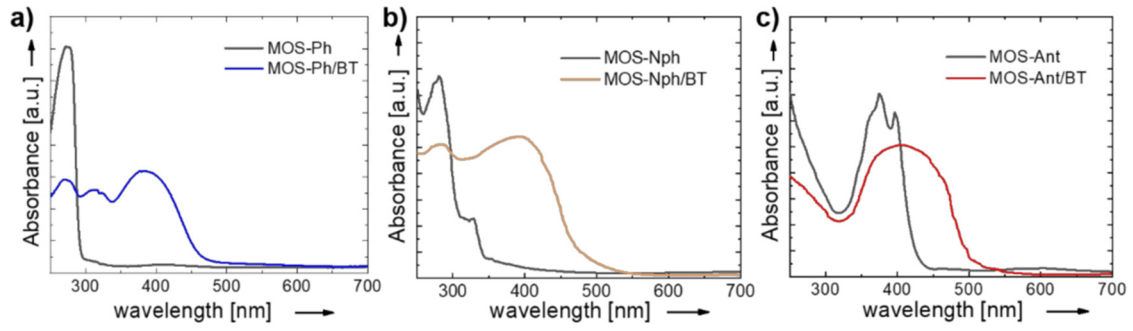

Figure 52. UV-vis diffuse reflectance spectra of a) MOS-Ph and MOS-Ph/BT, b) MOS-Nph and MOS-Nph/BT, c) MOS-Ant and MOS-Ant/BT

Figure 53 displayed the emission spectra of MOS-Ar and MOS-Ar/BT. MOS-Ph showed strong fluorescence (λ_{max} = 310 nm) because of the phenyl groups in the framework,[476] whereas

MOS-Ph/BT showed emission decreasing of phenyl group but exhibited a new emission band at 400-700 nm because of the $BTPh_2$ unit. The results suggest that the excitation energy of the phenyl groups is transferred into the $BTPh_2$. MOS-Nph/BT faced a similar situation to phenyl, shown a new emission band at 420-700 nm because of the $BTPh_2$ unit. The emission peak of MOS-Ant (480 nm) was close to $BTPh_2$ (510 nm). The emission peak of MOS-Ant/BT shown that the anthracene group has been completely integrated into $BTPh_2$ and made the peak wider. The phenyl emission at 310 nm weakens with adding $BTPh_2$ unit, and is accompanied by strengthening of the $BTPh_2$ emission at 510 nm. MOS-Nph/BT and MOS-Ant/BT shown the same trend of change. The results indicated that the excitation energy of the aromatic is transferred to the $BTPh_2$.[469]

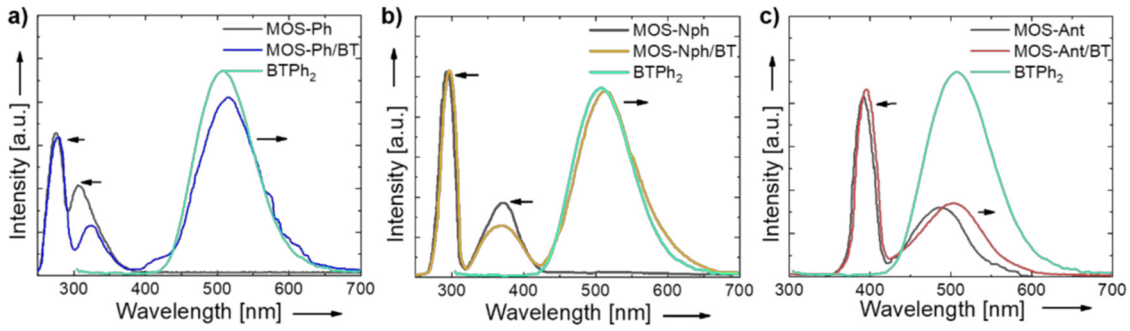

Figure 53. Fluorescence emission spectra of a) MOS-Ph, MOS-Ph/BT and $BTPh_2$ excited at 270 nm, b) MOS-Nph, MOS-Nph/BT and $BTPh_2$ excited at 280 nm, c) MOS-Ant, MOS-Ant/BT and $BTPh_2$ excited at 380 nm

Fluorescence lifetime measurements (**Figure 54**) show the dynamic quenching of the excited state of $BTPh_2$ in the presence of phenyl groups. Through Förster resonance energy transfer, energy is transferred to $BTPh_2$ by the phenyl group, thereby reducing the fluorescence lifetime of the $BTPh_2$ unit.[44, 477] After replacing the phenyl group with the anthryl group, since the overlapping area of the absorption range of anthracene and $BTPh_2$ is larger than the phenyl group, the energy transfer is more potent than that of the phenyl group. Therefore its fluorescence lifetime is also shorter.[478] On the other hand, energy transfer is also related to the

arrangement of aromatic rings in mesoporous organosilica. The aromatic moieties align more regularly in the organosilica framework are more conducive for the energy transfer process.[476, 479] The irregular structure of MOS-Nph/BT and MOS-Ant/BT made the energy transfer capacity worse than expected.

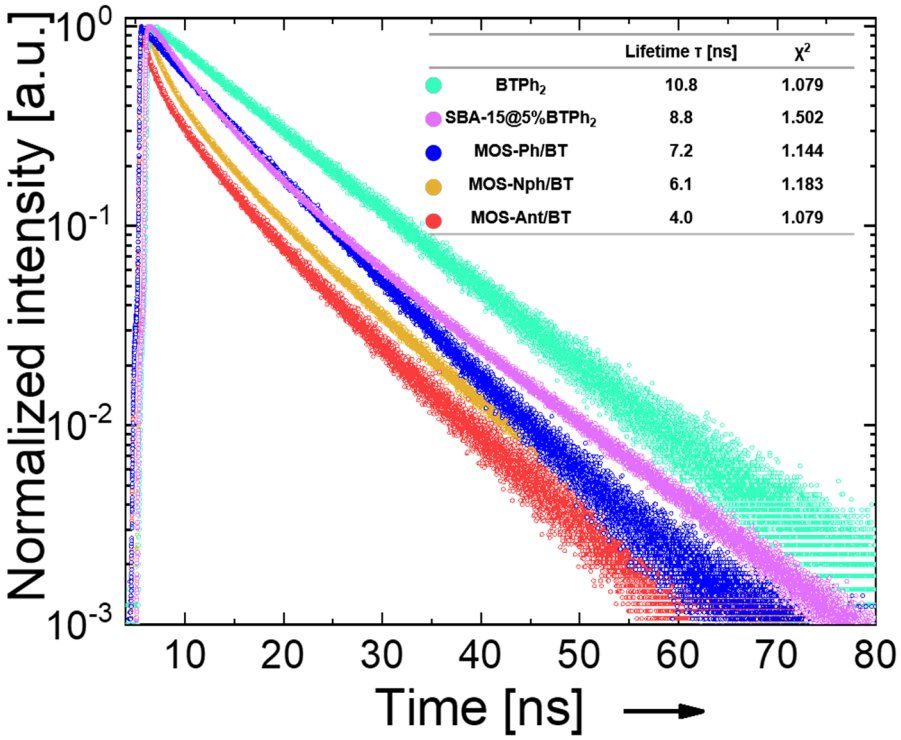

Figure 54. Emission decay profiles of $BTPh_2$, SBA-15@5%$BTPh_2$, MOS-Ph/BT, MOS-Nph/BT and MOS-Ant/BT in a CH_3CN suspension monitored at 510 nm.

5.3.3 Photocatalytic regeneration of NADH enhanced by light-harvesting mesoporous organosilica

NADH, acting as a hydride donor, played an indispensable role in the activation of enzyme-involved redox reactions. The photocatalysis of NADH regeneration was evaluated for mesoporous organosilica dispersed in a mixture of buffer and a sacrificial agent triethanolamine (TEOA) under non-oxidizing gas argon. As shown in the **Figure 55**, MOS-Ph/BT shows excellent NADH regeneration catalytic efficiency with conversion of 66% after

30 min, and reaches 82% after 60 min. In comparison, without light harvesting unit, mesoporous silica grafting $BTPh_2$ unit (SBA-15@5%$BTPh_2$) demonstrated a significantly lower conversion And MOS-Ph which was without photocatlytic unit had almost no ability to catalyze the regeneration of NADH.

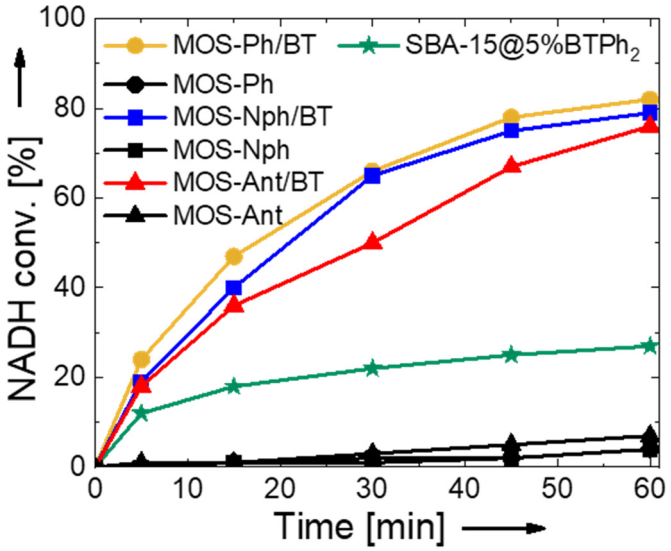

Figure 55. Time-resolved NADH regeneration conversion with mesoporous organosilica photocatalysts.

Compared with MOS-Ph/BT, the two mesoporous silicas containing naphthalene and anthracene had lower reduction ability on NAD^+, converting 76% and 79% of NADH respectively at 60 min. It shown that naphthalene and anthracene as light harvesting units also contributed to the improvement of photocatalytic performance.

In the first 30 min, the conversion of NADH regenerated by MOS-Nph/BT and MOS-Ant/BT were not as good as MOS-Ph/BT. It may be caused by the uneven distribution of catalytic sites coming from irregular pore structure. The irregular structure not only affect the mass transfer of the reaction, but also interfered with the energy transfer.[476] It might be caused by monomer agglomeration during the co-condensation process, which made the photocatalytic unit intensively to affect the catalytic ability. Correspondingly, mesoporous silica without $BTPh_2$ unit had almost no photocatalytic activity for NADH regeneration.

5.3.4 Conclusion

In conclusion, the mesoporous organosilica photocatalyst was prepared with diphenylbenzothiadiazole as the photosensitive unit and the aromatic ring bridged organosilane as the skeleton via co-condensation through the sol-gel method. The light energy effectively absorbed by the aromatic group in MOS-Ar/BT enters $BTPh_2$ through the RET funnel and strengthens the photocatalytic regeneration of NADH. Due to the light-harvesting of the aromatic group, the regeneration conversion is improved compared with the direct excitation of $BTPh_2$. These results demonstrated the potential of light-harvesting photocatalysts based on mesoporous organosilica, which can design and use various photocatalytic systems to simulate natural photosynthesis.

6. Experimental section

6.1 Visible light-promoted aryl azoline formation over mesoporous organosilica as heterogeneous photocatalyst

6.1.1 Materials

1-Bromo-4-iodobenzene, triethoxysilane, tetraethylorthosilicate, bromobenzene, 2,1,3-benzothiadiazole-4,7-bis(boronic acid pinacol ester), bis(acetonitrile)(1,5-cyclooctadiene)rhodium(I)tetrafluorobotate, tetrakis(triphenylphosphine)palladium(0) were purchased from commercial sources and used without further purification. The reactions conversions were monitored by GC-MS. Reaction yield refer to pure compound after being purified with column.

6.1.2 Characterization methods

UV-vis absorption and FTIR spectra were recorded on a Perkin Elmer Lambda 100 spectrophotometer and Varian 1000 FT-IR spectrometer at ambient temperature, respectively. Electron paramagnetic resonance (EPR) spectrum was performed on a Magnettech Miniscope MS200 spectrometer with spin trapping EPR at DMPO (0.1 M), catalyst (1 mg/ml) and thiophenol (0.1 M) in dimethyl sulfoxide. Another spin trapping EPR for PBN trapping experiment was conducted at PBN (0.1 M), catalyst (1 mg/ml) benzaldehyde (0.1 M), 1,2-diaminoethane (0.3 M) and thiophenol (0.1 M) in dimethyl sulfoxide on a Bruker EMX-plua spectrometer (Bruker B-VT 2000). The related simulation for the EPR spectrum was according to the condition: g factor was 2.00604. Frequency of measurement was 9.313456 (GHz) and B_c (magnetic center field) is 3317 (G). Cyclic voltammetry measurement was recorded on a Metrohm Autolab PGSTAT204 potentiostat/galvanostat in a three-electrode-cell system:

glassy carbon electrode as the working electrode, $Hg/HgCl_2$ electrode as the reference electrode, platinum wire as the counter electrode, and Bu_4NPF_6 (0.1 M acetonitrile) as supporting electrolyte with a scan rate of 100 mV/s in the range of -3 eV to 1 eV. The morphology was recorded by a scanning electron microscope (SEM) (LEO Gemini 1530, Germany) with an in lens SE detector and a transmission electron microscope (TEM) (JEOL JEM-1400). Thermogravimetric analysis (TGA) was conducted in a nitrogen atmosphere with temperature increasing from room temperature to 1000 °C at a rate of 10 K/min. GC-MS measurement was conducted on Shimadzu GC-2010 plus gas chromatography and QP2010 ultra mass spectrometer with fused silica column (122-5532, DB-5MS) and flame ionization detector. ^1H and ^{13}C NMR spectra for all compounds were measured using Bruker AVANCE 300 MR (at 300 MHz) and are referenced to 0.00 ppm and 0.0 ppm for $SiMe_4$. High-resolution mass spectra (HRMS) were recorded on Bruker microTof by using EI method. Surface areas and pore size distributions were carried out by nitrogen adsorption and desorption at 77.3 K by Micromeritics TriStar II Plus. Pore size distributions and pore volumes were calculated from the adsorption branches of the isotherms using Quenched Solid Density Functional Theory (QSDFT, N_2, evaluating carbon adsorbent with slit pores). MOS-BTs was degassed at 120 °C for 12 h under vacuum before analysis. The BET surface area was obtained based on data points received from $0 < P/P_0 < 0.25$ with the nonlinear density functional theory (NLDFT) equilibrium model being employed as the BET model fitting.

6.1.3 Synthesis of MOS-BT

Synthesis of 4-bromophenyltriethoxysilane[480]

1-Brom-4-iodobenzene (563 mg, 2 mmol), triethoxysilane (0.73 mL, 4 mmol), triethylamine (0.83 mL, 12 mmol) and bis(acetonitrile)(1,5-cyclooctadiene)rhodium(I)tetrafluoroborate (22 mg, 0.06 mmol) were dissolved in dry DMF

(8 mL) and added in 25 mL Schlenk tube. Then, the Schlenk tube was degas in liquid nitrogen temperature and backfilled with argon 3 times. After degassing process, the reactive mixture was heated at 80 °C for 2 h. While cooled down in room temperature, the mixture was diluted with 100mL diethyl ether and washed with NH_4Cl saturated solution 3 times. A crude product was obtained after drying over anhydrous $MgSO_4$ and purified by chromatography on silica with petroleum ether/dichloromethane (1/1) as the elution to afford the pure product as clear light yellow oil.

Synthesis of MOS-Br

The mesoporous organosilica MOS-Br was prepared by sol-gel process with surfactant P123. Typically, P123 (0.6g) and H_2O (0.9 mL) was dissolved in 18 mL 2.0 M HCl aqueous solution and stirred in 40 °C for 2 h. Then, 603.4 mg of 4-bromophenyltriethoxysilane (BPTS) was dropped in them while stirring. After 12h stirring and heating at 40 °C, the suspensions were filtered and washed by water. The obtained precipitates were extracted in Soxhlet extractor with 0.1 M HCl ethanol solution for 48 h. Finally, a canary yellow solid product (MOS-Br) were collected after dry in vacuum oven at 60 °C for 24 h.

Synthesis of MOS-BT

The mesoporous organosilica MOS-BT was prepared by palladium catalyzed Suzuki-Miyaura coupling reaction. 20.7 mg MOS-Br, 38.1 mg 2,1,3-benzothiadiazole-4,7-bis(boronic acid pinacol ester), 5.8 mg tetrakis(triphenylphosphine)palladium(0) were dissolved in 5 mL DMF. Then 1 mL trimethylamine was added following by degassing with Argon for 30 min. After degassing process, the reactive mixture was heated with stirring at 100 °C for 24 h. After that, 20.8 μL bromobenzene was injected in the reaction and continue heating at 100℃ for 24 h with stirring. The obtained precipitate was washed with chloroform, water and acetone for

three times and then extracted in a Soxhlet extractor with acetone and THF for 48 h each, respectively. Finally, a green solid product (MOS-BT) was collected after dry in vacuum oven at 60 °C for 24 h.

6.1.4 Characterizations

The content of Br and BT unit in MOS-Br and MOS-BT were characterized by thermogravimetric analysis (**Figure 56**). According to measurement and calculation, the mole ratio of Br and BT unit in MOS-Br and MOS-BT are 99% and 96%, respectively.

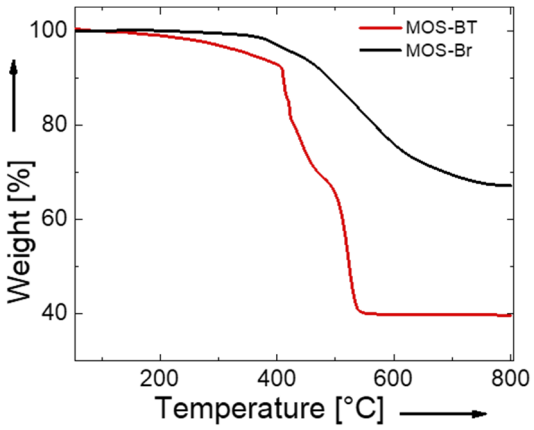

Figure 56. Thermogravimetric analysis of MOS-Br and MOS-BT.

The remaining palladium element from the Suzuki coupling catalysts in MOS-BT could affect the experiment of its catalytic ability. According to the inductively coupled plasma spectrometry of palladium, 0.3 ppm palladium in MOS-BT was confirmed (**Figure 57**).

ICP-Spectroscopy: "ACTIVA" Nr.: 0.0.0.0.0.

Analysis report from: 16.10.2019 Run: 161019 0.6mg/l Pd

Measurement parameters

DateTime: 16.10.2019 13:13

Method: 170419 1mg/l Pd | Power: 1200 | Plasma Flow: P1 | Sheath Flow: G1 | Auxiliary Flow: 0.0 | Pump Speed: 15 | Argon Humidificator: No | Nebulizer Flow: 1.28 | Nebulizer Pressure: 2.87

Time	El.	Line	Raw Intensity	Bkg. left	Bkg. right	Net Intensity	Solution[C]	Sample[C]
Name: 3-SiBr5BT100		Type: Analysis	#: 10	Rack:	Tube:	Weight: 1.0000	Volume: 1.00	Dilution: 1.00
WaveLength Calibration =>		*Element :* N		*Ref.:* 174.211		*Calc.:* 174.1994	*Offset:* -0.0003	
13:13:17	Pd	340.458	21 540.81			21 540.81	0.29	0.29
13:13:23	Pd	340.458	21 635.62			21 635.62	0.30	0.30
13:13:29	Pd	340.458	22 218.84			22 218.84	0.31	0.31
[Pd] = 0.30 mg/l			RSD: 2.76 %	Offset: -0.0023				
13:12:59	Pd	342.124	13 230.03			13 230.03	0.29	0.29
13:13:04	Pd	342.124	13 058.35			13 058.35	0.28	0.28
13:13:10	Pd	342.124	13 139.61			13 139.61	0.28	0.28
[Pd] = 0.28 mg/l			RSD: 1.79 %	Offset: -0.0024				
13:13:39	Pd	360.955	12 284.40			12 284.40	0.26	0.26
13:13:44	Pd	360.955	12 565.33			12 565.33	0.27	0.27
13:13:50	Pd	360.955	13 028.29			13 028.29	0.29	0.29
[Pd] = 0.27 mg/l			RSD: 6.41 %	Offset: -0.0035				

Measurement parameters

DateTime: 16.10.2019 13:13

Method: 170419 1mg/l Pd | Power: 1200 | Plasma Flow: P1 | Sheath Flow: G1 | Auxiliary Flow: 0.0 | Pump Speed: 15 | Argon Humidificator: No | Nebulizer Flow: 1.28 | Nebulizer Pressure: 2.87

Review:

Analyst: Administrator Date: Visa:

Figure 57. Inductively coupled plasma spectrometry of Pd in MOS-BT; 3-SiBr5-BT100 correspond to MOS-BT.

The formation of H_2O_2 could be approved by using the catalytic oxidation of N,N-diethyl-1,4-phenylenediammonium sulfate (DPD) by horseradish peroxidase (POD).[481] H_2O_2 and POD oxidizes two molecules of DPD to the corresponding cationic radical ($DPD^{\bullet+}$). The latter forms a stable red-purple colored chromogenic compound with two absorption maxima at 510 nm and 551 nm (**Figure 58**) The existence of H_2O_2 was confirmed.

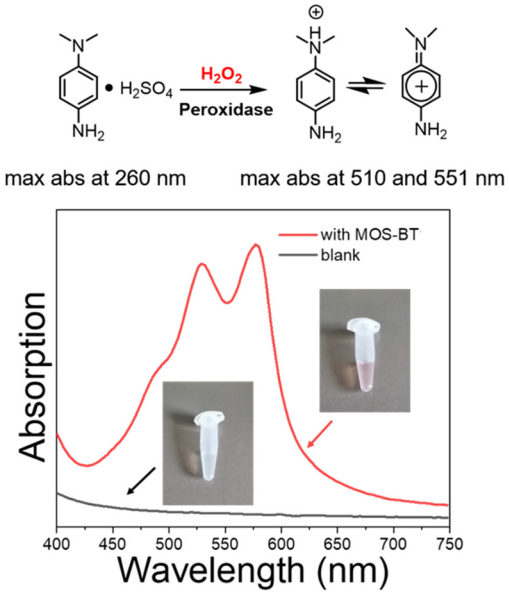

Figure 58. UV/Vis absorption spectra of the reaction system without and with the presence of MOS-BT after adding DPD and POD for H_2O_2 determination.

6.1.5 General procedure of the visible light-promoted aryl azoline formation using MOS-BT and compound characterization

A 40 mL vial was charged with 1.5 mmol 1,2-diaminoethane, 0.5 mmol benzaldehyde and 0.5 mmol thiophenol, MOS-BT (3.4 mg) and DMSO (3 mL). Then the solvent was bubbled by O_2 for 5 min and in front of a blue LED lamp (460 nm, 1.2 W/cm^2). The conversion of 2-phenyl-2-imidazoline was determined by GC-MS measurement. Upon consumption of 2-phenyl-2-imidazoline, the mixture was put into a centrifuge tube and centrifuged at 12000 rpm for 15 min to separate MOS-BT. The MOS-BT which has been washed with acetone and DCM and then dried is ready for the next use. The supernatant poured into a separatory funnel containing the mixture of ethyl acetate and water (v/v, 1/1). The organic layers were separated and extracted with ethyl acetate (30 ml). A crude product was obtained after drying over anhydrous $MgSO_4$ and concentrating with a rotary evaporator. Finally, the cycloaddition products could be obtained after purification with flash-column chromatography.

2-Phenyl-2-imidazoline (3)[482]

According to the general procedure, a 40 mL vial with a magnetic stir bar was charged with 1,2-diaminoethane (106 μL, 1.5 mmol), benzaldehyde (50.8 μL, 0.5 mmol) and thiophenol (51.4 μL, 0.5 mmol), MOS-BT (3.4 mg) and DMSO (3 mL). After the reaction was completed, the mixture was performed as the workup protocol and purified by chromatography on silica with petroleum ether/ethyl acetate (2/1) as the elution to afford the pure product as white solid. R_f (petroleum ether/ethyl acetate 2/1): 0.38. ^{1}H NMR ($CDCl_3$, 300 MHz): δ 7.78 (d, *J* = 7.1 Hz, 2H), 7.40 (dt, *J* = 23.1, 7.2 Hz, 3H), 3.75 (s, 4H). ^{13}C NMR ($CDCl_3$, 75 MHz): δ 165.0, 130.9, 130.3, 128.5, 127.2, 50.1. HRMS(EI-TOF) calcd. for $C_9H_{11}N_2$ $(M+H)^+$ 147.0917, found 147.0919.

2-Phenylbenzimidazole (3a)[483]

According to the general procedure, a 40 mL vial with a magnetic stir bar was charged with *o*-phenylenediamine (157 μL, 1.5 mmol), benzaldehyde (50.8 μL, 0.5 mmol) and thiophenol (51.4 μL, 0.5 mmol), MOS-BT (3.4 mg) and DMSO (3 mL). After the reaction was completed, the mixture was performed as the workup protocol and purified by chromatography on silica with petroleum ether/ethyl acetate (1/4) as the elution to afford the pure product as white crystal. R_f (Petroleum ether/ethyl acetate 1/4): 0.31. ^{1}H NMR (DMSO, 300 MHz): δ 12.91 (s, 1H), 8.18 (d, *J* = 7.2 Hz, 2H), 7.59 (d, *J* = 12.7 Hz, 2H), 7.54 (d, *J* = 7.5 Hz, 2H), 7.51-7.46 (m, 1H), 7.21 (dd, *J* = 5.4, 2.9 Hz, 2H).. ^{13}C NMR (DMSO, 75 MHz): δ 151.16, 130.11, 129.80, 128.91, 126.38, 122.29. HRMS(EI-TOF) calcd. for $C_{13}H_{11}N_2$ $(M+H)^+$ 195.0917, found 195.0928.

2-(4-Methoxyphenyl)-2-imidazoline (3b)[484]

According to the general procedure, a 40 mL vial with a magnetic stir bar was charged with 1,2-diaminoethane (106 μL, 1.5 mmol), 4-methoxybenzaldehyde (60.8 μL, 0.5 mmol) and

thiophenol (51.4 μL, 0.5 mmol), MOS-BT (3.4 mg) and DMSO (3 mL). After the reaction was completed, the mixture was performed as the workup protocol and purified by chromatography on silica with petroleum ether/ethyl acetate (10/3) as the elution to afford the pure product as white powder. R_f (petroleum ether/ethyl acetate 10/3): 0.39. ^{1}H NMR (DMSO, 300 MHz): δ =7.70–7.75 (2H, m), 6.92–6.97 (2H, m), 6.32 (s, 1H), 3.82 (3H, s),3.71 (4H, s). ^{13}C NMR (DMSO, 75 MHz): δ =159.66, 145.19, 126.72, 122.06, 114.19, 55.20. HRMS(EI-TOF) calcd. for $C_{10}H_{12}N_2O$ $(M+H)^+$ 177.2151, found 177.2155.

2-(4-Nitrophenyl)-2-imidazoline (3c)[485]

According to the general procedure, a 40 mL vial with a magnetic stir bar was charged with 1,2-diaminoethane (106 μL, 1.5 mmol), 4-nitrobenzaldehyde (75.6 mg, 0.5 mmol) and thiophenol (51.4 μL, 0.5 mmol), MOS-BT (3.4 mg) and DMSO (3 mL). After the reaction was completed, the mixture was performed as the workup protocol and purified by chromatography on silica with petroleum ether /ethyl acetate (5/1) as the elution to afford the pure product as brown powder. R_f (petroleum ether/ethyl acetate 5/1): 0.55. ^{1}H NMR (DMSO, 300 MHz): 8.30 (d, *J* = 8.5 Hz, 2H), 8.07 (d, *J* = 8.5 Hz, 2H), 7.19 (s, 1H), 3.66 (s, 4H). ^{13}C NMR (DMSO, 75 MHz):162.23, 148.42, 136.41, 128.40, 123.53, 49.85. HRMS(EI-TOF) calcd. for $C_9H_9N_3O$ $(M+H)^+$ 192.1867, found 192.1871.

2-(4-Cyanophenyl)-2-imidazoline (3d)[486]

According to the general procedure, a 40 mL vial with a magnetic stir bar was charged with 1,2-diaminoethane (106 μL, 1.5 mmol), 4-cyanobenzaldehyde (65.6 mg, 0.5 mmol) and thiophenol (51.4 μL, 0.5 mmol), MOS-BT (3.4 mg) and DMSO (3 mL). After the reaction was completed, the mixture was performed as the workup protocol and purified by chromatography on silica with petroleum ether /ethyl acetate (4/1) as the elution to afford the pure product as

white powder. R_f (petroleum ether/ethyl acetate 4/1): 0.48. ^{1}H NMR (DMSO, 300 MHz): 7.99-7.97 (d, *J* = 9.0 Hz, 2 H), 7.93-7.90 (d, *J* = 7.8 Hz, 2 H), 7.13 (s, 1H), 3.64 (s, 4H). ^{13}C NMR (DMSO, 75 MHz): δ =162.31, 134.69, 132.25, 127.76, 118.50, 112.53. HRMS(EI-TOF) calcd. for $C_{10}H_9N_3$ $(M+H)^+$ 172.0875, found 172.0883.

2-(4-Bromphenyl)-2-imidazoline (3e)[487]

According to the general procedure, a 40 mL vial with a magnetic stir bar was charged with 1,2-diaminoethane (106 μL, 1.5 mmol), 4-bromobenzaldehyde (92.5 mg, 0.5 mmol) and thiophenol (51.4 μL, 0.5 mmol), MOS-BT (3.4 mg) and DMSO (3 mL). After the reaction was completed, the mixture was performed as the workup protocol and purified by chromatography on silica with dichloromethane /methanol (16/1) as the elution to afford the pure product as white powder. R_f (dichloromethane /methanol 16/1): 0.37. ^{1}H NMR (300 MHz, DMSO-d_6) δ 7.83 – 7.73 (m, 2H), 7.63 (d, *J* = 8.2 Hz, 2H), 7.10 (s, 1H), 3.60 (s, 4H).^{13}C NMR (75 MHz, DMSO) δ 162.68, 131.18, 129.65, 129.06, 123.71, 49.56.

. HRMS(EI-TOF) calcd. for $C_9H_9N_2Br$ $(M+H)^+$ 225.0021, found 225.0027.

2-(3-Bromphenyl)-2-imidazoline (3f)[488]

According to the general procedure, a 40 mL vial with a magnetic stir bar was charged with 1,2-diaminoethane (106 μL, 1.5 mmol), 3-bromobenzaldehyde (58.3 μL, 0.5 mmol) and thiophenol (51.4 μL, 0.5 mmol), MOS-BT (3.4 mg) and DMSO (3 mL). After the reaction was completed, the mixture was performed as the workup protocol and purified by chromatography on silica with dichloromethane /methanol (10/1) as the elution to afford the pure product as white powder. R_f (dichloromethane /methanol 10/1): 0.51. ^{1}H NMR (DMSO, 300 MHz): δ 7.99 (s, 1H), 7.83-7.81 (d, *J* = 2.2 Hz, 1H), 7.68-7.65 (d, *J* = 7.8 Hz, 1H), 7.42-7.37 (t, *J* = 7.9, 1.8 Hz, 1H), 7.06 (s, *J* = 7.8 Hz, 1H), 3.61 (s, 4H). ^{13}C NMR (DMSO, 75 MHz): δ 162.22, 132.86,

132.78, 130.42, 129.61, 126.03, 121.44, 49.99. HRMS(EI-TOF) calcd. for $C_9H_9N_2Br$ $(M+H)^+$ 225.0021, found 225.0025.

2-(2-Bromphenyl)-2-imidazoline (3g)[489]

According to the general procedure, a 40 mL vial with a magnetic stir bar was charged with 1,2-diaminoethane (106 μL, 1.5 mmol), 2-bromobenzaldehyde (58.2 μL, 0.5 mmol) and thiophenol (51.4 μL, 0.5 mmol), MOS-BT (3.4 mg) and DMSO (3 mL). After the reaction was completed, the mixture was performed as the workup protocol and purified by chromatography on silica with dichloromethane /methanol (15/1) as the elution to afford the pure product as white powder. R_f (dichloromethane /methanol 15/1): 0.42. ^{1}H NMR (DMSO, 300 MHz): δ 7.65 (dd, *J* = 7.2, 1.9 Hz, 1H), 7.48 (dd, *J* = 7.8, 1.4Hz, 1H), 7.39 (td, *J* = 7.8, 1.4 Hz, 1H), 7.32 (td, *J* = 7.7,1.8 Hz, 1H), 6.78 (s, 1H), 3.59 (s, 4H). ^{13}C NMR (75 MHz, DMSO) δ 163.74, 133.98, 132.91, 130.89, 130.48, 127.36, 120.72, 49.90. HRMS(EI-TOF) calcd. for $C_9H_9N_2Br$ $(M+H)^+$ 225.0021, found 225.0029.

2-Phenyl-1,4,5,6-tetrahydropyrimidine (3h)[490]

According to the general procedure, a 40 mL vial with a magnetic stir bar was charged with 1,3-diaminopropane (125 μL, 1.5 mmol), benzaldehyde (50.8 μL, 0.5 mmol) and thiophenol (51.4 μL, 0.5 mmol), MOS-BT (3.4 mg) and DMSO (3 mL). After the reaction was completed, the mixture was performed as the workup protocol and purified by chromatography on base alumina with dichloromethane/petroleum ether/methanol (6/3/1) as the elution to afford the pure product as beige powder. R_f (dichloromethane/petroleum ether/methanol 6/3/1): 0.42. ^{1}H NMR (300 MHz, DMSO-d_6) δ 7.77 – 7.68 (m, 2H), 7.48 (tt, *J* = 8.8, 4.6 Hz, 3H), 3.40 (t, *J* = 5.8 Hz, 4H), 1.80 (p, *J* = 5.8 Hz, 2H). ^{13}C NMR (75 MHz, DMSO) δ 155.59, 133.34, 130.80, 128.27, 126.61, 40.32, 19.34. HRMS(EI-TOF) calcd. for $C_{10}H_{12}N_2$ $(M+H)^+$ 160.2157, found

160.2161.

2-Phenyl-2-oxazoline (3i)[491]

According to the general procedure, a 40 mL vial with a magnetic stir bar was charged with ethanolamine (90.6 μL, 1.5 mmol), benzaldehyde (50.8 μL, 0.5 mmol) and thiophenol (51.4 μL, 0.5 mmol), MOS-BT (3.4 mg) and DMSO (3 mL). After the reaction was completed, the mixture was performed as the workup protocol and purified by chromatography on silica with ethyl acetate as the elution to afford the pure product as white powder. R_f (ethyl acetate): 0.50. ^{1}H NMR (300 MHz, Chloroform-*d*) δ 7.91 (d, *J* = 7.0 Hz, 2H), 7.44 (t, *J* = 6.9 Hz, 1H), 7.37 (t, *J* = 6.9 Hz, 1H), 4.35 (t, *J* = 9.5 Hz, 2H), 3.99 (t, *J* = 9.5 Hz, 2H). ^{13}C NMR ($CDCl_3$, 75 MHz): δ 164.89, 130.69, 128.38, 128.25, 67.73, 67.36, 54.65. HRMS(EI-TOF) calcd. for C_9H_9NO $(M+H)^+$ 148.1818, found 148.1821.

2-(4-Methoxyphenyl)-oxazoline (3j)[486]

According to the general procedure, a 40 mL vial with a magnetic stir bar was charged with ethanolamine (90.6 μL, 1.5 mmol), 4-methoxybenzaldehyde (60.8 μL, 0.5 mmol) and thiophenol (51.4 μL, 0.5 mmol), MOS-BT (3.4 mg) and DMSO (3 mL). After the reaction was completed, the mixture was performed as the workup protocol and purified by chromatography on silica with petroleum ether/ethyl acetate as the elution to afford the pure product as white powder. R_f (petroleum ether/ethyl acetate 3/7): 0.67. ^{1}H NMR (DMSO, 300 MHz): δ 7.95 (d, *J* = 7.2 Hz, 2H), 7.48-7.38 (m, 3H), 4.40 (t, *J* = 9.6 Hz, 2H), 4.04 (t, *J* = 9.6 Hz, 2H). ^{13}C NMR (DMSO, 75 MHz): δ 162.62, 161.52, 129.41, 119.87, 113.88, 67.12, 55.80, 54.27. HRMS(EI-TOF) calcd. for $C_{10}H_{12}NO_2$ $(M+H)^+$ 179.2157, found 179.2161.

5,6-Dihydro-2-phenyl-1,3-oxazine (3k)[492]

According to the general procedure, a 40 mL vial with a magnetic stir bar was charged with 3-

aminopropanol (114 μL, 1.5 mmol), benzaldehyde (50.8 μL, 0.5 mmol) and thiophenol (51.4 μL, 0.5 mmol), MOS-BT (3.4 mg) and DMSO (3 mL). After the reaction was completed, the mixture was performed as the workup protocol and purified by chromatography on silica with petroleum ether/ethyl (1/1) acetate as the elution to afford the pure product as beige powder. R_f (petroleum ether/ethyl acetate 1/1): 0.53. ^{1}H NMR (DMSO, 300 MHz): δ 7.83-7.81 (m, 2H), 7.47-7.36 (m, 3H), 4.35-4.31 (t, *J* = 5.4 Hz, 2H), 3.51-3.47 (t, *J* = 5.9 Hz, 2H), 1.92-1.84 (m, *J* = 5.7 Hz, 2H). ^{13}C NMR (DMSO, 75 MHz):δ 153.68, 133.81, 130.20, 128.02, 126.38, 64.80, 41.88, 21.46. HRMS(EI-TOF) calcd. for $C_{10}H_{11}NO$ $(M+H)^+$ 162.2004, found 162.2008.

4,5-Dihydro-2-phenyl-thiazole (3l)[493]

According to the general procedure, a 40 mL vial with a magnetic stir bar was charged with cysteamine (115 mg, 1.5 mmol), benzaldehyde (50.8 μL, 0.5 mmol) and thiophenol (51.4 μL, 0.5 mmol), MOS-BT (3.4 mg) and DMSO (3 mL). After the reaction was completed, the mixture was performed as the workup protocol and purified by chromatography on silica with dichloromethane /methanol (10/1) as the elution to afford the pure product as yellow oil. R_f (dichloromethane /methanol 10/1): 0.46. ^{1}H NMR (DMSO, 300 MHz): δ 7.85 – 7.73 (m, 1H), 7.51 (dd, *J* = 10.1, 7.1 Hz, 1H), 4.40 (t, *J* = 8.4 Hz, 1H), 3.44 (t, *J* = 8.4 Hz, 1H).

^{13}C NMR (DMSO, 75 MHz): δ 166.23, 132.75, 131.26, 128.74, 127.93, 65.00, 33.01. HRMS(EI-TOF) calcd. for C_9H_9NS $(M+H)^+$ 164.2395, found 164.2399.

4,5-Dihydro-2-(4-methoxyphenyl)-thiazole (3m)[493]

According to the general procedure, a 40 mL vial with a magnetic stir bar was charged with cysteamine (115 mg, 1.5 mmol), 4-methoxybenzaldehyde (60.8 μL, 0.5 mmol) and thiophenol (51.4 μL, 0.5 mmol), MOS-BT (3.4 mg) and DMSO (3 mL). After the reaction was completed, the mixture was performed as the workup protocol and purified by chromatography on silica

with dichloromethane /ethyl acetate (1/1) as the elution to afford the pure product as yellow oil. R_f (dichloromethane /ethyl acetate 1/1): 0.37. ^{1}H NMR (DMSO, 300 MHz): δ 7.83 – 7.61 (m, 1H), 7.08 – 6.94 (m, 1H), 4.35 (t, *J* = 8.3 Hz, 1H), 3.80 (s, 2H), 3.41 (d, *J* = 8.2 Hz, 1H). ^{13}C NMR (DMSO, 75 MHz): δ 165.40, 161.48, 129.65, 125.46, 113.97, 64.84, 55.30, 33.04. HRMS(EI-TOF) calcd. for $C_{10}H_{11}NS$ $(M+H)^+$ 178.2661, found 178.2665.

6.1.6 NMR spectra

The NMR spectra of the mesoporous organosilica monomers and catalytic products were shown as followed:

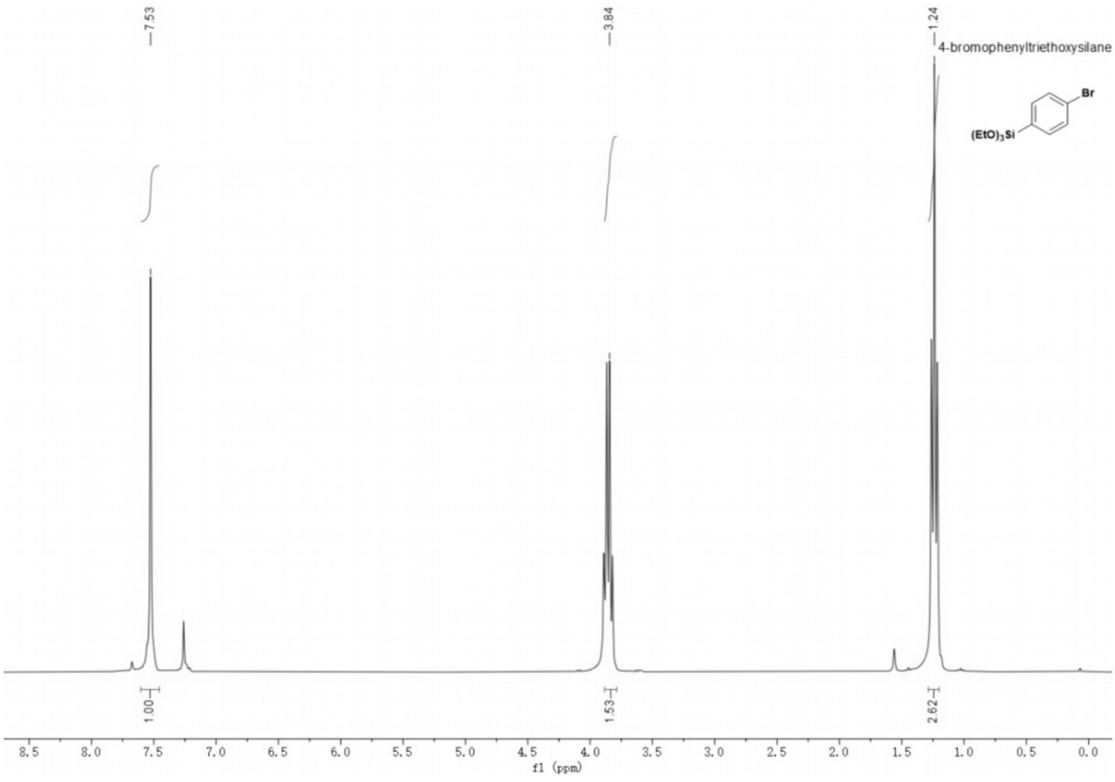

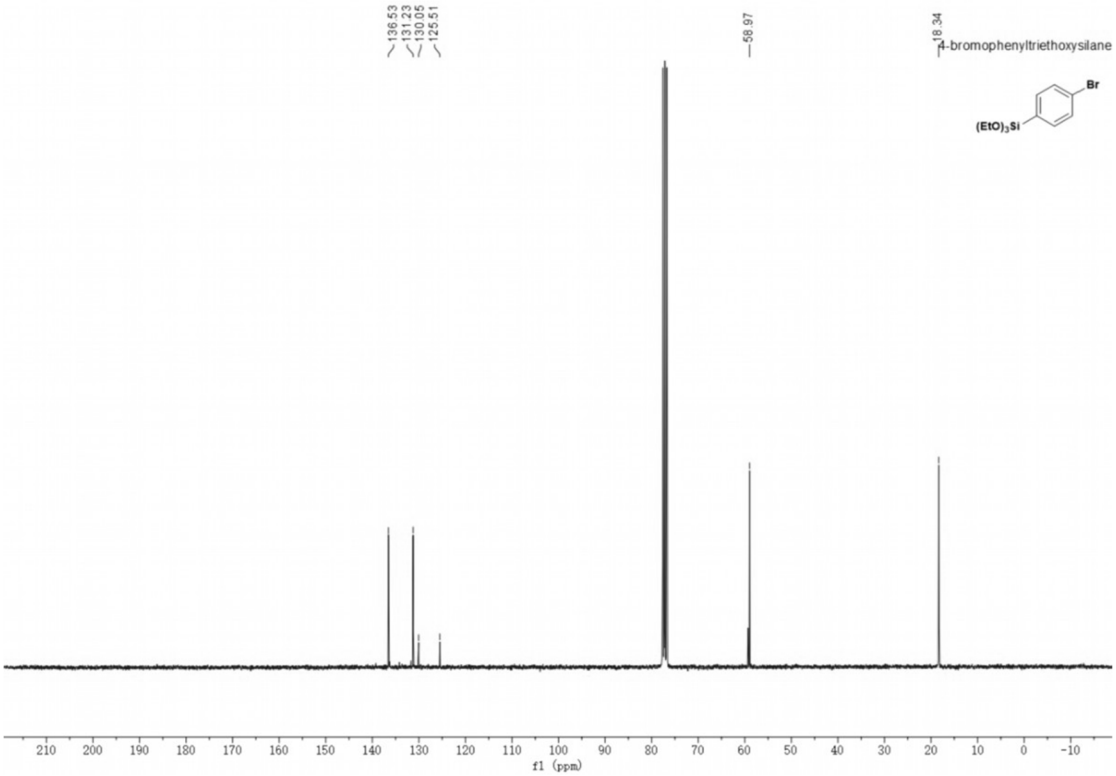
136.53
131.23
130.05
125.51
58.97
18.34
4-bromophenyltriethoxysilane
Br
(EtO)3Si
f1 (ppm)

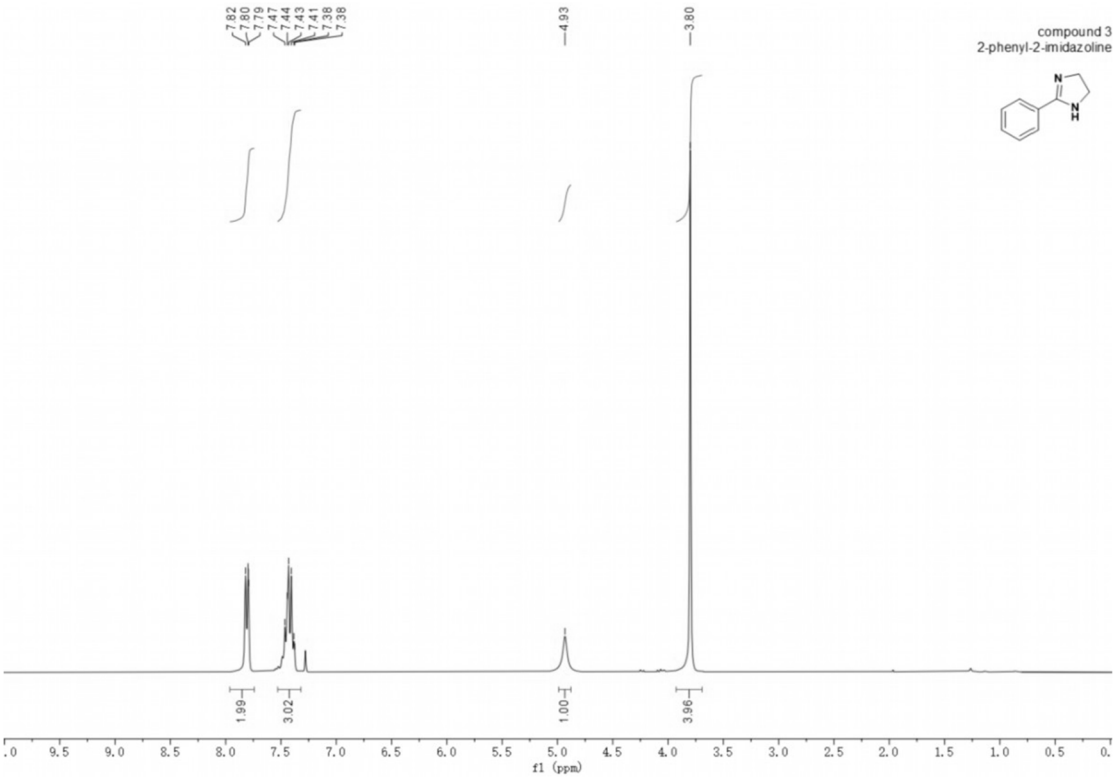
7.82
7.80
7.79
7.47
7.44
7.43
7.41
7.38
7.38
4.93
3.80
compound 3
2-phenyl-2-imidazoline
N
N
H
1.99
3.02
1.00
3.96
f1 (ppm)

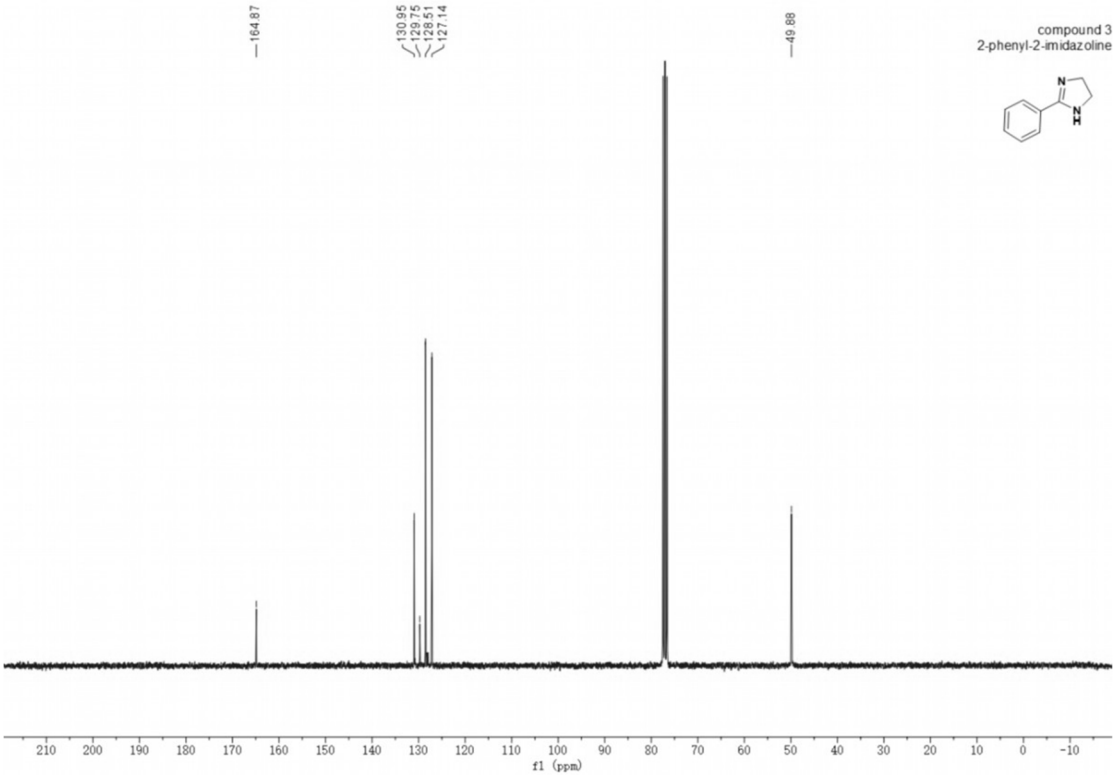
164.87
130.95
129.75
128.51
127.14
49.88
compound 3
2-phenyl-2-imidazoline
f1 (ppm)

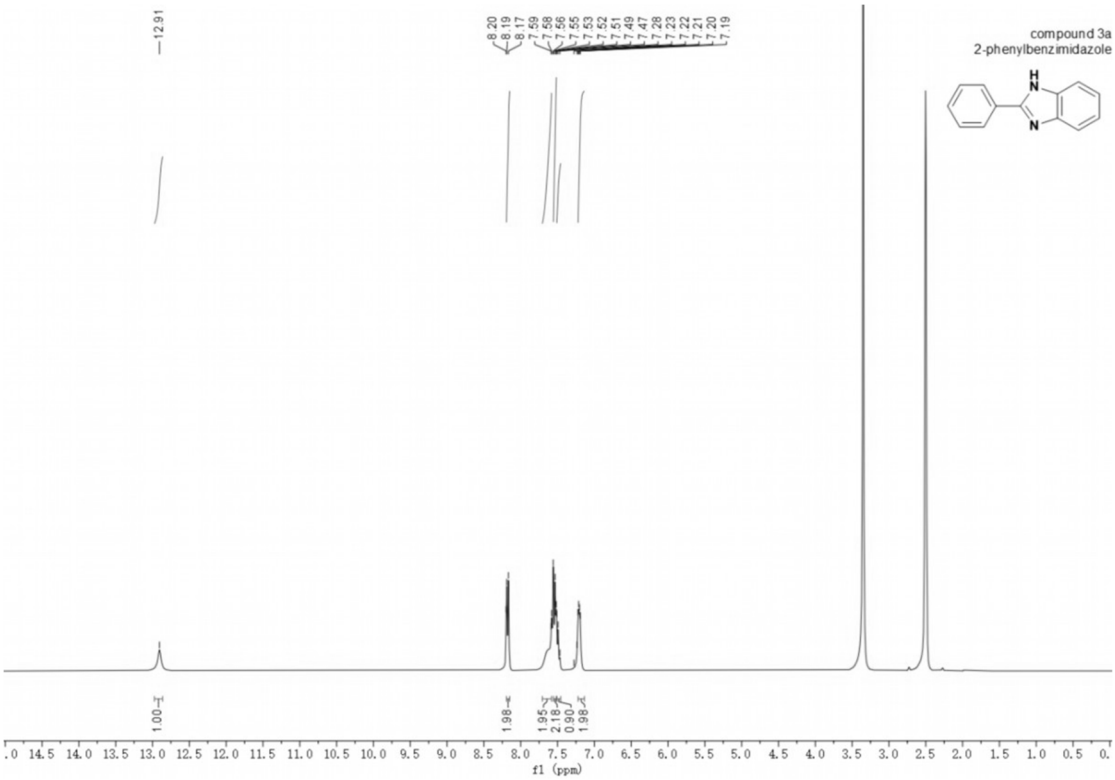
12.91
8.20
8.19
8.17
7.59
7.58
7.56
7.55
7.53
7.52
7.51
7.49
7.47
7.28
7.23
7.22
7.21
7.20
7.19
compound 3a
2-phenylbenzimidazole
1.00
1.98
1.95
2.18
0.90
1.98
f1 (ppm)

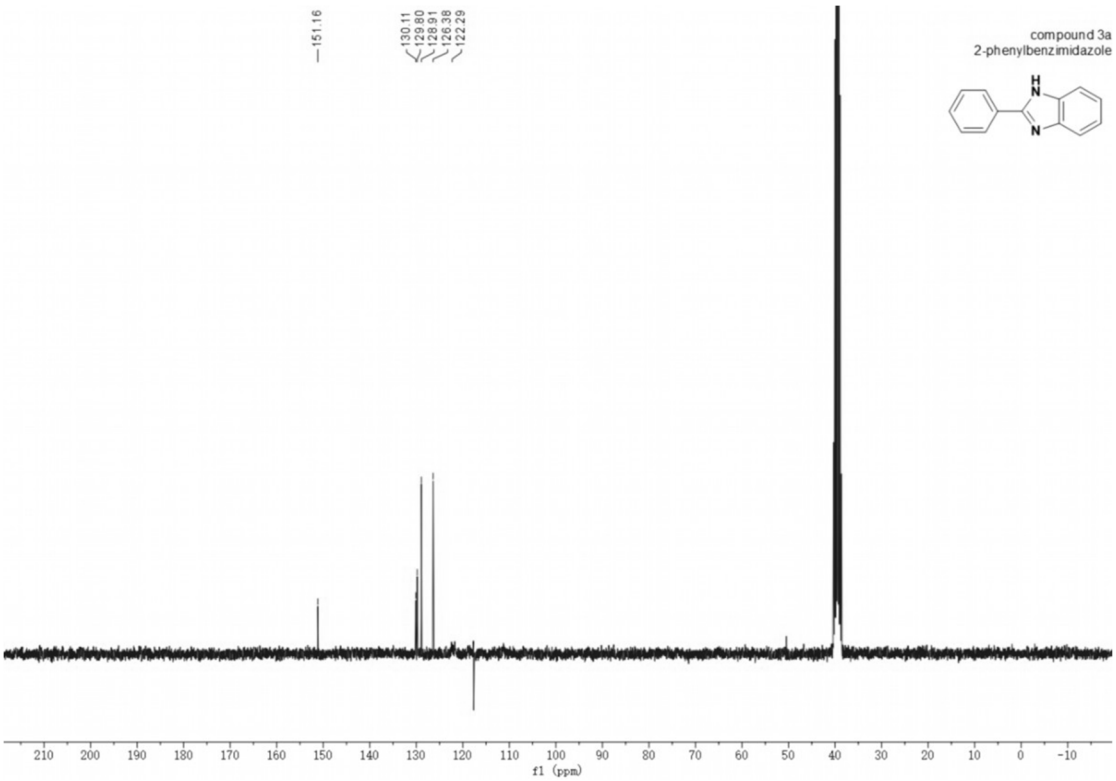
151.16
130.11
129.80
128.91
126.38
122.29
compound 3a
2-phenylbenzimidazole
f1 (ppm)

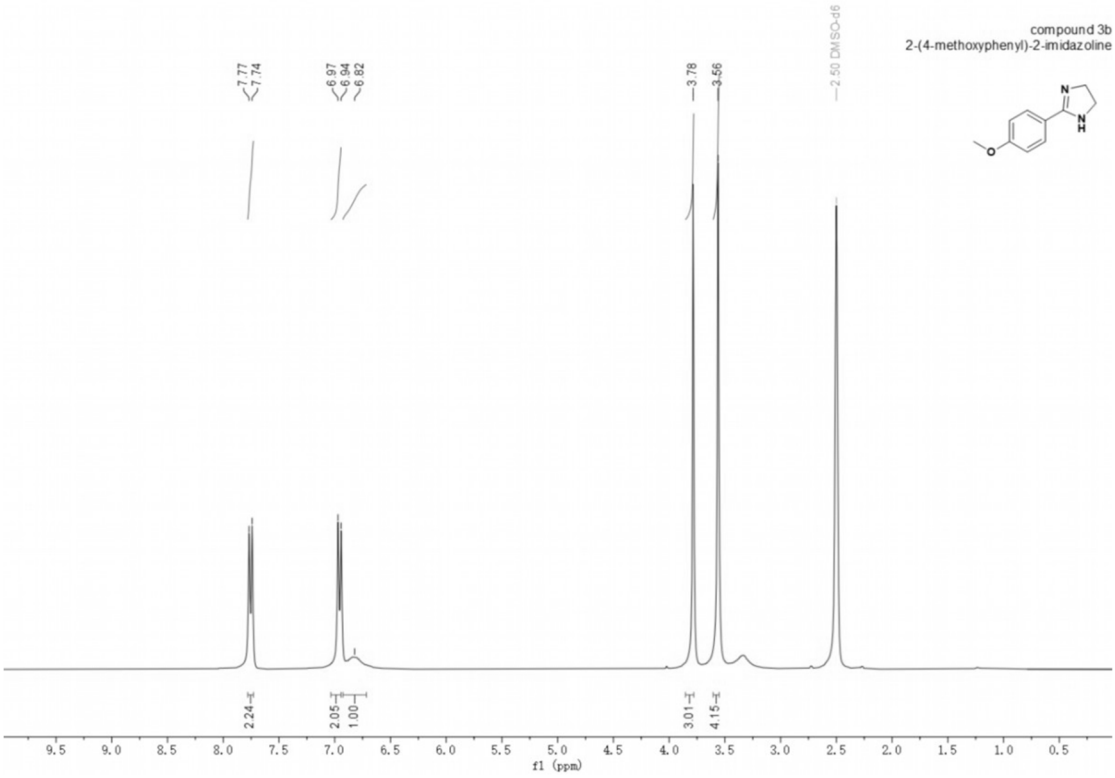
7.77
7.74
6.97
6.94
6.82
3.78
3.56
2.50 DMSO-d6
compound 3b
2-(4-methoxyphenyl)-2-imidazoline
2.24
2.05
1.00
3.01
4.15
f1 (ppm)

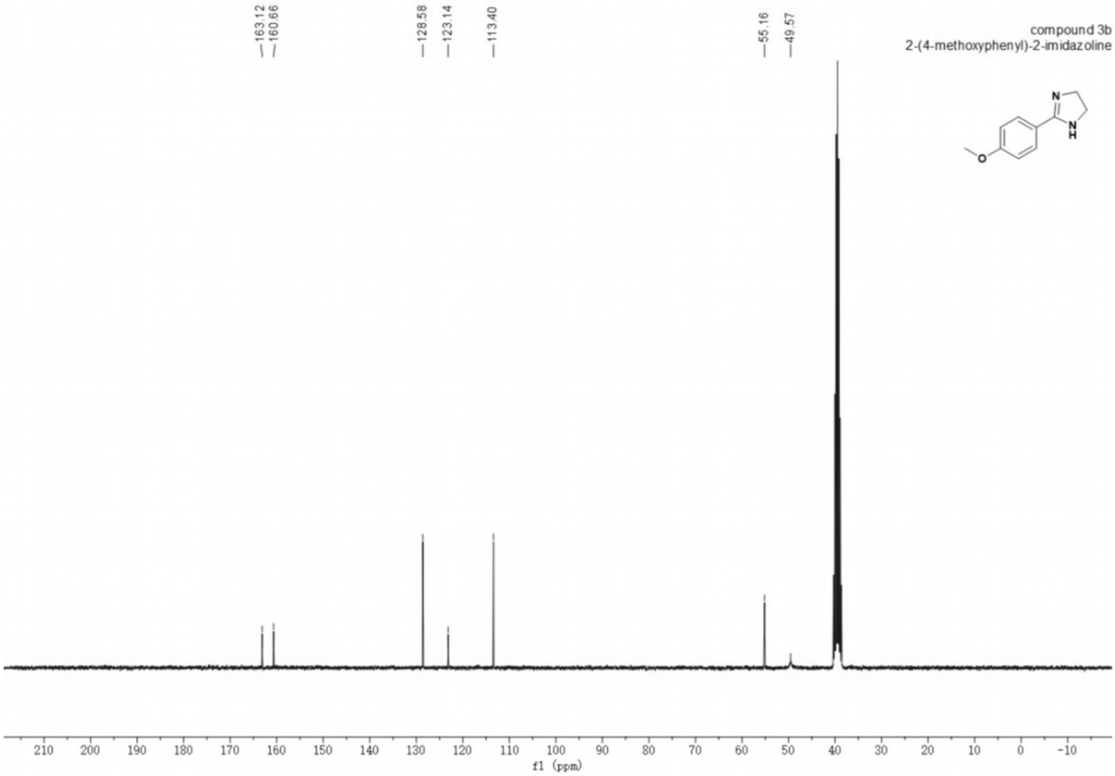
163.12
160.66
128.58
123.14
113.40
55.16
49.57
compound 3b
2-(4-methoxyphenyl)-2-imidazoline
f1 (ppm)

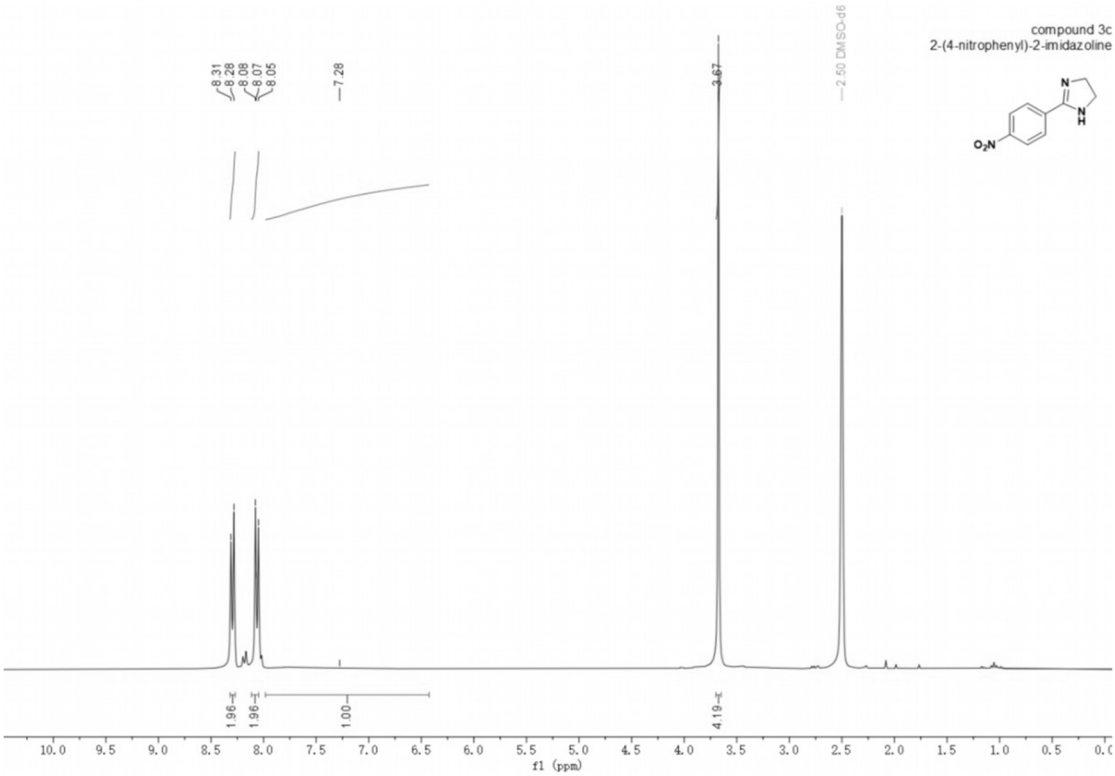
8.31
8.28
8.08
8.07
8.05
7.28
3.67
2.50 DMSO-d6
compound 3c
2-(4-nitrophenyl)-2-imidazoline
1.96
1.96
1.00
4.19
f1 (ppm)

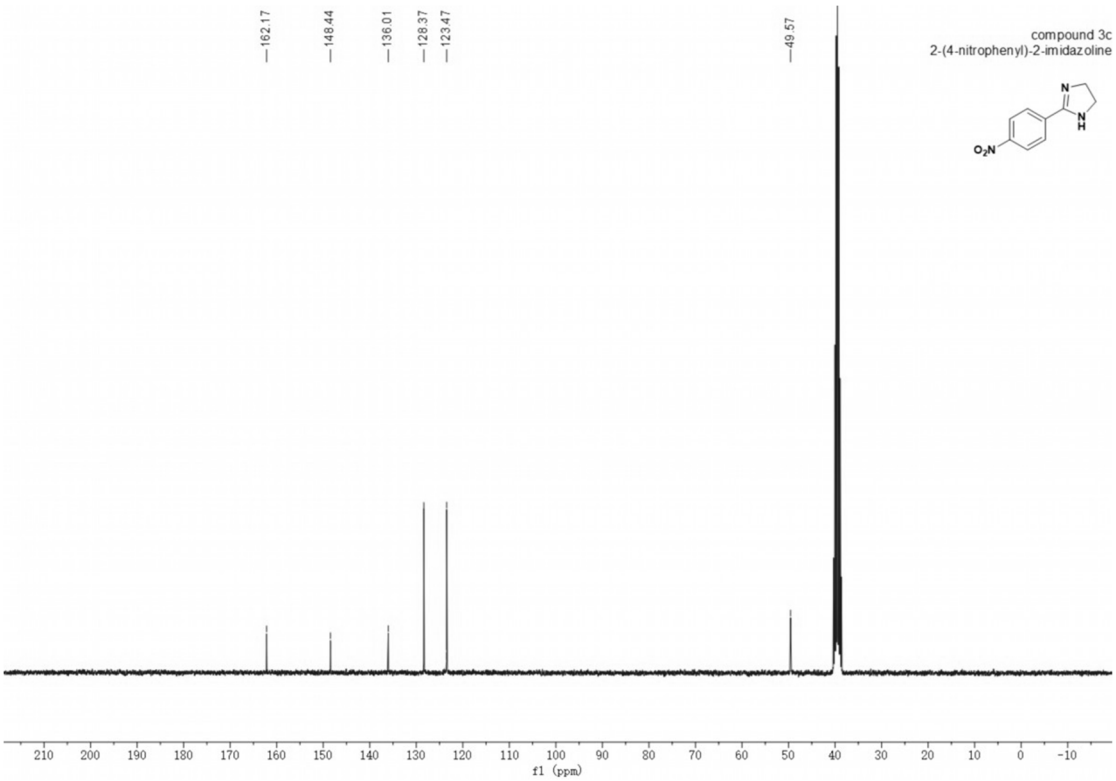
162.17
148.44
136.01
128.37
123.47
49.57
compound 3c
2-(4-nitrophenyl)-2-imidazoline
f1 (ppm)

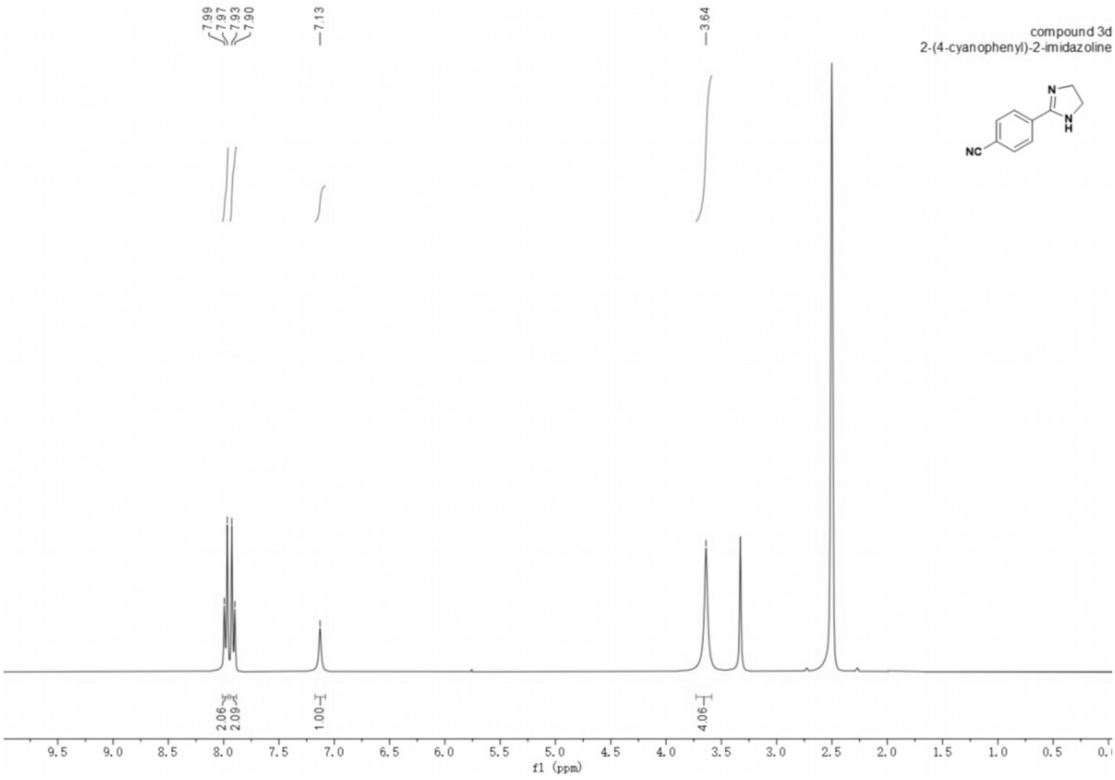
7.99
7.97
7.93
7.90
7.13
3.64
compound 3d
2-(4-cyanophenyl)-2-imidazoline
2.06
2.09
1.00
4.06
f1 (ppm)

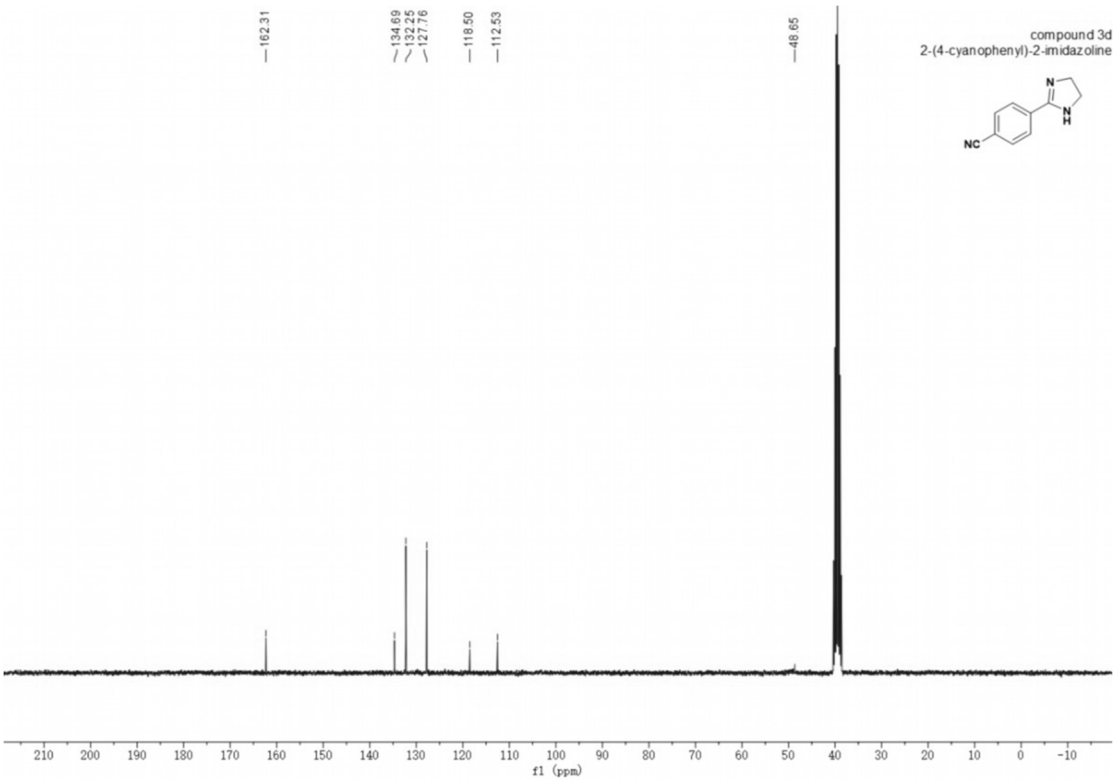
162.31
134.69
132.25
127.76
118.50
112.53
48.65
compound 3d
2-(4-cyanophenyl)-2-imidazoline
N
N
H
NC
f1 (ppm)

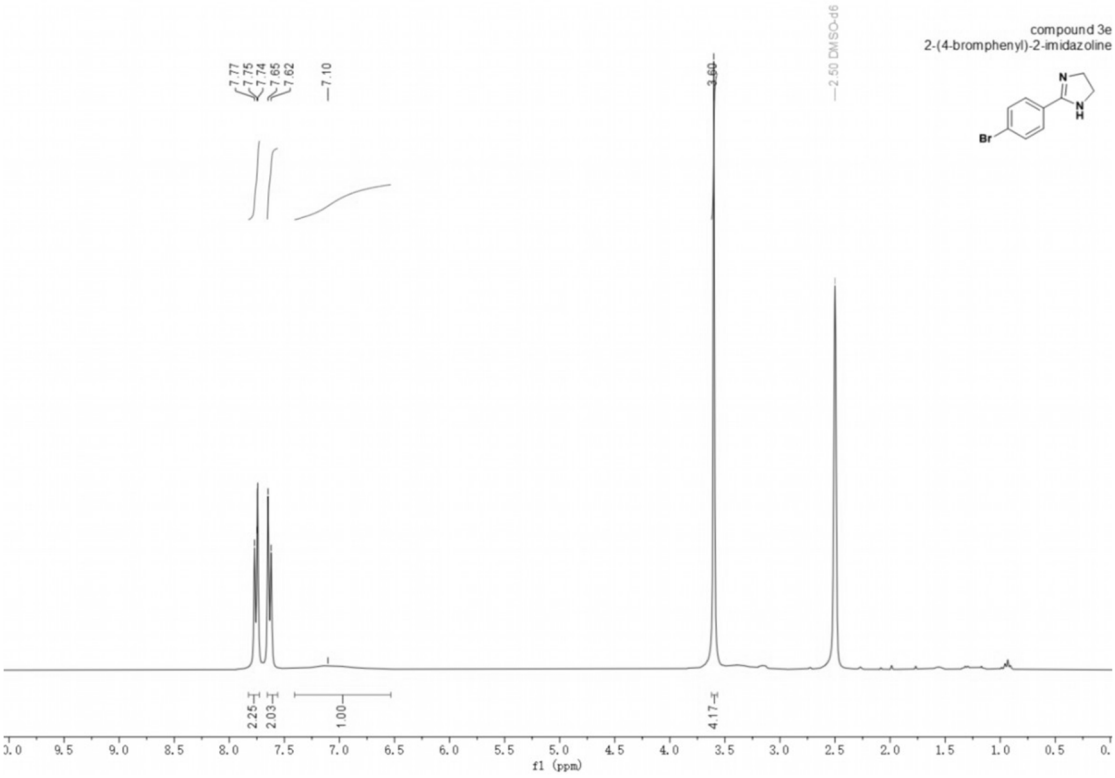
7.77
7.75
7.74
7.65
7.62
7.10
3.60
2.50 DMSO-d6
compound 3e
2-(4-bromphenyl)-2-imidazoline
N
N
H
Br
2.25
2.03
1.00
4.17
f1 (ppm)

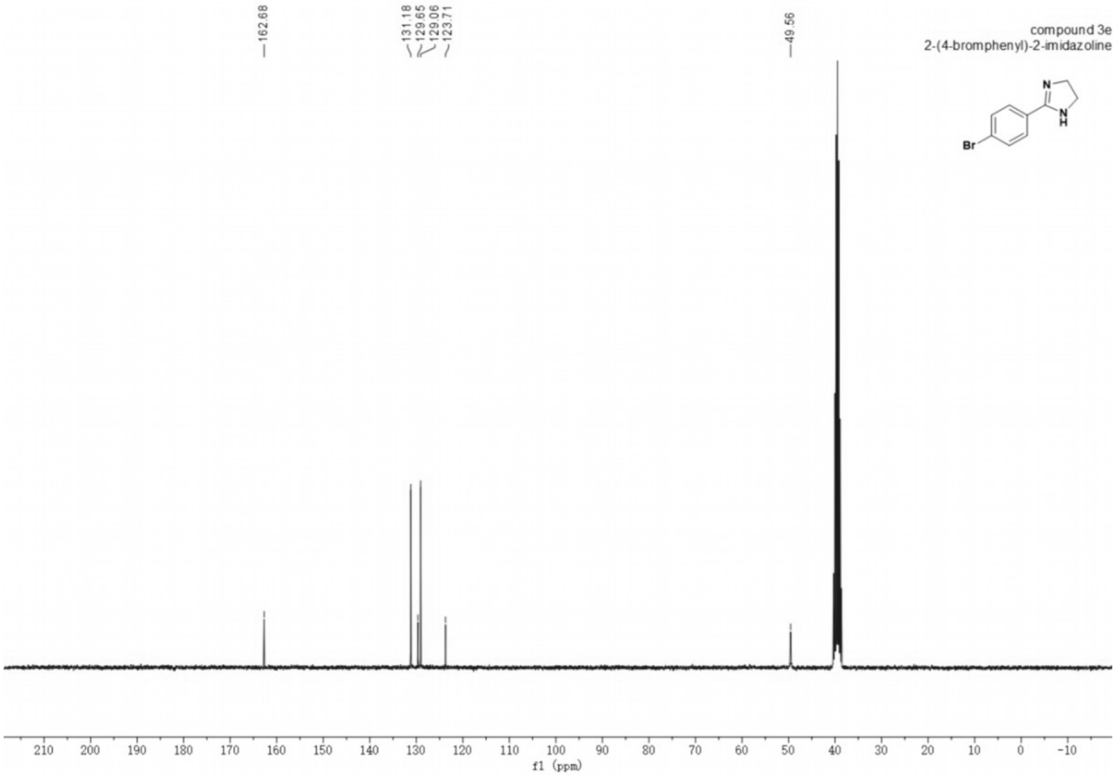
162.68
131.18
129.65
129.06
123.71
49.56
compound 3e
2-(4-bromphenyl)-2-imidazoline
Br
N
N
H
f1 (ppm)

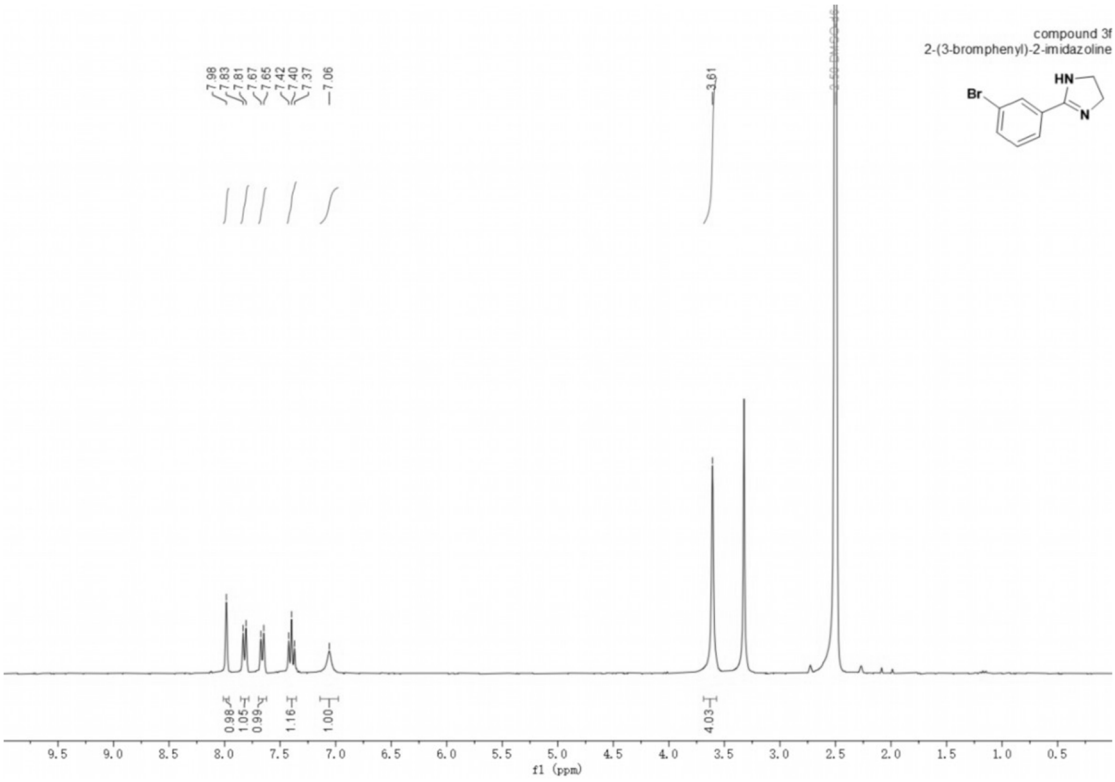
7.98
7.83
7.81
7.67
7.65
7.42
7.40
7.37
7.06
3.61
compound 3f
2-(3-bromphenyl)-2-imidazoline
Br
HN
N
0.98
1.05
0.99
1.16
1.00
4.03
f1 (ppm)

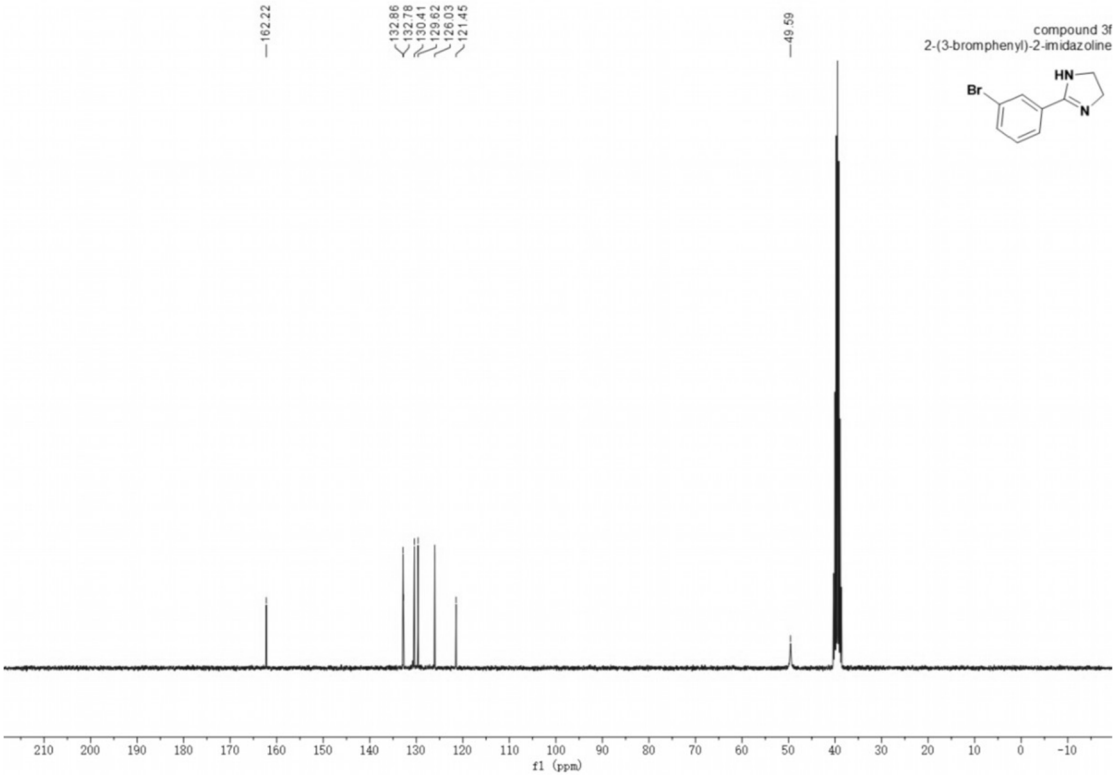
162.22
132.86
132.78
132.41
129.62
126.03
121.45
49.59
compound 3f
2-(3-bromphenyl)-2-imidazoline
Br
HN
N
f1 (ppm)

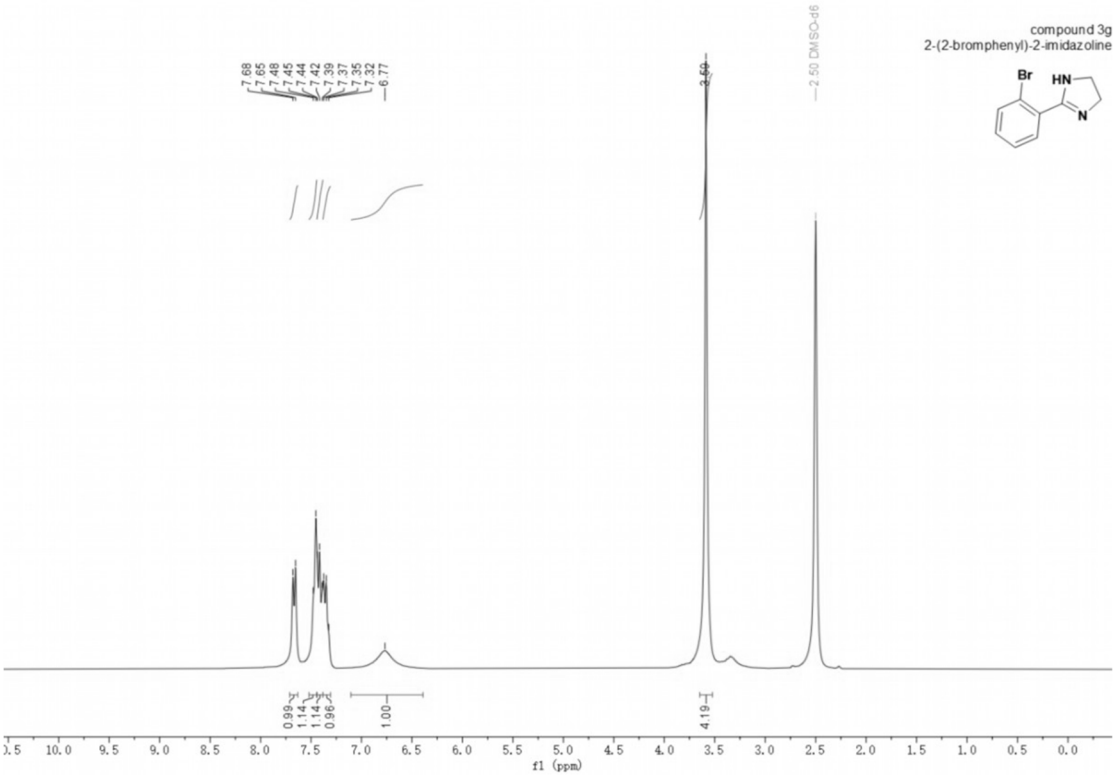
7.68
7.65
7.48
7.45
7.44
7.42
7.39
7.37
7.35
7.32
6.77
3.59
2.50 DMSO-d6
compound 3g
2-(2-bromphenyl)-2-imidazoline
Br
HN
N
0.99
1.14
1.14
0.96
1.00
4.19
f1 (ppm)

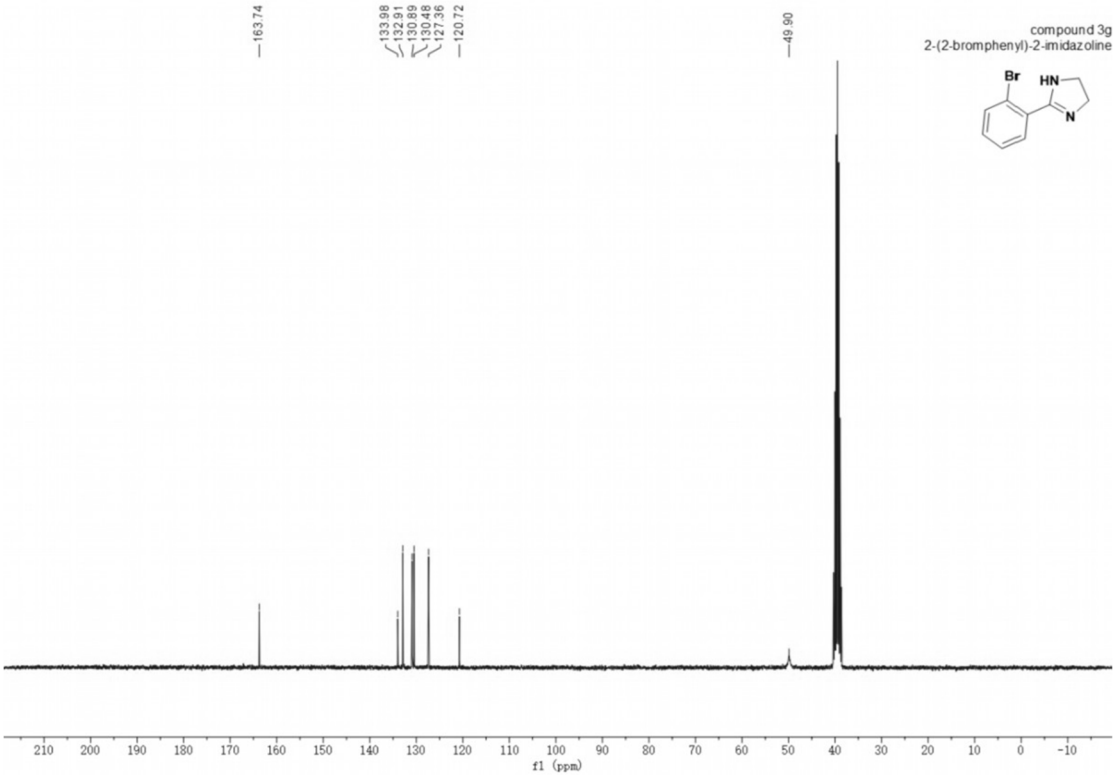
163.74
133.98
132.91
130.89
130.48
127.36
120.72
49.90
compound 3g
2-(2-bromphenyl)-2-imidazoline
Br
HN
N
f1 (ppm)

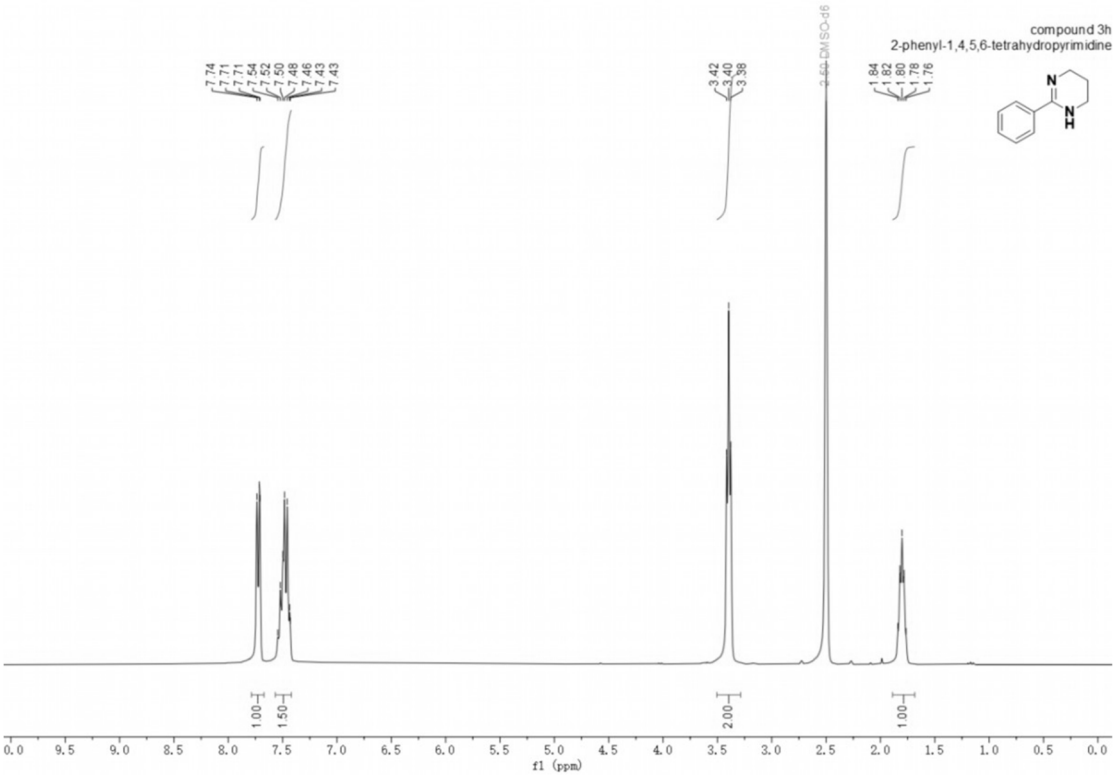
7.74
7.71
7.71
7.54
7.52
7.50
7.48
7.46
7.43
7.43
3.42
3.40
3.38
2.50 DMSO-d6
1.84
1.82
1.80
1.78
1.76
compound 3h
2-phenyl-1,4,5,6-tetrahydropyrimidine
N
N
H
1.00
1.50
2.00
1.00
f1 (ppm)

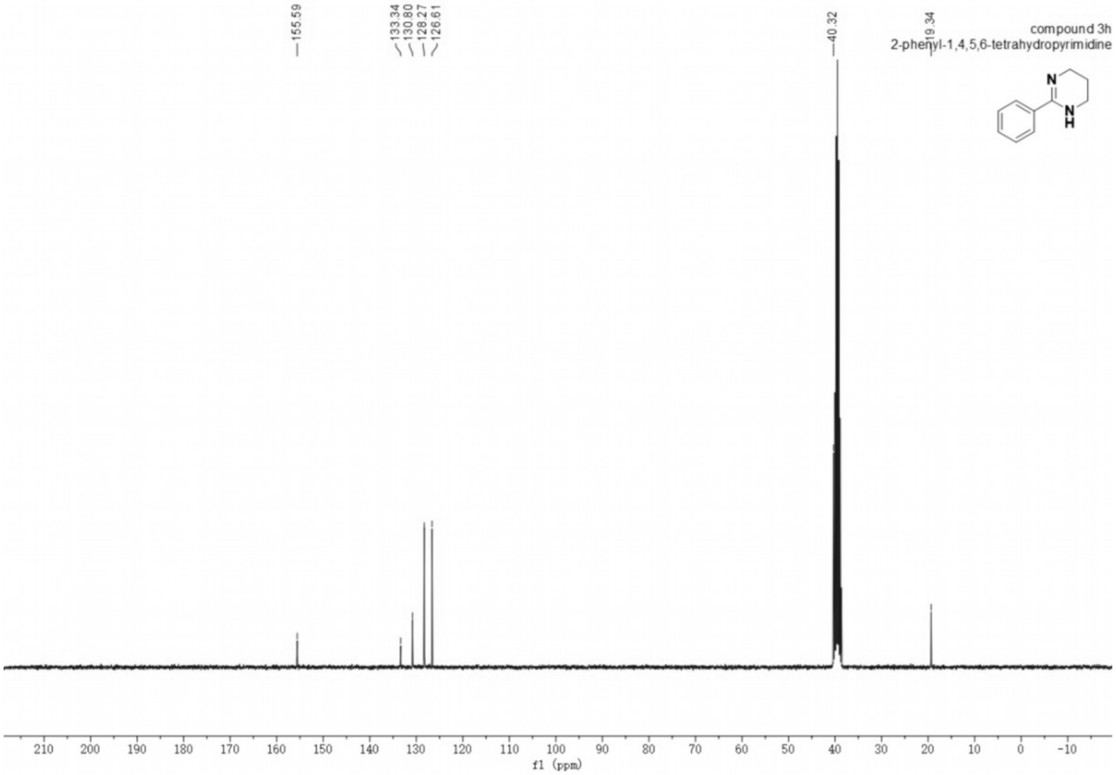
155.59
133.34
130.60
128.27
126.61
40.32
19.34
compound 3h
2-phenyl-1,4,5,6-tetrahydropyrimidine
N
N
H
f1 (ppm)

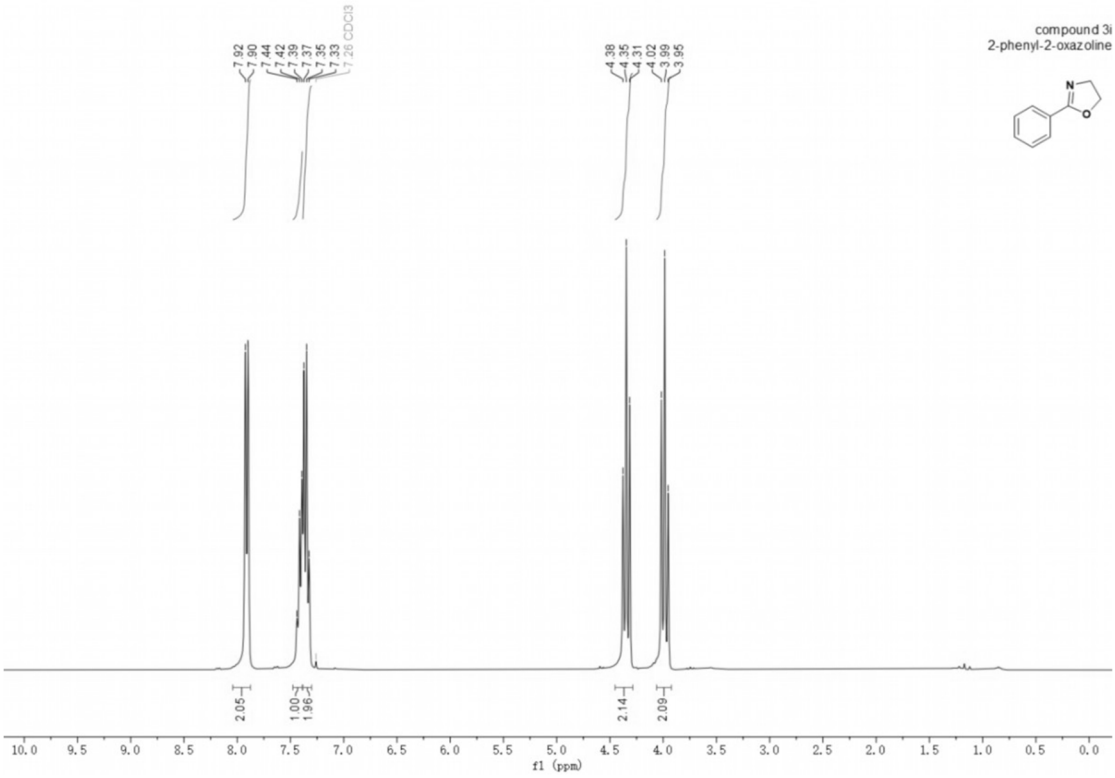
7.92
7.90
7.44
7.42
7.39
7.37
7.35
7.33
7.26 CDCl3
4.38
4.35
4.31
4.02
3.99
3.95
compound 3i
2-phenyl-2-oxazoline
N
O
2.05
1.00
1.96
2.14
2.09
f1 (ppm)

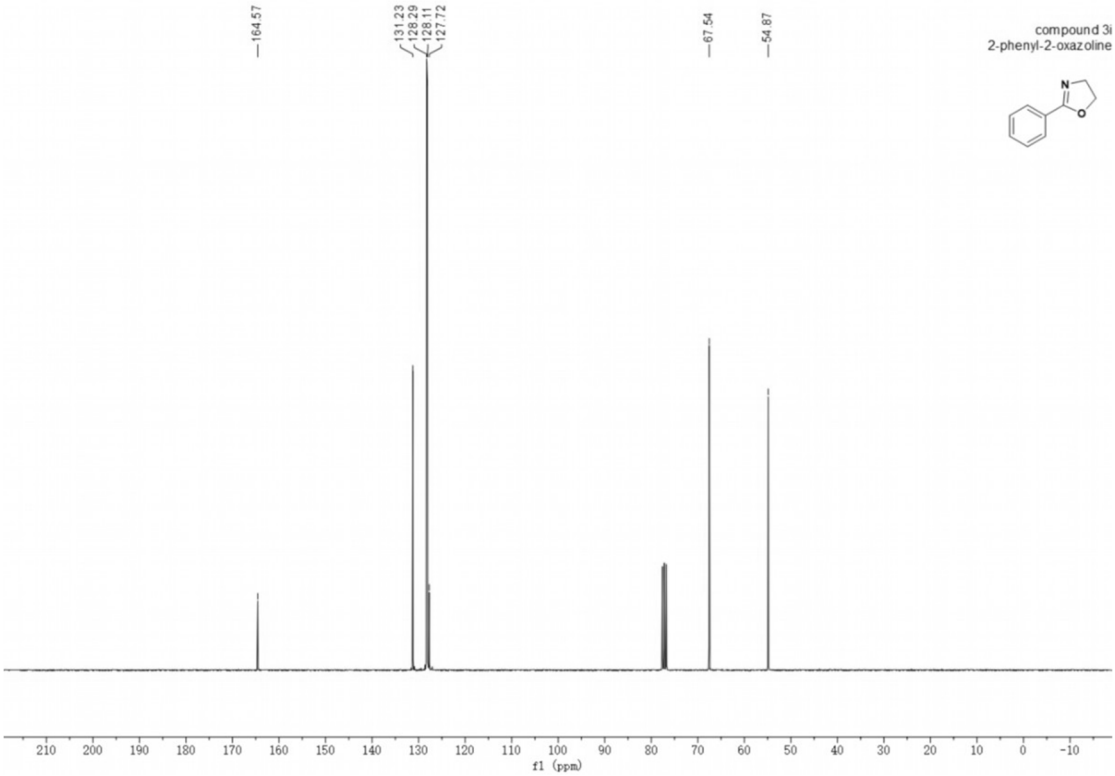
164.57
131.23
128.29
128.11
127.72
67.54
54.87
compound 3i
2-phenyl-2-oxazoline
f1 (ppm)

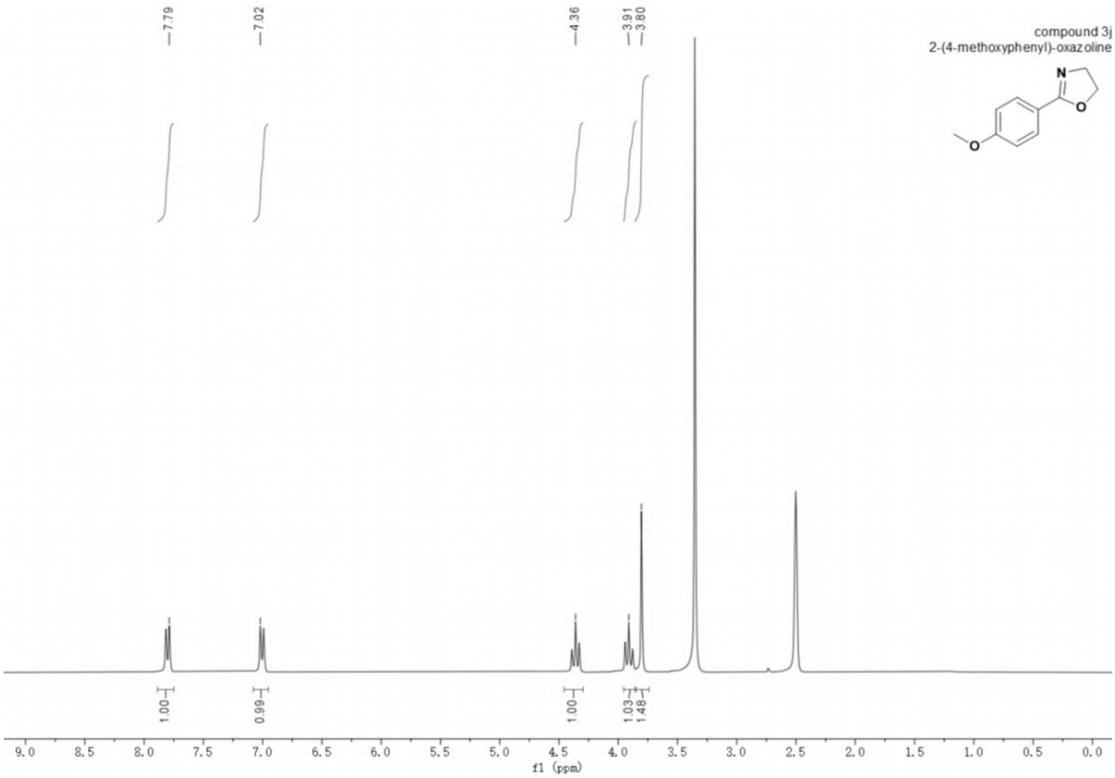
7.79
7.02
4.36
3.91
3.80
compound 3j
2-(4-methoxyphenyl)-oxazoline
1.00
0.99
1.00
1.03
1.48
f1 (ppm)

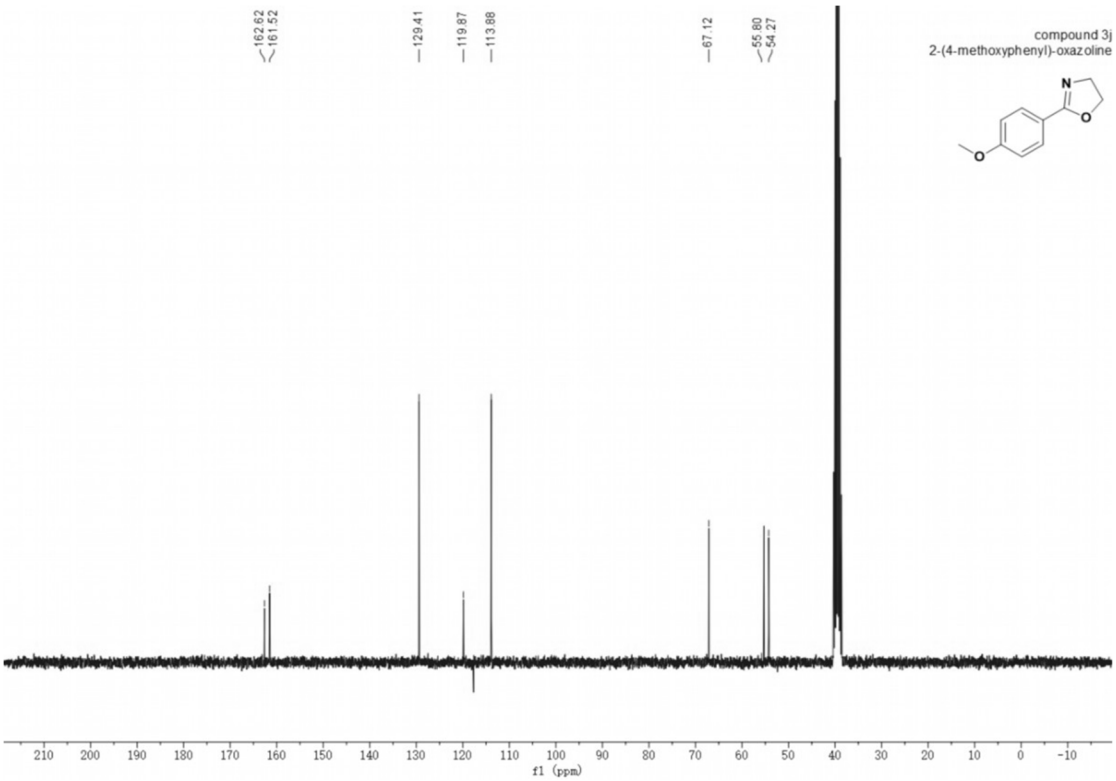
162.62
161.52
129.41
119.87
113.88
67.12
55.80
54.27
compound 3j
2-(4-methoxyphenyl)-oxazoline
f1 (ppm)

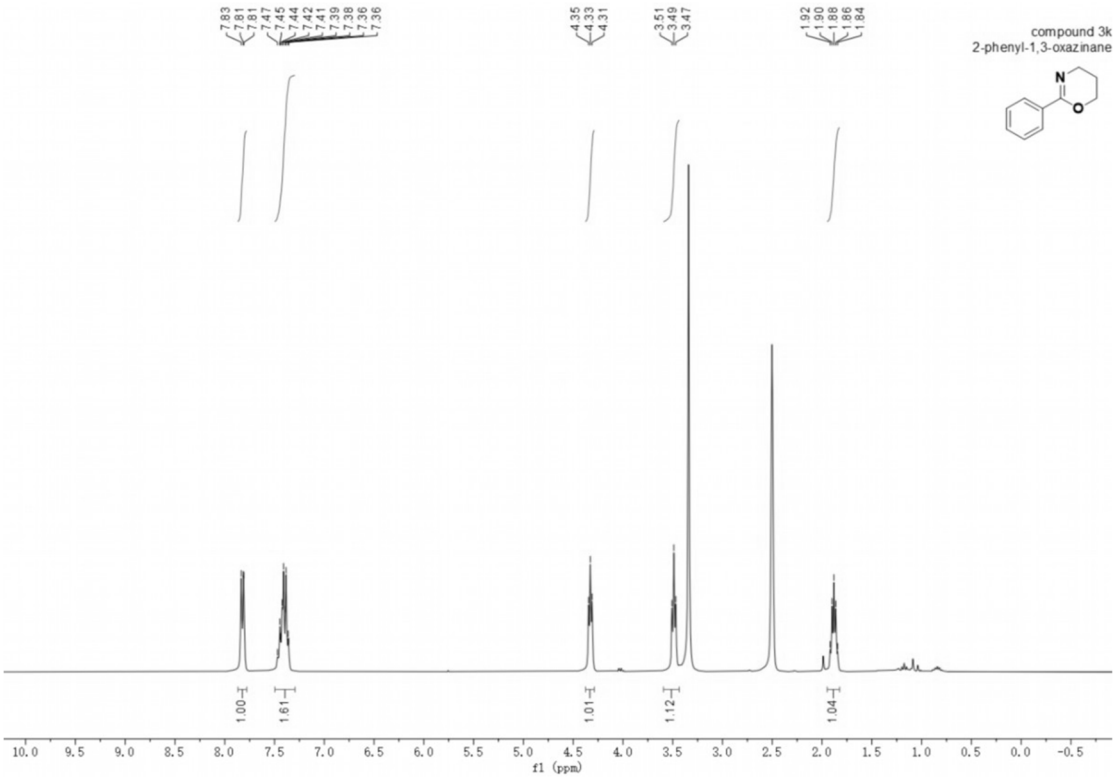
7.83
7.81
7.81
7.47
7.45
7.44
7.42
7.41
7.39
7.38
7.36
7.36
4.35
4.33
4.31
3.51
3.49
3.47
1.92
1.90
1.88
1.86
1.84
compound 3k
2-phenyl-1,3-oxazinane
1.00
1.61
1.01
1.12
1.04
f1 (ppm)

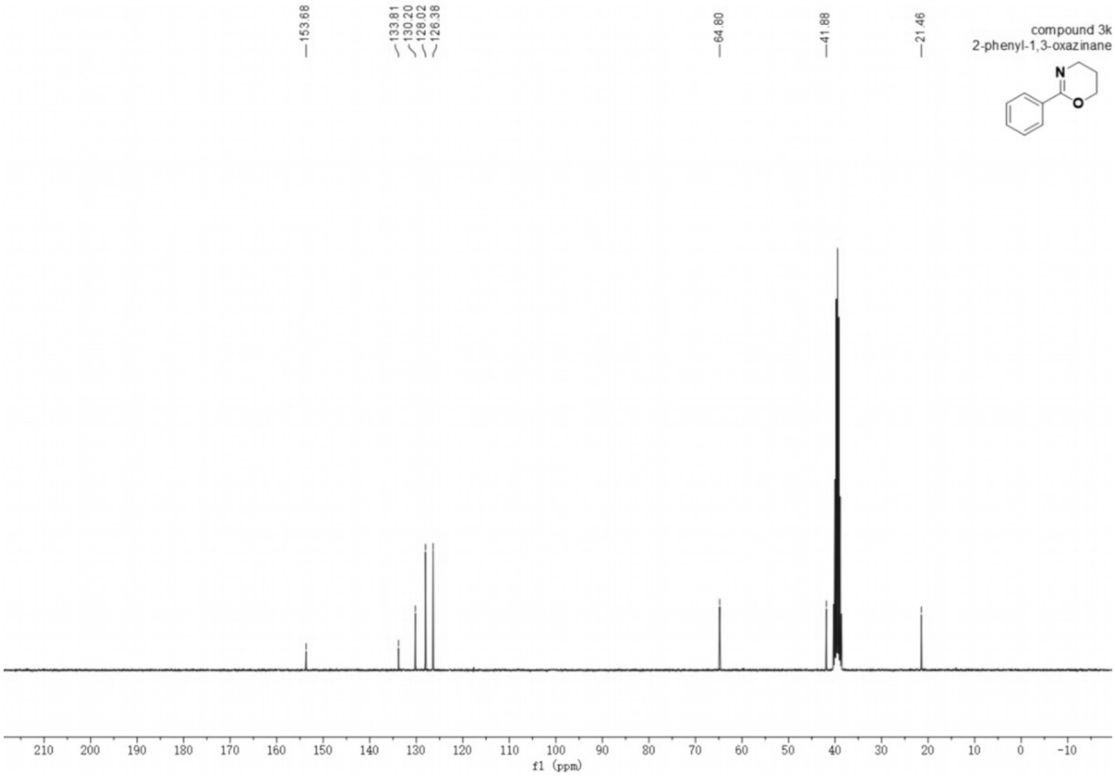
153.68
133.81
130.20
129.02
126.38
64.80
41.88
21.46
compound 3k
2-phenyl-1,3-oxazinane
N
O
f1 (ppm)

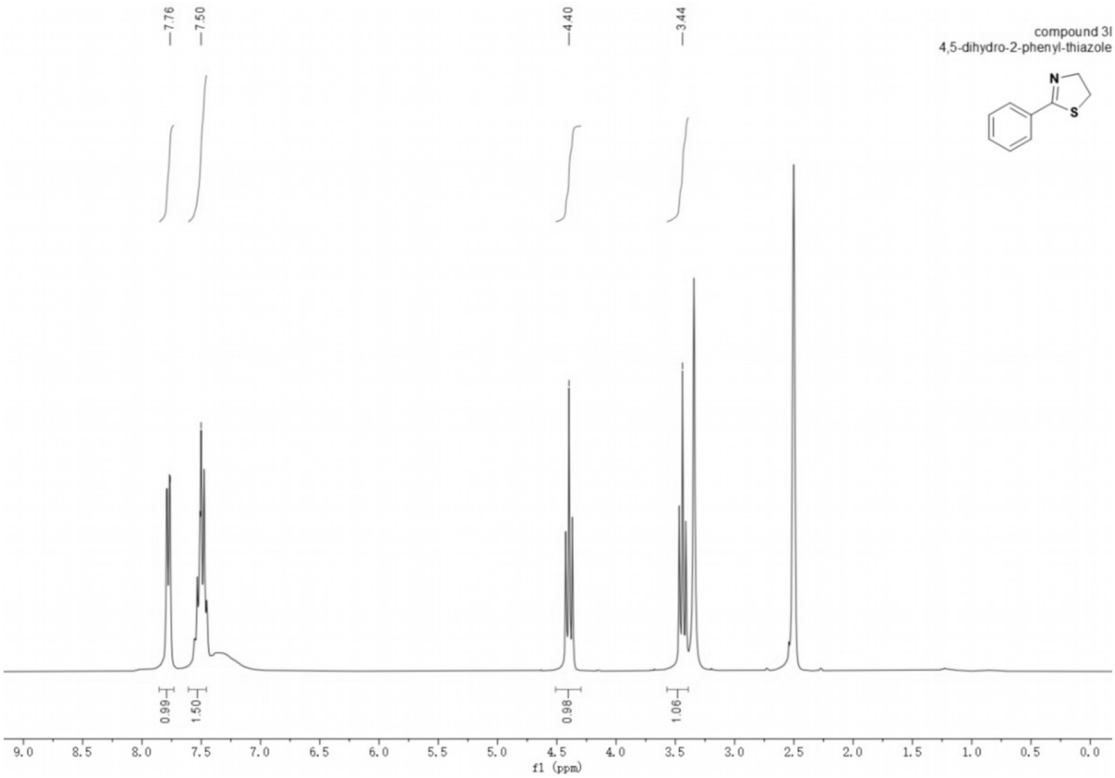
7.76
7.50
4.40
3.44
compound 3l
4,5-dihydro-2-phenyl-thiazole
N
S
0.99
1.50
0.98
1.06
f1 (ppm)

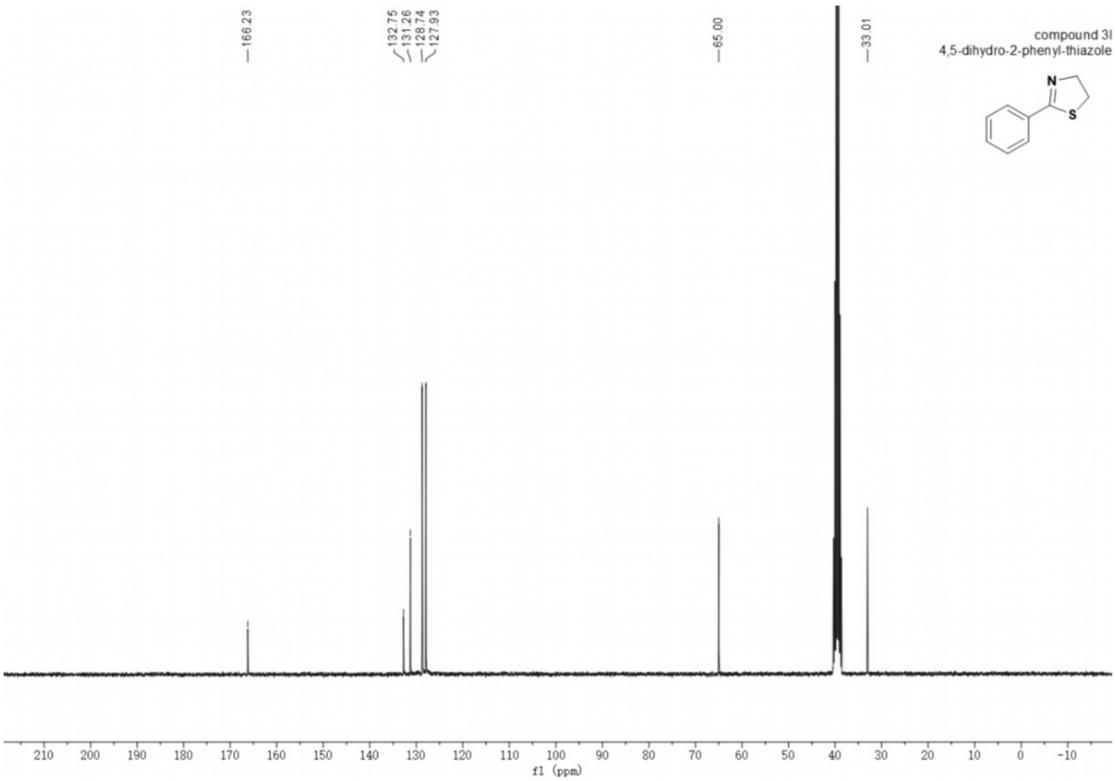
166.23
132.75
131.26
128.74
127.93
65.00
33.01
compound 3l
4,5-dihydro-2-phenyl-thiazole
N
S
f1 (ppm)

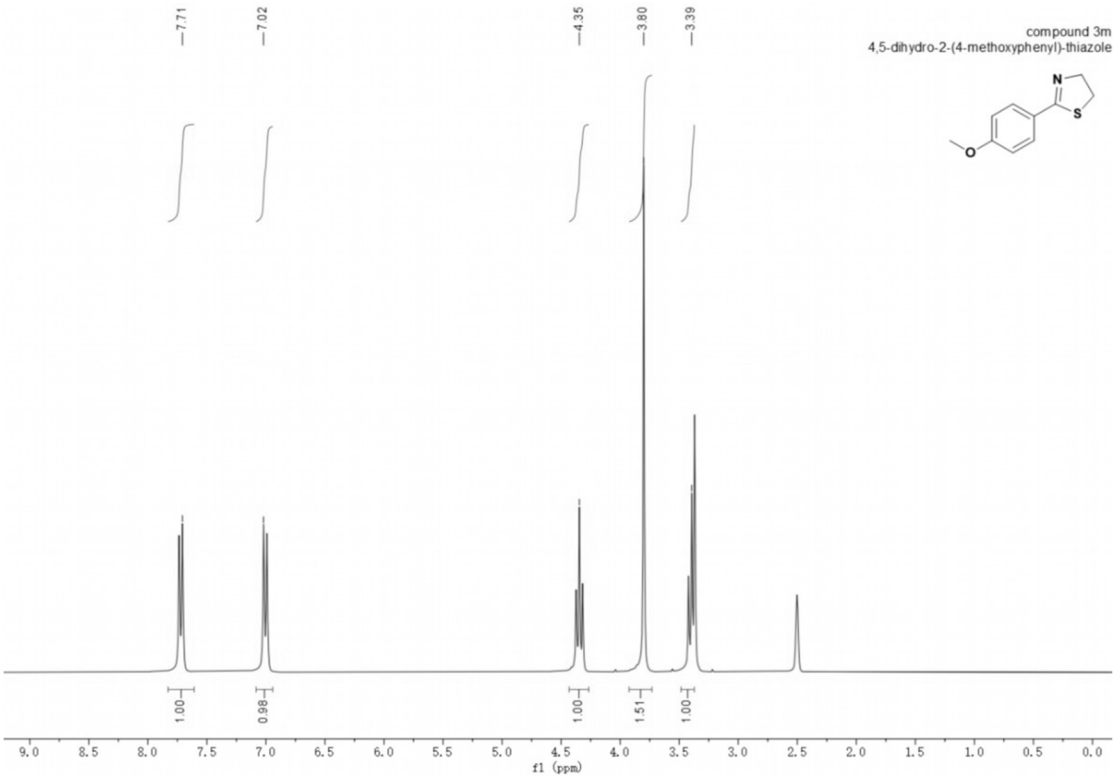
7.71
7.02
4.35
3.80
3.39
compound 3m
4,5-dihydro-2-(4-methoxyphenyl)-thiazole
N
S
O
1.00
0.98
1.00
1.51
1.00
f1 (ppm)

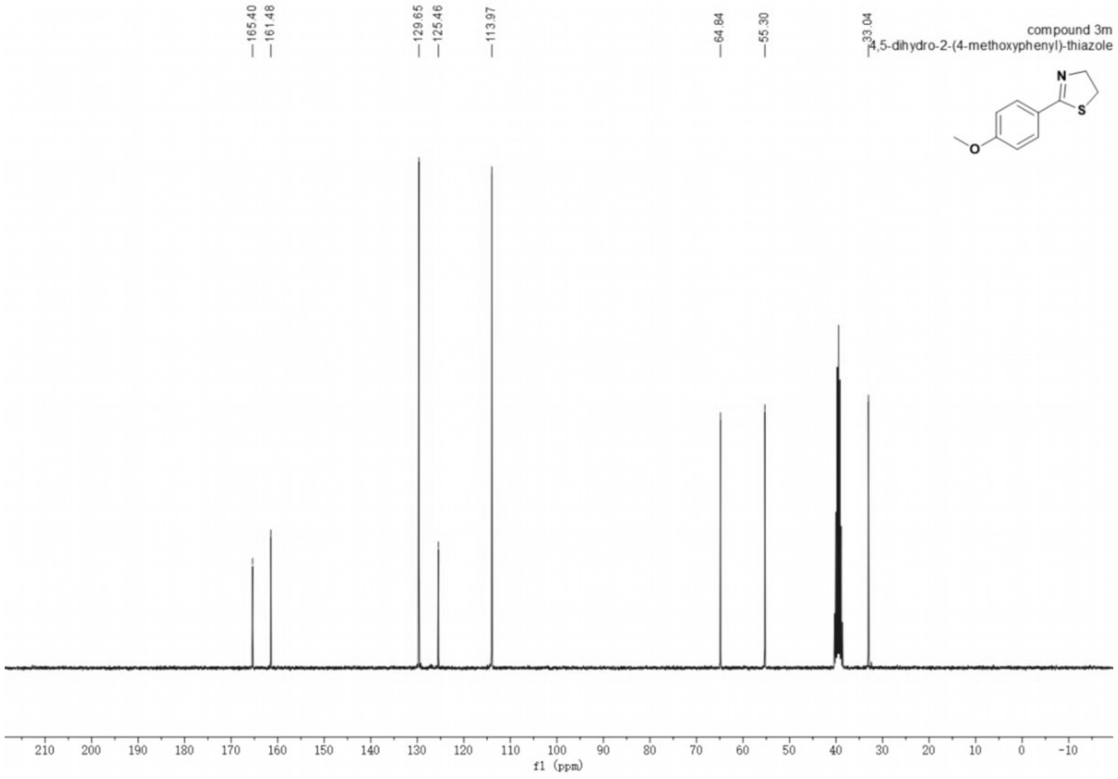
165.40
161.48
129.65
125.46
113.97
64.84
55.30
33.04
compound 3m
4,5-dihydro-2-(4-methoxyphenyl)-thiazole
N
S
O
210 200 190 180 170 160 150 140 130 120 110 100 90 80 70 60 50 40 30 20 10 0 -10
f1 (ppm)

6.2 Aerobic photobiocatalysis enabled by combining core-shell nanophotoreactors and native enzymes

6.2.1 Materials

1-Bromo-4-iodobenzene, triethoxysilane, tetraethylorthosilicate, bromobenzene, 2,1,3-benzothiadiazole-4,7-bis(boronic acid pinacol ester), allylmagnesium bromide, hexadecyltrimethylammonium chloride, hexadecyltrimethylammonium bromide bis(acetonitrile)(1,5-cyclooctadiene)rhodium(I)tetrafluorobotate, tetrakis(triphenylphosphine)palladium(0) were purchased from Sigma-Aldrich Chemie GmbH (Steinheim, Germany). β-nicotinamide adenine dinucleotide reduced disodium salt hydrate, β-nicotinamide adenine dinucleotide sodium salt were purchased from Carl Roth GmbH & Co. KG (Karlsruhe, Germany) and used without further purification. Glycerol dehydrogenase from *Cellulomonas* sp. and glucose dehydrogenase from *Pseudomonas* sp. are purchased from Sigma-Aldrich Chemie GmbH (Steinheim, Germany).

6.2.2 Characterization methods

^{1}H and ^{13}C NMR spectra for all compounds were measured using the Bruker Avance 250 MHz and 300 MHz spectrometer. UV-Vis absorption spectra of were recorded on a Perkin Elmer Lambda 25 UV-vis spectrometer and Thermo Scientific NanoDrop 8000 spectrophotometer. Solid-state diffuse reflectance UV-Vis absorption and fluorescence spectra were recorded on a Perkin Elmer Lambda 100 spectrophotometer and J&M TIDAS spectrofluorometer at ambient temperature, respectively. Nitrogen sorption was measured using a Micromeritics Tristar II Plus with samples degassed for 12 h at 120 °C under vacuum prior to analysis. Morphology of nanoparticles were examined with a Gemini 1530 (Carl Zeiss AG, Oberkochem, Germany) scanning electron microscope (SEM) operating at 0.35 kV and a

Jeol 1400 (Jeol Ltd, Tokyo, Japan) transmission electron microscope (TEM) operating at an accelerating voltage of 120 kV. SEM and TEM samples of nanoparticles were prepared by casting the diluted dispersion on silicon wafers and carbon layer-coated copper grids, respectively. Cyclic voltammetry measurements were carried out on a Metrohm Autolab PGSTAT204 potentiostat/galvanostat with a three-electrode-cell system: glassy carbon electrode as the working electrode, $Hg/HgCl_2$ electrode as the reference electrode, platinum wire as the counter electrode, and Bu_4NPF_6 (0.1 M in acetonitrile) as supporting electrolyte with a scan rate of 100 $mV \cdot s^{-1}$ in the range of -2 eV to 2 eV. All DFT calculations were carried out with the Gaussian 09W package. The structures were optimized at the B3LYP level of theory,[494] with the basis set of 6- 31G*.[495] Thermogravimetric analysis (TGA) was conducted in an air atmosphere with temperature increasing from room temperature to 800 °C at a rate of 10 K/min. FT-IR measurements were conducted with a Varian 1000 FT-IR spectrometer. EPR (Electron Paramagnetic Resonance) was measured on a Magnettech Miniscope MS200 spectrometer at room temperature.

6.2.3 Synthesis of core-shell nanophotoreactor

Synthesis of BTPh2-bridged organosilica monomer (Figure 59)

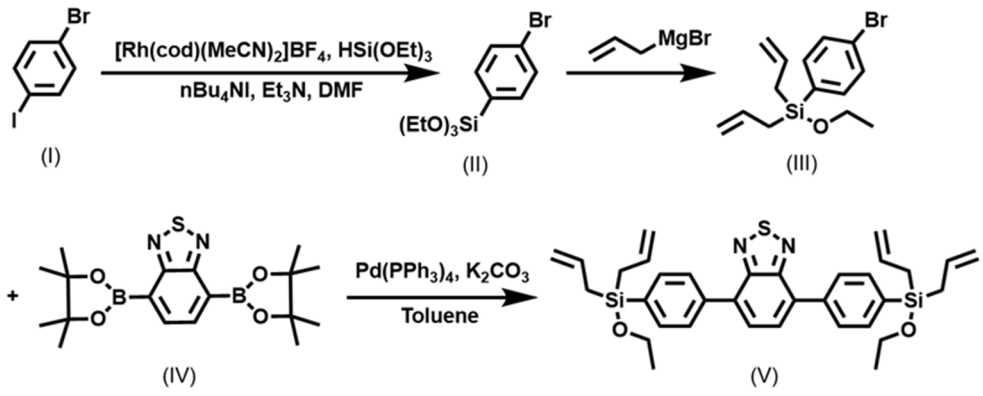

Figure 59. Synthetic route of BTPh2-bridged organosilica monomer.

4-Bromophenyltriethoxysilane[480] (II): 1-Brom-4-iodobenzene (563 mg, 2 mmol),

triethoxysilane (0.73 mL, 4 mmol), triethylamine (0.83 mL, 12 mmol) and bis(acetonitrile)(1,5-cyclooctadiene)rhodium(I)tetrafluoroborate (22 mg, 0.06 mmol) were dissolved in dry DMF (8 mL) and added in 25 mL Schlenk tube. Then, the Schlenk tube was degas in liquid nitrogen temperature and backfilled with argon 3 times. After degassing process, the reactive mixture was heated at 80 °C for 2 h. While cooled down in room temperature, the mixture was diluted with 100mL diethyl ether and washed with NH_4Cl saturated solution 3 times. A crude product was obtained after drying over anhydrous $MgSO_4$ and purified by chromatography on silica with petroleum ether/dichloromethane (1/1) as the elution to afford the pure product as clear light yellow oil.

^{1}H NMR (300 MHz, $CDCl_3$) δ 7.52 (d, *J*=8.4 Hz, 2H), 7.43 (d, *J*=8.4 Hz, 2H), 5.79 (ddt, *J*=15.7 Hz, 9.7 Hz, 7.8 Hz, 2H), 4.95 (ddt, *J*=15.7 Hz, 1.6 Hz, 1.4 Hz, 2H), 4.92 (ddt, *J*=9.7 Hz, 1.6 Hz, 1.1 Hz, 2H), 3.76 (q, *J*=6.8 Hz, 2H), 1.91 (ddd, *J*=7.8 Hz, 1.4 Hz, 1.1 Hz, 4H)1.21 (t, *J*=6.8 Hz, 3H);

^{13}C NMR (75 MHz, $CDCl_3$) δ 135.50, 133.88, 132.63, 130.90, 124.68, 114.96, 59.27, 21.08, 18.32.

1-Bromo-4-(diallylethoxysilyl)benzene[480] (III): 4-Bromophenyltriethoxysilane (474 mg, 1.49 mmol) was added allylmagnesium bromide (5.94 mL, 1 M in diethyl ether, 5.94 mmol) in diethyl ether with argon atmosphere. The reaction mixture was stirred at room temperature for 10 h and quenched with 10% HCl. It was then diluted with diethyl ether and the organic layer was washed with saturated $NaHCO_3$ solution and brine, dried over anhydrous $MgSO_4$, and evaporated under reduced pressure. The crude mixture was purified by chromatography on silica with to give the pure product as yellow oil.

^{1}H NMR (300 MHz, $CDCl_3$) δ 7.52 (d, *J*=8.4 Hz, 2H), 7.48 (d, *J*=8.4 Hz, 2H), 5.81

(ddt, *J*=15.7 Hz, 9.7 Hz, 7.8 Hz, 2H), 4.95 (ddt, *J*=15.7 Hz, 1.6 Hz, 1.4 Hz, 2H), 4.92 (ddt, *J*=9.7 Hz, 1.6 Hz, 1.1 Hz, 2H), 3.76 (q, *J*=6.8 Hz, 2H), 1.91 (ddd, *J*=7.8 Hz, 1.4 Hz, 1.1 Hz, 4H),1.21 (t, *J*=6.8 Hz, 3H);

^{13}C NMR (75 MHz, $CDCl_3$) δ 135.50, 133.88, 132.63, 130.90, 124.68, 114.96, 59.27, 21.08, 18.32.

4,7-Bis(4-allylethoxysilylphenyl)-2,1,3-benzothiadiazole (V): To a mixture of 4-(diallylethoxysilyl)bromobenzene (164.3 mg, 0.60 mmol), $Pd(PPh_3)_4$ (16.9 mg, 0.015 mmol), K_2CO_3 (101 mg, 0.73 mmol), and 2,1,3-benzothiadiazole-4,7-bis(boronic acid pinacol ester) (97.6 mg, 0.25 mmol) was added toluene (5 mL). The reaction mixture was degassing in liquid nitrogen temperature and backfilled with argon 3 times. After degassing process, the reactive mixture was heated at 80 °C for 24 h. Then the reaction mixture was diluted with diethyl ether, which was filtered through a Celite plug, and the filter cake was rinsed with diethyl ether. The combined filtrates were concentrated under reduced pressure. The residue was chromatographed on silica gel with petroleum ether/ethyl acetate (20/1) to give a sticky yellow oil. The NMR spectra was shown in **Figure 61**.

^{1}H NMR (300 MHz, $CDCl_3$) δ 7.92 (d, J = 7.7 Hz, 2H), 7.77-7.66 (m, 2H), 7.50 (s, 1H), 5.79 (dq, J = 18.1, 9.6 Hz, 2H), 5.00-4.81 (m, 4H), 3.82-3.66 (m, 2H), 1.90 (dd, J = 20.1, 8.0 Hz, 4H), 1.17 (q, J = 6.7 Hz, 3H).

^{13}C NMR (75 MHz, $CDCl_3$) δ 154.04, 134.38, 133.22, 133.11, 129.27, 128.54, 128.32, 114.93, 59.42, 21.31, 18.46.

Preparation of NP-C and NP-CS

NP-C: A mixture of CTAB (25 mg), distilled water (12 mL), and sodium hydroxide (87.5 μL, 2 M) was stirred at 80 °C for 50 min at 700 rpm in a 25 mL round bottom flask. Then, TEOS

(0.1 mL, 0.45 mmol) was added along with 4,7-bis(4-allylethoxysilylphenyl)-2,1,3-benzothiadiazole (26.7 mg in 1 mL of dry THF). The mixture was treated ultrasonically for 20 min to disperse the hydrophobic BTBADS in the aqueous solution, and the condensation process was carried out for 12 h. Afterwards, the solution was cooled to room temperature with stirring. Fractions were gathered in propylene tubes and collected by centrifugation.[496]

NP-CS: 60 mg NP-C, 2.4 ml of (25 wt %) CTAC solution and 18mg of TEA were added to 3.6 ml of water and stirred gently at 60 °C for 1 h in a 10-mL round bottom flask, then 2 mL of (20 v/v %) TEOS in cyclohexane was carefully added to the water-CTAC-TEA solution and kept at 60 °C in an oil bath under a magnetic stirring. The stirring rate was set to be 150 rpm. The reaction was then kept at a constant temperature with continuous stirring for 16 h to obtain the products. The products were collected by centrifugation and washed for several times with ethanol to remove the residual reactants. Then, the collected products were extracted with a 0.6 wt % ammonium nitrate (NH_4NO_3) ethanol solution at 60.0 °C for 6 h twice to remove the template and dried in vacuum.[497]

A possible mechanism of core-shell formation was follow (**Figure 60**): At first, due to the gravity and hydrophilic/hydrophobic interaction an oil@water hemi emulsion micelles with interfacial curvature could be induced by the surfactant assembled with hydrophobic organic solvent at the interface because a shear force from stirring. With the continuous and gentle stirring for the aqueous solution, the silicate/surfactant/oil composite nanoseeds could move randomly in aqueous phase and reach the interface and contact the curvature emulsion micelles containing oligomers to realize further growing and assembling with the “funneling” curvature. Then the silicate oligomers were further polymerized and condensed to form neonatal pore walls with the hemi emulsion as a template, then enter into the aqueous phase. The processes of interfacial emulsion, assembly, condensation, and “funneling” gradient growth could be

continued circularly, since the nano seeds get in touch with the interface repeatedly via their free movement by the stirring, leading to the uniform growth of mesopores on 3D direction. The dendritic mesochannels with a "funneling" shape could be obtained by successive growth processes revolving round the nanoseeds.

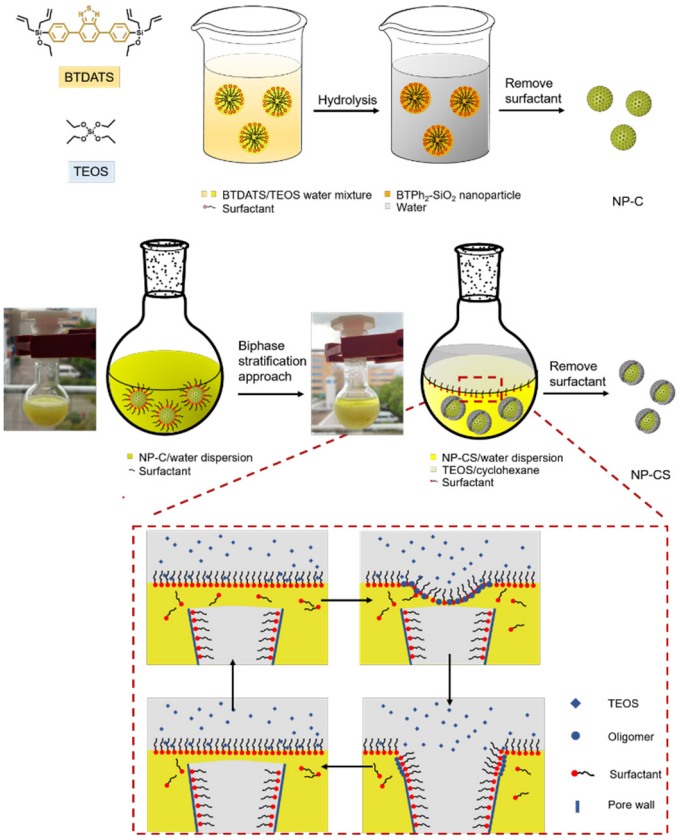

Figure 60. Synthetic route for photocatalytic core nanoparticle (NP-C) and photocatalytic core-shell nanoparticle (NP-CS).

Photocatalytic oxidation of NADH by NP-C and NP-CS

An aqueous dispersion (milliQ water, D_2O for NMR experiments) of NP-C and NP-CS (1 $mg \cdot mL^{-1}$) and NADH (10 $mmol \cdot L^{-1}$) were added to a 1 mL glass vial. The reaction mixture was stirred at 25 °C, saturated with O_2 or put in the air, irradiated with a blue-LED (460 nm, 0.10 W cm^{-2}) for 1 h. At different time intervals, aliquots of the sample were collected and analyzed by solution ^1H NMR (250 MHz) and UV-vis absorption spectroscopy. The changes of

absorption of NADH at 340 nm were monitored over different time intervals respectively.

NAD^+/NADH interconversion under LED irradiation

With glycerol dehydrogenase: The reaction mixture was composed of NP-C (1 $mg \cdot mL^{-1}$) and NP-CS (3 $mg \cdot mL^{-1}$), glycerol dehydrogenase lyophilized powder (100 $\mu g \cdot mL^{-1}$), $(NH_4)_2SO_4$ (40 $mmol \cdot L^{-1}$) and NAD^+ (20 $mmol \cdot L^{-1}$) in $Na_2CO_3/NaHCO_3$ buffer (100 $mmol \cdot L^{-1}$, pH 9.5). To initiate the enzyme reaction, glycerol (0.5 $mmol \cdot L^{-1}$) was added to the mixture. The progress of the reaction was followed by the corresponding changes in the absorbance intensity of NADH at 340 nm. Absorbance data was collected every 30 min. Each cycle, dark and light, was monitored for 30 min. For the light irradiation cycle, blue LED (460 nm, 0.10 W cm^{-2}) was used. Dark-light cycles were repeated for ten times.

With glucose dehydrogenase: In 1 mL glass vial, NAD^+ (5 $mmol \cdot L^{-1}$), NP-C (0.8 $mg \cdot mL^{-1}$) and NP-CS (2.4 $mg \cdot mL^{-1}$), glucose dehydrogenase (80 $\mu g \cdot mL^{-1}$), were added in 0.6 mL phosphate buffer (50 $mmol \cdot L^{-1}$, pH 7.4). To start reaction, glucose (1 $mmol \cdot L^{-1}$) was added to the mixture and kept it under dark condition. Changes in absorbance at 340 nm were measured after 30 min. Then, blue LED (460 nm, 0.10 W cm^{-2}) was irradiated to the vial to activate NP-C and NP-CS for 30 min and the absorbance was measured. We repeated these procedures for ten times to obtain ten cycles.

6.2.4 Characterizations

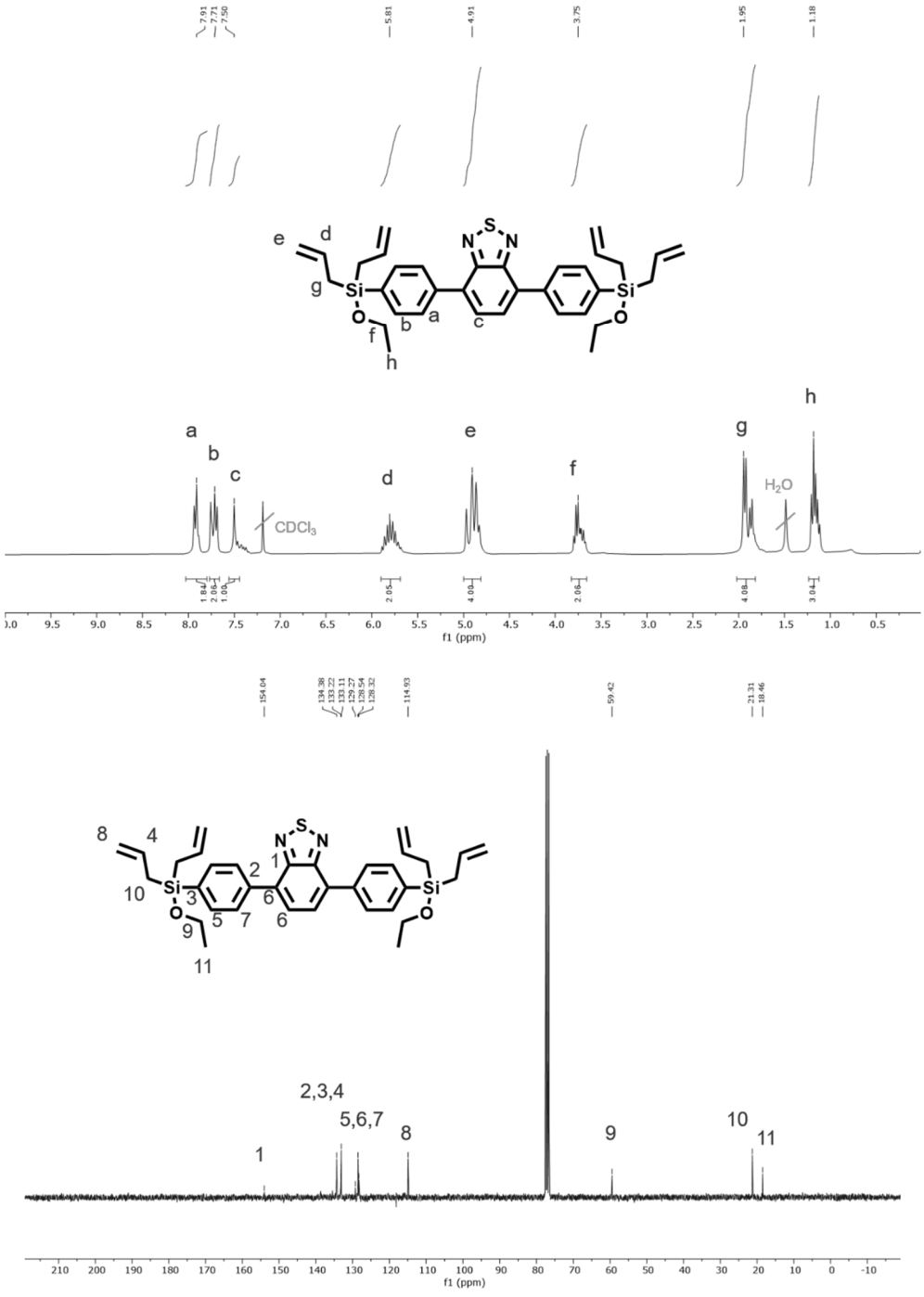

Figure 61. ^{1}H and ^{13}C NMR spectra of monomer 4,7-bis(4-allylethoxysilylphenyl)-2,1,3-benzothiadiazole.

The content of $BTPh_2$ unit in NP-C and NP-CS were characterized by thermogravimetric analysis (**Figure 62**). According to measurement and calculation, the mole ratio of $BTPh_2$ unit in NP-C and NP-CS are 8% and 3%, respectively. The decrease of the NP-CS curve at 200 °C

is attributed to the surfactant.

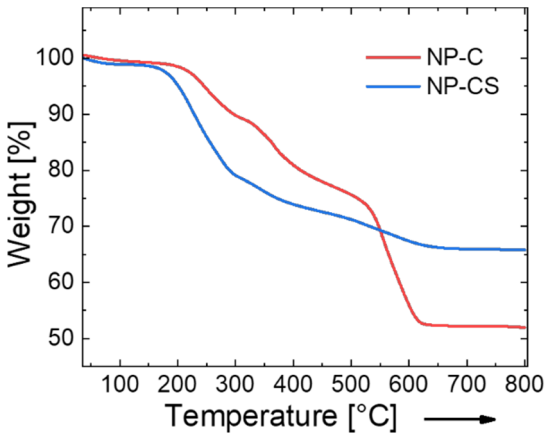

Figure 62. Thermogravimetric analysis (TGA) of NP-C and NP-CS under air with temperature increasing from room temperature to 800 °C at a rate of 10 K/min. The decrease of the NP-CS curve at 200 °C is attributed to the surfactant.

Theoretical calculations for 4,7-bis(4-allylethoxysilylphenyl)-2,1,3-benzothiadiazole using the density functional theory (DFT) at B3LYP/6-31G(d) level revealed the value and electron density distribution of HOMO and LUMO (**Figure 63**).

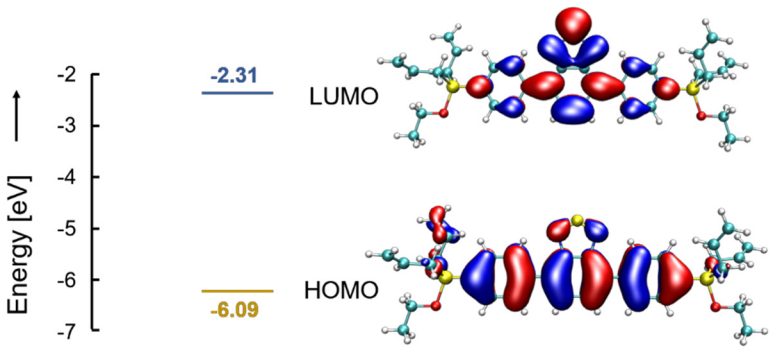

Figure 63. DFT calculations on the B3LYP/6-31G(d) level for monomer 4,7-bis(4-allylethoxysilylphenyl)-2,1,3-benzothiadiazole.

The photocurrent response confirms the responsiveness of NP-CS to blue light (**Figure 64**).

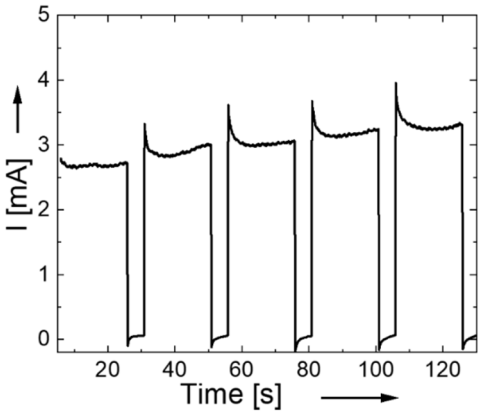

Figure 64. Photocurrent responses upon switching the light (blue LED, λ = 460 nm) on and off (on: 25 s, off: 5 s).

A proposed mechanism of NADH oxidation by NP-CS and NP-C was follow (**Figure 65**): On light excitation, the HOMO extracts an electron from 1,4-dihydronicotinamide, forming $NADH^{+\bullet}$ radicals. $NADH^{+\bullet}$ readily deprotonates to generate the neutral carbon-centred $NAD^{\bullet}$ radical. Under air, oxygen was oxidized by LUMO to form superoxide radicals, completing the photocatalytic cycle. The superoxide radical extracts an electron from $NAD^{\bullet}$ and consumes two protons from the medium, forming H_2O_2 and NAD^{+}.

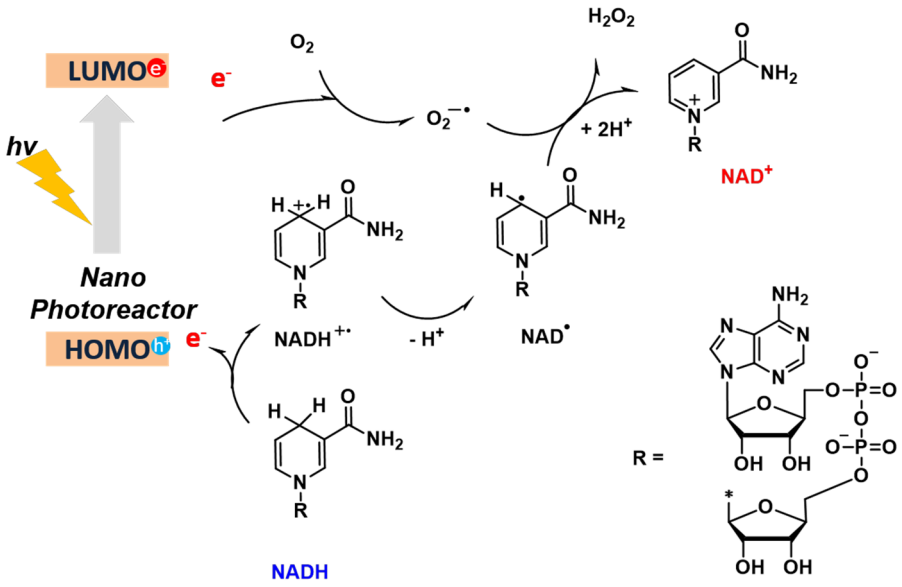

Figure 65. Proposed mechanism of NADH oxidation by nanophotoreactor.[498, 499]

6.3 Enhanced photocatalysis by light-harvesting mesoporous organosilica

6.3.1 Materials

1-Bromo-4-iodobenzene, triethoxysilane, tetraethylorthosilicate, bromobenzene, 2,1,3-benzothiadiazole-4,7-bis(boronic acid pinacol ester), allylmagnesium bromide, 2,6-dibromonaphthalene, 2,6-dihydroxyanthraquinone, trifluoromethanesulfonic anhydride, 1,4-bis(triethoxysilyl)benzene, octadecyltrimethylammonium chloride, bis(acetonitrile)(1,5-cyclooctadiene)rhodium(I)tetrafluorobotate were purchased from Sigma-Aldrich Chemie GmbH (Steinheim, Germany), trimethyloctadecylammonium chloride, tetrakis(triphenylphosphine)palladium(0), β-nicotinamide adenine dinucleotide sodium salt were purchased from Carl Roth GmbH & Co. KG (Karlsruhe, Germany) and used without further purification.

6.3.2 Characterization methods

^{1}H and ^{13}C NMR spectra for all compounds were measured using the Bruker Avance 250 MHz and 300 MHz. UV-Vis absorption spectra of were recorded on a Perkin Elmer Lambda 25 UV-vis spectrometer and Thermo Scientific NanoDrop 8000 spectrophotometer. Solid-state diffuse reflectance UV-Vis absorption and fluorescence spectra were recorded on a Perkin Elmer Lambda 100 spectrophotometer and J&M TIDAS spectrofluorometer at ambient temperature, respectively. Nitrogen sorption was measured using a Micromeritics Tristar II Plus with samples degassed for 12 h at 120 °C under vacuum prior to analysis. Morphology of nanoparticles were examined with a Gemini 1530 (Carl Zeiss AG, Oberkochem, Germany) scanning electron microscope (SEM) operating at 0.35 kV and a Jeol 1400 (Jeol Ltd, Tokyo, Japan) transmission electron microscope (TEM) operating at an accelerating voltage of 120 kV. SEM and TEM samples of nanoparticles were prepared by casting the diluted dispersion on

silicon wafers and carbon layer-coated copper grids, respectively. Cyclic voltammetry measurements were carried out on a Metrohm Autolab PGSTAT204 potentiostat/galvanostat with a three-electrode-cell system: glassy carbon electrode as the working electrode, $Hg/HgCl_2$ electrode as the reference electrode, platinum wire as the counter electrode, and Bu_4NPF_6 (0.1 M in acetonitrile) as supporting electrolyte with a scan rate of 100 $mV \cdot s^{-1}$ in the range of -2 eV to 2 eV. Thermogravimetric analysis (TGA) was conducted in an air atmosphere with temperature increasing from room temperature to 800 °C at a rate of 10 K/min. FT-IR measurements were conducted with a Varian 1000 FT-IR spectrometer. EPR (Electron Paramagnetic Resonance) was measured on a Magnettech Miniscope MS200 spectrometer at room temperature. flouroscence lifetime measurements were conducted with a FluoTime200 time-correlated single photon counting setup. Samples were excited with a blue laser at 380 nm which was controlled by PicoQuant PDL 800-D. The signal was detected using a micro-channel plate photomultiplier tube that was connected to PicoHarp 300 time-correlated single photon counting system.

6.3.3 Synthesis of MOS-Ar and MOS-Ar/BT

4,7-Bis(4-allylethoxysilylphenyl)-2,1,3-benzothiadiazole: To a mixture of 4-(diallylethoxysilyl)bromobenzene (164.3 mg, 0.60 mmol), $Pd(PPh_3)_4$ (16.9 mg, 0.015 mmol), K_2CO_3 (101 mg, 0.73 mmol), and 2,1,3-benzothiadiazole-4,7-bis(boronic acid pinacol ester) (97.6 mg, 0.25 mmol) was added toluene (5 mL). The reaction mixture was degassing in liquid nitrogen temperature and backfilled with argon 3 times. After degassing process, the reactive mixture was heated at 80 °C for 24 h. Then the reaction mixture was diluted with diethyl ether, which was filtered through a Celite plug, and the filter cake was rinsed with diethyl ether. The combined filtrates were concentrated under reduced pressure. The residue was chromatographed on silica gel with petroleum ether/ethyl acetate (20/1) to give a sticky yellow

oil. The NMR spectra was shown in **Figure 68**.

^{1}H NMR (300 MHz, $CDCl_3$) δ 7.92 (d, J = 7.7 Hz, 2H), 7.77-7.66 (m, 2H), 7.50 (s, 1H), 5.79 (dq, J = 18.1, 9.6 Hz, 2H), 5.00-4.81 (m, 4H), 3.82-3.66 (m, 2H), 1.90 (dd, J = 20.1, 8.0 Hz, 4H), 1.17 (q, J = 6.7 Hz, 3H).

^{13}C NMR (75 MHz, $CDCl_3$) δ 154.04, 134.38, 133.22, 133.11, 129.27, 128.54, 128.32, 114.93, 59.42, 21.31, 18.46.

2,6-Bis(triethoxysilyl)naphthalene:[266] A mixture of 2,6-dibromonaphthalene (1.00 g, 3.50 mmol), $[Rh(CH_3CN)_2(cod)]BF_4$ (66.4 mg, 0.18 mmol), tetrabutylammonium iodide (2.59 g, 7.00 mmol), dimethylformamide (25 mL), and triethylamine (2.94 mL) was cooled to 0 °C. After adding triethoxysilane (2.60 mL, 14.06 mmol), the mixture was stirred at 80 °C for 2 h. The reaction mixture was concentrated under reduced pressure and then extracted with ether. The organic phase was filtrated using Celite, and the solvent was removed by rotary evaporator and in vacuum. Purification of the residue by reduced-pressure distillation gave 2,6-bis(triethoxysilyl)naphthalene as a transparent oil. The NMR spectra was shown in **Figure 69**.

^{1}H NMR (250 MHz, $CDCl_3$) δ 8.23 (s, 2H), 7.91 (d, *J* = 8.1 Hz, 2H), 7.75 (d, *J* = 8.2 Hz, 2H), 3.94 (q, *J* = 7.0 Hz, 12H), 1.29 (t, *J* = 7.0 Hz, 18H).

^{13}C NMR (75 MHz, $CDCl_3$) δ 136.09, 133.68, 130.47, 129.60, 127.62, 58.84, 18.26.

2,6-Bis(triethoxysilyl)anthracene:[267] To a solution of 2,6-dihydroxyanthracene (172 mg, 0.82 mmol) and pyridine (2 mL) in dichloromethane (25 mL) was added dropwise trifluoromethanesulfonic anhydride (0.56 mL, 3.33 mmol) at 0 °C. The mixture was stirred at room teperature for 15 h, quenched with water and extracted with dichloromethane. The organic layer was washed with saturated sodium hydrogencarbonate solution and brine, dried over anhydrous sodium sulfate, and evaporated under reduced pressure. The residue was

chromatographed on silica gel (hexane/EtOAc = 5:1 as eluent) to give 2,6-bis(trifluoromethanesulfonyloxy)anthracene. To a solution of 2,6-bis(trifluoromethanesulfonyloxy)anthracene (157 mg, 0.33 mmol), tetrabutylammonium iodide (245 mg, 0.66 mmol), triethylamine (0.28 mL, 1.99 mmol) and $[Rh(cod)(CH_3CN)_2]BF_4$ (7.56 mg, 0.02 mmol) in DMF (5 mL) was added dropwise triethoxysilane (0.25 mL, 1.33 mmol) at 0 °C. The mixture was stirred at 80 °C for 2 h. The resulting mixture was diluted with diethyl ether. The precipitates were filtered off through a Celite plug and rinsed with diethyl ether. The combined filtrates were concentrated under vacuum and the residue was passed through charcoal to give pure 2,6-bis(triethoxysilyl)anthracene. The NMR spectra was shown in **Figure 70**.

^{1}H NMR (250 MHz, $CDCl_3$) δ 8.47 (s, 2H), 8.42 (s, 2H), 8.03 (d, *J* = 8.5 Hz, 2H), 7.68 (dd, *J* = 8.5, 1.0 Hz, 2H), 3.96 (q, *J* = 7.0 Hz, 12H), 1.30 (t, *J* = 7.0 Hz, 18H).

^{13}C NMR (75 MHz, $CDCl_3$) δ 137.27, 132.30, 131.64, 129.05, 128.49, 127.55, 126.85, 58.89, 18.30.

Preparation of mesoporous organosilica: Take MOS-Ph and MOS-Ph/BT as an example.[257] MOS-Ph/BT was synthesized from 1,4-bis(triethoxysilyl)benzene and 4,7-bis(4-allylethoxysilylphenyl)-2,1,3-benzothiadiazole in the presence of octadecyltrimethylammonium chloride (C_{18}TACl) surfactant. C_{18}TACl (1.67 g, 4.79 mmol) was dissolved in a mixture of ion-exchanged water (50 g) and 6 M NaOH aqueous solution (4 g, 20 mmol NaOH) at 50 °C. 1,4-bis(triethoxysilyl)benzene (2 g, 4.97 mmol) was added to the solution under vigorous stirring at room temperature. The mixture was treated ultrasonically for 20 min to disperse the hydrophobic 1,4-bis(triethoxysilyl)benzene in the aqueous solution. Then, bis(4-allylethoxysilylphenyl)-2,1,3-benzothiadiazole was added in the solution with stiring. The mixture was treated ultrasonically for 30 min and stirred for 20 h at room

temperature. The solution was kept at 95 °C for 24 h under static conditions. Surfactant was removed by stirring 1.0 g of as-synthesized material in 250 ml of ethanol with 9 g of 36% HCl aqueous solution at 70 °C. The synthesis of MOS-Ph refers to this method to remove 4,7-bis(4-allylethoxysilylphenyl)-2,1,3-benzothiadiazole.

Photocatalytic regeneration of NADH: The reaction medium was composed of photocatalysts (1.0 mg·mL^{-1}), β-NAD^{+} (4 mM), TEOA (15% w/v) in 1 mL phosphate buffer (0.01 M). After degassing with argon for 5 min, the reaction mixture was placed under the illumination of an whilt LED lamp at a distance of 5 cm. During the reaction, the system was kept at room temperature and the concentration of NADH was determined by a UV-vis measurement.

6.3.4 Characterizations

Cyclic voltammetry measurements indicated that the lowest unoccupied molecular orbital (LUMO) position of MOS-Ph and MOS-Ph/BT were at −0.90 V vs SCE and −1.37 V vs SCE, the highest occupied molecular orbital (HOMO) position at 1.72 V vs SCE and 1.75 V vs SCE, respectively (**Figure 66**).

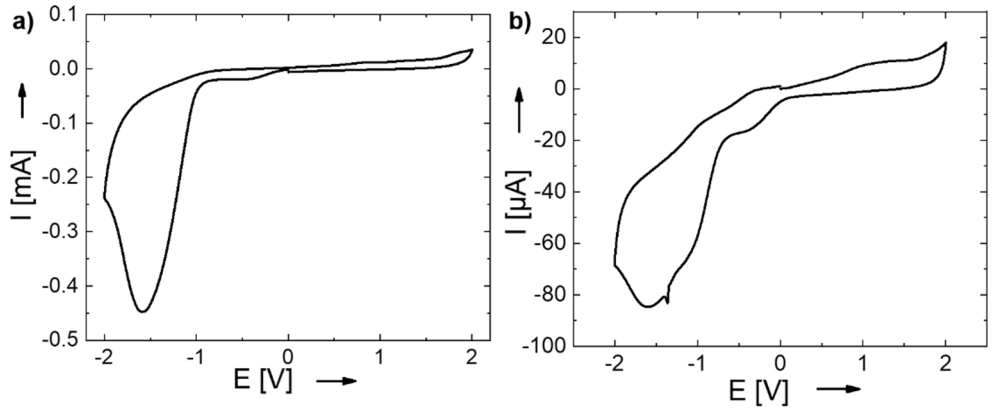

Figure 66. Cyclic voltammetry of a) MOS-Ph and b) MOS-Ph/BT.

Fourier transform infrared (FTIR) spectroscopy (**Figure 67**) revealed recognizable signals

at 1348, 1377, 1567 and 1577 cm^{-1}, which were the typical characteristics for C=N and N−S stretching modes in benzothiadiazole units. The strong and wide absorption signals at 1095 cm^{-1} could be assigned to Si−O−Si antisymmetric stretching vibration. The signals at 3100-3000 cm^{-1} could be divided to C−H stretching vibration on phenyl rings. The absorption signals at 1600 cm^{-1} could be assigned to frame stretching vibration (C=C) of phenyl rings.

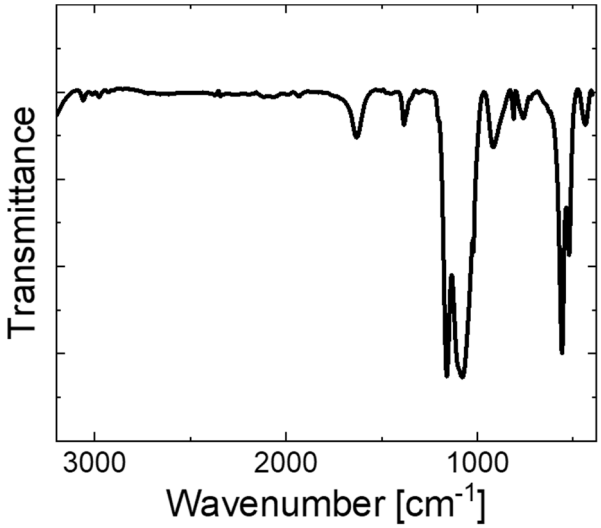

Figure 67. Fourier transform infrared (FTIR) spectra of MOS-Ph/BT.

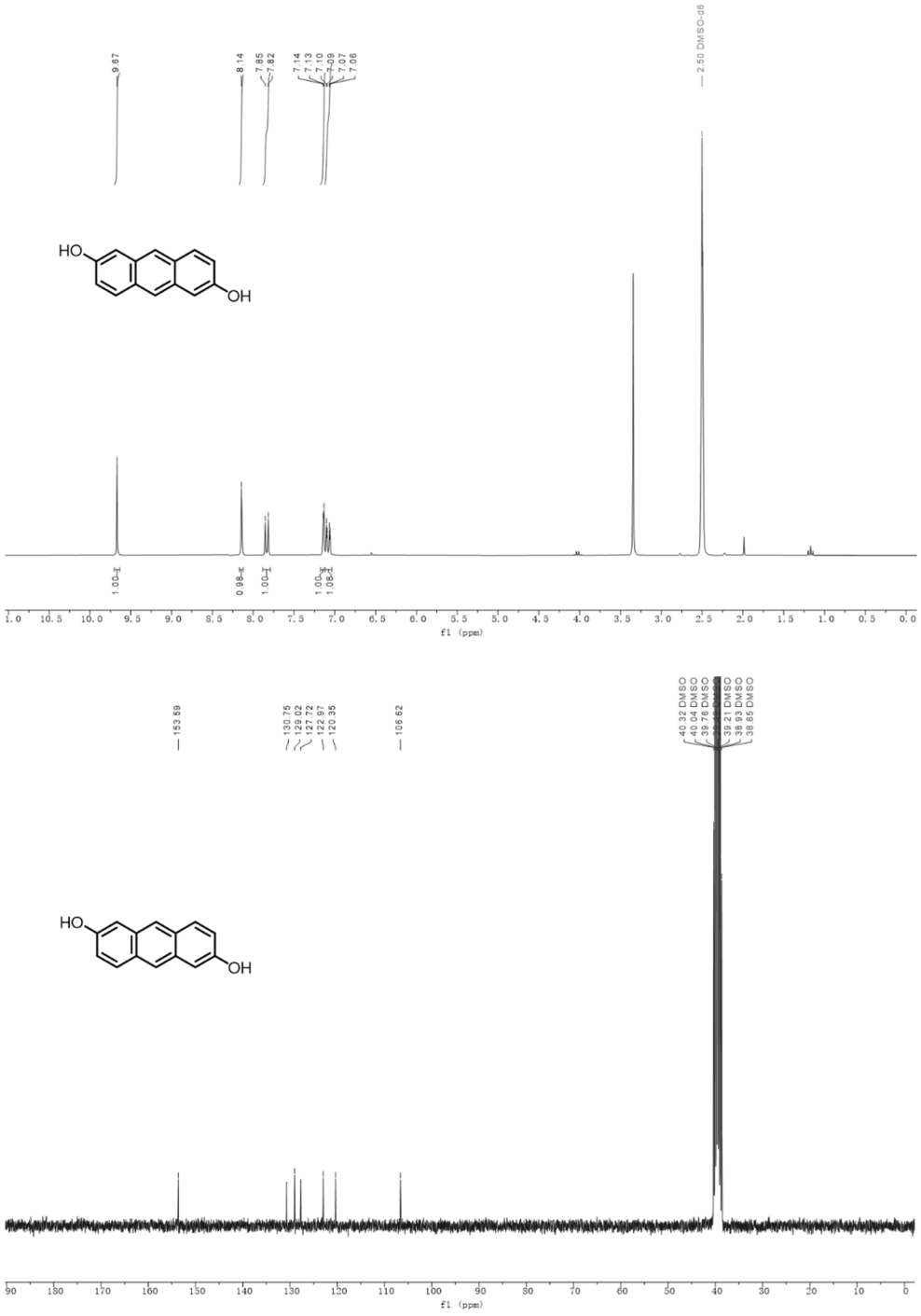

Figure 68. ^{1}H and ^{13}C NMR spectrum of 2,6-dihydroxyanthracene.

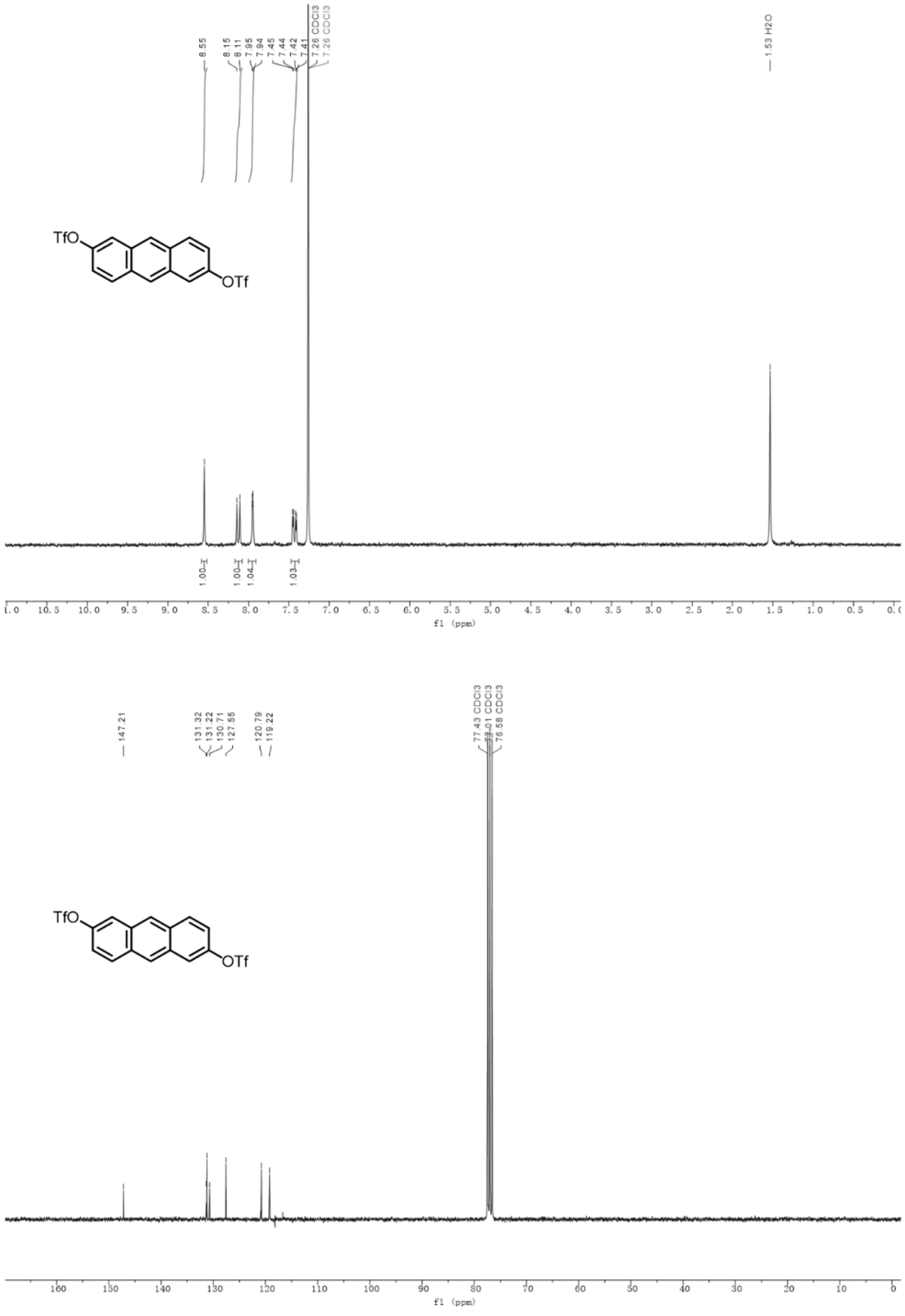

Figure 69. ^{1}H and ^{13}C NMR spectra of 2,6-bis(trifluoromethanesulfonyloxy)anthracene.

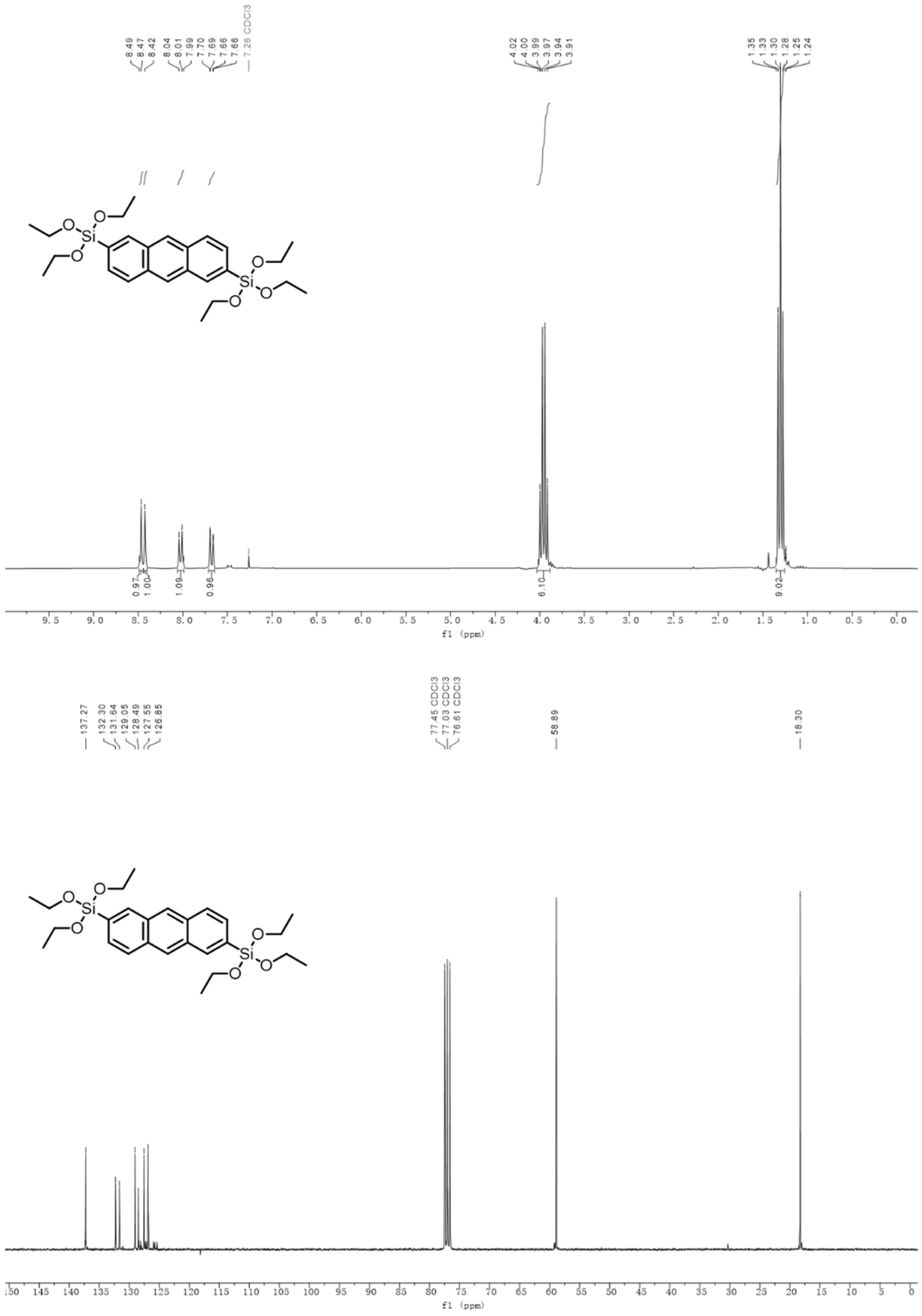

Figure 70. ^{1}H and ^{13}C NMR spectra of 2,6-bis(triethoxysilyl)anthracene.

7. Summary and outlook

In this thesis, mesoporous organosilicas were developed as metal-free heterogeneous visible light-active photocatalysts for organic synthesis and biocatalysis. The design and synthesis of organosilane monomers have been developed, and the relation of the structure and morphology of the obtained organosilica materials to their photocatalytic applications investigated.

First, a series of mesoporous organosilica photocatalysts are designed for visible light-promoted aryl azoline formation. Different ratios of 1,4-bromophenyltriethoxysilane (BPTS) (50%, 75% and 100%) were chosen as the monomers for the synthesis of the backbone precursor with tetraethyl orthosilicate (TEOS) by hydrolysis condensation. The photoactive diphenyl benzothiadiazole ($BTPh_2$) units were then formed via successive coupling methods, obtaining the final organosilica. Via formation of aromatic aldehydes with various amines, 2-phenyl-2-imidazoline, 2-phenyl-2-oxazoline, 2-phenyl-2-thiazoline and their derivatives could be formed with high conversion 89% and selectivity 97%. Additionally, the organosilica photocatalyts showed high stability and reusability.

As next, to solve the issue of photocatalysis-enzyme cooperation, core-shell structured porous nanophotoreactors are designed for highly stable and recyclable photobiocatalysis under aerobic conditions. The enzymatic cofactor NAD^+ from NADH can be efficiently regenerated by the photoactive organosilica core, while photogenerated active oxygen species are trapped and deactivated through the non-photoactive shell, protecting the enzymatic material. The versatility of these photocatalytic core-shell nanoreactors was demonstrated in tandem with two different enzymatic systems, glycerol dehydrogenase and glucose 1-dehydrogenase, where long term enzyme stability was observed for the core-shell

photocatalytic system.

At last, in order to improve the light absorption and energy transfer in the organosilica to increase the photocatalytic efficiency, the photocatalytic center embedded in the aromatic ring structure framework is designed to enhance light collection. The aromatic ring effectively absorbs different wavelengths of light, and the excited energy is funneled into the photocatalytic center through energy transfer. Compared with the direct excitation of $BTPh_2$ as single photocatalytic units to regenerate NADH, the efficiency of the multi-component organosilica is increased by 50%, and no additional hydrogen atom source is required. These results demonstrate the design principle of mesoporous organosilica photocatalysts containing multiple photoactive components that mimic the light-trapping antenna mechanism in natural photosynthesis.

In summary, this thesis highlights mesoporous organosilica as efficient heterogeneous, visible light active photocatalysts for a wide range of applications under environmentally benign reaction conditions.

8. Literature

[1] G. Ciamician *Science*. **1912**, *36*, 385-394.

[2] Y. You, W. Nam *Chem. Soc. Rev.* **2012**, *41*, 7061-7084.

[3] H. H. Huo, X. D. Shen, C. Y. Wang, L. L. Zhang, P. Rose, L. A. Chen, K. Harms, M. Marsch, G. Hilt, E. Meggers *NATURE*. **2014**, *515*, 100-103.

[4] J. Twilton, C. Le, P. Zhang, M. H. Shaw, R. W. Evans, D. W. C. MacMillan *Nat. Rev. Chem.* **2017**, *1*.

[5] W. M. Cheng, R. Shang *ACS Catal.* **2020**, *10*, 9170-9196.

[6] F. Glaser, O. S. Wenger *Coord. Chem. Rev.* **2020**, *405*.

[7] N. Hoffmann *JOURNAL OF PHOTOCHEMISTRY AND PHOTOBIOLOGY C-PHOTOCHEMISTRY REVIEWS*. **2008**, *9*, 43-60.

[8] N. Hoffmann *J. Phys. Org. Chem.* **2015**, *28*, 121-136.

[9] Y. Z. Chen, W. H. Li, L. Li, L. N. Wang *Rare Met.* **2018**, *37*, 1-12.

[10] Y. Gong, J. Wang, Z. Wei, P. Zhang, H. Li, Y. Wang *ChemSusChem*. **2014**, *7*, 2303-2309.

[11] V. Dusastre, Materials for sustainable energy: a collection of peer-reviewed research and review articles from Nature Publishing Group, World Scientific, **2010**.

[12] C. George, M. Ammann, B. D'Anna, D. Donaldson, S. A. Nizkorodov *Chem. Rev.* **2015**, *115*, 4218-4258.

[13] Z. Zou, J. Ye, K. Sayama, H. Arakawa *nature*. **2001**, *414*, 625-627.

[14] A. J. Bard, M. A. Fox *Acc. Chem. Res.* **1995**, *28*, 141-145.

[15] N. Zhang, M.-Q. Yang, S. Liu, Y. Sun, Y.-J. Xu *Chem. Rev.* **2015**, *115*, 10307-10377.

[16] J. Yang, D. Wang, H. Han, C. Li *Acc. Chem. Res.* **2013**, *46*, 1900-1909.

[17] W. Tu, Y. Zhou, Z. Zou *Adv. Funct. Mater.* **2013**, *23*, 4996-5008.

[18] W. Fan, Q. Zhang, Y. Wang *PCCP*. **2013**, *15*, 2632-2649.

[19] L. Wondraczek, E. Tyystjärvi, J. Méndez-Ramos, F. A. Müller, Q. Zhang *Adv. Sci.* **2015**, *2*, 1500218.

[20] M. Kapilashrami, Y. Zhang, Y.-S. Liu, A. Hagfeldt, J. Guo *Chem. Rev.* **2014**, *114*, 9662-9707.

[21] A. Kubacka, M. Fernandez-Garcia, G. Colon *Chem. Rev.* **2012**, *112*, 1555-1614.

[22] H. Li, Y. Zhou, W. Tu, J. Ye, Z. Zou *Adv. Funct. Mater.* **2015**, *25*, 998-1013.

[23] F. Fresno, R. Portela, S. Suárez, J. M. Coronado *J. Mater. Chem. A*. **2014**, *2*, 2863-2884.

[24] M. G. Walter, E. L. Warren, J. R. McKone, S. W. Boettcher, Q. Mi, E. A. Santori, N. S. Lewis *Chem. Rev.* **2010**, *110*, 6446-6473.

[25] H. Zhang, G. Liu, L. Shi, H. Liu, T. Wang, J. Ye *Nano Energy*. **2016**, *22*, 149-168.

[26] Y. Lan, Y. Lu, Z. Ren *Nano Energy*. **2013**, *2*, 1031-1045.

[27] M. L. Marin, L. Santos-Juanes, A. Arques, A. M. Amat, M. A. Miranda *Chem. Rev.* **2012**, *112*, 1710-1750.

[28] A. Fujishima, K. Honda *Nature*. **1972**, *238*, 37-38.

[29] A. V. Pamfilov, Mazurkev.Ys, S. Y. Mukhlya *Russ. J. Phys. Chem. Ussr*. **1970**, *44*, 958.

[30] H. D. Müller, F. Steinbach *Nature*. **1970**, *225*, 728-729.

[31] F. Steinbach *Nature*. **1969**, *221*, 657-658.

[32] W. Doerffler, K. Hauffe *J. Catal.* **1964**, *3*, 171-178.

[33] M. R. Hoffmann, S. T. Martin, W. Choi, D. W. Bahnemann *Chem. Rev.* **1995**, *95*, 69-96.

[34] A. L. Linsebigler, G. Lu, J. T. Yates Jr *Chem. Rev.* **1995**, *95*, 735-758.

[35] R. Wang, K. Hashimoto, A. Fujishima, M. Chikuni, E. Kojima, A. Kitamura, M. Shimohigoshi, T. Watanabe *Nature*. **1997**, *388*, 431-432.

[36] J. H. Carey, J. Lawrence, H. M. Tosine *Bulletin of environmental contamination and toxicology*. **1976**, *16*, 697-701.

[37] T. Inoue, A. Fujishima, S. Konishi, K. Honda *Nature*. **1979**, *277*, 637-638.

[38] N. Razgoniaeva, P. Moroz, S. Lambright, M. Zamkov *The journal of physical chemistry letters*. **2015**, *6*, 4352-4359.

[39] N. Zhang, Y.-J. Xu *CrystEngComm*. **2016**, *18*, 24-37.

[40] Y. Li, H. Xu, S. Ouyang, J. Ye *PCCP*. **2016**, *18*, 7563-7572.

[41] L. Wang, T. Sasaki *Chem. Rev.* **2014**, *114*, 9455-9486.

[42] C. An, S. Wang, Y. Sun, Q. Zhang, J. Zhang, C. Wang, J. Fang *J. Mater. Chem. A*. **2016**, *4*, 4336-4352.

[43] L. Wang, R. Li, K. A. I. Zhang *Macromol. Rapid Commun.* **2018**, *39*, 1800466.

[44] L. Wang, W. Huang, R. Li, D. Gehrig, P. W. M. Blom, K. Landfester, K. A. I. Zhang *Angew. Chem. Int. Ed.* **2016**, *55*, 9783-9787.

[45] A. Hagfeldt, M. Graetzel *Chem. Rev.* **1995**, *95*, 49-68.

[46] M. A. Fox, M. T. Dulay *Chem. Rev.* **1993**, *93*, 341-357.

[47] X. Wang, X. Wan, X. Xu, X. Chen *Appl. Surf. Sci.* **2014**, *321*, 10-18.

[48] E. Hapeshi, A. Achilleos, M. I. Vasquez, C. Michael, N. P. Xekoukoulotakis, D. Mantzavinos, D. Kassinos *Water Res.* **2010**, *44*, 1737-1746.

[49] K. Kalyanasundaram *Coord. Chem. Rev.* **1982**, *46*, 159-244.

[50] C. K. Prier, D. A. Rankic, D. W. MacMillan *Chem. Rev.* **2013**, *113*, 5322-5363.

[51] T. Jack, C. Le, P. Zhang, M. H. Shaw, R. W. Evans *Nature Reviews. Chemistry*. **2017**, *1*.

[52] D. A. Nicewicz, T. M. Nguyen *ACS Catal.* **2014**, *4*, 355-360.

[53] D. Ravelli, M. Fagnoni *ChemCatChem*. **2012**, *4*, 169-171.

[54] V. Srivastava, P. P. Singh *RSC Adv.* **2017**, *7*, 31377-31392.

[55] S. D. Tambe, R. S. Rohokale, U. A. Kshirsagar *Eur. J. Org. Chem.* **2018**, *2018*, 2117-2121.

[56] I. K. Sideri, E. Voutyritsa, C. G. Kokotos *Org. Biomol. Chem.* **2018**, *16*, 4596-4614.

[57] H. Miyabe in *Organic Reactions Promoted by Metal-Free Organic Dyes Under Visible Light Irradiation, Vol.*, IntechOpen, **2017**.

[58] H. Hao, X. Lang *ChemCatChem*. **2019**, *11*, 1378-1393.

[59] M. M. Khan, S. F. Adil, A. Al-Mayouf *Journal of Saudi Chemical Society*. **2015**, *19*, 462-464.

[60] E. Pelizzetti, C. Minero *Comments Inorg. Chem.* **1994**, *15*, 297-337.

[61] R. Marschall, L. Wang *Catal. Today*. **2014**, *225*, 111-135.

[62] A. Akhundi, A. Badiei, G. M. Ziarani, A. Habibi-Yangjeh, M. J. Muñoz-Batista, R. Luque *Molecular Catalysis*. **2020**, *488*, 110902.

[63] Y. Markushyna, C. A. Smith, A. Savateev *Eur. J. Org. Chem.* **2020**.

[64] J. W. Maina, J. A. Schütz, L. Grundy, E. Des Ligneris, Z. Yi, L. Kong, C. Pozo-Gonzalo, M. Ionescu, L. F.

Dumée *ACS Appl. Mater. Interfaces*. **2017**, *9*, 35010-35017.

[65] H. Zhang, J. Li, Q. Tan, L. Lu, Z. Wang, G. Wu *Chem. Eur. J.* **2018**, *24*, 18137-18157.

[66] M. Liras, M. Barawi, A. Víctor *Chem. Soc. Rev.* **2019**, *48*, 5454-5487.

[67] Z. J. Wang, S. Ghasimi, K. Landfester, K. A. Zhang *Chem. Mater.* **2015**, *27*, 1921-1924.

[68] A. Juris, V. Balzani, F. Barigelletti, S. Campagna, P. l. Belser, A. v. von Zelewsky *Coord. Chem. Rev.* **1988**, *84*, 85-277.

[69] H. Takeda, O. Ishitani *Coord. Chem. Rev.* **2010**, *254*, 346-354.

[70] O. S. Wenger *Acc. Chem. Res.* **2013**, *46*, 1517-1526.

[71] D. R. Weinberg, C. J. Gagliardi, J. F. Hull, C. F. Murphy, C. A. Kent, B. C. Westlake, A. Paul, D. H. Ess, D. G. McCafferty, T. J. Meyer *Chem. Rev.* **2012**, *112*, 4016-4093.

[72] T. Bach *Synthesis*. **1998**, *1998*, 683-703.

[73] A. Albini *Synthesis*. **1981**, *1981*, 249-264.

[74] M. Fagnoni, D. Dondi, D. Ravelli, A. Albini *Chem. Rev.* **2007**, *107*, 2725-2756.

[75] D. Jespersen, B. Keen, J. I. Day, A. Singh, J. Briles, D. Mullins, J. D. Weaver *Organic Process Research & Development*. **2019**, *23*, 1087-1095.

[76] B. M. Hockin, C. Li, N. Robertson, E. Zysman-Colman *Catal. Sci. Technol.* **2019**, *9*, 889-915.

[77] L. Traub, O. Reiser in *9. Homogeneous visible light mediated transition metal catalysis other than Ruthenium and Iridium, Vol.*, De Gruyter, **2020**, pp.193-222.

[78] C. Minozzi, A. Caron, J. C. Grenier-Petel, J. Santandrea, S. K. Collins *Angew. Chem. Int. Ed.* **2018**, *57*, 5477-5481.

[79] A. J. Lennox, S. Fischer, M. Jurrat, S. P. Luo, N. Rockstroh, H. Junge, R. Ludwig, M. Beller *Chem. Eur. J.* **2016**, *22*, 1233-1238.

[80] H. Takeda, Y. Monma, H. Sugiyama, H. Uekusa, O. Ishitani *Front. Chem.* **2019**, *7*, 418.

[81] W. J. Liu, H. H. Huang, T. Ouyang, L. Jiang, D. C. Zhong, W. Zhang, T. B. Lu *Chem. Eur. J.* **2018**, *24*, 4503-4508.

[82] S. Gisbertz, B. Pieber *ChemPhotoChem*. **2020**, *4*, 456-475.

[83] C. Gao, J. Wang, H. Xu, Y. Xiong *Chem. Soc. Rev.* **2017**, *46*, 2799-2823.

[84] D. Friedmann, A. Hakki, H. Kim, W. Choi, D. Bahnemann *Green Chem.* **2016**, *18*, 5391-5411.

[85] R. Asahi, T. Morikawa, T. Ohwaki, K. Aoki, Y. Taga *science*. **2001**, *293*, 269-271.

[86] A.-W. Xu, Y. Gao, H.-Q. Liu *J. Catal.* **2002**, *207*, 151-157.

[87] H. Irie, Y. Watanabe, K. Hashimoto *Chem. Lett.* **2003**, *32*, 772-773.

[88] T. Ohno, T. Mitsui, M. Matsumura *Chem. Lett.* **2003**, *32*, 364-365.

[89] S. Sato *Chem. Phys. Lett.* **1986**, *123*, 126-128.

[90] X. Chen, C. Burda *J. Am. Chem. Soc.* **2008**, *130*, 5018-5019.

[91] W. Yu, J. Zhang, T. Peng *Appl. Catal., B*. **2016**, *181*, 220-227.

[92] E. Reisner, D. J. Powell, C. Cavazza, J. C. Fontecilla-Camps, F. A. Armstrong *J. Am. Chem. Soc.* **2009**, *131*, 18457-18466.

[93] Y. Cho, W. Choi, C.-H. Lee, T. Hyeon, H.-I. Lee *Environ. Sci. Technol.* **2001**, *35*, 966-970.

[94] M. Zhang, C. Chen, W. Ma, J. Zhao *Angew. Chem. Int. Ed.* **2008**, *47*, 9730-9733.

[95] A. Naldoni, M. Allieta, S. Santangelo, M. Marelli, F. Fabbri, S. Cappelli, C. L. Bianchi, R. Psaro, V. Dal Santo *J. Am. Chem. Soc.* **2012**, *134*, 7600-7603.

[96] X. Lang, J. Zhao, X. Chen *Angewandte Chemie*. **2016**, *128*, 4775-4778.

[97] J. Zoller, D. C. Fabry, M. Rueping *ACS Catal.* **2015**, *5*, 3900-3904.

[98] L. Zhang, J. M. Cole *ACS Appl. Mater. Interfaces*. **2015**, *7*, 3427-3455.

[99] P. Riente, T. Noël *Catal. Sci. Technol.* **2019**, *9*, 5186-5232.

[100] M. Rueping, J. Zoller, D. C. Fabry, K. Poscharny, R. M. Koenigs, T. E. Weirich, J. Mayer *Chem. Eur. J.* **2012**, *18*, 3478-3481.

[101] V. Jeena, R. S. Robinson *Chem. Commun.* **2012**, *48*, 299-301.

[102] J. Wang, R. Chen, L. Xiang, S. Komarneni *Ceram. Int.* **2018**, *44*, 7357-7377.

[103] T. Shishido, T. Miyatake, K. Teramura, Y. Hitomi, H. Yamashita, T. Tanaka *The Journal of Physical Chemistry C*. **2009**, *113*, 18713-18718.

[104] S. Furukawa, Y. Ohno, T. Shishido, K. Teramura, T. Tanaka *ACS Catal.* **2011**, *1*, 1150-1153.

[105] Y. Su, Z. Han, L. Zhang, W. Wang, M. Duan, X. Li, Y. Zheng, Y. Wang, X. Lei *Appl. Catal., B*. **2017**, *217*, 108-114.

[106] O. Tomita, T. Otsubo, M. Higashi, B. Ohtani, R. Abe *ACS Catal.* **2016**, *6*, 1134-1144.

[107] O. Tomita, R. Abe, B. Ohtani *Chem. Lett.* **2011**, *40*, 1405-1407.

[108] P. Riente, M. A. Pericàs *ChemSusChem*. **2015**.

[109] L. Buglioni, P. Riente, E. Palomares, M. A. Pericàs *Eur. J. Org. Chem.* **2017**, *2017*, 6986-6990.

[110] P. Riente, A. Matas Adams, J. Albero, E. Palomares, M. A. Pericàs *Angew. Chem. Int. Ed.* **2014**, *53*, 9613-9616.

[111] L. Zhang, W. Wang, J. Yang, Z. Chen, W. Zhang, L. Zhou, S. Liu *Appl. Catal., A*. **2006**, *308*, 105-110.

[112] B. Yuan, R. Chong, B. Zhang, J. Li, Y. Liu, C. Li *Chem. Commun.* **2014**, *50*, 15593-15596.

[113] Y.-Y. Liu, D. Liang, L.-Q. Lu, W.-J. Xiao *Chem. Commun.* **2019**, *55*, 4853-4856.

[114] W. Zhao, C. Liu, L. Cao, X. Yin, H. Xu, B. Zhang *RSC Adv.* **2013**, *3*, 22944-22948.

[115] C. Liu, Z. Chen, C. Su, X. Zhao, Q. Gao, G.-H. Ning, H. Zhu, W. Tang, K. Leng, W. Fu *Nat. Commun.* **2018**, *9*, 1-9.

[116] M. J. Enright, K. Gilbert-Bass, H. Sarsito, B. M. Cossairt *Chem. Mater.* **2019**, *31*, 2677-2682.

[117] A. D. Yoffe *Adv. Phys.* **2001**, *50*, 1-208.

[118] B. Saparov, D. B. Mitzi *Chem. Rev.* **2016**, *116*, 4558-4596.

[119] W.-B. Wu, Y.-C. Wong, Z.-K. Tan, J. Wu *Catal. Sci. Technol.* **2018**, *8*, 4257-4263.

[120] X. Wang, K. Maeda, A. Thomas, K. Takanabe, G. Xin, J. M. Carlsson, K. Domen, M. Antonietti *Nat. Mater.* **2009**, *8*, 76-80.

[121] X. Ye, Y. Cui, X. Wang *ChemSusChem*. **2014**, *7*, 738-742.

[122] Y. Zheng, L. Lin, X. Ye, F. Guo, X. Wang *Angew. Chem. Int. Ed.* **2014**, *53*, 11926-11930.

[123] X.-H. Li, X. Wang, M. Antonietti *Chem. Sci.* **2012**, *3*, 2170-2174.

[124] Z. J. Wang, S. Ghasimi, K. Landfester, K. A. I. Zhang *J. Mater. Chem. A*. **2014**, *2*, 18720-18724.

[125] G. Zhang, J. Zhang, M. Zhang, X. Wang *J. Mater. Chem.* **2012**, *22*, 8083-8091.

[126] J. Zhang, G. Zhang, X. Chen, S. Lin, L. Möhlmann, G. Dołęga, G. Lipner, M. Antonietti, S. Blechert, X.

Wang *Angew. Chem. Int. Ed.* **2012**, *51*, 3183-3187.

[127] Z. Lin, X. Wang *Angew. Chem. Int. Ed.* **2013**, *52*, 1735-1738.

[128] Y. Zhang, T. Mori, J. Ye, M. Antonietti *J. Am. Chem. Soc.* **2010**, *132*, 6294-6295.

[129] J. P. Paraknowitsch, J. Zhang, D. Su, A. Thomas, M. Antonietti *Adv. Mater.* **2010**, *22*, 87-92.

[130] Y. Wang, J. Zhang, X. Wang, M. Antonietti, H. Li *Angew. Chem. Int. Ed.* **2010**, *49*, 3356-3359.

[131] S. Yang, Y. Gong, J. Zhang, L. Zhan, L. Ma, Z. Fang, R. Vajtai, X. Wang, P. M. Ajayan *Adv. Mater.* **2013**, *25*, 2452-2456.

[132] X. Wang, K. Maeda, X. Chen, K. Takanabe, K. Domen, Y. Hou, X. Fu, M. Antonietti *J. Am. Chem. Soc.* **2009**, *131*, 1680-1681.

[133] J. Qin, S. Wang, H. Ren, Y. Hou, X. Wang *Appl. Catal., B*. **2015**, *179*, 1-8.

[134] R. Kuriki, K. Sekizawa, O. Ishitani, K. Maeda *Angew. Chem. Int. Ed.* **2015**, *54*, 2406-2409.

[135] Y. Chen, J. Zhang, M. Zhang, X. Wang *Chem. Sci.* **2013**, *4*, 3244-3248.

[136] F. Su, S. C. Mathew, L. Möhlmann, M. Antonietti, X. Wang, S. Blechert *Angew. Chem. Int. Ed.* **2011**, *50*, 657-660.

[137] P. Zhang, Y. Wang, H. Li, M. Antonietti *Green Chem.* **2012**, *14*, 1904-1908.

[138] X. Chen, J. Zhang, X. Fu, M. Antonietti, X. Wang *J. Am. Chem. Soc.* **2009**, *131*, 11658-11659.

[139] S. Dadashi-Silab, M. A. Tasdelen, B. Kiskan, X. Wang, M. Antonietti, Y. Yagci *Macromol. Chem. Phys.* **2014**, *215*, 675-681.

[140] B. Tian, X. Liu, L. A. Solovyov, Z. Liu, H. Yang, Z. Zhang, S. Xie, F. Zhang, B. Tu, C. Yu, O. Terasaki, D. Zhao *J. Am. Chem. Soc.* **2004**, *126*, 865-875.

[141] S. S. Kim, H. I. Lee, J. K. Shon, J. Y. Hur, M. S. Kang, S. S. Park, S. S. Kong, J. A. Yu, M. Seo, D. Li *Chem. Lett.* **2008**, *37*, 140-141.

[142] W. Yue, X. Xu, J. T. S. Irvine, P. S. Attidekou, C. Liu, H. He, D. Zhao, W. Zhou *Chem. Mater.* **2009**, *21*, 2540-2546.

[143] D. Chandra, A. Bhaumik *Microporous Mesoporous Mater.* **2008**, *112*, 533-541.

[144] P. V. Braun, P. Osenar, V. Tohver, S. B. Kennedy, S. I. Stupp *J. Am. Chem. Soc.* **1999**, *121*, 7302-7309.

[145] Z.-Y. Yuan, B.-L. Su *J. Mater. Chem.* **2006**, *16*, 663-677.

[146] Z.-Y. Yuan, T.-Z. Ren, B.-L. Su *Adv. Mater.* **2003**, *15*, 1462-1465.

[147] T.-Z. Ren, Z.-Y. Yuan, A. Azioune, J.-J. Pireaux, B.-L. Su *Langmuir*. **2006**, *22*, 3886-3894.

[148] B. Tian, X. Liu, B. Tu, C. Yu, J. Fan, L. Wang, S. Xie, G. D. Stucky, D. Zhao *Nat. Mater.* **2003**, *2*, 159-163.

[149] W. Dong, Y. Sun, C. W. Lee, W. Hua, X. Lu, Y. Shi, S. Zhang, J. Chen, D. Zhao *J. Am. Chem. Soc.* **2007**, *129*, 13894-13904.

[150] D. Grosso, G. J. de A.A. Soler-Illia, E. L. Crepaldi, B. Charleux, C. Sanchez *Adv. Funct. Mater.* **2003**, *13*, 37-42.

[151] M. C. Orilall, N. M. Abrams, J. Lee, F. J. DiSalvo, U. Wiesner *J. Am. Chem. Soc.* **2008**, *130*, 8882-8883.

[152] H. G. Yang, H. C. Zeng *The Journal of Physical Chemistry B*. **2004**, *108*, 3492-3495.

[153] Z. Liu, D. D. Sun, P. Guo, J. O. Leckie *Chemistry – A European Journal*. **2007**, *13*, 1851-1855.

[154] J. Yu, S. Liu, H. Yu *J. Catal.* **2007**, *249*, 59-66.

[155] P. V. Kamat *The Journal of Physical Chemistry C*. **2007**, *111*, 2834-2860.

[156] H. Zhang, G. Chen, D. W. Bahnemann *J. Mater. Chem.* **2009**, *19*, 5089-5121.

[157] Q. Zhang, N. Bao, X. Wang, X. Hu, X. Miao, M. Chaker, D. Ma *Sci. Rep.* **2016**, *6*, 38066.

[158] V. L. Colvin *Nat. Biotechnol.* **2003**, *21*, 1166-1170.

[159] A. Kahru, H.-C. Dubourguier, I. Blinova, A. Ivask, K. Kasemets *Sensors*. **2008**, *8*, 5153-5170.

[160] K. V. Hoecke, J. T. K. Quik, J. Mankiewicz-Boczek, K. A. C. D. Schamphelaere, A. Elsaesser, P. V. d. Meeren, C. Barnes, G. McKerr, C. V. Howard, D. V. D. Meent, K. Rydzyński, K. A. Dawson, A. Salvati, A. Lesniak, I. Lynch, G. Silversmit, B. D. Samber, L. Vincze, C. R. Janssen *Environ. Sci. Technol.* **2009**, *43*, 4537-4546.

[161] A. Simon-Deckers, S. Loo, M. Mayne-L'hermite, N. Herlin-Boime, N. Menguy, C. Reynaud, B. Gouget, M. Carrière *Environ. Sci. Technol.* **2009**, *43*, 8423-8429.

[162] G. K. Mor, O. K. Varghese, M. Paulose, K. Shankar, C. A. Grimes *Sol. Energy Mater. Sol. Cells*. **2006**, *90*, 2011-2075.

[163] J. Byun, K. A. Zhang *Mater. Horiz.* **2020**, *7*, 15-31.

[164] D. Taylor, S. J. Dalgarno, Z. Xu, F. Vilela *Chem. Soc. Rev.* **2020**, *49*, 3981-4042.

[165] J.-S. M. Lee, A. I. Cooper *Chem. Rev.* **2020**, *120*, 2171-2214.

[166] Y. Xu, S. Jin, H. Xu, A. Nagai, D. Jiang *Chem. Soc. Rev.* **2013**, *42*, 8012-8031.

[167] F. Vilela, K. Zhang, M. Antonietti *Energy Environ. Sci.* **2012**, *5*, 7819-7832.

[168] K. Zhang, D. Kopetzki, P. H. Seeberger, M. Antonietti, F. Vilela *Angew. Chem. Int. Ed.* **2013**, *52*, 1432-1436.

[169] Z. J. Wang, K. Landfester, K. A. I. Zhang *Polym. Chem.* **2014**, *5*, 3559-3562.

[170] Z. J. Wang, S. Ghasimi, K. Landfester, K. A. I. Zhang *Chem. Commun.* **2014**, *50*, 8177-8180.

[171] Z. J. Wang, S. Ghasimi, K. Landfester, K. A. I. Zhang *Adv. Mater.* **2015**, *27*, 6265-6270.

[172] S. Bi, Z.-A. Lan, S. Paasch, W. Zhang, Y. He, C. Zhang, F. Liu, D. Wu, X. Zhuang, E. Brunner, X. Wang, F. Zhang *Adv. Funct. Mater.* **2017**, *27*, 1703146.

[173] R. S. Sprick, J.-X. Jiang, B. Bonillo, S. Ren, T. Ratvijitvech, P. Guiglion, M. A. Zwijnenburg, D. J. Adams, A. I. Cooper *J. Am. Chem. Soc.* **2015**, *137*, 3265-3270.

[174] V. S. Vyas, V. W.-h. Lau, B. V. Lotsch *Chem. Mater.* **2016**, *28*, 5191-5204.

[175] K. Wang, L.-M. Yang, X. Wang, L. Guo, G. Cheng, C. Zhang, S. Jin, B. Tan, A. Cooper *Angew. Chem. Int. Ed.* **2017**, *56*, 14149-14153.

[176] C. Yang, B. C. Ma, L. Zhang, S. Lin, S. Ghasimi, K. Landfester, K. A. I. Zhang, X. Wang *Angew. Chem. Int. Ed.* **2016**, *55*, 9202-9206.

[177] L. Wang, Y. Wan, Y. Ding, Y. Niu, Y. Xiong, X. Wu, H. Xu *Nanoscale*. **2017**, *9*, 4090-4096.

[178] L. Wang, Y. Wan, Y. Ding, S. Wu, Y. Zhang, X. Zhang, G. Zhang, Y. Xiong, X. Wu, J. Yang, H. Xu *Adv. Mater.* **2017**, *29*, 1702428.

[179] W. Huang, Z. J. Wang, B. C. Ma, S. Ghasimi, D. Gehrig, F. Laquai, K. Landfester, K. A. I. Zhang *J. Mater. Chem. A*. **2016**, *4*, 7555-7559.

[180] R. Li, B. C. Ma, W. Huang, L. Wang, D. Wang, H. Lu, K. Landfester, K. A. I. Zhang *ACS Catal.* **2017**, *7*, 3097-3101.

[181] S. Ghasimi, S. A. Bretschneider, W. Huang, K. Landfester, K. A. I. Zhang *Adv. Sci.* **2017**, *4*, 1700101.

[182] W. Huang, B. C. Ma, D. Wang, Z. J. Wang, R. Li, L. Wang, K. Landfester, K. A. I. Zhang *J. Mater. Chem. A*. **2017**, *5*, 3792-3797.

[183] J.-X. Jiang, F. Su, A. Trewin, C. D. Wood, N. L. Campbell, H. Niu, C. Dickinson, A. Y. Ganin, M. J. Rosseinsky, Y. Z. Khimyak, A. I. Cooper *Angew. Chem. Int. Ed.* **2007**, *46*, 8574-8578.

[184] L. Sun, Z. Liang, J. Yu, R. Xu *Polym. Chem.* **2013**, *4*, 1932-1938.

[185] J. Schmidt, M. Werner, A. Thomas *Macromolecules*. **2009**, *42*, 4426-4429.

[186] A. Li, H.-X. Sun, D.-Z. Tan, W.-J. Fan, S.-H. Wen, X.-J. Qing, G.-X. Li, S.-Y. Li, W.-Q. Deng *Energy Environ. Sci.* **2011**, *4*, 2062-2065.

[187] G. Lu, H. Yang, Y. Zhu, T. Huggins, Z. J. Ren, Z. Liu, W. Zhang *J. Mater. Chem. A*. **2015**, *3*, 4954-4959.

[188] V. Senkovskyy, I. Senkovska, A. Kiriy *ACS Macro Lett.* **2012**, *1*, 494-498.

[189] J. Luo, X. Zhang, J. Zhang *ACS Catal.* **2015**, *5*, 2250-2254.

[190] J. Schmidt, J. Weber, J. D. Epping, M. Antonietti, A. Thomas *Adv. Mater.* **2009**, *21*, 702-705.

[191] M. G. Schwab, M. Hamburger, X. Feng, J. Shu, H. W. Spiess, X. Wang, M. Antonietti, K. Müllen *Chem. Commun.* **2010**, *46*, 8932-8934.

[192] L. Stegbauer, K. Schwinghammer, B. V. Lotsch *Chem. Sci.* **2014**, *5*, 2789-2793.

[193] V. S. Vyas, F. Haase, L. Stegbauer, G. Savasci, F. Podjaski, C. Ochsenfeld, B. V. Lotsch *Nat. Commun.* **2015**, *6*, 8508.

[194] Z. J. Wang, R. Li, K. Landfester, K. A. I. Zhang *Polymer*. **2017**, *126*, 291-295.

[195] S. Chu, C. Wang, Y. Yang, Y. Wang, Z. Zou *RSC Adv.* **2014**, *4*, 57153-57158.

[196] Y. Kou, Y. Xu, Z. Guo, D. Jiang *Angew. Chem. Int. Ed.* **2011**, *50*, 8753-8757.

[197] C. W. Kang, D. H. Lee, Y. J. Shin, J. Choi, Y.-J. Ko, S. M. Lee, H. J. Kim, K. C. Ko, S. U. Son *J. Mater. Chem. A*. **2018**, *6*, 17312-17317.

[198] P. Kuhn, M. Antonietti, A. Thomas *Angew. Chem. Int. Ed.* **2008**, *47*, 3450-3453.

[199] L. Hao, J. Ning, B. Luo, B. Wang, Y. Zhang, Z. Tang, J. Yang, A. Thomas, L. Zhi *J. Am. Chem. Soc.* **2015**, *137*, 219-225.

[200] K. Sakaushi, E. Hosono, G. Nickerl, T. Gemming, H. Zhou, S. Kaskel, J. Eckert *Nat. Commun.* **2013**, *4*, 1-7.

[201] A. Bhunia, I. Boldog, A. Möller, C. Janiak *J. Mater. Chem. A*. **2013**, *1*, 14990-14999.

[202] P. Katekomol, J. Roeser, M. Bojdys, J. Weber, A. Thomas *Chem. Mater.* **2013**, *25*, 1542-1548.

[203] X. Zhu, C. Tian, G. M. Veith, C. W. Abney, J. r. m. Dehaudt, S. Dai *J. Am. Chem. Soc.* **2016**, *138*, 11497-11500.

[204] J. Artz, R. Palkovits *ChemSusChem*. **2015**, *8*, 3832-3838.

[205] S. N. Talapaneni, T. H. Hwang, S. H. Je, O. Buyukcakir, J. W. Choi, A. Coskun *Angew. Chem. Int. Ed.* **2016**, *55*, 3106-3111.

[206] K. Kamiya, R. Kamai, K. Hashimoto, S. Nakanishi *Nat. Commun.* **2014**, *5*, 5040.

[207] J. Roeser, K. Kailasam, A. Thomas *ChemSusChem*. **2012**, *5*, 1793-1799.

[208] X. Jiang, P. Wang, J. Zhao *J. Mater. Chem. A*. **2015**, *3*, 7750-7758.

[209] K. Sakaushi, G. Nickerl, H. C. Kandpal, L. Cano-Cortés, T. Gemming, J. r. Eckert, S. Kaskel, J. van den

Brink *The Journal of Physical Chemistry Letters*. **2013**, *4*, 2977-2981.

[210] P. Kuhn, A. Forget, J. Hartmann, A. Thomas, M. Antonietti *Adv. Mater.* **2009**, *21*, 897-901.

[211] K. Schwinghammer, S. Hug, M. B. Mesch, J. Senker, B. V. Lotsch *Energy Environ. Sci.* **2015**, *8*, 3345-3353.

[212] X. Zhu, C. Tian, S. M. Mahurin, S.-H. Chai, C. Wang, S. Brown, G. M. Veith, H. Luo, H. Liu, S. Dai *J. Am. Chem. Soc.* **2012**, *134*, 10478-10484.

[213] W. Huang, B. C. Ma, H. Lu, R. Li, L. Wang, K. Landfester, K. A. Zhang *ACS Catal.* **2017**, *7*, 5438-5442.

[214] S. Ren, M. J. Bojdys, R. Dawson, A. Laybourn, Y. Z. Khimyak, D. J. Adams, A. I. Cooper *Adv. Mater.* **2012**, *24*, 2357-2361.

[215] F. J. Uribe-Romo, J. R. Hunt, H. Furukawa, C. Klock, M. O'Keeffe, O. M. Yaghi *J. Am. Chem. Soc.* **2009**, *131*, 4570-4571.

[216] A. P. Côté, A. I. Benin, N. W. Ockwig, M. O'Keeffe, A. J. Matzger, O. M. Yaghi *Science*. **2005**, *310*, 1166-1170.

[217] E. Jin, M. Asada, Q. Xu, S. Dalapati, M. A. Addicoat, M. A. Brady, H. Xu, T. Nakamura, T. Heine, Q. Chen *Science*. **2017**, *357*, 673-676.

[218] K. Geng, T. He, R. Liu, S. Dalapati, K. T. Tan, Z. Li, S. Tao, Y. Gong, Q. Jiang, D. Jiang *Chem. Rev.* **2020**, *120*, 8814-8933.

[219] H. Wang, H. Wang, Z. Wang, L. Tang, G. Zeng, P. Xu, M. Chen, T. Xiong, C. Zhou, X. Li *Chem. Soc. Rev.* **2020**, *49*, 4135-4165.

[220] W. K. Haug, E. M. Moscarello, E. R. Wolfson, P. L. McGrier *Chem. Soc. Rev.* **2020**, *49*, 839-864.

[221] D. Zhou, X. Tan, H. Wu, L. Tian, M. Li *Angew. Chem. Int. Ed.* **2019**, *58*, 1376-1381.

[222] X.-T. Li, J. Zou, T.-H. Wang, H.-C. Ma, G.-J. Chen, Y.-B. Dong *J. Am. Chem. Soc.* **2020**, *142*, 6521-6526.

[223] A. P. Côté, A. I. Benin, N. W. Ockwig, M. Keeffe, A. J. Matzger, O. M. Yaghi *Science*. **2005**, *310*, 1166.

[224] H.-C. J. Zhou, S. Kitagawa *Chem. Soc. Rev.* **2014**, *43*, 5415-5418.

[225] H. Furukawa, N. Ko, Y. B. Go, N. Aratani, S. B. Choi, E. Choi, A. Ö. Yazaydin, R. Q. Snurr, M. O'Keeffe, J. Kim, O. M. Yaghi *Science*. **2010**, *329*, 424-428.

[226] T. Devic, C. Serre *Chem. Soc. Rev.* **2014**, *43*, 6097-6115.

[227] E. M. Dias, C. Petit *J. Mater. Chem. A*. **2015**, *3*, 22484-22506.

[228] J. Bedia, V. Muelas-Ramos, M. Peñas-Garzón, A. Gómez-Avilés, J. J. Rodríguez, C. Belver *Catalysts*. **2019**, *9*, 52.

[229] C.-C. Wang, X.-D. Du, J. Li, X.-X. Guo, P. Wang, J. Zhang *Appl. Catal., B*. **2016**, *193*, 198-216.

[230] J.-D. Xiao, D. Li, H.-L. Jiang *Scientia Sinica Chimica*. **2018**, *48*, 1058-1075.

[231] J.-L. Wang, C. Wang, W. Lin *ACS Catal.* **2012**, *2*, 2630-2640.

[232] J. He, Y. Zhang, J. He, X. Zeng, X. Hou, Z. Long *Chem. Commun.* **2018**, *54*, 8610-8613.

[233] M. Nasalevich, M. Van der Veen, F. Kapteijn, J. Gascon *CrystEngComm*. **2014**, *16*, 4919-4926.

[234] D. Wang, M. Wang, Z. Li *ACS Catal.* **2015**, *5*, 6852-6857.

[235] C. Wang, X. Liu, N. K. Demir, J. P. Chen, K. Li *Chem. Soc. Rev.* **2016**, *45*, 5107-5134.

[236] M. N. Chong, B. Jin, C. W. Chow, C. Saint *Water Res.* **2010**, *44*, 2997-3027.

[237] P. Li, J. Li, X. Feng, J. Li, Y. Hao, J. Zhang, H. Wang, A. Yin, J. Zhou, X. Ma *Nat. Commun.* **2019**, *10*, 1-

10.
[238] Y. Shi, A.-F. Yang, C.-S. Cao, B. Zhao *Coord. Chem. Rev.* **2019**, *390*, 50-75.
[239] X. Ma, L. Wang, Q. Zhang, H.-L. Jiang *Angew. Chem. Int. Ed.* **2019**, *58*, 12175-12179.
[240] C.-C. Wang, Y.-Q. Zhang, J. Li, P. Wang *J. Mol. Struct.* **2015**, *1083*, 127-136.
[241] X. Yu, L. Wang, S. M. Cohen *CrystEngComm*. **2017**, *19*, 4126-4136.
[242] S.-N. Zhao, G. Wang, D. Poelman, P. Van Der Voort *Molecules*. **2018**, *23*, 2947.
[243] H. Liu, C. Xu, D. Li, H.-L. Jiang *Angew. Chem. Int. Ed.* **2018**, *57*, 5379-5383.
[244] C.-C. Wang, J.-R. Li, X.-L. Lv, Y.-Q. Zhang, G. Guo *Energy Environ. Sci.* **2014**, *7*, 2831-2867.
[245] J. Qiu, X. Zhang, Y. Feng, X. Zhang, H. Wang, J. Yao *Appl. Catal., B*. **2018**, *231*, 317-342.
[246] D. Wang, Z. Li *Res. Chem. Intermed.* **2017**, *43*, 5169-5186.
[247] J.-D. Xiao, H.-L. Jiang *Acc. Chem. Res.* **2018**, *52*, 356-366.
[248] Z. Zhang, X. Li, B. Liu, Q. Zhao, G. Chen *RSC Adv.* **2016**, *6*, 4289-4295.
[249] S. R. Thakare, S. M. Ramteke *Catal. Commun.* **2017**, *102*, 21-25.
[250] F. Hoffmann, M. Cornelius, J. Morell, M. Fröba *Angew. Chem. Int. Ed.* **2006**, *45*, 3216-3251.
[251] S. Inagaki, S. Guan, Y. Fukushima, T. Ohsuna, O. Terasaki *J. Am. Chem. Soc.* **1999**, *121*, 9611-9614.
[252] B. J. Melde, B. T. Holland, C. F. Blanford, A. Stein *Chem. Mater.* **1999**, *11*, 3302-3308.
[253] Y. Xia, W. Wang, R. Mokaya *J. Am. Chem. Soc.* **2005**, *127*, 790-798.
[254] Y. Xia, R. Mokaya *The Journal of Physical Chemistry B*. **2006**, *110*, 3889-3894.
[255] C. Yoshina-Ishii, T. Asefa, N. Coombs, M. J. MacLachlan, G. A. Ozin *Chem. Commun.* **1999**, 2539-2540.
[256] Y. Goto, S. Inagaki *Microporous Mesoporous Mater.* **2006**, *89*, 103-108.
[257] S. Inagaki, S. Guan, T. Ohsuna, O. Terasaki *Nature*. **2002**, *416*, 304-307.
[258] K. Landskron, B. D. Hatton, D. D. Perovic, G. A. Ozin *Science*. **2003**, *302*, 266-269.
[259] G. Temtsin, T. Asefa, S. Bittner, G. A. Ozin *J. Mater. Chem.* **2001**, *11*, 3202-3206.
[260] W. J. Hunks, G. A. Ozin *Chem. Mater.* **2004**, *16*, 5465-5472.
[261] M. C. Burleigh, M. A. Markowitz, M. S. Spector, B. P. Gaber *Environ. Sci. Technol.* **2002**, *36*, 2515-2518.
[262] C. Li, J. Yang, X. Shi, J. Liu, Q. Yang *Microporous Mesoporous Mater.* **2007**, *98*, 220-226.
[263] M. Cornelius, F. Hoffmann, M. Fröba *Chem. Mater.* **2005**, *17*, 6674-6678.
[264] N. Mizoshita, Y. Goto, T. Tani, S. Inagaki *Adv. Funct. Mater.* **2008**, *18*, 3699-3705.
[265] M. P. Kapoor, Q. Yang, S. Inagaki *J. Am. Chem. Soc.* **2002**, *124*, 15176-15177.
[266] Y. Goto, N. Mizoshita, O. Ohtani, T. Okada, T. Shimada, T. Tani, S. Inagaki *Chem. Mater.* **2008**, *20*, 4495-4498.
[267] Y. Goto, K. Nakajima, N. Mizoshita, M. Suda, N. Tanaka, T. Hasegawa, T. Shimada, T. Tani, S. Inagaki *Microporous Mesoporous Mater.* **2009**, *117*, 535-540.
[268] N. Mizoshita, Y. Goto, M. P. Kapoor, T. Shimada, T. Tani, S. Inagaki *Chemistry – A European Journal*. **2009**, *15*, 219-226.
[269] M. Alvaro, M. Benitez, D. Das, H. Garcia, E. Peris *Chem. Mater.* **2005**, *17*, 4958-4964.
[270] M. Cornelius, F. Hoffmann, B. Ufer, P. Behrens, M. Fröba *J. Mater. Chem.* **2008**, *18*, 2587-2592.
[271] D. Chandra, T. Yokoi, T. Tatsumi, A. Bhaumik *Chem. Mater.* **2007**, *19*, 5347-5354.
[272] H. Peng, J. Tang, L. Yang, J. Pang, H. S. Ashbaugh, C. J. Brinker, Z. Yang, Y. Lu *J. Am. Chem. Soc.* **2006**,

128, 5304-5305.

[273] R. J. P. Corriu, A. Mehdi, C. Reyé, C. Thieuleux *Chem. Commun.* **2002**, 1382-1383.

[274] O. Olkhovyk, M. Jaroniec *J. Am. Chem. Soc.* **2005**, *127*, 60-61.

[275] W.-H. Zhang, X. Zhang, L. Zhang, F. Schroeder, P. Harish, S. Hermes, J. Shi, R. A. Fischer *J. Mater. Chem.* **2007**, *17*, 4320-4326.

[276] O. Olkhovyk, S. Pikus, M. Jaroniec *J. Mater. Chem.* **2005**, *15*, 1517-1519.

[277] E.-B. Cho, D. Kim, M. Jaroniec *Langmuir*. **2009**, *25*, 13258-13263.

[278] Y. Maegawa, Y. Goto, S. Inagaki, T. Shimada *Tetrahedron Lett.* **2006**, *47*, 6957-6960.

[279] H. Takeda, Y. Goto, Y. Maegawa, T. Ohsuna, T. Tani, K. Matsumoto, T. Shimada, S. Inagaki *Chem. Commun.* **2009**, 6032-6034.

[280] M. Waki, N. Mizoshita, T. Ohsuna, T. Tani, S. Inagaki *Chem. Commun.* **2010**, *46*, 8163-8165.

[281] M. Waki, N. Mizoshita, T. Tani, S. Inagaki *Angew. Chem. Int. Ed.* **2011**, *50*, 11667-11671.

[282] M. Álvaro, B. Ferrer, V. Fornés, H. García *Chem. Commun.* **2001**, 2546-2547.

[283] M. Alvaro, B. Ferrer, H. García, F. Rey *Chem. Commun.* **2002**, 2012-2013.

[284] K. J. Balkus, T. J. Pisklak, G. Hundt, J. Sibert, Y. Zhang *Microporous Mesoporous Mater.* **2008**, *112*, 1-13.

[285] N. Mizoshita, K.-i. Yamanaka, T. Shimada, T. Tani, S. Inagaki *Chem. Commun.* **2010**, *46*, 9235-9237.

[286] B. Lee, H.-J. Im, H. Luo, E. W. Hagaman, S. Dai *Langmuir*. **2005**, *21*, 5372-5376.

[287] B. Karimi, D. Elhamifar, J. H. Clark, A. J. Hunt *Chem. Eur. J.* **2010**, *16*, 8047-8053.

[288] T. P. Nguyen, P. Hesemann, P. Gaveau, J. J. E. Moreau *J. Mater. Chem.* **2009**, *19*, 4164-4171.

[289] T. P. Nguyen, P. Hesemann, J. J. E. Moreau *Microporous Mesoporous Mater.* **2011**, *142*, 292-300.

[290] G. Morales, G. Athens, B. F. Chmelka, R. van Grieken, J. A. Melero *J. Catal.* **2008**, *254*, 205-217.

[291] M. P. Kapoor, Y. Kasama, T. Yokoyama, M. Yanagi, S. Inagaki, H. Nanbu, L. R. Juneja *J. Mater. Chem.* **2006**, *16*, 4714-4722.

[292] M. Ohashi, M. P. Kapoor, S. Inagaki *Chem. Commun.* **2008**, 841-843.

[293] S. El Hankari, B. Motos-Pérez, P. Hesemann, A. Bouhaouss, J. J. E. Moreau *J. Mater. Chem.* **2011**, *21*, 6948-6955.

[294] M. P. Kapoor, A. Bhaumik, S. Inagaki, K. Kuraoka, T. Yazawa *J. Mater. Chem.* **2002**, *12*, 3078-3083.

[295] J. A. Melero, J. Iglesias, J. M. Arsuaga, J. Sainz-Pardo, P. de Frutos, S. Blazquez *J. Mater. Chem.* **2007**, *17*, 377-385.

[296] S. Sisodiya, S. Shylesh, A. Singh *Catal. Commun.* **2011**, *12*, 629-633.

[297] S. Shylesh, A. P. Singh *Microporous Mesoporous Mater.* **2006**, *94*, 127-138.

[298] A. Feliczak, K. Walczak, A. Wawrzyńczak, I. Nowak *Catal. Today*. **2009**, *140*, 23-29.

[299] S. Shylesh, P. P. Samuel, A. Singh *Microporous Mesoporous Mater.* **2007**, *100*, 250-258.

[300] S. Shylesh, A. Wagener, A. Seifert, S. Ernst, W. R. Thiel *Angew. Chem. Int. Ed.* **2010**, *49*, 184-187.

[301] M. Sasidharan, S. Fujita, M. Ohashi, Y. Goto, K. Nakashima, S. Inagaki *Chem. Commun.* **2011**, *47*, 10422-10424.

[302] A. Kuschel, M. Drescher, T. Kuschel, S. Polarz *Chem. Mater.* **2010**, *22*, 1472-1482.

[303] X. Li, Y. Yang, Q. Yang *J. Mater. Chem. A*. **2013**, *1*, 1525-1535.

[304] B. Xiao, J. Zhao, X. Liu, P. Wang, Q. Yang *Microporous Mesoporous Mater.* **2014**, *199*, 1-6.

[305] A. Walcarius, L. Mercier *J. Mater. Chem.* **2010**, *20*, 4478-4511.

[306] P. K. Jal, S. Patel, B. K. Mishra *Talanta*. **2004**, *62*, 1005-1028.

[307] M. Burleigh, S. Dai, E. Hagaman, J. Lin *Chem. Mater.* **2001**, *13*, 2537-2546.

[308] A. Comotti, S. Bracco, P. Valsesia, L. Ferretti, P. Sozzani *J. Am. Chem. Soc.* **2007**, *129*, 8566-8576.

[309] C. P. Moura, C. B. Vidal, A. L. Barros, L. S. Costa, L. C. Vasconcellos, F. S. Dias, R. F. Nascimento *J. Colloid Interface Sci.* **2011**, *363*, 626-634.

[310] M. P. Kapoor, S. Inagaki *Chem. Lett.* **2004**, *33*, 88-89.

[311] V. Rebbin, M. Jakubowski, S. Pötz, M. Fröba *Microporous Mesoporous Mater.* **2004**, *72*, 99-104.

[312] G. Zhu, D. Jiang, Q. Yang, J. Yang, C. Li *J. Chromatogr. A*. **2007**, *1149*, 219-227.

[313] S. Qiao, H. Djojoputro, Q. Hu, G. Lu *Prog. Solid State Chem.* **2006**, *34*, 249-256.

[314] M. Park, S. S. Park, M. Selvaraj, D. Zhao, C.-S. Ha *Microporous Mesoporous Mater.* **2009**, *124*, 76-83.

[315] S. Hudson, J. Cooney, B. Hodnett, E. Magner *Chem. Mater.* **2007**, *19*, 2049-2055.

[316] N. Lin, L. Gao, Z. Chen, J. H. Zhu *New J. Chem.* **2011**, *35*, 1867-1875.

[317] M. M. Wan, L. Gao, Z. Chen, Y. K. Wang, Y. Wang, J. H. Zhu *Microporous Mesoporous Mater.* **2012**, *155*, 24-33.

[318] J. H. Shin, S. S. Park, M. Selvaraj, C.-S. Ha *J. Porous Mater.* **2012**, *19*, 29-35.

[319] M. S. Moorthy, S.-S. Park, D. Fuping, S.-H. Hong, M. Selvaraj, C.-S. Ha *J. Mater. Chem.* **2012**, *22*, 9100-9108.

[320] T. Hudlicky, J. W. Reed *Chem. Soc. Rev.* **2009**, *38*, 3117-3132.

[321] N. J. Turner, L. Humphreys, Biocatalysis in organic synthesis: The retrosynthesis approach, Royal Society of Chemistry, **2018**.

[322] L. Hilterhaus, A. Liese, U. Kettling, G. Antranikian, Applied biocatalysis: from fundamental science to industrial applications, John Wiley & Sons, **2016**.

[323] F. Schwizer, Y. Okamoto, T. Heinisch, Y. Gu, M. M. Pellizzoni, V. Lebrun, R. Reuter, V. Kohler, J. C. Lewis, T. R. Ward *Chem. Rev.* **2018**, *118*, 142-231.

[324] R. A. Sheldon, J. M. Woodley *Chem. Rev.* **2018**, *118*, 801-838.

[325] U. T. Bornscheuer, G. Huisman, R. Kazlauskas, S. Lutz, J. Moore, K. Robins *Nature*. **2012**, *485*, 185-194.

[326] F. H. Arnold *Acc. Chem. Res.* **1998**, *31*, 125-131.

[327] A. Schmid, J. Dordick, B. Hauer, A. Kiener, M. Wubbolts, B. Witholt *nature*. **2001**, *409*, 258-268.

[328] J. Tao, J.-H. Xu *Curr. Opin. Chem. Biol.* **2009**, *13*, 43-50.

[329] J.-M. Choi, S.-S. Han, H.-S. Kim *Biotechnol. Adv.* **2015**, *33*, 1443-1454.

[330] S. A. Kelly, S. Pohle, S. Wharry, S. Mix, C. C. Allen, T. S. Moody, B. F. Gilmore *Chem. Rev.* **2018**, *118*, 349-367.

[331] G. De Gonzalo, P. D. de María, Biocatalysis: an industrial perspective, Royal Society of Chemistry, **2017**.

[332] C. R. Stephenson, T. P. Yoon, D. W. MacMillan, Visible light photocatalysis in organic chemistry, John Wiley & Sons, **2018**.

[333] L. Marzo, S. K. Pagire, O. Reiser, B. König *Angew. Chem. Int. Ed.* **2018**, *57*, 10034-10072.

[334] A. Savateev, M. Antonietti *ACS Catal.* **2018**, *8*, 9790-9808.

[335] N. A. Romero, D. A. Nicewicz *Chem. Rev.* **2016**, *116*, 10075-10166.

[336] C. m. Michelin, N. Hoffmann *ACS Catal.* **2018**, *8*, 12046-12055.

[337] D. Ravelli, D. Dondi, M. Fagnoni, A. Albini *Chem. Soc. Rev.* **2009**, *38*, 1999-2011.

[338] J. Xuan, W. J. Xiao *Angew. Chem. Int. Ed.* **2012**, *51*, 6828-6838.

[339] K. L. Skubi, T. R. Blum, T. P. Yoon *Chem. Rev.* **2016**, *116*, 10035-10074.

[340] S. H. Lee, D. S. Choi, S. K. Kuk, C. B. Park *Angew. Chem. Int. Ed.* **2018**, *57*, 7958-7985.

[341] M. A. Emmanuel, N. R. Greenberg, D. G. Oblinsky, T. K. Hyster *Nature*. **2016**, *540*, 414-417.

[342] T. Lazarides, I. V. Sazanovich, A. J. Simaan, M. C. Kafentzi, M. Delor, Y. Mekmouche, B. Faure, M. Réglier, J. A. Weinstein, A. G. Coutsolelos *J. Am. Chem. Soc.* **2013**, *135*, 3095-3103.

[343] S. D. M. Islam, T. Konishi, M. Fujitsuka, O. Ito, Y. Nakamura, Y. Usui *Photochem. Photobiol.* **2000**, *71*, 675-680.

[344] S. H. Lee, D. S. Choi, M. Pesic, Y. W. Lee, C. E. Paul, F. Hollmann, C. B. Park *Angewandte Chemie*. **2017**, *129*, 8807-8811.

[345] J. A. Maciá Agulló, A. Corma Canós, H. García Gómez *Chemistry-a European Journal*. **2015**, *21*, 10940-10959.

[346] J. Kim, C. B. Park *Curr. Opin. Chem. Biol.* **2019**, *49*, 122-129.

[347] W. Zhang, F. Hollmann *Chem. Commun.* **2018**, *54*, 7281-7289.

[348] Y. Wang, J. Sun, H. Zhang, Z. Zhao, W. Liu *Catal. Sci. Technol.* **2018**, *8*, 2578-2587.

[349] D. Adam, L. Bösche, L. Castañeda-Losada, M. Winkler, U. P. Apfel, T. Happe *ChemSusChem*. **2017**, *10*, 894-902.

[350] C. Tapia, S. Shleev, J. C. Conesa, A. L. De Lacey, M. Pita *ACS Catal.* **2017**, *7*, 4881-4889.

[351] M. K. Peers, H. S. Toogood, D. J. Heyes, D. Mansell, B. J. Coe, N. S. Scrutton *Catal. Sci. Technol.* **2016**, *6*, 169-177.

[352] M. Mifsud, S. Gargiulo, S. Iborra, I. W. Arends, F. Hollmann, A. Corma *Nat. Commun.* **2014**, *5*, 1-6.

[353] S. Choudhury, J.-O. Baeg, N.-J. Park, R. K. Yadav *Green Chem.* **2014**, *16*, 4389-4400.

[354] K. A. Brown, M. B. Wilker, M. Boehm, H. Hamby, G. Dukovic, P. W. King *ACS Catal.* **2016**, *6*, 2201-2204.

[355] J. Kim, S. H. Lee, F. Tieves, D. S. Choi, F. Hollmann, C. E. Paul, C. B. Park *Angew. Chem. Int. Ed.* **2018**, *57*, 13825-13828.

[356] W. Zhang, E. Fernández-Fueyo, Y. Ni, M. Van Schie, J. Gacs, R. Renirie, R. Wever, F. G. Mutti, D. Rother, M. Alcalde *Nat. Catal.* **2018**, *1*, 55-62.

[357] S. b. J.-P. Willot, E. Fernández-Fueyo, F. Tieves, M. Pesic, M. Alcalde, I. W. Arends, C. B. Park, F. Hollmann *ACS Catal.* **2018**, *9*, 890-894.

[358] S. Schmidt, K. Castiglione, R. Kourist *Chem. Eur. J.* **2018**, *24*, 1755-1768.

[359] N. Scalacci, G. W. Black, G. Mattedi, N. L. Brown, N. J. Turner, D. Castagnolo *ACS Catal.* **2017**, *7*, 1295-1300.

[360] V. Erdmann, B. R. Lichman, J. Zhao, R. C. Simon, W. Kroutil, J. M. Ward, H. C. Hailes, D. Rother *Angew. Chem. Int. Ed.* **2017**, *56*, 12503-12507.

[361] T. Classen, M. Korpak, M. Schölzel, J. r. Pietruszka *ACS Catal.* **2014**, *4*, 1321-1331.

[362] Z. C. Litman, Y. Wang, H. Zhao, J. F. Hartwig *Nature*. **2018**, *560*, 355-359.

[363] W. Zhang, E. F. Fueyo, F. Hollmann, L. L. Martin, M. Pesic, R. Wardenga, M. Höhne, S. Schmidt *Eur. J. Org. Chem.* **2019**, *2019*, 80.

[364] K. Lauder, A. Toscani, Y. Qi, J. Lim, S. J. Charnock, K. Korah, D. Castagnolo *Angew. Chem. Int. Ed.* **2018**, *57*, 5803-5807.

[365] X. Guo, Y. Okamoto, M. R. Schreier, T. R. Ward, O. S. Wenger *Chem. Sci.* **2018**, *9*, 5052-5056.

[366] K. Köninger, Á. Gómez Baraibar, C. Mügge, C. E. Paul, F. Hollmann, M. M. Nowaczyk, R. Kourist *Angew. Chem. Int. Ed.* **2016**, *55*, 5582-5585.

[367] R. E. Rasmussen, S. M. Erstad, E. M. Ramos-Martinez, L. Fimognari, A. J. De Porcellinis, Y. Sakuragi *Microb. Cell Fact.* **2016**, *15*, 1-11.

[368] A. Hoschek, B. Bühler, A. Schmid *Angew. Chem. Int. Ed.* **2017**, *56*, 15146-15149.

[369] X. Ma, H. Liang, C. Ning, S. Deng, E. Su *J. Biotechnol.* **2017**, *259*, 120-125.

[370] M. Heining, R. Buchholz *Biotechnol. J.* **2015**, *10*, 1131-1137.

[371] A. Sutor, M. Heining, C. Lindenberger, R. Buchholz *IEEE Trans. Magn.* **2014**, *50*, 1-4.

[372] H. E. Bonfield, J. D. Williams, W. X. Ooi, S. G. Leach, W. J. Kerr, L. J. Edwards *ChemPhotoChem*. **2018**, *2*, 938-944.

[373] M. Heining, A. Sutor, S. Stute, C. Lindenberger, R. Buchholz *J. Appl. Phycol.* **2015**, *27*, 59-66.

[374] C. C. Le, M. K. Wismer, Z.-C. Shi, R. Zhang, D. V. Conway, G. Li, P. Vachal, I. W. Davies, D. W. MacMillan *ACS Cent. Sci.* **2017**, *3*, 647-653.

[375] D. Lenhart, A. Bauer, A. Pöthig, T. Bach *Chem. Eur. J.* **2016**, *22*, 6519-6523.

[376] D. Rackl, V. Kais, P. Kreitmeier, O. Reiser *Beilstein J. Org. Chem.* **2014**, *10*, 2157-2165.

[377] H. Borchert, Solar cells based on colloidal nanocrystals, Springer, **2014**.

[378] N. Elgrishi, K. J. Rountree, B. D. McCarthy, E. S. Rountree, T. T. Eisenhart, J. L. Dempsey *J. Chem. Educ.* **2018**, *95*, 197-206.

[379] J.-L. Bredas *Mater. Horiz.* **2014**, *1*, 17-19.

[380] P. Rieger, Electron spin resonance: analysis and interpretation, Royal Society of Chemistry, **2007**.

[381] K. Nakagawa, S. Eaton, G. Eaton *Appl. Radiat. Isot.* **1993**, *44*, 73-76.

[382] J. A. Weil, J. R. Bolton, Electron paramagnetic resonance: elementary theory and practical applications, John Wiley & Sons, **2007**.

[383] Z. Wang, W. Ma, C. Chen, H. Ji, J. Zhao *Chemical Engineering Journal*. **2011**, *170*, 353-362.

[384] S. Brunauer, P. H. Emmett, E. Teller *J. Am. Chem. Soc.* **1938**, *60*, 309-319.

[385] S. Yurdakal, C. Garlisi, L. Özcan, M. Bellardita, G. Palmisano in *Chapter 4 - (Photo)catalyst Characterization Techniques: Adsorption Isotherms and BET, SEM, FTIR, UV–Vis, Photoluminescence, and Electrochemical Characterizations, Vol.* (Eds.: G. Marcì, L. Palmisano), Elsevier, **2019**, pp.87-152.

[386] M. Thommes, K. Kaneko, A. V. Neimark, J. P. Olivier, F. Rodriguez-Reinoso, J. Rouquerol, K. S. Sing *Pure Appl. Chem.* **2015**, *87*, 1051-1069.

[387] K. H. Mroue, A. Viswan, N. Sinha, A. Ramamoorthy in *Chapter Six - Solid-State NMR Spectroscopy: The Magic Wand to View Bone at Nanoscopic Resolution, Vol. 92* (Ed. G. A. Webb), Academic Press, **2017**, pp.365-413.

[388] R. DeSimone, K. Currie, S. Mitchell, J. Darrow, D. Pippin *Combinatorial chemistry & high throughput*

screening. **2004**, *7*, 473-493.

[389] L. Kollár, G. Keglevich *Chem. Rev.* **2010**, *110*, 4257-4302.

[390] B. Pfeiffer, K. Hauenstein, P. Merz, J. Gertsch, K.-H. Altmann *Bioorganic & medicinal chemistry letters*. **2009**, *19*, 3760-3763.

[391] R. S. Roy, A. M. Gehring, J. C. Milne, P. J. Belshaw, C. T. Walsh *Nat. Prod. Rep.* **1999**, *16*, 249-263.

[392] X. Fernandez, R. Fellous, E. Duñach *Tetrahedron Lett.* **2000**, *41*, 3381-3384.

[393] K. Sun, D. Li, G.-P. Lu, C. Cai *ChemCatChem*. **2021**, *13*, 373-381.

[394] L. Wang, B. Guo, H. X. Li, Q. Li, H. Y. Li, J. P. Lang *Dalton Trans.* **2013**, *42*, 15570-15580.

[395] A. Sakakura, R. Kondo, K. Ishihara *Org. Lett.* **2005**, *7*, 1971-1974.

[396] I. Mohammadpoor-Baltork, M. Moghadam, S. Tangestaninejad, V. Mirkhani, S. F. Hojati *Catal. Commun.* **2008**, *9*, 1153-1161.

[397] P. Anitha, P. Viswanathamurthi, D. Kesavan, R. J. Butcher *J. Coord. Chem.* **2015**, *68*, 321-334.

[398] M. Hosseini-Sarvari, A. Khanivar, F. Moeini *J. Mater. Sci.* **2015**, *50*, 3065-3074.

[399] Z. Li, H. Song, R. Guo, M. Zuo, C. Hou, S. Sun, X. He, Z. Sun, W. Chu *Green Chem.* **2019**, *21*, 3602-3605.

[400] W. Huang, B. C. Ma, H. Lu, R. Li, L. Wang, K. Landfester, K. A. I. Zhang *ACS Catal.* **2017**, *7*, 5438-5442.

[401] Z. Z. Gao, Z. K. Wang, L. Wei, G. Q. Yin, J. Tian, C. Z. Liu, H. Wang, D. W. Zhang, Y. B. Zhang, X. P. Li *ACS Appl. Mater. Interfaces*. **2019**, *12*, 1404-1411.

[402] J. Wang, S. Zhuang *Coord. Chem. Rev.* **2019**, *400*, 213046.

[403] X. Wang, S. Blechert, M. Antonietti *ACS Catal.* **2012**, *2*, 1596-1606.

[404] Y. Wu, J. Ward-Bond, D. Li, S. Zhang, J. Shi, Z. Jiang *ACS Catal.* **2018**, *8*, 5664-5674.

[405] R. Li, B. C. Ma, W. Huang, L. Wang, D. Wang, H. Lu, K. Landfester, K. A. Zhang *ACS Catal.* **2017**, *7*, 3097-3101.

[406] G. Zhang, G. Li, T. Heil, S. Zafeiratos, F. Lai, A. Savateev, M. Antonietti, X. Wang *Angew. Chem. Int. Ed.* **2019**, *58*, 3433-3437.

[407] Z. Zhou, Y. Zhang, Y. Shen, S. Liu, Y. Zhang *Chem. Soc. Rev.* **2018**, *47*, 2298-2321.

[408] R. Qu, W. Zhang, N. Liu, Q. Zhang, Y. Liu, X. Li, Y. Wei, L. Feng *ACS Sustainable Chem. Eng.* **2018**, *6*, 8019-8028.

[409] X. Guan, F. Chen, Q. Fang, S. Qiu *Chem. Soc. Rev.* **2020**, *49*, 1357-1384.

[410] M. Hartmann, A. G. Machoke, W. Schwieger *Chem. Soc. Rev.* **2016**, *45*, 3313-3330.

[411] X. Liu, S. Inagaki, J. Gong *Angew. Chem. Int. Ed.* **2016**, *55*, 14924-14950.

[412] H. Takeda, M. Ohashi, T. Tani, O. Ishitani, S. Inagaki *Inorg. Chem.* **2010**, *49*, 4554-4559.

[413] E. D. Koutsouroubi, A. K. Xylouri, G. S. Armatas *Chem. Commun.* **2015**, *51*, 4481-4484.

[414] T. Selvam, A. Machoke, W. Schwieger *Appl. Catal., A*. **2012**, *445-446*, 92-101.

[415] J. G. Croissant, X. Cattoën, J.-O. Durand, M. W. C. Man, N. M. Khashab *Nanoscale*. **2016**, *8*, 19945-19972.

[416] X. Qian, K. Fuku, Y. Kuwahara, T. Kamegawa, K. Mori, H. Yamashita *ChemSusChem*. **2014**, *7*, 1495-1495.

[417] D. Aldakov, M. A. Palacios, P. Anzenbacher *Chem. Mater.* **2005**, *17*, 5238-5241.

[418] F. S. Mancilha, B. A. DaSilveira Neto, A. S. Lopes, P. F. Moreira Jr, F. H. Quina, R. S. Gonçalves, J. Dupont *Eur. J. Org. Chem.* **2006**, *2006*, 4924-4933.

[419] M. S. Lowry, J. I. Goldsmith, J. D. Slinker, R. Rohl, R. A. Pascal, G. G. Malliaras, S. Bernhard *Chem.*

Mater. **2005**, *17*, 5712-5719.

[420] M. T. Reetz *J. Am. Chem. Soc.* **2013**, *135*, 12480-12496.

[421] F. Hollmann, D. J. Opperman, C. E. Paul *Angew. Chem. Int. Ed.* **2021**, *60*, 5644-5665.

[422] D. Yi, T. Bayer, C. P. S. Badenhorst, S. Wu, M. Doerr, M. Höhne, U. T. Bornscheuer *Chem. Soc. Rev.* **2021**, *50*, 8003-8049.

[423] S. Wu, R. Snajdrova, J. C. Moore, K. Baldenius, U. T. Bornscheuer *Angew. Chem. Int. Ed.* **2021**, *60*, 88-119.

[424] P. D. de María, G. de Gonzalo, A. R. Alcántara *Catalysts*. **2019**, *9*, 802.

[425] T. Hering, B. Mühldorf, R. Wolf, B. Koenig *Angew. Chem. Int. Ed.* **2016**, *55*, 5342-5345.

[426] L. Schroeder, M. Frese, C. Müller, N. Sewald, T. Kottke *ChemCatChem*. **2018**, *10*, 3336-3341.

[427] J. Zelenka, E. Svobodová, J. Tarabek, I. Hoskovcová, V. Boguschová, S. Bailly, M. Sikorski, J. Roithová, R. Cibulka *Org. Lett.* **2018**, *21*, 114-119.

[428] W. Y. Zhang, E. Fernández-Fueyo, Y. Ni, M. Van Schie, J. Gacs, R. Renirie, R. Wever, F. G. Mutti, D. Rother, M. Alcalde, F. Hollmann *Nat. Catal.* **2018**, *1*, 55-62.

[429] E. Churakova, M. Kluge, R. Ullrich, I. Arends, M. Hofrichter, F. Hollmann *Angew. Chem. Int. Ed.* **2011**, *50*, 10716-10719.

[430] S. Lin, S. Y. Sun, K. Wang, K. X. Shen, B. B. Ma, Y. Q. Ren, X. Y. Fan *Nanomaterials*. **2018**, *8*, 127.

[431] S. H. Lee, D. S. Choi, M. Pesic, Y. W. Lee, C. E. Paul, F. Hollmann, C. B. Park *Angew. Chem. Int. Ed.* **2017**, *56*, 8681-8685.

[432] D. Holtmann, F. Hollmann *ChemBioChem*. **2016**, *17*, 1391-1398.

[433] K. Liu, C. Q. Yuan, Q. L. Zou, Z. C. Xie, X. H. Yan *Angew. Chem. Int. Ed.* **2017**, *56*, 7876-7880.

[434] M. Mifsud, S. Gargiulo, S. Iborra, I. W. C. E. Arends, F. Hollmann, A. Corma *Nat. Commun.* **2014**, *5*.

[435] M. M. C. H. Van Schie, W. Zhang, F. Tieves, D. S. Choi, C. B. Park, B. O. Burek, J. Z. Bloh, I. W. C. E. Arends, C. E. Paul, M. Alcalde, F. Hollmann *ACS Catal.* **2019**, *9*, 7409-7417.

[436] X. Ding, C. L. Dong, Z. Guan, Y. H. He *Angew. Chem. Int. Ed.* **2019**, *58*, 118-124.

[437] C. Y. Chan, H. S. Chan, P. K. Wong *Chemosphere*. **2019**, *222*, 371-380.

[438] E. B. Simsek, D. Saloglu *J. Mol. Liq.* **2021**, 116612.

[439] C. Lowe *Philosophical Transactions of the Royal Society of London. B, Biological Sciences*. **1983**, *300*, 335-353.

[440] A. W. Munro, K. J. McLean in *Electron Transfer Cofactors, Vol.* (Ed. G. C. K. Roberts), Springer Berlin Heidelberg, Berlin, Heidelberg, **2013**, pp.601-606.

[441] J. Ryu, S. H. Lee, D. H. Nam, C. B. Park *Adv. Mater.* **2011**, *23*, 1883-1888.

[442] S. H. Lee, D. H. Nam, C. B. Park *Adv. Synth. Catal.* **2009**, *351*, 2589-2594.

[443] R. K. Yadav, A. Kumar, N. J. Park, D. Yadav, J. O. Baeg *ChemCatChem*. **2017**, *9*, 3153-3159.

[444] J. Liu, J. Huang, H. Zhou, M. Antonietti *ACS Appl. Mater. Interfaces*. **2014**, *6*, 8434-8440.

[445] Y. Z. Wu, J. Ward-Bond, D. L. Li, S. H. Zhang, J. F. Shi, Z. Y. Jiang *ACS Catal.* **2018**, *8*, 5664-5674.

[446] D. Yang, Y. S. Zhang, S. H. Zhang, Y. Q. Cheng, Y. Z. Wu, Z. Y. Cai, X. D. Wang, J. F. Shi, Z. Y. Jiang *ACS Catal.* **2019**, *9*, 11492-11501.

[447] W. G. Liu, W. J. Hu, L. J. Yang, J. Liu *Nano Energy*. **2020**, *73*, 104750.

[448] J. Liu, M. Antonietti *Energy Environ. Sci.* **2013**, *6*, 1486-1493.

[449] Y. C. Wang, H. Liu, Q. Y. Pan, C. Y. Wu, W. B. Hao, J. Xu, R. Z. Chen, J. Liu, Z. B. Li, Y. J. Zhao *J. Am. Chem. Soc.* **2020**, *142*, 5958-5963.

[450] F. Lan, Q. Wang, H. Chen, Y. Chen, Y. Zhang, B. Huang, H. Liu, J. Liu, R. Li *ACS Catal.* **2020**, *10*, 12976-12986.

[451] C. T. J. Ferguson, N. Huber, K. Landfester, K. A. I. Zhang *Angew. Chem. Int. Ed.* **2019**, *58*, 10567-10571.

[452] Y. Zhang, Y. Zhao, R. Li, J. Liu *Solar RRL*. **2021**, *5*, 2000339.

[453] L. Schmermund, V. Jurkaš, F. F. Özgen, G. D. Barone, H. C. Büchsenschütz, C. K. Winkler, S. Schmidt, R. Kourist, W. Kroutil *ACS Catal.* **2019**, *9*, 4115-4144.

[454] B. C. Ma, L. Caire Da Silva, S. M. Jo, F. R. Wurm, M. B. Bannwarth, K. A. I. Zhang, K. Sundmacher, K. Landfester *ChemBioChem*. **2019**, *20*, 2593-2596.

[455] S. M. Jo, K. A. I. Zhang, F. R. Wurm, K. Landfester *ACS Appl. Mater. Interfaces*. **2020**, *12*, 25625-25632.

[456] W. Shin, M. Y. Jo, D. S. You, Y. S. Jeong, D. Y. Yoon, J. W. Kang, J. H. Cho, G. D. Lee, S. S. Hong, J. H. Kim *Synth. Met.* **2012**, *162*, 768-774.

[457] W. Wei, R. Li, N. Huber, G. Kizilsavas, C. T. J. Ferguson, K. Landfester, K. A. I. Zhang *ChemCatChem*. **2021**, *13*, 3410-3413.

[458] F. S. Mancilha, B. A. DaSilveira Neto, A. S. Lopes, P. F. Moreira Jr, F. H. Quina, R. S. Gonçalves, J. Dupont in Are Molecular 5, 8-π-Extended Quinoxaline Derivatives Good Chromophores for Photoluminescence Applications?, Vol. (Ed.^Eds.: Editor), Wiley Online Library, City, **2006**.

[459] T. Pullerits, V. Sundström *Acc. Chem. Res.* **1996**, *29*, 381-389.

[460] A. A. Pascal, Z. Liu, K. Broess, B. van Oort, H. van Amerongen, C. Wang, P. Horton, B. Robert, W. Chang, A. Ruban *Nature*. **2005**, *436*, 134-137.

[461] J. H. Alstrum-Acevedo, M. K. Brennaman, T. J. Meyer *Inorg. Chem.* **2005**, *44*, 6802-6827.

[462] V. Balzani, A. Credi, M. Venturi *ChemSusChem: Chemistry & Sustainability Energy & Materials*. **2008**, *1*, 26-58.

[463] A. Ajayaghosh, V. K. Praveen *Acc. Chem. Res.* **2007**, *40*, 644-656.

[464] G. Calzaferri, K. Lutkouskaya *Photochemical & photobiological sciences*. **2008**, *7*, 879-910.

[465] P. Van Der Voort, D. Esquivel, E. De Canck, F. Goethals, I. Van Driessche, F. J. Romero-Salguero *Chem. Soc. Rev.* **2013**, *42*, 3913-3955.

[466] N. Mizoshita, Y. Goto, T. Tani, S. Inagaki *Adv. Mater.* **2009**, *21*, 4798-4801.

[467] N. Mizoshita, M. Ikai, T. Tani, S. Inagaki *J. Am. Chem. Soc.* **2009**, *131*, 14225-14227.

[468] M. Ohashi, M. Aoki, K. i. Yamanaka, K. Nakajima, T. Ohsuna, T. Tani, S. Inagaki *Chem. Eur. J.* **2009**, *15*, 13041-13046.

[469] S. Inagaki, O. Ohtani, Y. Goto, K. Okamoto, M. Ikai, K. i. Yamanaka, T. Tani, T. Okada *Angewandte Chemie*. **2009**, *121*, 4102-4106.

[470] S. Ito, S. Fukuya, T. Kusumi, Y. Ishibashi, H. Miyasaka, Y. Goto, M. Ikai, T. Tani, S. Inagaki *The Journal of Physical Chemistry C*. **2009**, *113*, 11884-11891.

[471] W. Lin, H. Frei *J. Am. Chem. Soc.* **2005**, *127*, 1610-1611.

[472] S. Takagi, M. Eguchi, D. A. Tryk, H. Inoue *Langmuir*. **2006**, *22*, 1406-1408.

[473] M. Borja, P. K. Dutta *Nature*. **1993**, *362*, 43-45.

[474] N. Huber, R. Li, C. T. J. Ferguson, D. W. Gehrig, C. Ramanan, P. W. M. Blom, K. Landfester, K. A. I. Zhang *Catal. Sci. Technol.* **2020**, *10*, 2092-2099.

[475] T. Tani, N. Mizoshita, S. Inagaki *J. Mater. Chem.* **2009**, *19*, 4451-4456.

[476] T. Okada, K.-i. Yamanaka, Y. Hirose, Y. Goto, T. Tani, S. Inagaki *PCCP*. **2011**, *13*, 7961-7967.

[477] T. W. Gadella, FRET and FLIM techniques, Elsevier, **2011**.

[478] G. A. Jones, D. S. Bradshaw *Front. Phys.* **2019**, *7*.

[479] K.-i. Yamanaka, T. Okada, Y. Goto, T. Tani, S. Inagaki *RSC Adv.* **2013**, *3*, 14774-14779.

[480] Y. Maegawa, T. Nagano, T. Yabuno, H. Nakagawa, T. Shimada *Tetrahedron*. **2007**, *63*, 11467-11474.

[481] H. Bader, V. Sturzenegger, J. Hoigné *Water Res.* **1988**, *22*, 1109-1115.

[482] C. Zhu, Y. Wei *ChemSusChem*. **2011**, *4*, 1082-1086.

[483] B. Guo, H. X. Li, S. Q. Zhang, D. J. Young, J. P. Lang *ChemCatChem*. **2018**, *10*, 5627-5636.

[484] K. Goossens, S. Wellens, K. Van Hecke, L. Van Meervelt, T. Cardinaels, K. Binnemans *Chemistry – A European Journal*. **2011**, *17*, 4291-4306.

[485] J. H. Barnard, C. Wang, N. G. Berry, J. Xiao *Chem. Sci.* **2013**, *4*, 1234-1244.

[486] M. Ishihara, H. Togo *Tetrahedron*. **2007**, *63*, 1474-1480.

[487] P. Garg, S. Chaudhary, M. D. Milton *The Journal of organic chemistry*. **2014**, *79*, 8668-8677.

[488] C. T. Supuran, S. Kalinin, M. Tanç, P. Sarnpitak, P. Mujumdar, S.-A. Poulsen, M. Krasavin *J. Enzyme Inhib. Med. Chem.* **2016**, *31*, 197-202.

[489] T. Mizuhara, S. Oishi, N. Fujii, H. Ohno *The Journal of organic chemistry*. **2010**, *75*, 265-268.

[490] H. Prokopcová, C. O. Kappe *Adv. Synth. Catal.* **2007**, *349*, 448-452.

[491] D. Singh, G. S. Kumar, M. Kapur *The Journal of organic chemistry*. **2019**, *84*, 12881-12892.

[492] B. Verbraeken, J. Hullaert, J. Van Guyse, K. Van Hecke, J. Winne, R. Hoogenboom *J. Am. Chem. Soc.* **2018**, *140*, 17404-17408.

[493] A. R. Katritzky, C. Cai, K. Suzuki, S. K. Singh *The Journal of organic chemistry*. **2004**, *69*, 811-814.

[494] V. S. Patil, V. S. Padalkar, A. B. Tathe, V. D. Gupta, N. Sekar *J. Fluoresc.* **2013**, *23*, 1019-1029.

[495] A. D. McLean, G. S. Chandler *J. Chem. Phys.* **1980**, *72*, 5639-5648.

[496] J. G. Croissant, C. Qi, O. Mongin, V. Hugues, M. Blanchard-Desce, L. Raehm, X. Cattoën, M. Wong Chi Man, M. Maynadier, M. Gary-Bobo, M. Garcia, J. I. Zink, J. O. Durand *J. Mater. Chem. B*. **2015**, *3*, 6456-6461.

[497] D. Shen, J. Yang, X. Li, L. Zhou, R. Zhang, W. Li, L. Chen, R. Wang, F. Zhang, D. Zhao *Nano Lett.* **2014**, *14*, 923-932.

[498] H. Huang, S. Banerjee, K. Qiu, P. Zhang, O. Blacque, T. Malcomson, M. J. Paterson, G. J. Clarkson, M. Staniforth, V. G. Stavros *Nat. Chem.* **2019**, *11*, 1041-1048.

[499] S. Fukuzumi, M. Ishikawa, T. Tanaka *J. Chem. Soc., Perkin Trans. 2*. **1989**, 1037-1045.

9. List of scientific contributions

Journal publications:

W. Wei, R. Li, N. Huber, G. Kizilsavas, C. T. J. Ferguson, K. Landfester, K. A. I. Zhang, *Visible light-promoted aryl azoline formation over mesoporous organosilica as heterogeneous photocatalyst*, ChemCatChem **2021**, *13*, 3410-3413.

W. Wei, F. Mazzotta, I. Lieberwirth, K. Landfester, C. T. J. Ferguson, K. A. I. Zhang, *Aerobic photobiocatalysis enabled by combining core-shell nanophotoreactors and native enzymes.* (submitted)

W. Wei, C. T. J. Ferguson, K. Landfester, K. A. I. Zhang, *Enhanced photocatalytic NADH regeneration by improved light-harvesting mesoporous organosilica.* (preparing)

E. Jin, S. Fu, H. Hanayama, M. A. Addicoat, W. Wei, Q. Chen, R. Graf, K. Landfester, M. Bonn, K. A. I. Zhang, H. I. Wang, K. Müllen, A. Narita, *A nanographene-based two-dimensional covalent organic framework as a stable and efficient photocatalyst.* (accepted)

Conference contribution:

W. Wei, W. Huang, R. Li, L. Wang, K. A. I. Zhang, *Conjugated Porous Polymers for Photocatalytic Application*, The 31st Annual Conference of GCCCD (Gesellschaft Chinesischer Chemiker und Chemieingenieure in der Bundesrepublik Deutschland e.V.) (Mainz, Germany) **2019.**